Rute Alexandra Borges de Almeida

Automatic ECG Characterization: Application to QT Interval Variability

Departamento de Matemática Aplicada
Faculdade de Ciências da Universidade do Porto
December 2006

Rute Alexandra Borges de Almeida

Automatic ECG Characterization: Application to QT Interval Variability

PhD thesis submitted to
Faculdade de Ciências da Universidade do Porto
(para obtenção do grau de Doutor em Matemática Aplicada)

Advisers:
Ana Paula de Frias Viegas Proença Rocha
Pablo Laguna Lasarosa

Departamento de Matemática Aplicada
Faculdade de Ciências da Universidade do Porto
December 2006

Acknowledgements

My research work during the last years would not be possible without the kind collaboration of many persons, either with collaborative scientific work, either with their personal support.

I would like to thanks to my advisers Doutora *Ana Paula Rocha* and Professor *Pablo Laguna* by their time and availability to painful and long brainstorming meetings, without which this work would not be possible. I acknowledge also the useful suggestions of Professor *Pedro Lago* and the clinical expertise of Professor *Ovídio Costa*, which have been a big contribute for this research. Also, I want to thank the kind contribution of Professor *António Falcão de Freitas* in the early phase of this work. His presence was missed.

To my several colleagues in the laboratory in DMA during these years I want to thanks the pleasant company and collaborative spirit, particularly to *Hugo Magalhães* and *Hernâni Gonçalves*. I am very grateful to *Sónia Gouveia* by her suggestions, time and enormous patience. My thanks go also to *Juan Pablo Martinez* for all the helpful collaboration and attention, to the other co-authors of the papers written under the collaborations during this research period, and to all people in CPS that have made me fell so welcome.

I acknowledge to Mortara Instr Inc, Milwaukee, WI, USA, represented in Portugal by CardioSolutions, Lda., for technical support, and to Centro de Matemática da Universidade do Porto (CMUP), financed by *FCT* (Portugal) through the programmes POCTI (Programa Operacional "Ciência, Tecnologia, Inovação") and POSI 2010 (Programa Operacional Sociedade da Informação), with national and European Community structural funds (ESF) [http://cmup.fc.up.pt/cmup/]. I also acknowledge the grant SFRH/BD/5484/2001 supported by *FCT* and ESF (CSF III), and the projects TEC2004-05263-C02-02 from CICYT/FEDER (Spain) and *"Análise de variabilidade cardiovascular em doença crítica: seguimento e prognóstico" (Projectos pluridisciplinares U Porto Caixa Geral de Depósitos Investigação Científica na pré graduação)*, as well as to all the participants. In particular, I would like to thank to the undergraduate FCUP students *Ana Castro*, *António Vela*, *Lara Lacerda*, *Luis Barros* and *Tiago Ventura* by their inspiring enthusiasm.

Finally, I want to thanks to my family for their support and encouragement, specially to my husband, the utmost victim of my bad mood and who backed up my decisions at all times.

I am deeply grateful to all.

Abstract

The electrocardiogram (ECG) is the record of the cardiac electrical activity. Electrical abnormalities may conduct or predispose to life threatening conditions and therefore the ECG signal is an indispensable diagnostic tool today.

The heart's electrical phenomena correspond to different ECG waves, typically known as P, Q, R, S and T waves, and the ECG can be used to access both the phenomena durations and its beat-to-beat variations. The series of RR intervals (the time intervals between consecutive R waves) is the simplest of the extracted ECG series and is currently used as heart rate signal. Also, the series of QT intervals (time between the onset of the QRS complex and the T wave end) is usually considered as an index of cardiac repolarization.

Automatic systems avoid inter and intra observer variability and can easily deal with large amounts of data, as in ambulatory Holter recordings, constituting an indispensable tool for today's electrocardiography. Namely, to measure the clinically relevant time intervals in the ECG, it is required the correct delineation of the signal, by locating its waves's peaks and boundaries (fiducial points).

In this thesis is presented a wavelet transform based delineation system, which provides the fiducial points location according to each ECG lead (the recording over a cardiac axis). Being a single-lead system, it's unable to deal with simultaneous leads, which constitute routine clinical ECGs. Most of the published delineation systems are single-lead, in spite some of them include a post-processing strategy to deal with multiple leads. That is, each lead is processed and then decision rules are applied over the sets of single-lead based locations to chose the most adequate one. However, applying post-processing lead selection rules is not truly a multilead delineation, as it does not take any advantage of the spacial information available.

In this thesis it's also proposed an alternative multilead based system for boundaries location, which is based in the vectocardiographic representation obtained with three orthogonal ECG leads. Both single and multilead systems are fully automatic and attained good results over standard manually annotated ECG databases, outperforming other published approaches. The multilead methodology was implemented regarding the Q wave onset and T wave end, outperforming single-lead based delineation in both cases. The error's standard deviation found was similar to using of single-lead plus post-processing decision rules over 12 or 15 leads.

The evaluation of the cardiac rhythms is a problem of major importance. Abnormal, QT lengths and QT beat-to-beat variability (QTV), have been associated to several pathological conditions and

increased risk situations. The RR interval variability (HRV) strongly affects ventricular repolarization and the QT interval is highly dependent on the preceding RR intervals. Nevertheless the quantification of this relation has not been established yet.

The good results obtained by the automatic delineation systems proposed, showing robustness against noise and morphological variations, provide accurate measuring of both RR and QT intervals. This allows to use the measured RR and QT intervals to explore the relation between HRV and QTV. Furthermore, the improvement obtained using multilead delineation when 3 leads are available represents an additional advantage in variability quantification.

In this thesis it is proposed to explore the short term relations between ventricular repolarization and heart rate variabilities using a dynamic linear approach over the series of QT and RR intervals variations. The methodology provides a quantification of the QTV fractions, either correlated or not correlated with HRV, with the aim to understand its significance and origin. Results over simulated series evidenced that this parametric methods provide an adequate estimation of the QTV fraction linearly driven by HRV.

The joint performance of the delineation systems plus the parametric methodology for QTV/HRV relations was evaluated using artificial ECG signals, which were constructed according simulated RR and QT series. Noise contamination considering several noise types and levels was incorporated in the artificial ECG to evaluate the robustness of the global methodology. The adequateness for studying QTV versus HRV relations of the automatic methods proposed in this thesis was confirmed and its applicability facing clinical ECG recordings was established.

The robustness of automatic delineation and parametric methodology allows to face their usage as a tool in the clinical practice. The methods were illustrated in real ECG recordings of young normal subjects from a standard published database, and in clinical Holter data.

Resumo

O electrocardiograma (ECG) é o registo da actividade eléctrica cardíaca. Anomalias eléctricas podem conduzir a condições graves de risco de vida e assim o sinal de ECG é hoje em dia uma ferramenta de diagnóstico indispensável.

Os fenómenos eléctricos cardíacos correspondem a diferentes ondas no ECG, tipicamente conhecidas por ondas P, Q, R, S e T, e o ECG pode ser usado para aceder a durações de fenómenos e às suas variações batimento a batimento. A série dos intervalos RR (os intervalos do tempo entre ondas R consecutivas) é a mais simples das séries extraídas do ECG, sendo usada actualmente como o sinal de frequência cardíaca. Também, a série dos intervalos do QT (intervalos entre o início do complexo QRS e o fim da onda de T) é geralmente considerada um índice do repolarização cardíaca.

Os sistemas automáticos evitam a variabilidade inter e intra observador e permitem processar facilmente grandes quantidades de dados, como no caso de registos ambulatórios de Holter, sendo uma ferramenta indispensável para a electrocardiografia actual. Em particular, para medir os intervalos de tempo clinicamente relevantes no ECG, é necessário o correcto delineamento do sinal, localizando os picos e limites das suas ondas (pontos fiduciais).

Nesta tese é apresentado um sistema de delineamento baseado em transformadas de ôndulas que fornece a posição dos pontos fiduciais de acordo com uma derivação de sinal ECG (registo efectuado ao longo de um eixo cardíaco). Este sistema não está preparado para lidar com sinais multi-derivacionais, como é o caso dos ECGs de rotina. A maioria dos sistemas de delineamento publicados baseiam-se numa única derivação, apesar de alguns deles incluírem uma estratégia do pós-processamento para combinar a informação de várias derivações. Nesse caso, cada derivação é processada separadamente, sendo aplicadas regras de decisão sobre os conjuntos de posições obtidos, de forma a escolher a posição mais adequada para cada ponto fiducial. No entanto, a aplicação de regras de selecção não é verdadeiramente uma estratégia multi-derivacional, não permitindo tirar qualquer vantagem da informação espacial disponível.

Nesta tese é também proposto um sistema alternativo multi-derivacional para localizar os limites das ondas no ECG, baseado no vectocardiograma definido por três derivações ortogonais. Ambos os sistemas de delineamento são completamente automáticos e permitiram alcançar bons resultados quando validados sobre bases de dados de referencia com anotações manuais, mostrando melhor desempenho que outros sistemas publicados. A metodologia multi-derivacional foi implementada para a localização do início da onda Q e do final da onda T, alcançando resultados melhores que o

sistema uni-derivacional para ambos os pontos. Foi obtido um valor para o desvio padrão do erro semelhante ao obtido processando separadamente 12 ou 15 derivações e aplicando regras de escolha.

A avaliação dos ritmos cardíacos é um problema de importância crucial. Valores anormais de duração do intervalo QT ou variabilidade batimento a batimento (QTV) foram associados a diversas condições patológicas e situações de risco acrescido. A variabilidade do intervalo do RR (HRV) afecta fortemente a repolarização ventricular e o intervalo QT é altamente dependente dos intervalos RR precedentes. Não obstante, a quantificação desta relação não foi ainda estabelecida.

Os bons resultados obtidos pelos sistemas automáticos do delineamento propostos, mostrando robustez ao ruído e às variações morfológicas, permitem a medição correcta dos intervalos RR e QT. Assim é possível utilizar os intervalos medidos para explorar a relação entre HRV e QTV. Além disso, a melhoria obtida usando o delineamento multi-derivacional quando estão disponíveis 3 derivações representa uma vantagem na quantificação da variabilidade.

Nesta tese propõe-se explorar as relações a curto prazo entre as variabilidades da repolarização ventricular e da frequência cardíaca, usando um modelo linear dinâmico sobre as séries de variações dos intervalos QT e RR. A metodologia fornece uma quantificação das fracções de QTV, correlacionadas ou não correlacionadas com a HRV, com o propósito de compreender o seu significado e origem. Resultados obtidos sobre séries simuladas evidenciaram que estes métodos paramétricos fornecem uma estimativa adequada da fracção de QTV linearmente dependente da HRV.

O desempenho conjunto dos sistemas de delineamento e metodologia paramétrica para relações de QTV/HRV foi avaliada usando sinais artificiais de ECG, construídos seguindo séries simuladas de intervalos RR e QT. Os sinais foram contaminados com diversos tipos e níveis de ruído de forma a avaliar a robustez global da metodologia. Os métodos automáticos propostos nesta tese mostraram-se adequados para o estudo das relações QTV/HRV e foi estabelecida a sua aplicabilidade em registos clínicos.

A robustez do delineamento automático e da metodologia paramétrica permitem o seu uso na prática clínica. Os métodos foram ainda ilustrados em registos reais de ECG de indivíduos normais jovens de uma base de dados publicada, e em dados clínicos de Holter.

Résumé

L'électrocardiogramme (ECG) est l'enregistrement de l'activité électrique cardiaque. Les anomalies électriques peuvent conduire ou prédisposer à des conditions représentant danger pour la vie et l' ECG est aujourd'hui un outil de diagnostique indispensable.

Les phénomènes électriques cardiaques correspondent à différentes ondes dans l' ECG, typiquement connues comme P, Q, R, S et T, et l' ECG peut ainsi être employé pour accéder à la durée des phénomènes et à sa variabilité. La série d'intervalles RR est la plus simple des séries d'ECG et la série d'intervalles de QT est habituellement considérée comme un index de repolarisation cardiaque.

Les systèmes automatiques évitent l'inter et l'intra variabilité de l'observateur et peuvent facilement traiter grandes quantités de données comme dans le cas d' enregistrements ambulatoires (Holter). Ainsi, les systèmes automatiques sont un outil indispensable pour l'électrocardiographie d'aujourd'hui, et la correcte délinéation du signal en localisant touts ses points fiduciels est indispensable.

Dans cette thèse est présentée un système de délinéation, basée en ondelettes capable de déterminer les points fiduciels selon chaque signal d'ECG (dérivation). Étant un système d'une unique dérivation, il ne peut pas traiter simultanément les différentes dérivations de l'ECG, qui sont les enregistrements sur différents axes cardiaques et que constituent l' ÉCG de routine. La plupart des systèmes de délinéation sont d'une seule dérivation, malgré quelques uns incluent une stratégie de traitement pour les différentes dérivations, en analysant chaque dérivation individuellement et en appliquent des règles de décision pour choisir la plus convenable. L'application des règles de choix de dérivation n'est pas vraiment une délinéation multi dérivation, car elle ne profite pas de l'information spatiale disponible.

Dans cette thèse on propose aussi un système alternatif basée sur la représentation vectorcardiographique de trois dérivations orthogonales de l'ECG. Les deux systèmes sont entièrement automatiques et ont conduit à bons résultats sur des bases de données manuellement annotées, en surpassant d'autres approches reportées en la littérature. La méthodologie multi dérivation a montré des résultats supérieurs en ce qui concerne le début de l'onde Q et l'extrémité de l' onde T, présentant un écart type de erreurs semblable à l'utilisation d'une dérivation simple plus des règles de décision sur 12 ou 15 dérivations.

L'évaluation des rythmes cardiaques est un problème d'importance majeure. Les longueurs anormales du QT et ses variations battement à battement (QTV) ont été associées à plusieurs conditions pathologiques et situations de risque. Les variations du intervalle RR (HRV) affectent fortement la repolarisation ventriculaire et le QTV dépend fortement des intervalles précédents de RR. Néanmoins

la quantification de cette relation n'a pas encore été établie.

Les bons résultats obtenus par les systèmes automatiques de délinéation proposés, montrant la robustesse contre le bruit et les variations morphologiques, permettent une mesure précise des intervalles RR et QT. Ceci permet employer les intervalles mesurés du RR et du QT pour explorer la relation entre HRV et QTV. En autre façon, l'amélioration obtenue en utilisant la délinéation de multi dérivation quand 3 dérivations sont disponibles, peut représenter un avantage sur la quantification de la variabilité.

Dans cette thèse on propose d'explorer les relations à terme court entre les variabilités de VR et HR en utilisant une approche linéaire dynamique sur la série des variations des intervalles de QT et de RR. La méthodologie fournit une quantification des fractions de QTV, corrélées ou non corrélées avec HRV, avec le but de comprendre sa vrai signification et origine. Les résultats sur séries simulées ont démontré que les méthodes sont capables de fournir l'évaluation de la fraction de QTV conduite par HRV.

L'exécution combinée des systèmes de délinéation et de la méthodologie paramétrique pour la relation QTV/HRV a été évaluée en utilisant les signaux artificiels d'ECG, qui ont été construits suivant la série simulée de RR et de QT. La contamination de bruit a considéré plusieurs types et niveaux de bruit ajouté au ECG artificiel pour évaluer la robustesse de la méthodologie globale.

La suffisance des méthodes automatiques proposés dans cette thèse pour étudier QTV contre des relations de HRV a été alors confirmée et son applicabilité face aux enregistrements cliniques d'ECG a été établie. Les méthodes ont été illustrés avec enregistrements d'ECG de sujets normaux d'une base de donnés standard et avec des données cliniques d'Holter.

Contents

Acronyms

PHYSIOLOGICAL

ANS - autonomic nervous system
AP - action potential
CHF - congestive heart failure
DAN - diabetic autonomic neuropathy
DMC - dilated cardiomyopathy
ECG - electrocardiogram
EHV - electric heart vector
HCM - hypertrophic cardiomyopathy
HR - heart rate
HRV - heart rate variability
LQTS - long QT syndrome
MI - myocardial infaction
QT - time interval between the QRS complex onset and the T wave end
QTc - QT interval corrected from HR
QTV - QT interval variability
QTVI -QT variability index
RR - time interval between the main wave peaks (usually the R wave) in consecutive QRS complexes
RT or RTapex - time interval between the main wave in QRS complex (usually the R wave) and T wave peaks'
RTV - RT interval variability
VCG - vectocardiogram
VF - ventricular fibrillation
VR - ventricular repolarization
VRV - ventricular repolarization variability

MATHEMATIC

AIC - Akaike information criteria
AR - autoregressive model
ARARX - autoregressive model with an autoregressive exogenous input
ARMA - autoregressive moving average model
CWT - continuous wavelet transform
DWT - discrete wavelet transform
FIR - finite impulse response
GLS - generalized least squares
HF - high frequency
IPFM - integral pulse frequency modulation
LF - low frequency
LS - least squares
ML - multilead delineation
PC - principal component
PSD - power spectral density
SL - single-lead delineation
SLR - single-lead delineation with post-processing decision rules
SNR - signal to noise ratio
STFT - short time Fourier transform
TLS - total least squares
TP - total power
VLF - very low frequency
WT - wavelet transform

Notation and Units

AR_p - order p autoregressive random process
$ARARX_q$ - order q autoregressive random process with an autogressive exogenous input
bpm - beats per minute
CV - coefficient of variation
$det\,(H)$ - determinant of the matrix H
F - linear frequency (Hz)
F_r - instantaneous respiratory frequency
F_s - sampling frequency
h - hours
k - sample number
$K^2(F)$ - magnitude of the squared spectral coherence at linear frequency F
L^2 - set of square integrable functions
$Max\,[y(k)]\,|_{k\in I}$ - Maximum of $y(k)$ for $k \in I$
$Max\,\{a,\ b\}$ - Maximum of the set $\{a,\ b\}$
$Min\,[y(k)]\,|_{k\in I}$ - Minimum of $y(k)$ for $k \in I$
$Min\,\{a,\ b\}$ - Minimum of the set $\{a,\ b\}$
ms - milliseconds
mV - millivolts
m_x - sample mean of x
n - beat number
N - data length
p - AR model order
P^+ - positive predictivity
$P_x^{\mathcal{B}}$ - power within a frequency band $\mathcal{B}$ of the signal x
q - ARARX model order
$R_{QT|RR}^{\mathcal{B}}$ - relative fraction of QTV driven by RR in the frequency band $\mathcal{B}$
rad - radians
$\mathrm{RMS}\,[y(k)]\,|_{k\in I}$ - Root Mean Square of $y(k)$ for $k \in I$ $\left(\mathrm{RMS}\,[y(k)]\,|_{k\in I,\ I=\{k1,k1+1,\ldots k2\}} = \sqrt{\frac{\sum_{k=k1}^{k2}|y(k)|^2}{k2-k1+1}}\right)$
$\mathrm{RMS}\,[y(k)]$ - Root Mean Square of $y(k)$ for all samples k
$S_{\mathrm{x}}(F)$ - Power Spectral Density function of the series $x(n)$
$S\ \ (F)$ - Power Spectral Density function of the series $x\ \ (n)$
sd - sample standard deviation

Se - sensitivity
sec - seconds
s_x - sample standard deviation of x
$\bar{s}_x$ - mean of sample standard deviation of x across different cases
t - time
T_{QT} - mean QT
T_R - mean RR
V - volts
$W^y_{2^m}(k)$ - Wavelet Transform of the signal $y(k)$ at the dyadic scale 2^m
$w_{\mathrm{X}}(n)$ - zero-mean white noise with variance λ^2_{X}
$x_{QT|RR}$ or $QT|RR$- fraction of QTV driven by RR
$x_{QT|QT}$ or $QT|QT$ - fraction of QTV uncorrelated with RR
$x_{\mathrm{QT}}(n)$ - QT interval series corrected for the mean
$x_{\mathrm{RR}}(n)$ - RR interval series corrected for the mean
$y(t)$ - continuous signal
$y(k)$ - sampled signal y at sample k
$\mathcal{B}$ - frequency band
λ^2_{X} - variance of a signal identified by X
$\mathbf{\Sigma}$ - covariance matrix
$\xi^{\mathcal{B}}$ - error in estimated variability measure for the frequency band $\mathcal{B}$
$\varepsilon^{\mathcal{B}}$ - percentage error in estimated relative fraction of QTV for the frequency band $\mathcal{B}$
$\psi(t)$ - wavelet prototype
$\psi^*(t)$ - complex conjugate of $\psi(t)$
$\Psi(\omega)$ - Fourier Transform of $\psi(t)$
$det\,(H)$ - determinant of the matrix H
$ph(F)$ - phase at linear frequency F
$\Re(.)$ - real part
$\hat{}$ - estimated
$*$ - convolution operation
$\mathbf{M}'$ - transpose of matrix $\mathbf{M}$
$\|\mathbf{U}\|$ - euclidean norm of a vector $\mathbf{U}$, with elements U^E $\left(\|\mathbf{U}\| = \sqrt{\sum_E |U^E|^2}\right)$
$\|\mathbf{M}\|_F$ - Frobenius norm of a matrix $\mathbf{M}_{NXM}$, with elements m_{ij} $\left(\|M\|_F = \sqrt{\sum_i \sum_j |m_{ij}|^2}\right)$

Chapter 1

The Electrocardiogram: Assessing the Heart function

The electrocardiogram (ECG) is the record of the cardiac electrical activity, usually made at the body surface. Recording the ECG is a noninvasive and painless procedure, not implying discomfort to the patients and extremely cheap compared with other methods to assess the heart function. This signal has been extensively used in clinical medicine for more than 80 years, being an indispensable diagnostic tool for many cardiac and non cardiac conditions (Fisch, 2000; Van Mieghem *et al.*, 2004). It allows to detect some congenital heart abnormalities, thickness or damage in the heart muscle, to diagnose prior or ongoing heart attacks (myocardial infarction) or to notice evidence of acutely impaired blood flow in the heart, among many other diseases.

The ECG is recorded by means of electrodes placed on the skin, recording the electrical field from active heart as a function of time. By using several electrodes it is possible to access several simultaneous recording directions, known as *electrocardiographic leads*. Having information from different viewpoints can be achieved a spacial perspective of the electrical phenomena.

Anomalous electric activity, as too fast/slow or irregular rhythms and abnormal conduction of the cardiac electrical impulses, may conduct or predispose to life threatening conditions. Thus, the evaluation of the cardiac rhythms is a problem of major importance.

The use of automatic analysis systems is essential to guaranty efficiency, namely in case of very long records and for automatic recognition of events and dubious signal segments to be further checked by a cardiologist.

The following sections will give some insight about the ECG generation and recording, its main characteristics and the clinically meaningful information that can be extracted from the ECG. The last section on this Chapter in dedicated to the outline of this research, being a guide for reading this thesis.

1.1 ECG genesis

The heart has the main function of making the blood reach all the body. The wall of the heart has 3 different structures: an internal membrane (*endocardium*), a middle muscular layer (*myocardium*) and an external serous membrane (*pericardium*). The heart has two upper chambers (*atria*) which collect the blood at each beat and send it to the lower chambers (*ventricles*) that pump the blood to the vessels of the circulatory system. The chambers on the right side feed the pulmonary circulation with venous blood to be oxygenated and the left side receives the arterial blood from the lungs and pumps it to all other parts of the body (Wagner and Marriott, 1994).

The mechanical cyclic phenomena of muscular contraction and relaxation that allow the heart to pump blood efficiently, result from the electrical activation and recovery of the myocardial cells that constitute the cardiac muscle. A specialized system provides coordination and synchronisation of the different muscular areas in order to allow a simultaneous contraction of each heart chamber and a correct timing between atrial and ventricular contractions.

A beat is generally initialized by a group of cells (*sinoatrial node* - SA) located in the upper part at the right atrium and with the ability of spontaneously producing an electrical impulse (*pacemaker*). The cardiac cells present a negative electrical potential at rest (relaxation state) and are quickly depolarized by that electrical stimuli. This voltage variation acts over compressible and electrically excitable proteins inside those cells, producing the heart mechanical contraction. The spreading of the electrical wavefront causes the muscular contraction of both atria, forcing the blood into the ventricles. The electrical impulse is then delayed by crossing the *atrioventricular node*, which presents a lower electrical conductivity and is normally the only structure capable to transmit electrical impulses from atria to ventricles. This delay in the electrical wavefront allows the atria to get fully empty. The large size of ventricles is compensated by the existence of specialized conducting pathways (*purkinje fibers*) that accelerate the propagation of the electrical wavefront, allowing an efficient pumping of the blood to all body (Wagner and Marriott, 1994; Malmivuo and Plonsey, 1995; Lilly, 2006).

The ECG signal corresponds to the record at the body surface of the different *action potential* (AP) curves, corresponding to the electrical activity over time in each heart region [1]. As described above, the propagation of the electrical wavefront is distinct in the several heart regions that are crossed at different stages of the cardiac cycle, producing AP curves with different characteristics that summed form the ECG. Each cardiac beat in the ECG is typically associated with the sequence of five principal waves known as P, Q, R, S and T, as illustrated in Figure 1.1, which result from the different cardiac phases (Garibyan and Lilly, 2006):

- the *atrial activation* (depolarization) produces a small amplitude smooth wave denoted as **P wave**, marking the beginning of a new beat
- the *activation of the ventricle* usually produces a group of three peaky waves known as **QRS complex**

[1] See Fig. 6.7 of Malmivuo and Plonsey (1995)
(online edition at http://butler.cc.tut.fi/~malmivuo/bem/bembook/index.htm, accessed at December 2006)

  - the initial depolarization on the wall between the ventricles produces an initial small wave
  - the depolarization of a bigger portion of ventricular muscle originates a dominant bigger wave with polarity inverted in relation to the first one
  - the finishing of ventricular activation and returning to the electrical baseline is reflected as a small wave appearing in the end, with the same polarity as the first one

- the *ventricular repolarization* (recovery) produces a smooth wave with variable morphology, named **T wave**; an extra small wave named **U wave** appearing after the T wave is also frequently reported, but its origin is still controversy.

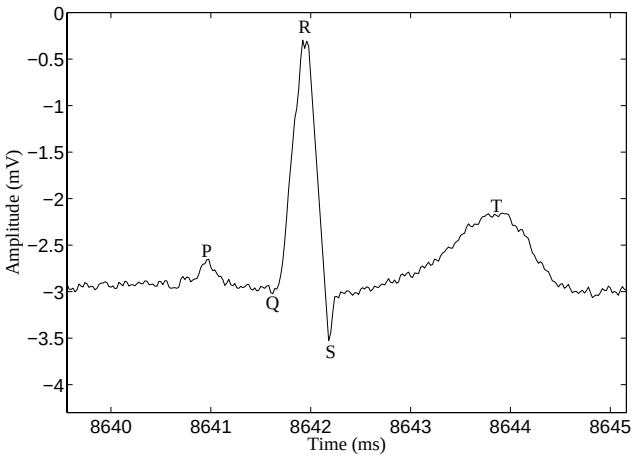

Figure 1.1: Schematic representation of relevant information in a cardiac beat. Beat extracted from a real file from the *MIT-BIH Polysomnographic Database* (Ichimaru and Moody, 1999).

The polarity of the waves depends on the electrical axis considered in the recording (that is on the electrode sites used). The P wave can be positive (as the one in Figure 1.1), negative (inverted) or biphasic (with two peaks, one positive and other inverted). In the QRS complex the first negative wave is named **Q wave**, the first positive wave is known as **R wave**, the second negative deflexion as **S wave** and the second positive deflexion as **R'** (The CSE Working Party, 1985). The dominant wave is usually positive and for that reason this group of waves is known as QRS complex, no matter which waves are present. However other less typical configurations can occur when one or both the smaller waves are not visible or the dominant wave is inverted (RS, QR, R, Q or RSR' complexes). The T wave can present any of the morphologies described for the P wave, or even be only an upwards or downwards deflexion (corresponding to a baseline level change). The recovery of the atria is not visible on the ECG as it occurs simultaneously with the ventricular activation and the dominant QRS waves obscure any possible signal of *atrial repolarization* (Garibyan and Lilly, 2006).

After a beat the cells are not immediately able to receive nor transmit a new electrical stimuli. The **refractory period** (approximately 200 ms) represents the biologically possible minimum interval between two heart beats (Iyer *et al.*, 2006; Rolls *et al.*, 2006).

1.2 Lead systems

In spite of the general characteristics of each ECG wave (as smoothness and relative polarity), the morphology observed depends on several factors. In particular the lead used, which is determined by the electrode sites, affects the shape and amplitude of the waves. Also, using different viewpoints result in different latencies on the electrical phenomena as visible at each lead. Thus, depending on the spatial orientation, a wave can become visible (or seems to end) in one lead before another, and even be not visible, in a particular lead. An example of a beat with waves presenting diverse morphologies in different leads is plotted in Figure 1.2.

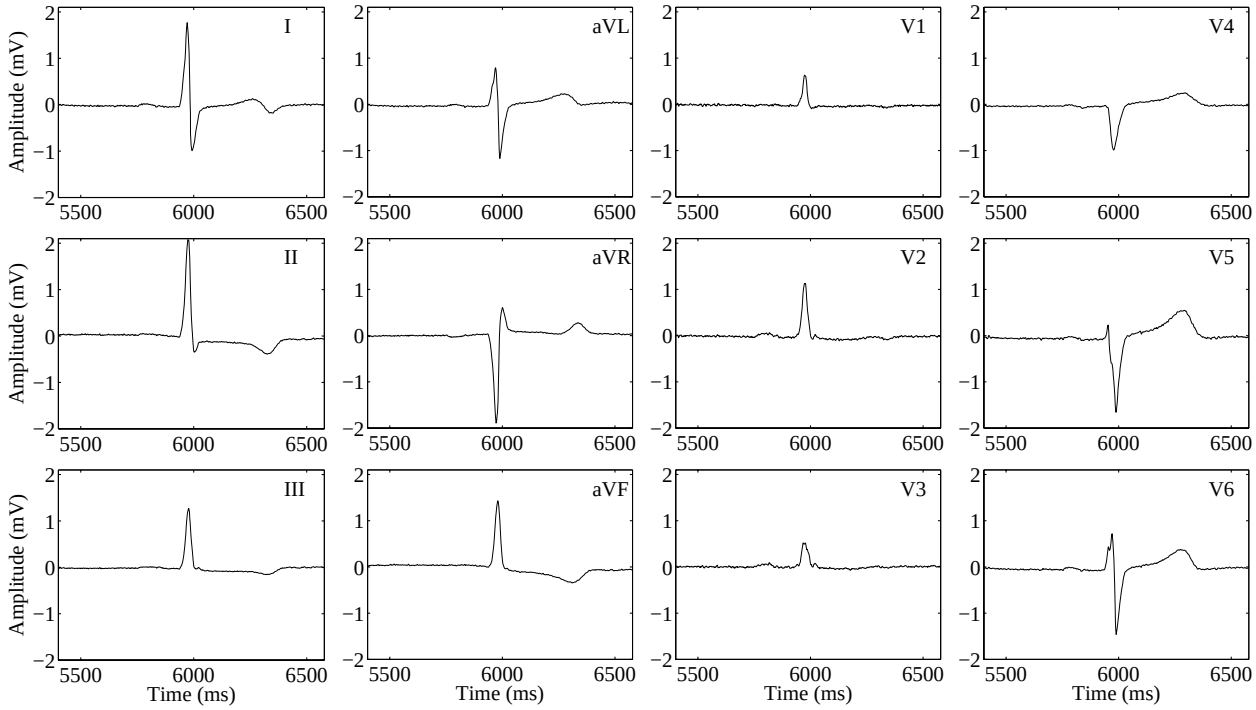

Figure 1.2: A beat recorded in the standard 12-lead system, with different wave's morphologies in the different leads. Beat extracted from a real file from the *STAFF III database* (Garcia *et al.*, 2000).

Taking as origin the heart location on the thorax, each lead is defined by a vector that gives the direction along which the electric potentials are measured. Symmetric vectors (with reverse polarity) correspond to symmetric ECG signals. Different lead systems have been proposed and used for clinical and investigation purposes: from orthogonal 3-lead systems to the extremely redundant body surface mapping using as many as 80 or 120 leads.

According to the dipole hypothesis, the electrical activity of the heart can be approximated by a time-variant electrical dipole, called the *electrical heart vector* (EHV). Thus, the voltage measured at a given lead is merely the projection of the EHV into the unitary vector defined by the lead axis (Malmivuo and Plonsey, 1995).

The theoretical basis for using a 3-lead system is the dipole hypothesis itself. The *vectocardiogram* (VCG) is a canonical representation of EHV given by a three dimensional record obtained according an orthogonal system. Although the electrical activity has some non-dipolar components, this approximation is widely used to represent the ECG spatially. According to the dipole hypothesis, any hypothetical lead can be synthesized by an adequate projection of the VCG. This allows to synthesise the leads of one lead system from the leads of a different system [2].

The corrected Frank system is the most used orthogonal system. It is based on three orthogonal body axes defined from the observer point of view as (Figure 1.3) right-to-left (lead X), head-to-foot (lead Y) and front-to-back (lead Z).

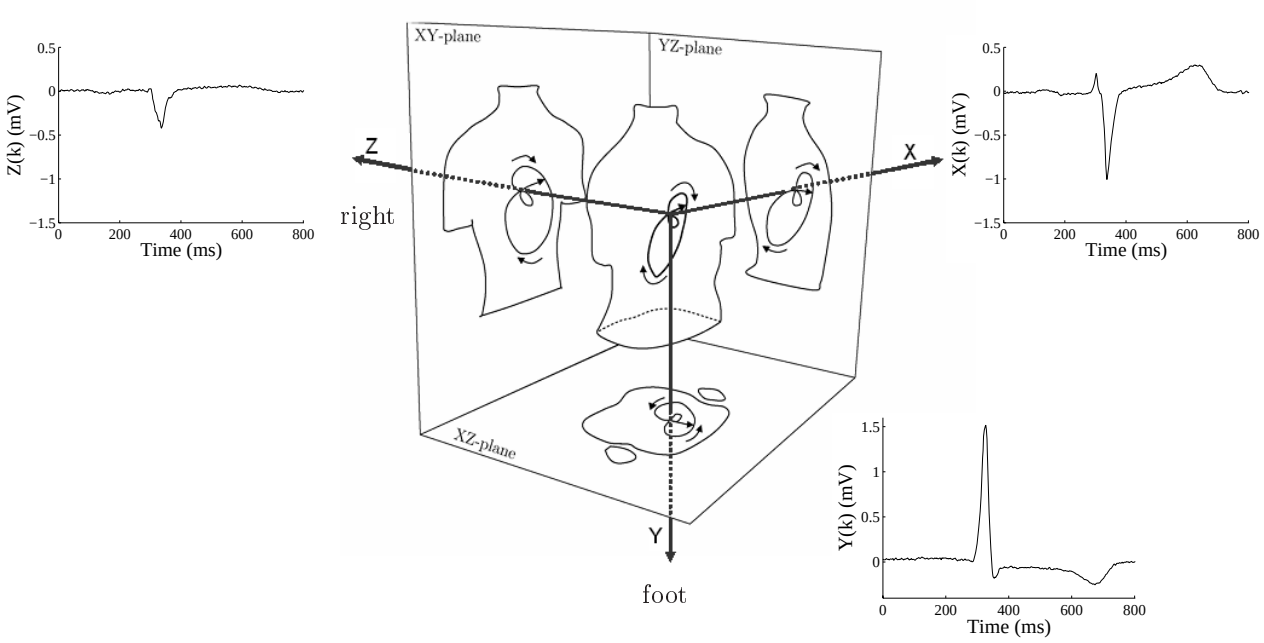

Figure 1.3: Example of a VCG loop (same beat as Figure 1.2), with its projection into the 3 orthogonal planes and ECG signals corresponding to the lead axes (X, Y, Z). Arrows outside each loop indicate time direction.

Examples of real ECG signals over Frank leads (X, Y and Z) are presented in Figure 1.4. The segments here presented are from records taken from young normal subjects that can be found in the POLI/MEDLAV ECG Database (Pinciroli *et al.*, 1998). Segments of these same records will be used latter to illustrated other features in this thesis and more details on this database can be found in Section 5.2. The differences in the waves's morphology are evident between leads in the examples of Figure 1.4. Frequently, the ECG records present noise contamination that can have diverse origin. Noise contamination consisting in very rapid variations and baseline wandering is visible is some of the plots, once more depending on the lead observed. Due to the electrode positions, lead Y is the one that is likely the be more contaminated, as is easily noticed in the Figure.

The lead set most widely used in clinical practice is not an orthogonal system, but rather the clearly redundant standard 12-lead system (Malmivuo and Plonsey, 1995; Wagner and Marriott, 1994).

[2]See Appendix A for more details in a lead synthesis

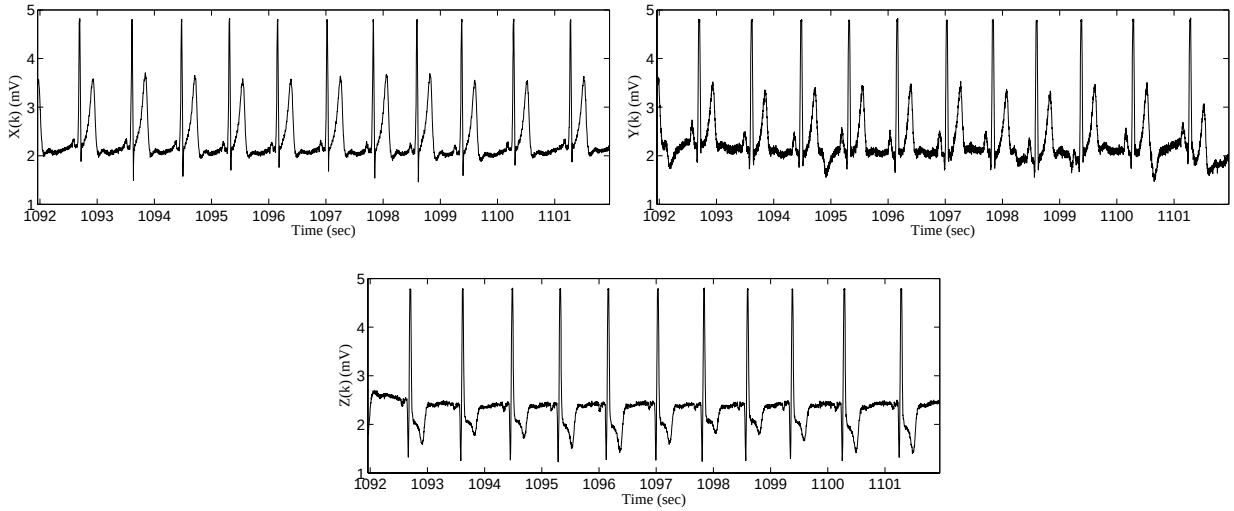

(a) Example 1 - leads X, Y and Z

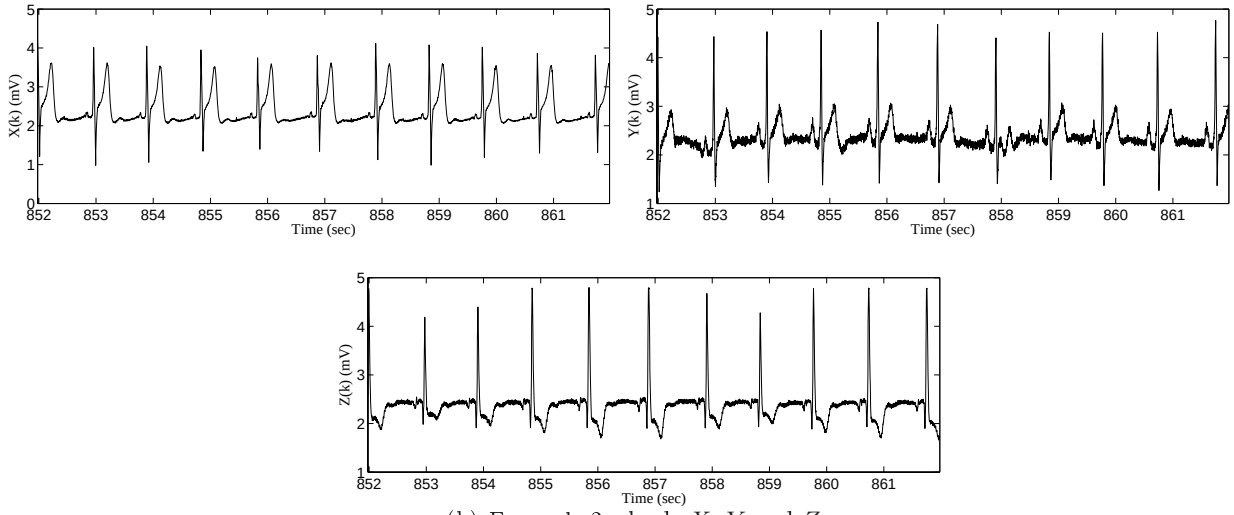

(b) Example 2 - leads X, Y and Z

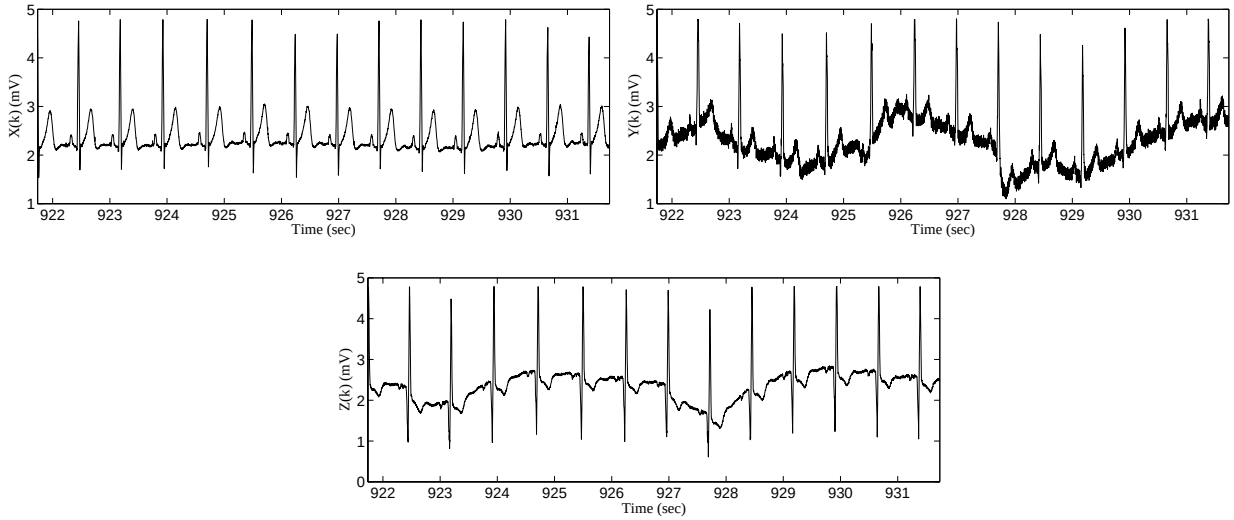

(c) Example 3 - leads X, Y and Z

Figure 1.4: Examples of real ECG signals in Frank leads (X, Y and Z) - segments from records of young normal subjects from the POLI/MEDLAV Database (Section 5.2). Some of the plots present relevant noise contamination level, in particular over lead Y.

In this system the leads span two orthogonal planes (Figure 1.5):

- the *frontal plane*, the vertical plane corresponding to the thorax of a standing individual, contains the three *limb* leads (I, III and II) and three *augmented* leads (aVL, aVR and aVF);
- the *transversal plane*, the horizontal plane that cross the thorax orthogonally to the frontal plane contains the six *precordial* leads (V1, V2, V3, V4, V5 and V6).

The beat plotted in Figure 1.2 illustrates an ECG recorded according to this system. The relations between the leads of the standard system can be found in Appendix A, along with the linear transformation that allows to derive the Frank orthogonal system (VCG) from the 12-lead system. In terms of the lead axis, the Frank leads correspond respectively to leads I, aVF and -V2, but (X, Y, Z) are constructed taking into consideration the distortions caused by the boundary and internal inhomogeneities of the body, (Malmivuo and Plonsey, 1995).

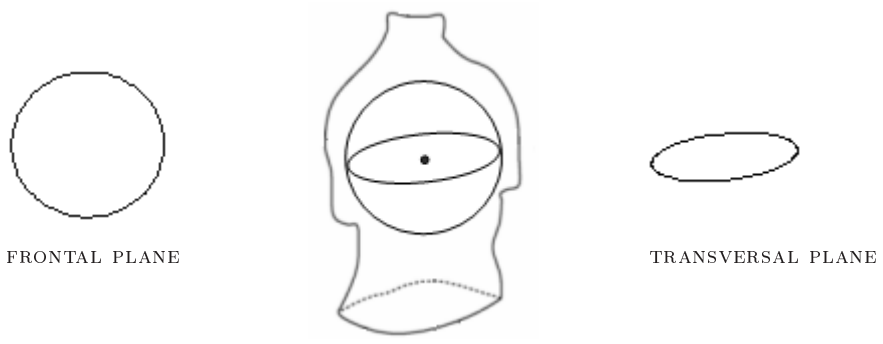

(a) Planes considered in the 12-lead standard system

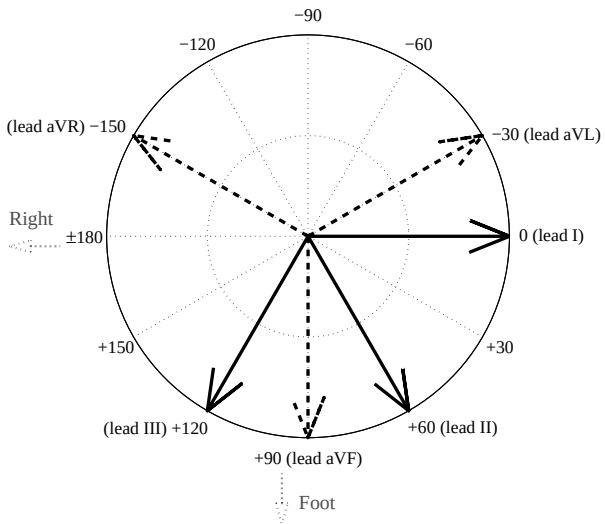

(b) Frontal plane

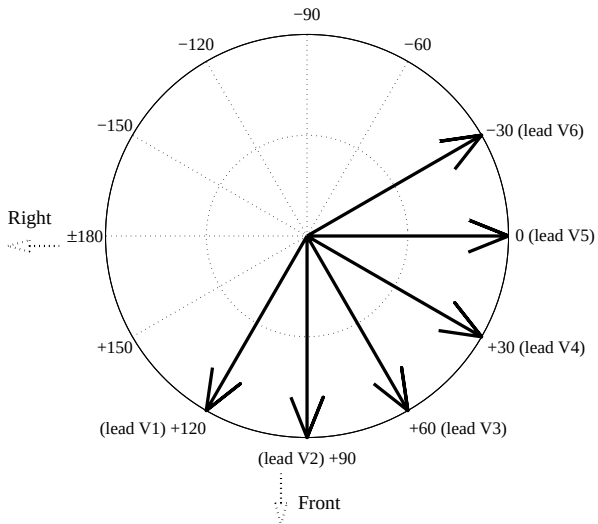

(c) Transversal plane

Figure 1.5: Vectors that define the 12-lead system - in the counterclockwise direction (a) leads I, aVL, aVR, III, aVF and II (*augmented* leads are plotted as dashed arrows); (b) leads V1, V2, V3, V4, V5 and V6.

1.3 The clinical use of ECG, cardiovascular and related series

Today the usage of the ECG is quite varied and, depending on the patient condition, the recording can be done in different ways (Malik and Camm, 2004; Sörnmo and Laguna, 2005).

To diagnose permanent conditions a rest ECG is commonly used, consisting in the a short time recording of simultaneous ECG leads on a lying down position. If the clinician suspects of any specific dysfunction, the recording can be done during maneuvers designed to test the cardiovascular performance. The *exercise stress* test fits this class of recordings and aims to study the heart's ability to cope with increased need of oxygen resulting from the physical work. To analyse situations of transient symptoms *Holter* monitoring can also be used. It consists in a ambulatory multilead ECG, using a portable recorder; typically 24-hour records are obtained, covering all sort of daily routine activities including sleep, awaking, moderate exercise as walking, etc. The patient is requested to note in a diary his activities and any symptoms, to help on the later signal interpretation. ECG monitoring and real time processing can also be used as an alarm system, crucial for patients in critical conditions as in intensive care units, and in telemedicine applications.

The ECG signal reflects not only the subject's heart condition, but also other body conditions such as electrolyte abnormalities (Van Mieghem *et al.*, 2004). Also, the heart is integrated in the cardiovascular system, having a tight relation with pulmonary respiration. Both systems are under the action of the *autonomic nervous system* (ANS) in which relays the involuntary coordination and control of the basic body functions. ANS is responsible for the body global response to external stimuli and for adapting the body functions to the needs inherent to different activities (as sleep, digestion, exercise, ...). It has two components with antagonistic functions: the *sympathetic* system that rules the functions' activation, and the *parasympathetic* system which rules the relaxations' states. The correct working of the physiological functions and the survival of the individual depends on the balance between these two subsystems (Franchini and Cowley, 2004). Using ECG recording, specific tests can be performed with the particular goal of testing the ANS condition. The *head-up tilt* test for example aims to evaluate the response to changes on body position, by moving the table where the patient is lying from horizontal to a nearly upright position.

As the electrodes are placed at body surface, the recorded ECG reflects the conductivity of tissues crossed from heart to skin. The different structures in the thorax make the electrical field to propagate in an anisotropic way, producing changes in the signal which need to be taken into consideration for its interpretation (Gulrajani, 1998). Also, the ECG is likely to be affected by non cardiac electrical fields, either of internal origin (other muscular activity) or external (electric power interference) and events such as the patient movement or electrodes' lack of contact, which can produce artifacts or signal loss. The clinical ECG commonly presents high levels of contamination, in particular for non resting signals, making its study difficult and subjective (Figure 1.4). Automatic systems avoid inter and intra observer variability, can easily deal with large amounts of data and much of the processing can be done in real time. Thus automatic systems are an indispensable tool for today's electrocardiography.

It has been already noticed that the durations of the heart's electrical phenomena and their variations over time are clinically relevant. Since these phenomena correspond to different ECG waves, their durations can be measured as time intervals between adequate fiducial points on the ECG, such as peaks (maximum or minimum of a waveform), onsets (departure from baseline level) and ends (return to baseline). Some of these intervals are represented in Figure 1.6. In particular:

- the time interval between consecutive P waves (PP interval) is used to access the atrial cycle duration;
- the time interval between consecutive R waves (RR interval) is used to access to the ventricular cycle duration;
- the time between the onset of the QRS complex and the T wave end (QT interval) represents the total duration of the ventricular depolarization and repolarization.

The interval between the R and T peaks (RT interval), which includes most of the ventricular activity, is also frequently used.

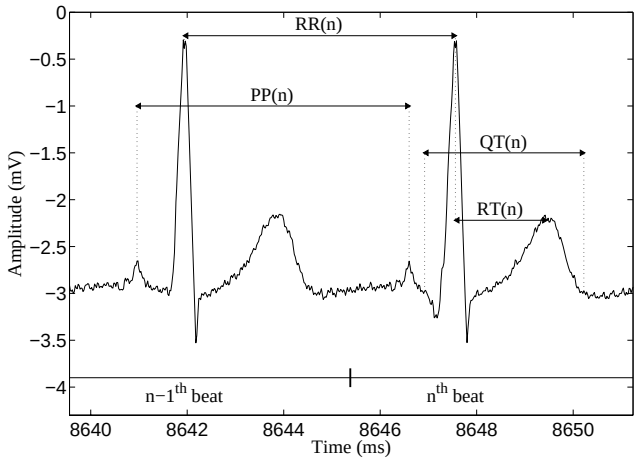

Figure 1.6: Some of the more relevant ECG intervals. Beat extracted from a real file from the *MIT-BIH Polysomnographic Database* (Ichimaru and Moody, 1999).

The sequence of any intervals measures, indexed to the beat order n forms a *cardiovascular series*. In the framework of this thesis the RR interval series (*tachogram*) and the QT series are particularly important. The RR series is currently used as an heart rate signal and expresses the cardiac rhythm. Normally the beats are generated by the SA node, under the ANS influence; abnormal heartbeats can be initiated by other cells rather than the SA node (ectopic focus) or be produced by an altered conduction of the electric wavefront. If the heart rate or the coordination between atrial and ventricular contractions is enough affected, efficiency of pumping can be at risk, and potentially fatal situations can occur. Abnormal QT interval length and beat-to-beat variations have been associated to several pathological conditions and increased risk situations. In Figure 1.7 are presented examples of RR and QT interval series extracted from the same real ECG recordings of Figure 1.4 (longer segments). As illustrated, these series are very different in terms of mean value and variability level.

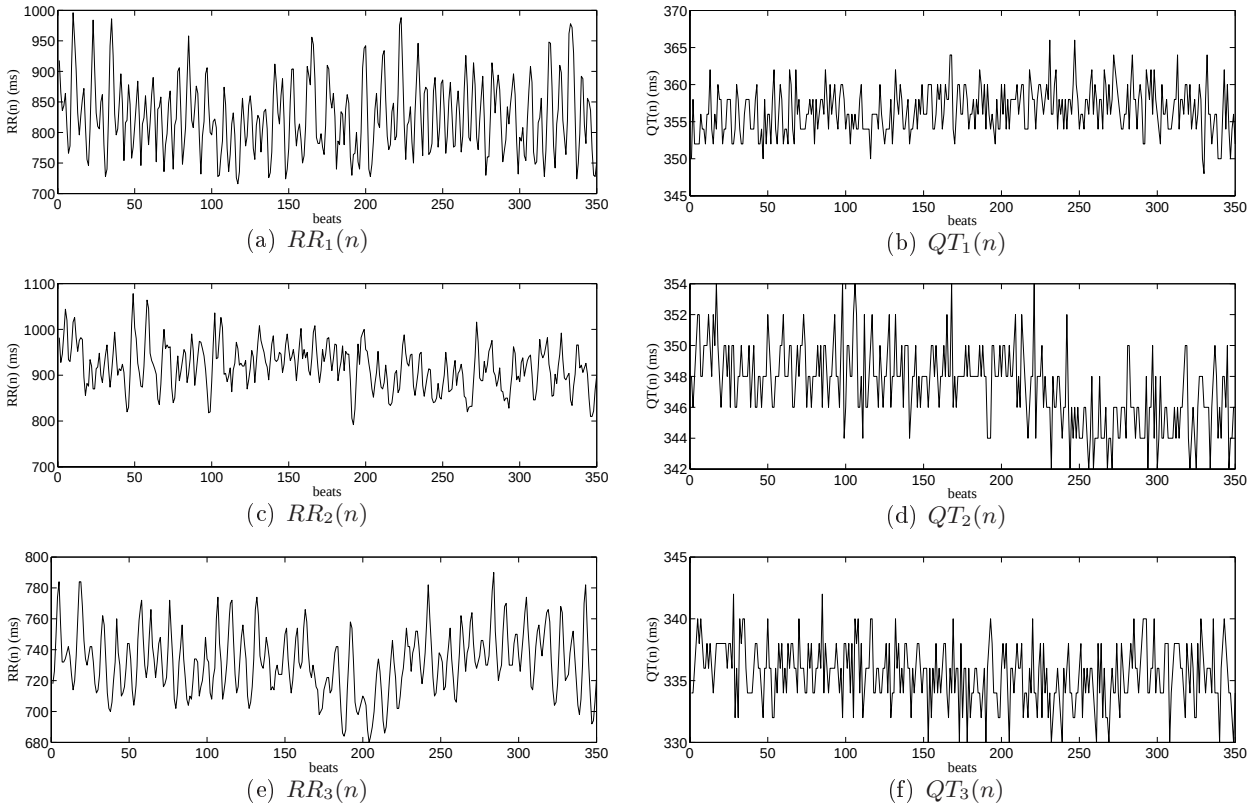

(a) $RR_1(n)$ (b) $QT_1(n)$

(c) $RR_2(n)$ (d) $QT_2(n)$

(e) $RR_3(n)$ (f) $QT_3(n)$

Figure 1.7: Examples of real simultaneous RR and QT intervals series (longer segments from the recordings used in Figure 1.4); ECG was sampled at 500 Hz.

1.3.1 Heart rate

The cardiac cycle initiates with the atrial activation, thus being reflected on the P wave onset; still, it is standard to use of the RR interval as the cardiac cycle duration (Task Force, 1996) instead of the interval between P onsets. As a matter of fact, wave peaks are easier to locate than boundaries and RR interval measures are likely to have less error than PP interval measures due to the smooth shape of P wave. The instantaneous heart rate (in sec^{-1}) is defined as RR^{-1} value and the tachogram is currently referred as the heart rate (HR) series, in spite of being the series of RR intervals (its inverse values). The HR and its beat-to-beat variations (HR variability - HRV) are being studied for many years, particularly in the framework of accessing the ANS balance.

The normal heartbeat, produced by the sinoatrial node (sinus rhythm), lies between 60 and 100 beats per minute (bpm) at rest (Zaret *et al.*, 1999; Rolls *et al.*, 2006). The SA is strongly modulated by the ANS, with sympathetic stimulation causing HR increase. Abnormal rhythms can occur in healthy people as response to the body needs. Lower rhythms occur in states of deep relaxation or in athletes (*sinus bradycardia*), while rhythms above 100 bpm (*sinus tachycardia*) appear during physical effort or mental stress. Even in periods of stable HR there are small beat-to-beat variations that result from the balance between the sympathetic system (increased activity increases HR) and the parasympathetic system (increased activity decreases HR). For this reason any pharmacologic agent that acts over ANS functions also changes HR (Rolls *et al.*, 2006).

The SA node is normally the structure with higher automaticity, thus usually it initiates the beat (native pacemaker), but those cells aren't the only ones to have pacemaking ability. If the normal pacemaker is decelerated for some reason, e.g. by effect of a pathology or a drug, an ectopic pacemaker can take over producing an escape beat (i.e. a late beat). Also, it can occur that other part of the heart is pacemaking faster and an **ectopic beat** can be initiated by other cells. Ectopic beats are usually single premature beats that can occur frequently in healthy subjects without any serious consequence (Rolls *et al.*, 2006). On the other hand, escape and ectopic beats have reduced or absent ANS modulation and if they are more frequent than the normal sinus beats, the coordination of the contraction and relaxation of the several cardiac structures can be affected, reducing the efficiency of pumping. If the SA node is permanently malfunctioning, with very slow rhythm or in the presence of malignant fast arrhythmias, an artificial pacemaker needs to be implanted to ensure a correct heart beat (Batsford, 1999; Lilly, 2006).

Premature beats are also related to other rhythm abnormalities, as *ventricular tachycardia* (rapid heart beat initiated within the ventricles), or even *ventricular fibrillation*, a state of uncoordinated ventricle contraction that usually evolves to death in a few minutes, if it not inverted using an electric discharge from a defibrillator (McPherson and Rosenfeld, 1999; Lilly, 2006).

The electric conduction can also be altered as result of reduced conductivity (blocked area) that delays (*partial block*) or makes the propagation to fail (*total block*). Damaged areas result frequently from a *myocardial infarction* (heart attack) and the implantation of an artificial pacemaker can be needed to obtain a coordinated ventricular contraction. Delayed conduction may result in an asynchronous refractory period of neighboring cells: some depolarized cells can receive the delayed impulse and treat it as new beat (premature beats). In this case the electric impulse can even be spread backwards (*reentry phenomena*) causing dangerous arrhythmias (McPherson and Rosenfeld, 1999).

1.3.2 Ventricular Repolarization

Anomalies in the rhythm and electric conduction can change not only the cardiac cycle length but also the timing and duration of each cardiac phase. In particular, ventricular repolarization alterations have been reported in risk increased situations by Extramiana *et al.* (1999*a*); Lass *et al.* (2001); Pellerin *et al.* (2001); Valensi *et al.* (2002); Cuomo *et al.* (2004); Milliez *et al.* (2005); Pathak *et al.* (2005), among others.

In spite of including the total (depolarization plus repolarization) ventricular electrical activity, the QT interval is currently considered as an index of the ventricular repolarization (VR) time. Abnormal QT values have been associated with malignant ventricular pro-arrhythmicity or even sudden death Gaita *et al.* (2003); Yap and Camm (2003); Rubart (2004)

The precision of QT interval length measures depends on the correct location of both QRS onset and T wave end. One of the main problems of measuring QT interval results from the low amplitude and flat boundaries of the T waves, with consequent uncertainty in its end delineation even using a high sampling frequency. For instance, in the QT series plotted in Figure 1.7, the ECG sampling frequency of 500 Hz (corresponding to a 2 ms time resolution) is insufficient for distinguish the smallest QT variations, producing the lack of resolution in QT series amplitude. The same stands for many other indexes for VR characterization that also require the location of T wave boundaries, as T wave area and symmetry.

Some authors use alternative VR measures which do not require T wave end location, such as the RTapex interval (time between the R wave and T waves peaks, sometimes referred just as RT). The use of the RTapex interval to assess VR is based on the assumption that the cardiac cycle length dependence of VR is concentrated on the early portion of the QT interval (Stramba-Badiale *et al.*, 1997). However, in spite of being easier to measure RTapex presents even shorter length than QT interval, what additionally reduces the variability range and ignores fluctuations in VR that mainly affect the last part of the T wave. Merri *et al.* (1989) and Benhorin *et al.* (1990) studied the intervals STapex (time between the S wave end and T wave peaks) and TapexTend (time between the T wave peak and end) among several other repolarization variables. Both in normal and in patients with long QT syndrome (LQTS) the intervals STapex were found to be related with HR and QT, whereas the TapexTend was reported as independent of HR and QT. Also, variations of QT and QTapex (time between the QRS onset and T wave peak) were comparatively studied in normal subjects, and in situations of *heart failure* (inability of the heart to pump efficiently) and *ventricular hypertrophy*: the terminal part of the T wave showed no HR dependence at rest and presented substantial variability not related to QTapex variability, both in exercise and in disease (Davey, 1999*b*). Furthermore, it was reported that important abnormalities in QT interval, including HR dependent ones, would be missed if the QTapex interval had been used to assess VR. As a matter of fact, Yan and Antzelevitch (1998) stated that the interval from T peak to T end represents transmural dispersion of repolarization and therefore may be considered as an index for arrhythmic risk.

1.3.3 Respiration effects

The pulmonary respiration is cyclic, having alternate periods of inspiration and expiration. Examples of real respiratory signal are plotted in Figure 1.8 (same subjects that in Figure 1.4), along with the *instantaneous respiratory frequency* (F_r), taken as the inverse of the respiratory cycle duration. The *mean respiratory frequency* is taken as the inverse of the mean respiratory cycle duration and usually lays above the 0.15 Hz (Yasuma and Hayano, 2004).

Lungs expansion and contraction during the respiratory cycle changes the heart electric axis within the chest, resulting also in scaling and rotation on the ECG. Thus respiratory activity has several effects over the ECG signal recorded at skin surface, namely in the wave's morphology. This influence is so marked that is possible to derive respiration as a function of time (respiratory signal) from the ECG (Moody *et al.*, 1986; Bailón *et al.*, 2006*b*,*a*).

On the other hand, the ANS controls and coordinates many other body functions besides the heart rate, in a way to make the body to work properly. In spite of the pulmonary respiration could be voluntarily controlled, the ANS has also an important role on it. Thus some of HRV and respiratory frequency variations have a common source and respiration induces changes in cardiac cycle length. This modulation of respiration over HRV in known as respiratory sinus arrhythmia (Yasuma and Hayano, 2004). During inspiration the HR increases and during expiration it decreases. This effect is notorious in example of Figure 1.9(a), with shorter time intervals between ECG peaks when the respiration curve is increasing and vice-versa.

To study the relations between respiratory frequency variations and HRV is usually considered the *respirogram*, that is the series of the respiratory values corresponding to the main ECG wave peak (R peak). Shorter segments of the same files used in Figure 1.8 can be found in Figure 1.9, overlapped to the respective ECG signals. The modulation of the respiration over the ECG is visibly dependent of the signal and the lead.

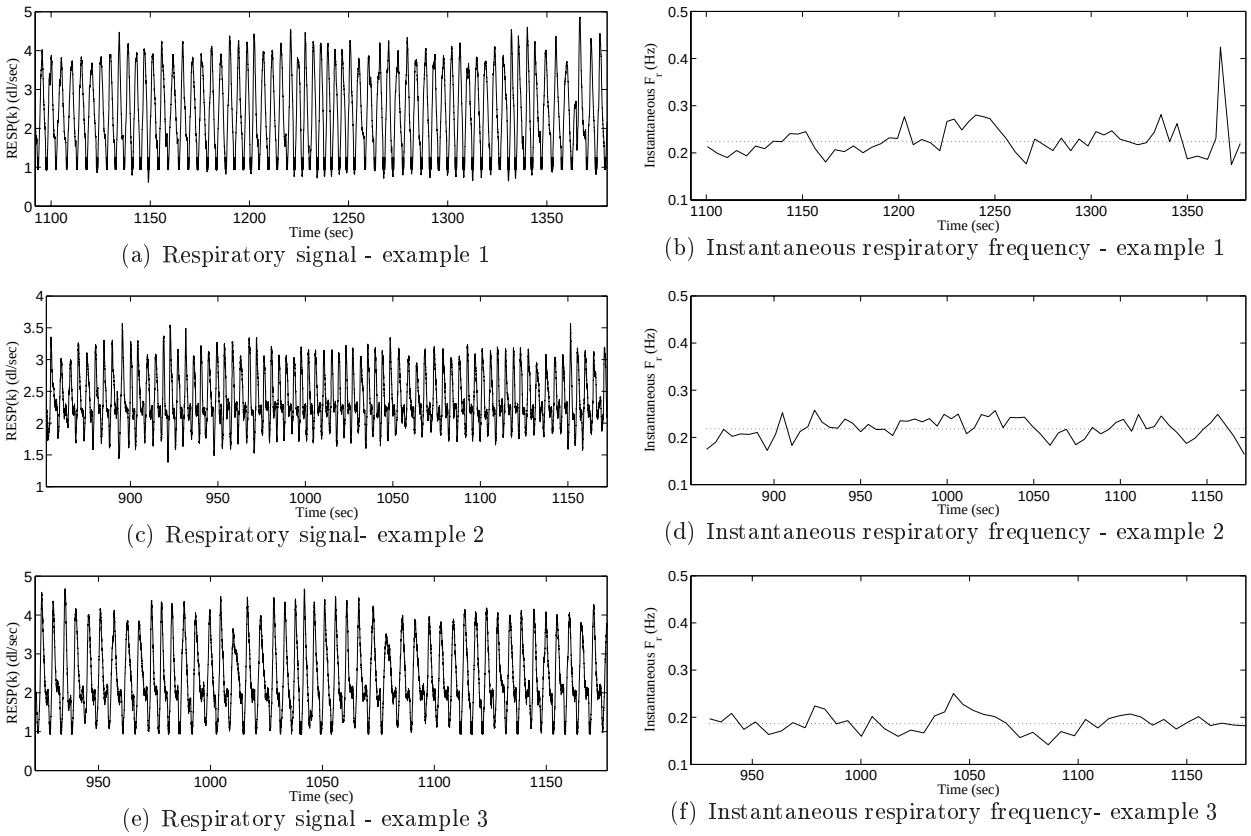

(a) Respiratory signal - example 1

(b) Instantaneous respiratory frequency - example 1

(c) Respiratory signal- example 2

(d) Instantaneous respiratory frequency - example 2

(e) Respiratory signal - example 3

(f) Instantaneous respiratory frequency- example 3

Figure 1.8: Examples of respiratory signals and correspondent series of instantaneous respiratory frequency (F_r) (same subjects that in Figure 1.4). F_r is the inverse of the respiratory cycle duration (time interval between two consecutive peaks in respiratory series). The mean respiratory frequency (inverse of mean cycle duration, 0.2238 Hz in example 1, 0.2182 Hz in example 2, 0.1866 Hz in example 3) is overlapped to F_r in dashed line.

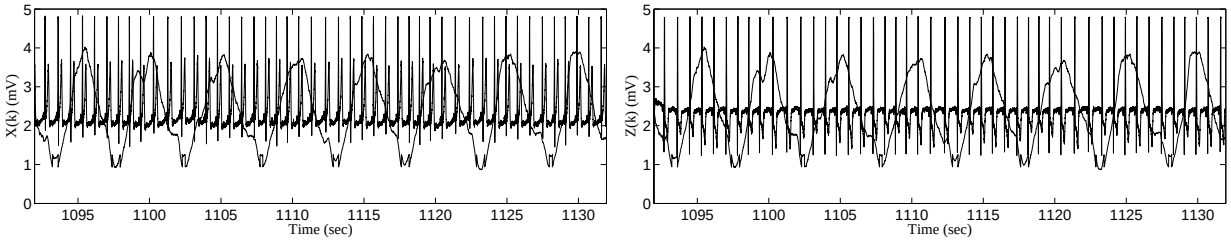

(a) ECG signal with the respiratory signal overlapped - example 1

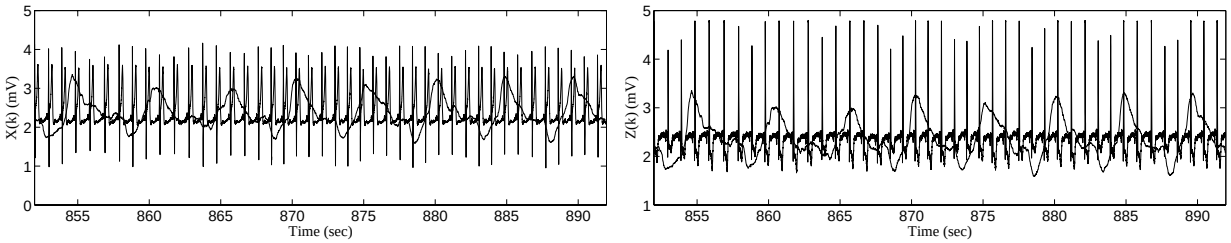

(b) ECG signal with the respiratory signal overlapped - example 2

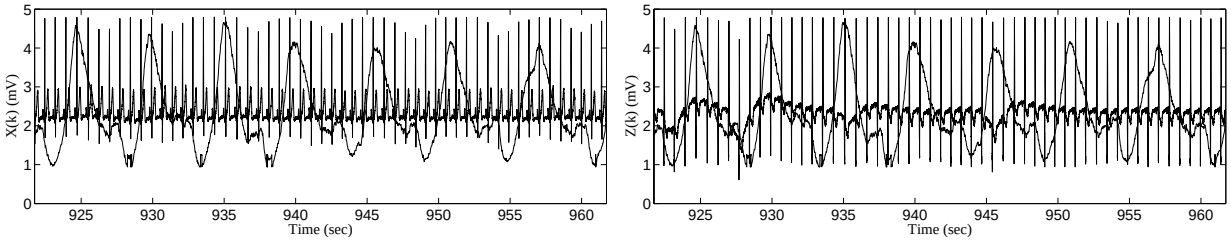

(c) ECG signal with the respiratory signal overlapped - example 3

Figure 1.9: Respiratory signal overlapped to ECG signals in leads X and Z (same subjects that in Figure 1.4).

1.4 Outline of this Work

Automatic systems are an indispensable tool for today's electrocardiography. They can deal with large amounts of data, allow real time processing and avoid inter and intra observer variability.

One of the aims of this research work was to develop tools for the ECG automatic analysis, that can be used in routine and establish some guidelines concerning its applicability. The methods studied need to be *efficient enough* to deal with large amounts of data, as in Holter recordings, and *robust* regarding the ECG morphological variations and noise contamination frequent in clinical data. In this framework, the main problem of the automatic delineation of the ECG, particularly the QT interval measurement, has been explored. The methods were also illustrated regarding the QT beat-to-beat variations measurements and their dependence on HRV.

The order of the issues in the Chapters of this thesis is not chronological, rather tries to be a guide through the problems in a general applicability point of view. To help the thesis reading, the physiological and clinical terms are defined in Appendix B.

The delineation of the ECG characteristic waves, by detecting their peaks and boundaries, is of extreme importance. It is the basis to study the ECG signal and supplies fundamental features for extracting clinically useful information, namely the timing and duration of the physiological

phenomena. Using the ECG to study cardiac rhythm, electrical conduction, chambers coordination or beat-to-beat variations requires the correct detection and delineation of the characteristic points and waves that express the cardiac function.

The problem of automatic detection and delineation of the ECG characteristic points is not new, but the traditional methods are still not able to satisfy the requirements of the beat-to-beat variability studies, in particular with respect to the QT interval. The boundaries location, specially from smooth waves as the T wave is a hard and challenging task. In fact, fully-automated methodologies for measuring QT are not presently recommended in the guidelines of the regulatory agencies, as they consider that available methods are not enough validated. This question has recently motivated an international competition aiming to provide adequately validated tools for QT measurement (Moody *et al.*, 2006).

Developing tools for ECG automatic delineation is the main and central contribution of this thesis and is extensively explored in Chapter 3. In this work initially a single-lead based automatic system for ECG delineation using wavelet transforms was extended and improved (Almeida *et al.*, 2003*c*; Martínez *et al.*, 2004, 2006) and then a multilead based methodology for boundaries location (based in the single-lead system and aiming QT delineation improvement) was proposed and validated (Almeida *et al.*, 2004*c*, 2006*a*). These automatic systems were evaluated and compared with other published methods, using records from standard ECG databases with manual reference annotations. The validation aimed to guaranty that the methods were accurate and robust, that is adequate to be used either in experimental conditions or in the clinical practice.

Besides its general importance, robust delineation tools are essential for the study of the QT interval and its beat-to-beat variability (QTV). QTV series are currently used to assess ventricular repolarization (VR) variations and changes in the repolarization have been associated to an increased risk of life threatening arrhythmias. Moreover, many works point out that the VR variations that are not driven by the HRV can themself have clinical meaning. In this research it is proposed to explore the relations between VR and HR variabilities using a parametric dynamic linear approach over the series of QT and RR intervals variations, quantifying the fraction of QTV driven by HRV (Almeida *et al.*, 2006*b*). The importance and difficulties of exploring VR/HR relation, the description of the modelling approach used and its validation using simulated series are presented in Chapter 2 of this thesis.

As it was remarked above, the first step to study cardiac variability series is their measurement, that is in real practice the parametric modelling approach explored is only feasible combined with the ECG delineation tools. For that reason, the joint performance of the two systems was extensively studied and quantified, considering both single-lead and multilead versions (Almeida *et al.*, 2003*b*,*a*, 2004*a*,*b*, 2005, 2006*b*). Chapter 4 of this thesis is dedicated to this validation and tries to establish the limitations and indicative applicability of the automatic methods considered.

Finally, the automatic methods proposed were applied to real data, namely ECG Holter recordings, in order to illustrate their use in clinical signals. The studies in real data are detailed presented in Chapter 5.

As a summary, this thesis *tries* to answer several questions with *clinical importance*. Namely:

- *Can ECG delineation, in particular the QT interval delineation, be done accurately using automatic methods?*
- *Are there actual advantages in using a multilead delineation approach for boundaries location?*
- *Are automatic methods adequate to access ECG beat-to-beat variability information?*

- *How can VRV and its relations to HRV be studied?*
- *How do these tools perform in realistic ECG data?*
- *Is there in QTV something not present in HRV and clinically useful?*

The mathematical notation used in this thesis follows the usual in Signal Processing literature. The methods described were implemented using MATLAB Version 6.5.0.180913a (R13), namely the facilities of the Optimization Toolbox (Version 2.2), Signal Processing Toolbox (Version 6.0), System Identification Toolbox (Version 5.0.2) and Wavelet Toolbox (Version 2.2).

Chapter 2

QT Variability and Heart Rate Variability Interactions

The beat-to-beat variability of the QT intervals (QTV) series is currently used to assess ventricular repolarization (VR) variations. Changes in repolarization have been associated to an increased risk of life threatening arrhythmias and several works point out that VR variations not driven by heart rate variability (HRV), can have clinical meaning. However, the QTV fraction effectively correlated with HRV has not been yet clearly quantified.

In this thesis it is proposed to explore the short term relations between VR and HR variabilities using a dynamic linear approach over the series of QT and RR intervals variations.

The importance and difficulties of exploring VR/HR relations are initially discussed. It is proposed a methodology for the study of QTV versus HRV interactions, providing a quantification of the QTV fractions, either correlated or not correlated with HRV, in order to understand its significance and origin. The estimation error in the power spectral density measures of each fraction is quantified over simulated series establishing the framework of applicability of the modelling approach, as a function of the QTV level.

2.1 Introduction

The RR interval (cycle length) strongly affects VR and the QT interval is highly dependent on the preceding RR intervals, thus on the HR, as is illustrated in Figure 2.1. Therefore, any considerations about the QT interval length or its beat-to-beat variations (QTV) need to be made relatively to the correspondent HR values.

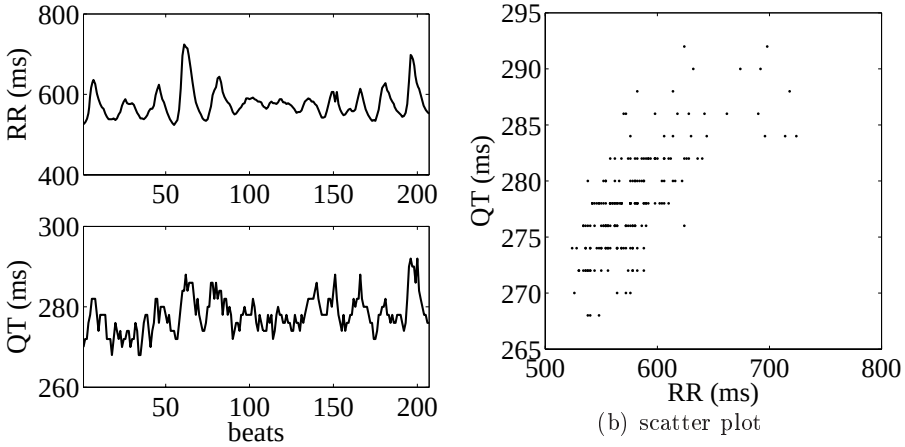

(a) series of intervals

(b) scatter plot

Figure 2.1: Example of real simultaneous series of RR and QT intervals and correspondent scatter diagram.

Several approaches have been proposed to explore the interaction between VR and RR intervals and to quantify the influence of RR beat-to-beat variability (HRV) over VR variability (VRV). Some works assume a constant global relation, others admit individual or circadian variations.

As a matter of fact, VR duration is strongly related with HR, but effects over VR uncorrelated with HR and changes in VR/HR dependence have also been reported, as will be detailed further in this Chapter. Therefore, the QTV fraction not driven by the HRV can itself have clinical meaning. However, the QTV fraction effectively driven by HRV has not been yet clearly quantified and it isn't yet known if there are clinical useful effects in QTV that are not present in HRV.

The study of VR dependence on HR and VR related risk indexes are initially reviewed and the goals of this Chapter are explained. Several methodologies traditionally used for studying ECG derived and other related series are briefly revisited in Section 2.2, with particular relevance given to parametric frequency domain techniques. In this research work QT and RR short term interactions were explored using a flexible-model orders version of a model proposed by Porta *et al.* (1998), which allows to quantify the fraction of VRV driven by HRV. The model formulation, identification and order selection details are presented in Section 2.3 and the model validation over simulated data series can be found in Section 2.4, along with the series simulation set-up. Main conclusions are summarized in Section 2.5.

Ventricular repolarization dependence on the cardiac cycle length

To evaluate if a particular QT interval length value is abnormal, many studies considered a HR-normalized or corrected QT (QTc), in which the HR influence is supposed to have been removed assuming a QT/RR static relation. Correction formulas can also be used to predict the QTc values as a function of RR interval length and are usually constructed from the assumed relation by taking RR = 1 sec, (that is an HR of 60 bpm). For example,

$$QT = a\sqrt{RR}, \tag{2.1}$$

taking RR = 1 sec, one will have $QTc = a$, and therefore replacing in (2.1)

$$QTc = QT/\sqrt{RR}. \tag{2.2}$$

The QT correction in equation (2.2) was published by Bazett in 1920 and it is the best know and the more widely used. Despite being still used in the clinical practice, the inadequacy of (2.2) is well reported for extreme HR values and has motivated various alternatives. Among others, were suggested cubic root, exponential and linear correction formulas (Sarma *et al.*, 1984; Sagie *et al.*, 1992; Molnar *et al.*, 1996). However no relevant improvement was achieved if group fitted formula parameters were applied to individual subjects. Moreover, very different parameters values were found for healthy subjects in different studies using the same correction formula (Batchvarov and Malik, 2002).

As no global formula fully describes the QT/RR relation, the HR influence can only be removed with individualised correction formulas, optimized both in shape and in parameters. As a matter of fact, individual based parameters perform quite well for the whole range of RR values (Molnar *et al.*, 1996). The slopes in the QT/RR and RT/RR linear regressions in young healthy subjects were reported as steeper in women than in men (Stramba-Badiale *et al.*, 1997). Considering QT measurements at different HRs (exercise test), Davey (1999*a*) used individually optimized linear regression QT/HR to obtain QTc intervals with removed HR dependency, keeping biological differences. Substantial intersubject variability in the QT/RR relation, including in the optimum shape, was repeatedly found in healthy volunteers (Malik *et al.*, 2002), while individual patterns are described as stable for periods of at least one month (Batchvarov *et al.*, 2002). Supported by their findings, those authors suggested that the inherent individual differences in cardiac repolarization are substantially greater than the effect of the environment or autonomic regulation.

Besides individual variations, also the reported circadian variations contributed to override the idea of a fixed QT/HR relation. Using a beat averaging technique over stable HR periods, Badilini *et al.* (1998) found a strong linear QT/RR relation with circadian variation in normal subjects, and Coumel *et al.* (1995) reported a steeper slope during day than at night in both QT/RR and RT/RR linear regressions. Extramiana *et al.* (1999*b*) observed a decrease of the circadian modulation and an attenuated diurnal QT/RR relation with increasing age (normals between 40 and 50 years old).

In spite of admitting circadian variations in the relation between VR and HR, the works cited above use averaged RR and QT intervals over stable HR periods, an approach to which Merri *et al.* (1993) called as *"static"*.

No inferences can be done about beat-to-beat VR variations and its dependence on HRV.

Merri *et al.* (1993) and Speranza *et al.* (1993) used RTapex intervals to access and study VR beat-to-beat variations in 24-Hour Holter recordings of healthy subjects, using non parametric frequency domain techniques. Both groups found strong similarities between the spectra of RTapex beat-to-beat variability (RTV) and the HRV spectra, and suggested VRV as a way to study the relation between autonomic nervous system disturbances and ventricular arrhythmias. Studies of the spectral coherence function between RTapex and RR also confirmed the strong dependence between VR and HR (Merri *et al.*, 1993; Sosnowski *et al.*, 1996; Barbosa *et al.*, 2000).

A linear dynamic approach was proposed by Porta *et al.* (1998) to study the interactions between the RR and RTapex intervals and to quantify the fraction of the RTV driven by HRV. RTV was described as RR driven in a window around the respiratory frequency and at low frequency (0.04 to 0.14 Hz), while a relevant RR-unrelated RTV fraction was found at lower frequencies (very low frequency) along with a slightly negative phase. Globally, similar relative and unrelated fractions were found in all studied situations (rest, tilt and during controlled respiration at 20 breaths per minute).

Ventricular Repolarization in risk stratification

Despite the well known fact that VR length and variability are to some extent driven by the autonomic nervous system through the RR interval, several authors refer direct influences of autonomic nervous system over VR (Merri *et al.*, 1993; Marciano *et al.*, 1998; Shusterman *et al.*, 1998, 1999) or report non autonomic influences (Gastaldelli *et al.*, 2000; Colzani *et al.*, 2001). In normal subjects, the direct effect of autonomic alterations over ventricular myocardium cells has been shown to change QT interval in a independent way of HR (Magnano *et al.*, 2002). Altered VR/HR relations have been reported in several pathological and risk increased conditions.

A normalized *QTV Index* (Berger *et al.*, 1997; Berger, 2003; Atiga *et al.*, 2000; Yeragani *et al.*, 2004) as been defined as $\left(QTVI = log_{10}\left[\left(s_{\mathrm{QT}}/(T_{QT}^2)\right) / \left(s_{\mathrm{HR}}/\ (T_{HR}^2)\right)\right]\right)$ were T_{HR}, T_{QT} stand respectively for the mean of HR and QT interval, and s_{HR} and s_{QT} for their standard deviations. QTVI is found found to be correlated with the severity of dilated cardiomyopathy (DMC) and increased values has also been associated to life-threatening arrhythmia as ventricular fibrillation, increased risk of sudden cardiac death in hypertrophic cardiomyopathy (HCM) and congestive heart failure (CHF) in atrial fibrillation. Increased QTVI uncoupled with HRV was found during ischemic episodes (Murabayashi *et al.*, 2002) and DMC (Berger *et al.*, 1997); variations in QT versus RR interactions, possibly related with the high incidence of sudden death, were reported in heart failure (Lang *et al.*, 2004).

A simpler variability ratio index, defined as $s_{\mathrm{QT}}/s_{\mathrm{RR}}$ (s_{RR} stands for RR interval standard deviation) was proposed by Jensen *et al.* (2004, 2005). This index was studied in 24-hour Holter recordings of healthy subjects and post myocardial infarction (MI) patients, together with other time based parameters and linear fitting of QT/RR. The variability ratio presented a strong prognostic value in risk stratification after MI, being the only parameter (among 17 studied) with independent prognostic value for sudden death. Those authors also reported a good reproducibility of QT dynamic parameters calculated in a beat-to-beat basis from automatically measured QT intervals.

Several authors were also able to find some predictive value on the HR rate dependence of VR in Holter ECG recordings, for a variety of pathologic situations, using the selective averaging beats approach (Badilini *et al.*, 1998). Extramiana *et al.* (1999*a*) suggested that QT dependence on the HR rate could discriminate between patients with and without vulnerability to ventricular tachyarrhythmias after MI. Pellerin *et al.* (2001) reported a loss of RT rate-dependence in patients with CHF. The QT rate dependence was reported by Valensi *et al.* (2002) as a better discriminator than time-domain HRV parameters between controls and subjects with diabetic autonomic neuropathy (DAN). In a retrospective study in patients after MI, Milliez *et al.* (2005) reported a steeper QT rate dependence in patients who died from cardiac death that in others, at all circadian periods studied (diurnal, sleeping and around the awakening heart rate acceleration in the morning) with significant steeper QT rate dependence during morning in those that died from arrhythmic cardiac death.

Pathak *et al.* (2005) studied the QT/RR linear regressions over averaged intervals at day and night times. The difference between the QT values expected at night and day given a 800 ms RR interval (according to the regressions) was used as index of VR rate dependence and proposed by the authors as a risk stratifier for sudden death in chronic heart failure patients.

Merri *et al.* (1992) used the slope of the linear fitting of the RTapex interval on the RR interval of the preceding beat to study the beat-to-beat relation between VR duration and cycle length. An increased slope was found in long QT syndrome (LQTS) patients compared to normal subjects; also initiation of β-blocker therapy by normal subjects produced a slope decrease compared with the initial values found in the same individuals. In a small group of patients with HCM, Cuomo *et al.* (2004) found abnormal QTV both in time and frequency domain parameters, with the standard deviation of averaged QT on normal beats in 5-min segments presenting a high predictive value for identifying patients with history of syncope. These findings support the idea that in those patients syncope may be related to repolarization changes. Using the model proposed by Porta *et al.* (1998), Lombardi *et al.* (1998) report a RTV fraction driven by HRV significantly greater in young subjects than in post MI patients and age matched control subjects.

In this work

Regardless the potential clinical meaning of VRV fraction not driven by the HRV pointed out by many works cited above, the QTV fraction effectively correlated with HRV has not been yet clearly quantified.

Based in the dynamic approach proposed by Porta *et al.* (1998), in this thesis it was proposed and discussed to explore the QT and RR short term interactions using a flexible-model order version of that model, aiming to quantify each QTV fraction. Preliminary versions of this approach were presented in Almeida *et al.* (2003*a*, 2004*a*,*b*), and a complete version of the method can be found in Almeida *et al.* (2006*b*). The methods were validated over simulated data series in way to determine the true QTV fractions and find the error in the quantification as a function of the QTV level.

2.2 Parametric Modelling in the study of cardiovascular series

Among the cardiovascular series, the *tachogram* or RR intervals series is the most simple, the easiest to measure and the most studied one. Methods either in time or in frequency domains are frequently used to characterize and study the beat-to-beat variations. Spectral methods give information about the variance distribution as a function of frequency and, following the Task Force (1996) standards for HRV studies, frequency domain methods were used for short-term analysis.

Parametric methods allow to obtain a smooth spectra which can be automatically decomposed into components associated to central frequencies, independently of the frequency bands of interest (Marple, 1987; Task Force, 1996). These advantages of parametric over non-parametric spectral methods led to an extensive use of model based approaches, for the study of HRV and of other cardiovascular variability series, aiming not only to characterize the series but also to study their interactions.

The main difficulty of parametric techniques is the need of a suitable estimated model, corresponding to a physiologically adequate structure and a well fitted model order. *Autoregressive* models are usual in cardiovascular variability studies, as those series are known to depend on its own past values (memory). To consider different series interactions, more complex models admitting two or more inputs can be assumed. In any case, the orders should be chosen according to an optimal criteria as *Akaike Information Criteria (AIC)*and the models' goodness of fit was checked using an whiteness error test (Marple, 1987).

Some of those models are described below, as they represent the basis for the parametric study of repolarization and HR variabilities interactions. The data to be analyzed by any parametric approach are the variability series, taken as the interval series corrected from the mean. For the remaining of this thesis $x(n)$ will denote a zero-mean variability series and T the corresponding sampling period.

2.2.1 Series Modelling and Spectral Decomposition

Autoregressive (AR) models are a particular case of a more general family known as *Autogressive Movering Average* (ARMA) models. An ARMA model assumes that the variability series $x(n)$ is a stationary random process generated from a white noise $w(n)$ by linear filtering (Marple, 1987):

$$x(n) = -\sum_{k_1=1}^{p_1} a(k_1)\ x(n-k_1) + \sum_{k_2=0}^{p_2} b(k_2)\ w(n-k_2), \tag{2.3}$$

where $a(k_1)$, $k_1 = 1, ..., p_1$ and $b(k_2)$, $k_2 = 0, ..., p_2$ are the autoregressive and moving average parameters, respectively. The model order p_1 corresponds to the memory of the process $x(n)$, from its past values.

Taking $A(z)$ and $B(z)$ polynomials with coefficients given by the autoregressive and moving average parameters, respectively, the power spectral density (PSD) of $x(n)$ can be written as (Marple, 1987)

$$S_x(F) = TS_x(z)|_{z=e^{j2\pi FT}} \tag{2.4}$$

$$= T\lambda^2 \left|\frac{B(z)}{A(z)}\right|^2_{z=e^{j2\pi FT}} \tag{2.5}$$

$$= T\lambda^2 H_x(z)H_x(z^{-1})|_{z=e^{j2\pi FT}}, \tag{2.6}$$

with F the frequency in Hz and λ^2 the *variance* of the source noise.

For $b(0) = 1$ and all other moving average parameters $b(k)$, $k = 1, ..., p_2$ equal to zero, the model in equation (2.3) corresponds to a *Autoregressive* process of order p_1 (AR_{p_1}). As has been referred above, AR models have been extensively used to study HRV.

In Figure 2.2 are plotted segments of zero-mean RR and respirogram variability series ($x_{RR}(n)$, $x_{Resp}(n)$), measured on the same real ECG files plotted in Figure 1.4 (longer segments). The respective PSD functions estimated using AR modelling are represented in Figure 2.3.

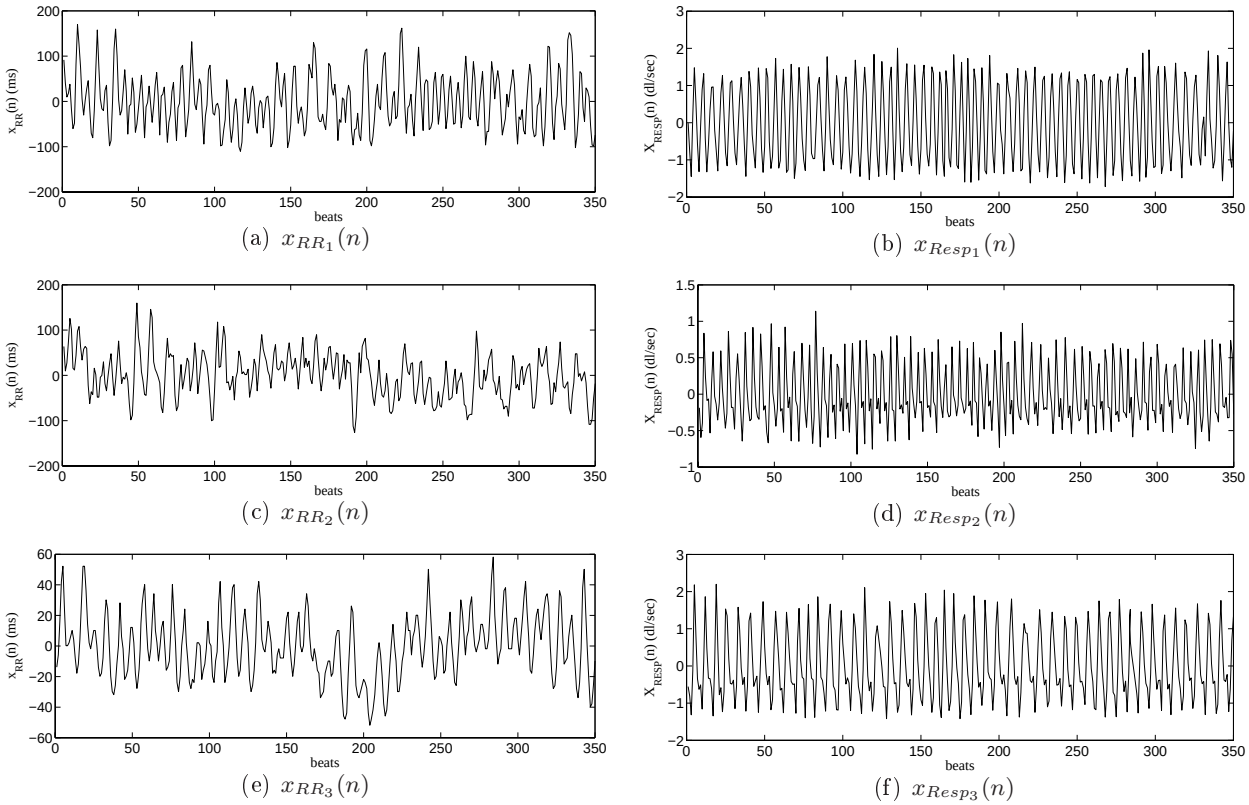

(a) $x_{RR_1}(n)$ (b) $x_{Resp_1}(n)$

(c) $x_{RR_2}(n)$ (d) $x_{Resp_2}(n)$

(e) $x_{RR_3}(n)$ (f) $x_{Resp_3}(n)$

Figure 2.2: Examples of 3 real simultaneous RR, $x_{\mathrm{RR}}(n)$, and respirogram, $x_{\mathrm{RESP}}(n)$, variability series. The mean of the correspondent RR interval series (mean cycle length) is (a) $T_{R1} = 826.2$ ms, (b) $T_{R2} = 918.2$ ms and (c) $T_{R1} = 731.8$ ms (see Figure 1.7). The respirogram variability series were extracted from the respiratory signals of Figure 1.4 and the correspondent mean respiratory frequencies are (a) 0.2238 Hz, (b) 0.2182 Hz and (c) 0.1866 Hz.

Cardiovascular series (such as the RR or QT interval, maximum of blood pressure in a beat, air flow value at the R peak time,...) are *beat indexed*, thus are *"evenly sampled in beats"* but not in time. For that reason, there is not any constant sampling period and an approximation, taken as the mean RR interval (T_R), can be used instead. The use the mean RR interval as sampling period T for estimating the PSD functions has been shown acceptable for low frequencies far from the Nyquist frequency (Mateo and Laguna, 2000). Furthermore, this normalization is required in order to make the respiratory frequency to be correctly reflected in the spectra, as it can easily be verified by comparing the mean respiratory frequency with the frequency location of the main peak on the spectra of respiratory series $S_{RESP}(F)$ (see Figures 2.2 and 2.3). Alternatives to this approximation are the regularly sampled interpolation of the series or the use of methods that do not require evenly sampling, as the spectrum of counts. As a standard, Task Force (1996) indicates the use of the interpolation with *non-parametric* spectral analysis and the use of the beat indexed series for parametric (model based) methods.

Regarding the spectra of short-term cardiovascular variability series, two main spectral components, corresponding to effects in different frequency ranges (frequency bands $\mathcal{B}$) are typically identified (Task Force, 1996):

- high frequency component (HF), range of 0.15-0.4 Hz,
- low frequency component (LF), range of 0.04-0.15 Hz.

Those bands were defined for HRV analysis but, as they reflect the main identified influences over the electrical cardiac activity, are usually considered in the study of other cardiovascular variability series.

The HF component in HRV spectra has been mainly associated to efferent vagal activity of the parasympathetic component of the autonomic nervous system (ANS) and reflects the respiratory activity, typically around 0.2-0.4 Hz. The LF component is traditionally associated with sympathetic modulation, in spite of a possible dominant parasympathetic effect could stand, specially in case of a low respiratory rhythm. An increase of the parasympathetic activity conducts to a power increase on the HF band, while an increase in sympathetic activity increments the LF band contribution. Some authors consider also a lower frequency band know as very low frequency (VLF), corresponding to the range below 0.04 Hz, but its measuring in short segments is dubious (Task Force, 1996), reason why it was not considered in this work. For the remaining of this thesis TP (total power) will denote the frequency range from 0.04 Hz to the highest frequency present in each spectrum $1/(2T_R)$ Hz.

The three typical frequency bands (VLF, LF and HF) are marked in Figure 2.3 using grey intensities. In the spectra of $x_{\mathrm{RR}}(n)$ is possible to identify these main frequency components. Namely, a noteworthy respiration-related peak is present on HF band. A lower respiratory frequency can be seen in the last example, and its dominant effect can be partially responsible by the model not being able to reflect the LF band activity in a clear way for the model selected by the AIC.

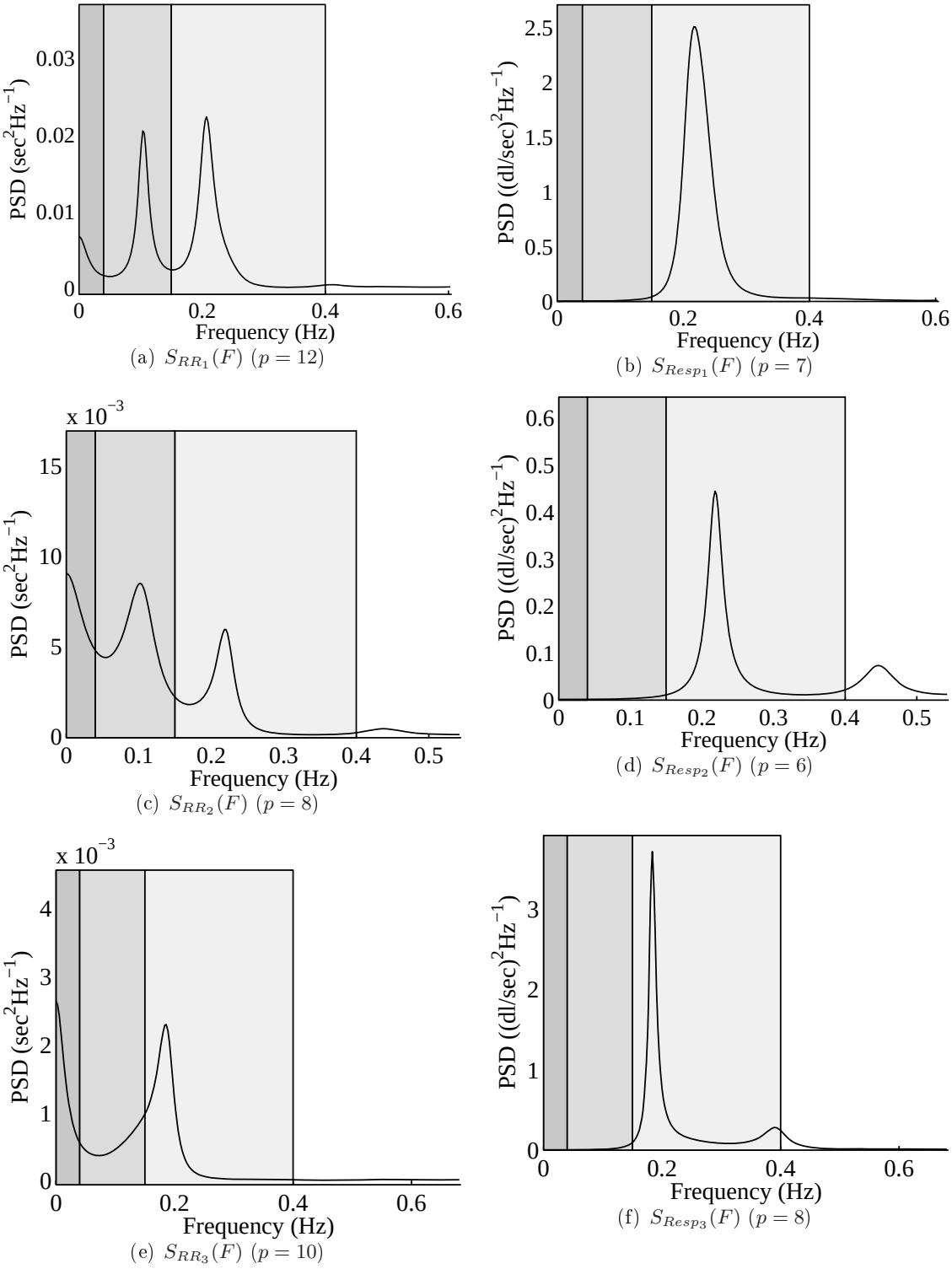

(a) $S_{RR_1}(F)$ $(p = 12)$

(b) $S_{Resp_1}(F)$ $(p = 7)$

(c) $S_{RR_2}(F)$ $(p = 8)$

(d) $S_{Resp_2}(F)$ $(p = 6)$

(e) $S_{RR_3}(F)$ $(p = 10)$

(f) $S_{Resp_3}(F)$ $(p = 8)$

Figure 2.3: PSD functions ($S_{RR}(F)$, $S_{Resp}(F)$) of estimated AR for the RR and respirogram variability series x_{RR_i} and x_{RESP_i}, $i \in 1, 2, 3$, plotted in Figure 2.2 (segments of 350 beats). Model order p indicated for each case was selected using AIC. The frequency ranges corresponding to HF, LF and VLF bands are marked using different grey intensities.

Parametric decomposition

Factorizing the transfer function $H_x(z)$ in equation (2.6) it is possible to decompose the complex spectral density $S_x(z)$ into l components, each one referred to one of its poles z_k, $k = 1, \ldots, l$ (Johnsen and Andersen, 1978; Baselli *et al.*, 1997)

$$S_x(z) = \lambda^2 \left| \frac{B(z)}{\prod_{k=1}^{l}(z - z_k)} \right|^2_{z=e^{j2\pi FT}}. \tag{2.7}$$

By definition, the complex spectrum $S_x(z)$ in equation (2.5) is obtained from the autocorrelation function[1] $r_x(\tau)$ as

$$S_x(z) = \sum_{\tau=-\infty}^{+\infty} r_x(\tau) z^{-\tau}, \tag{2.8}$$
$$r_x(\tau) = E[x(n)x(n-\tau)]$$

and inverting the z-transform,

$$r_x(\tau) = \frac{1}{2\pi j} \oint_{|z|=1} S_x(z) z^{\tau-1}, \tau = 0, 1, 2, ...$$
$$r_x(-\tau) = r_x(\tau). \tag{2.9}$$

Computing this line integral using the *Cauchy Residue Theorem*, the autocorrelation function $r_x(\tau)$ can be decomposed as

$$r_x(\tau) = \sum_{k=1}^{l} \left(\text{Res} \left[\frac{S(z)}{z} \right]_{z=z_k} \right) z_k^{\tau} \tag{2.10}$$
$$= \sum_{k=1}^{l} \gamma_k z_k^{\tau} \tag{2.11}$$
$$= \sum_{k=1}^{l} r_x^{(k)}(\tau) \tag{2.12}$$

and the correspondent complex spectral density

$$S_x(z) = \sum_{k=1}^{l} \mathcal{Z} \left\{ r_E^{(k)}(\tau) \right\} = \sum_{k=1}^{l} S_x^{(k)}(z). \tag{2.13}$$

According to Baselli *et al.* (1997), each term in equation (2.13) can be written as,

$$S_x^{(k)}(z) = \frac{\gamma_k z_k}{(z^{-1} - z_k)} + \gamma_k + \frac{\gamma_k z_k}{(z - z_k)}, \tag{2.14}$$

for $\gamma_k = \text{Res}\,[S_x(z)/z]$, calculated at $z = z_k$.

The residues γ_k can be computed and simplified using equations (2.5) and (2.7)

$$\gamma_k = \frac{B(z_k)\lambda^2 B(z_k^{-1})}{\prod_{\substack{h=1 \\ h \neq k}}^{l} (z_k - z_h) \prod_{h=1}^{l} (z_k^{-1} - z_h) z_k}.$$

[1] The definition of autocorrelation function considered in this thesis follows the usual notation in signal processing theory (Marple, 1987), which differs from time series analysis notation.

Since the residues for complex conjugate poles are complex conjugate, the total power in the spectrum can be written as the sum of $g \leq l$ components: one for each pair of complex conjugate poles z_g and z_g^* (located at frequencies F_g and $-F_g$) and one for each real pole z_g (at $F_g = 0$ or $F_g = (2T)^{-1}$), thus

$$r_x(0) = \sum_{k=1}^{l} \gamma_k = \sum_{\substack{g \\ 0<F_g<\frac{1}{2T}}} \left(\gamma_g + \gamma_g^*\right) + \sum_{\substack{g \\ F_g \in \{0, \frac{1}{2T}\}}} \gamma_g. \tag{2.15}$$

Due to the symmetry of $S_x(F)$ with respect to $F = 0$, frequencies associated to complex conjugate poles correspond to complex conjugate components which can be combined in a real $S_x^{(g)}(F)$, related to a power component $\gamma_g + \gamma_g^* = 2\Re(\gamma_g)$ (Johnsen and Andersen, 1978). Each term γ_g in the last sum of equation (2.15) can be seen as the power of a real component $S_x^{(g)}(F)$ corresponding to a real pole z_g (that is, for $F_g = 0$ or $F_g = (2T)^{-1}$). Therefore, $S_x(F)$ in equation (2.4) can be decomposed into components $S_x^{(g)}(F)$, contributing mainly at frequencies F_g ($0 \leq F_g \leq (2T)^{-1}$).

The power within a given frequency band $\mathcal{B}$, denoted by $P_x^{\mathcal{B}}$, can be obtained by summing the contributions of the poles located in band $\mathcal{B}$. That is,

$$P_x^{\mathcal{B}} = \sum_{\substack{g \\ F_g \in \mathcal{B}}} c_g \, \Re(\gamma_g) \tag{2.16}$$

where $c_g = 1$ for real poles and $c_g = 2$ for complex conjugate poles.

In Figure 2.4 are plotted the automatic decomposition of the estimated parametric spectra relative to the RR variability series represented in Figure 2.3. Components corresponding to complex poles are plotted with dashed lines and the three typical frequency bands used in HRV analysis are marked using grey intensities.

Only the spectral components corresponding to poles near to the unit circle and with larger amplitude are clearly visible in each spectra. Among them, a component corresponding to the main respiratory frequency is easily identifiable in all three examples by comparing to $S_{Resp}(F)$ in Figure 2.3 (b), (d) and (f). The decomposition of $S_{RR_3}(F)$ allowed to identify a component near the limit between LF and HF bands, overlapped but distinct from the respiratory related peak, what would not be noticed just looking to $S_{RR_3}(F)$.

It should be remarked that the algebraic decomposition of the spectrum here described does not guarantee the achievement of spectral components that are themselves admissible PSD functions. Moreover, negative power components can occur if poles are too close together (Marple, 1987). If this happens near the limit of a frequency band $\mathcal{B}$, a negative value can be obtained for $P_x^{\mathcal{B}}$. The components with relatively much lower amplitude, usually more spread along frequency, are also more likely to reflect cross effects between close poles. The S_{RR_1} decomposition (Figure 2.4(a)), for example, presents one of those low amplitude spectral components partially negative (visible near the x axis), giving origin to a negative power component.

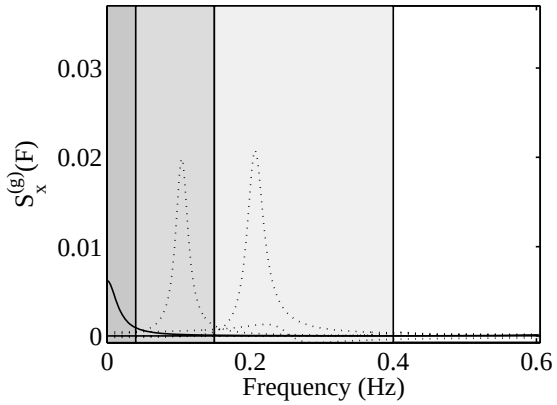

(a) spectral components of $S_{RR_1}(F)$ ($p = 12$)

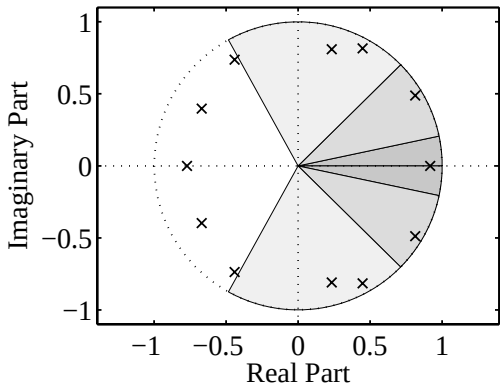

(b) diagram of poles and zeros of $S_{RR_1}(F)$

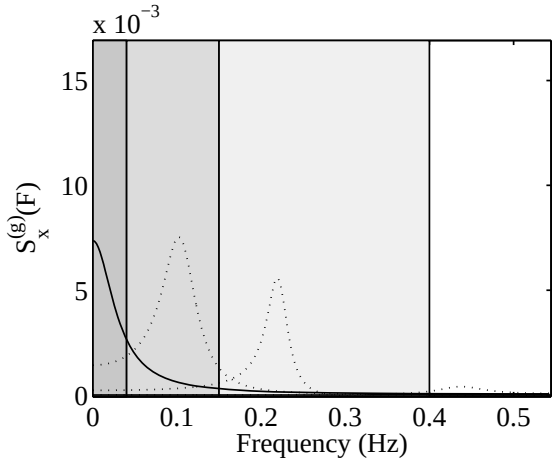

(c) spectral components of $S_{RR_2}(F)$ ($p = 8$)

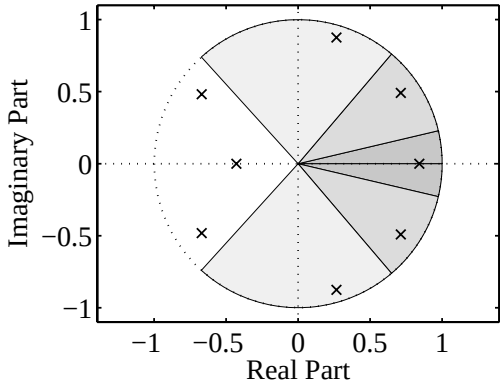

(d) diagram of poles and zeros of $S_{RR_2}(F)$

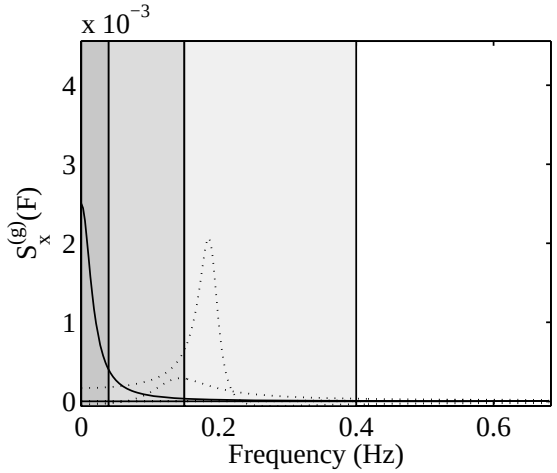

(e) spectral components of $S_{RR_3}(F)$ ($p = 10$)

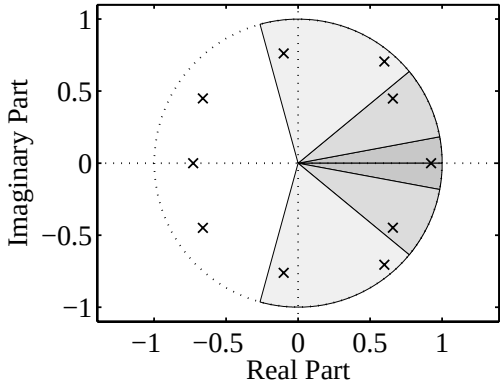

(f) diagram of poles and zeros of $S_{RR_3}(F)$

Figure 2.4: Parametric decomposition of the PSD functions in Figure 2.3. The model order p is indicated for each case, components corresponding to complex poles are plotted with dashed line and the three typical frequency bands are marked using grey intensities.

2.2.2 Models Including Series Interactions

The above referred models allow to study each cardiac series by itself not taking into account that those series have common physiological sources of variability and interact with each other. Let's consider $x_1(n)$ and $x_2(n)$ as zero-mean related time series, with sampling period T. Multi-input models have been used to explore series interactions and two of those models will be briefly reviewed in this subsection.

ARX model

Given a process $x_1(n)$, an ARX model (Figure 2.5) can be described as an AR model with an extra (or external) input $x_2(n)$, that is

$$x_1(n) = -\sum_{k=1}^{q} a_{11}(k)\ x_1(n-k) + w(n) + \sum_{k=0}^{p} a_{12}(k)\ x_2(n-k). \tag{2.17}$$

The series $x_1(n)$ is assumed to depend on its on past values and on two uncorrelated inputs: white noise $w(n)$ and one other driven by $x_2(n)$. The input series $x_2(n)$ is not explained by the model. One example of ARX modelling application is the study of the effect of respiration over the HR (Baselli *et al.*, 1995).

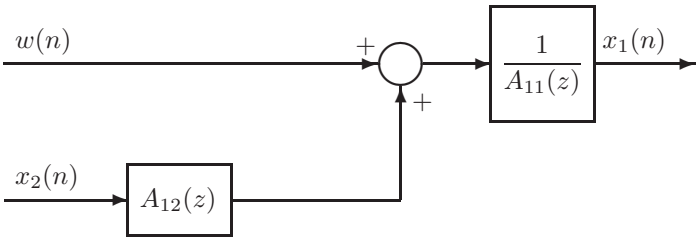

Figure 2.5: ARX Structure - model of a process $x_1(n)$.

Bivariate AR modelling

A bivariate AR_p process assumes reciprocal interactions (dependence) between time series $x_1(n)$ and $x_2(n)$. It can be written as (Barbieri and Saul, 1999)

$$x_1(n) = -\sum_{k=1}^{p} a_{11}(k)x_1(n-k) - \sum_{k=1}^{p} a_{12}(k)x_2(n-k) + w_1(n), \tag{2.18}$$

$$x_2(n) = -\sum_{k=1}^{p} a_{21}(k)x_1(n-k) - \sum_{k=1}^{p} a_{22}(k)x_2(n-k) + w_2(n), \tag{2.19}$$

where $w_1(n)$ and $w_2(n)$ are stationary zero-mean white noises with variances λ_1^2 and λ_2^2 and covariance λ_c^2. The matrix of spectra is calculated as

$$\mathbf{S}(F) = \ diag([T\ T])\mathbf{S}(z)|_{z=e^{j2\pi FT}} \tag{2.20}$$

$$\mathbf{S}(z) = \mathbf{H}(z)\mathbf{\Sigma}\mathbf{H}'(z^{-1}), \tag{2.21}$$

where $diag([T\ T])$ is a diagonal matrix whose elements are the sampling period T of both time series and

$$\mathbf{S}(z) = \begin{bmatrix} S_{11}(z) & S_{12}(z) \\ S_{21}(z) & S_{22}(z) \end{bmatrix}, \quad \mathbf{\Sigma} = \begin{bmatrix} \lambda_1^2 & \lambda_c^2 \\ \lambda_c^2 & \lambda_2^2. \end{bmatrix}$$

From equations (2.18) and (2.19) the matrix of transfer functions is

$$\mathbf{H}(z) = \begin{bmatrix} \frac{A_{22}(z)}{A(z)} & -\frac{A_{12}(z)}{A(z)} \\ -\frac{A_{21}(z)}{A(z)} & \frac{A_{11}(z)}{A(z)} \end{bmatrix}, \tag{2.22}$$

$$A(z) = A_{22}(z)A_{11}(z) - A_{12}(z)A_{21}(z), \tag{2.23}$$

for A_{11}, A_{12}, A_{21} and A_{22} polynomials with coefficients respectively, $a_{11}(k)$, $a_{12}(k)$, $a_{21}(k)$ and $a_{22}(k)$ $(k = 1, ..., p)$. From (2.21) we have

$$\begin{aligned} S_{11}(z) &= H_{11}(z)\lambda_1^2 H_{11}(z^{-1}) + H_{12}(z)\lambda_2^2 H_{12}(z^{-1}) + H_{12}(z)\lambda_c^2 H_{11}(z^{-1}) + H_{11}(z)\lambda_c^2 H_{12}(z^{-1}), \\ S_{22}(z) &= H_{21}(z)\lambda_1^2 H_{21}(z^{-1}) + H_{22}(z)\lambda_2^2 H_{22}(z^{-1}) + H_{22}(z)\lambda_c^2 H_{21}(z^{-1}) + H_{21}(z)\lambda_c^2 H_{22}(z^{-1}), \\ S_{12}(z) &= H_{11}(z)\lambda_1^2 H_{21}(z^{-1}) + H_{12}(z)\lambda_2^2 H_{22}(z^{-1}) + H_{12}(z)\lambda_c^2 H_{21}(z^{-1}) + H_{11}(z)\lambda_c^2 H_{22}(z^{-1}), \\ S_{21}(z) &= S_{12}(z^{-1}). \end{aligned} \tag{2.24}$$

The bivariate AR structure has been used in cardiovascular variability analysis for example to model the mutual interactions between the tachogram and the systolic blood pressure variability series $(x_{RR}(n), x_{SBP}(n))$ (Barbieri and Saul, 1999).

Generalization to obtain multivariate scheme for more than two signals is straightforward and has been applied for studying the mutual relations between the zero-mean variability series series $x_{RR}(n)$, $x_{SBP}(n)$ and $x_{RESP}(n)$, for example (Barbieri *et al.*, 1997).

The *magnitude of the squared spectral coherence* obtained from the spectra and the cross-spectrum

$$K^2(F) = \left[\frac{|S_{12}(z)|^2}{S_{11}(z)S_{22}(z)} \right]_{z=e^{j2\pi FT}}, \tag{2.25}$$

is a measure of the linear relation between the series $x_1(n)$ and $x_2(n)$. A perfect linear relation corresponds to $K^2(F) = 1$. Any time delays on the linear dependence between the time series $x_1(n)$ and $x_2(n)$ can be assessed evaluating the *phase* $(ph(F))$ of the cross-spectra $S_{12}(F)$ or $S_{21}(F)$.

The function $K^2(F)$ can also be used to evaluate the similarity between two series: high values of $K^2(F)$ correspond to frequencies in which the contents of the two series are alike. In order to illustrate this, the $RR(n)$ variability series segments of Figure 2.2 were divided in two subsegments that were jointly modelled using an AR bivariate model of the same order of the previously estimated AR model. The estimated functions $S_{11}(F)$, $S_{22}(F)$ and $K^2(F)$ are plotted in Figure 2.6. The small number of samples used in each subsegment contributes to the differences between the two spectra, specially in the *VLF* band. For the frequencies in which the values of $K^2(F)$ are highest it can be observed that the two spectra are more similar.

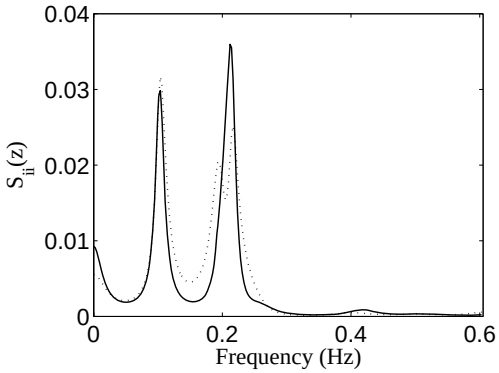

(a) Spectra of the two subsegments in $x_{RR_1}(n)$ ($p = 12$)

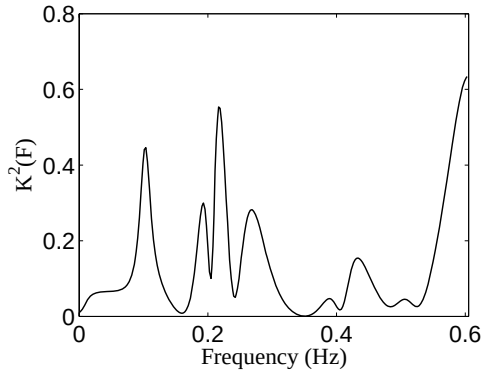

(b) magnitude of the squared spectral coherence between the subsegments in $RR_1(n)$

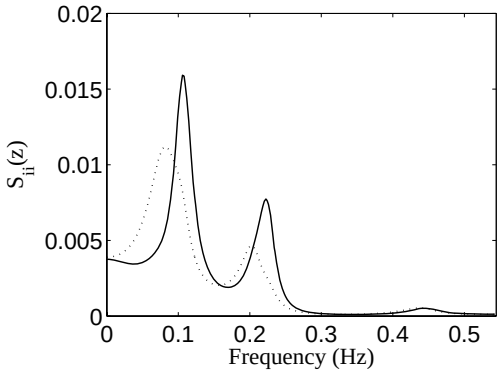

(c) Spectra of the two subsegments in $x_{RR_2}(n)$ ($p = 8$)

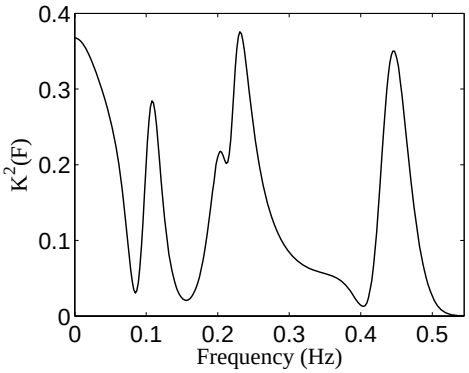

(d) magnitude of the squared spectral coherence between the subsegments in $RR_2(n)$

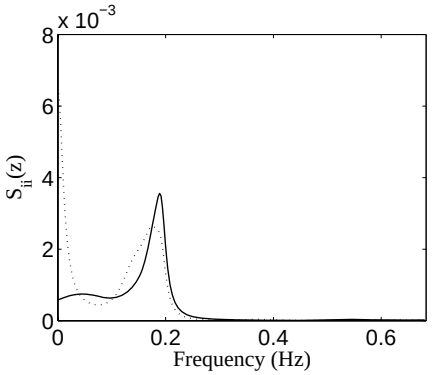

(e) Spectra of the two subsegments in $x_{RR_3}(n)$ ($p = 10$)

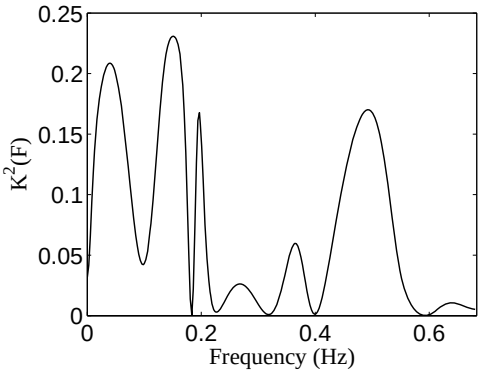

(f) magnitude of the squared spectral coherence between the subsegments in $RR_3(n)$

Figure 2.6: Estimated PSD functions and magnitude of the squared spectral coherence using a AR_p bivariate model (p indicated for each case) between the two subsegments (175 beats) of the series in Figure 2.2 (second subsegment spectra correspond to the dotted line).

2.3 ARARX Model for QTV and HRV interactions

Following the notation of Figure 1.6, in this thesis $RR(n)$ stands for the interval associated to the n^{th} beat, defined as the time interval from previous $(n-1)^{\text{th}}$ beat to actual n^{th} beat, and $QT(n)$ stands for the QT interval related to the n^{th} beat. The data to be analyzed by the parametric methodology are the variability series $x_{\text{RR}}(n) = RR(n) - T_R$ and $x_{\text{QT}}(n) = QT(n) - T_{\text{QT}}$, where T_R and T_{QT} stand respectively for the mean of $RR(n)$ and $QT(n)$ in the analysed segment.

2.3.1 Model formulation and spectral decomposition

The parametric methodology explores QTV and HRV interactions assuming an open loop linear model (Porta *et al.*, 1998) schematically presented in Figure 2.7, where $A_{11}(z)$, $A_{12}(z)$, $A_{22}(z)$ and $D(z)$ are polynomials with coefficients $a_{11}(k)$, $a_{12}(k)$, $a_{22}(k)$ and $d(k)$, respectively.

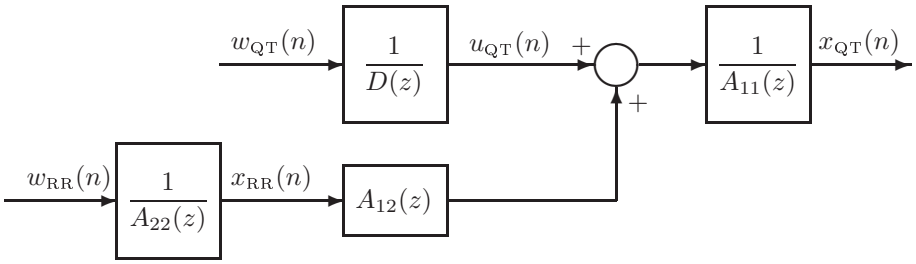

Figure 2.7: Model of QTV versus HRV interactions

The series $w_{\text{RR}}(n)$ and $w_{\text{QT}}(n)$ are uncorrelated stationary zero mean white noises with standard deviations λ_{RR} and λ_{QT}. The series $x_{\text{RR}}(n)$ is modelled as an order p autoregressive (AR_p) stationary random process

$$x_{\text{RR}}(n) = -\sum_{k=1}^{p} a_{22}(k)\; x_{\text{RR}}(n-k) + w_{\text{RR}}(n). \tag{2.26}$$

The QTV trend is assumed to result from two uncorrelated sources, one driven by HR (external) and another one resulting from an AR process with a white noise input (Figure 2.7). That is

$$\begin{aligned} x_{\text{QT}}(n) &= \sum_{k=0}^{q} a_{12}(k)\; x_{\text{RR}}(n-k) + u_{\text{QT}}(n) - \sum_{k=1}^{q} a_{11}(k)\; x_{\text{QT}}(n-k), \\ u_{\text{QT}}(n) &= -\sum_{k=1}^{q} d(k)\; u_{\text{QT}}(n-k) + w_{\text{QT}}(n). \end{aligned} \tag{2.27}$$

Therefore, this model known as $ARARX_q$ model (Ljung, 1999) accounts for the $QT(n)$ dependence on its past values (as an AR model) and on those of the RR interval (like in the ARX), as recent studies have evidenced (Pueyo *et al.*, 2003). For simplicity, the same order q was assumed for all ARARX model polynomials, while a possibly different order p was allowed for the AR model for the $x_{\text{RR}}(n)$ series. This is a generalization from previous approaches, where the same order was considered for all polynomials in the model ($p = q$) (Porta *et al.*, 1998). The order p in equation (2.26) represents

the memory of $x_{\mathrm{RR}}(n)$ of its own past while order q in equation (2.27) produces a cumulative memory effect between the polynomials A_{11} and A_{12} or D, depending on the $x_{\mathrm{QT}}(n)$ dependence considered. Notice that $p = q$ corresponds to assign to the $x_{\mathrm{QT}}(n)$ series a double memory than to $x_{\mathrm{RR}}(n)$ series.

The assumption of uncorrelated sources allows to compute the PSD functions of $x_{\mathrm{QT}}(n)$, $S_{\mathrm{QT}}(F)$, as the sum of two partial spectra

$$\begin{aligned} S_{\mathrm{QT|RR}}(F) &= T_R \lambda_{\mathrm{RR}}^2 \left| \frac{A_{12}(z)}{A_{11}(z)A_{22}(z)} \right|^2_{z=e^{j2\pi F T_R}}; \\ S_{\mathrm{QT|QT}}(F) &= T_R \lambda_{\mathrm{QT}}^2 \left| \frac{1}{A_{11}(z)D(z)} \right|^2_{z=e^{j2\pi F T_R}}, \end{aligned} \tag{2.28}$$

which express the contributions related and unrelated to RR interval, respectively $x_{\mathrm{QT|RR}}(n)$ and $x_{\mathrm{QT|QT}}(n)$, as illustrated in Figure 2.8.

The relative fraction of the QTV driven by RR in frequency band $\mathcal{B}$ ($R^{\mathcal{B}}_{\mathrm{QT|RR}}$) is given by

$$R^{\mathcal{B}}_{\mathrm{QT|RR}} = \frac{P^{\mathcal{B}}_{\mathrm{QT|RR}}}{P^{\mathcal{B}}_{\mathrm{QT|RR}} + P^{\mathcal{B}}_{\mathrm{QT|QT}}} \times 100, \tag{2.29}$$

where the power within each frequency band $\mathcal{B}$, for each of the QTV fractions $\left(P^{\mathcal{B}}_{\mathrm{QT|RR}}, P^{\mathcal{B}}_{\mathrm{QT|QT}}\right)$, can be calculated by decomposing these spectra as described in Section 2.2.1 and using equation (2.16).

2.3.2 Model identification and order selection

From the $x_{\mathrm{RR}}(n)$ series, $A_{22}(z)$ was estimated using least squares (LS), with the combined forward and backward linear prediction algorithm (Marple, 1987).

The ARARX model parameters ($A_{11}(z)$, $A_{12}(z)$ and $D(z)$) were iteratively obtained using the generalized least squares method (GLS) (Soderstrom, 1974). Briefly, GLS was implemented as:

1. to take $\tilde{D}(z) = 1$ as initial estimation of $D(z)$ (*INITIALIZATION*);
2. to take as data the original variability series $x_{\mathrm{RR}}(n)$ and $x_{\mathrm{QT}}(n)$ filtered by $\tilde{D}(z)$;
3. to consider an ARX model, by making $D(z) = 1$, and estimate $A_{11}(z)$ and $A_{12}(z)$ from the data using LS;
4. to estimate $\tilde{D}(z)$ by fitting an AR model to the ARX residuals in the Step 3 using LS;
5. if the residuals $w_{\mathrm{QT}}(n)$ after $\tilde{D}(z)$ estimation on Step 4 cannot be considered white noise, repeat from Step 2, taking as data the original $x_{\mathrm{RR}}(n)$ and $x_{\mathrm{QT}}(n)$ variability series of Step 1, filtered by estimated $\tilde{D}(z)$ in Step 4.

A large enough signal-to-noise ratio (SNR) guaranties that the minima of the square residue are global (Ljung, 1999), and for adequate model orders the GLS convergence to white noise residuals $w_{\mathrm{QT}}(n)$ is expected in a reasonable small number of iterations.

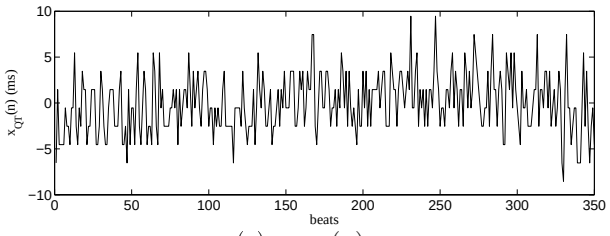

(a) $x_{\mathrm{QT}_1}(n)$

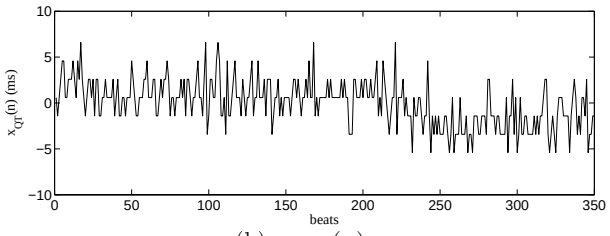

(b) $x_{\mathrm{QT}_2}(n)$

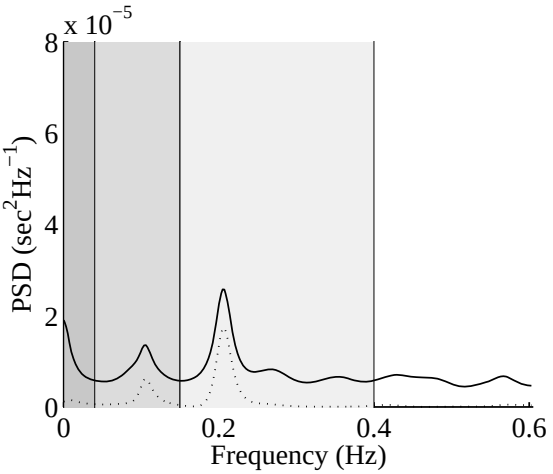

(c) $S_{\mathrm{QT}_1}(F)$ and $S_{\mathrm{QT|RR}_1}(F)$ $(q = 5)$

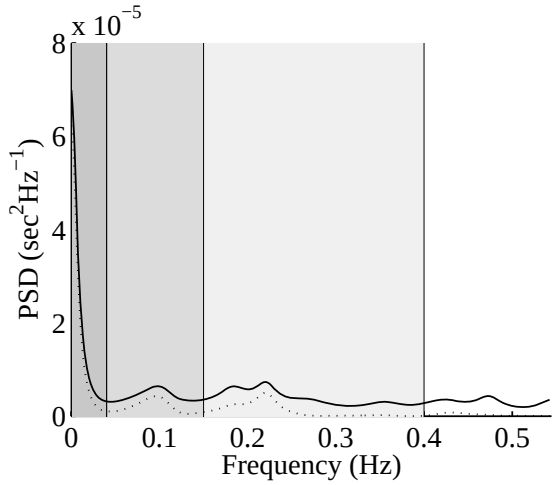

(d) $S_{\mathrm{QT}_2}(F)$ and $S_{\mathrm{QT|RR}_2}(F)$ $(q = 6)$

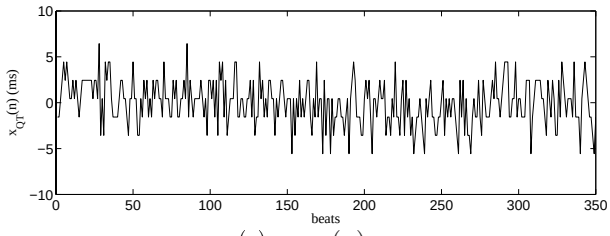

(e) $x_{\mathrm{QT}_3}(n)$

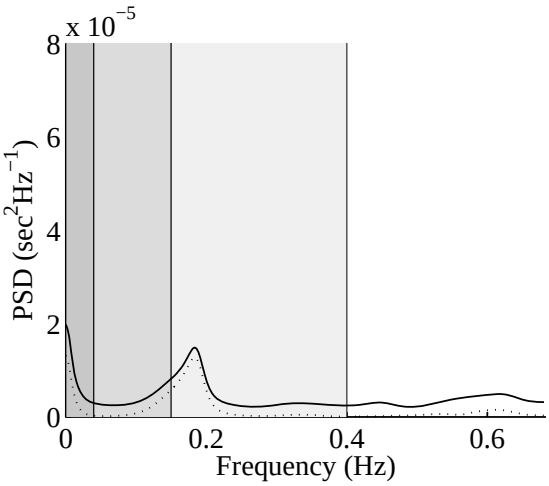

(f) $S_{\mathrm{QT}_3}(F)$ and $S_{\mathrm{QT|RR}_3}(F)$ $(q = 5)$

Figure 2.8: Examples of real QT series $x_{\mathrm{QT}}(n)$ (same series used in Figure 1.7) and respective estimated spectra using an $ARARX_q$ model for the total ($S_{\mathrm{QT}}(F)$, full line) and HRV related contribution ($S_{\mathrm{QT|RR}}(F)$, dashed line), q indicated for each case.

The residuals $w_{\mathrm{RR}}(n)$ and $w_{\mathrm{QT}}(n)$ were considered to be uncorrelated white noises if their normalized autocorrelations and cross-correlation were not different from zero according to 5% significance bilateral tests, both for the first 40 (Porta *et al.*, 1998) lags and for all lags.

Orders p and q between 2 and 18 were admitted, for the sake of comparison in Porta *et al.* (1998) and to allow lower orders for the QTV dependency on HRV. Model orders not corresponding to white noise / uncorrelated residuals, or producing a negative global contribution in a frequency band were considered as inadequate and excluded. Optimal p and q were automatically selected from the admitted orders, allowing to selected an *adequate model* for the data, if it exists. First the order p of $A_{11}(z)$ in the AR model is chosen by minimizing the *Akaike Information Criteria* (AIC). The order q is taken as the one minimizing the multivariate AIC

$$log\left(det\left(\mathbf{\Sigma}\right)\right) + 2 * (p + 3q + 1)/N, \tag{2.30}$$

where $det\left(\mathbf{\Sigma}\right)$ stands for the determinant of the covariance matrix of the residuals ($w_{\mathrm{RR}}(n)$ and $w_{\mathrm{QT}}(n)$) and N is the number of intervals (beats) in the segment. As the order p, and therefore the $w_{\mathrm{RR}}(n)$ variance, have been already determined in the previous step and only the q order remains to be chosen, this is not a multivariate minimization in strict sense.

The segment length has to attend several compromises, namely has to be adequate for short term analysis and to the model orders admitted. To reduce overfit problems with AIC, the number of estimated parameters ($M = p+3q+1$) has to be small (less that 10%) relatively to the total number of data values in the variability series (Waele and Broersen, 2003). Concerning the extreme case $p = q = 18$ ($M = 73$) and as the data consists in 2 series of values, segments with around 365 beats should be considered. According to Task Force (1996) a maximum order of $p = 20$ is recommended for RR series modeling, but admitting higher orders would require longer segments and to use longer segments decreases the probability of finding adequate segments for analysis, in particular dealing with QT series which require the problematic location of the T wave end.

2.4 Validation of QTV quantification

The validation of the parametric methodology described can only be performed over series with known QTV fractions (related and unrelated with HRV). With this purpose, test series were generated assuming that the linear model in Figure 2.7 holds. The simulation of series $x_{\mathrm{QT}}(n)$ from the linear model requires some reference parameters for the polynomial coefficients involved and therefore reference simulation models were first constructed. The methods used for the test data simulation and validation are outlined in the block diagram of Figure 2.9.

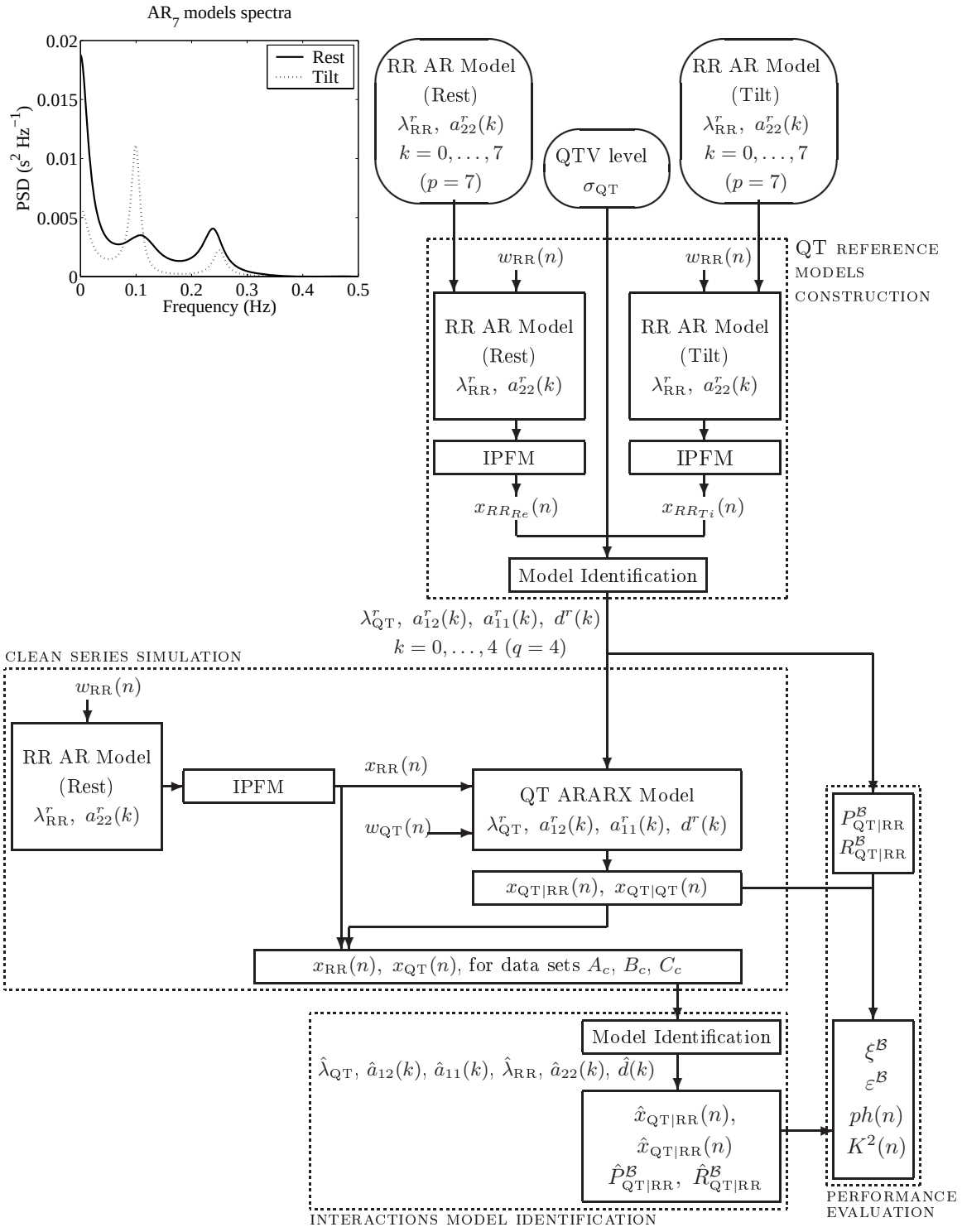

Figure 2.9: Methods block diagram - QT reference models construction (upper block), clean series simulation (central block), QTV versus HRV interactions model estimation (lower block), performance evaluation (right side). The values for several parameters used in the simulation can be found in Appendix C.

2.4.1 QT reference models construction

Aiming to obtain realistic series $x_{\mathrm{QT}}(n)$ resulting from $x_{\mathrm{RR}}(n)$ and an uncorrelated source $w_{\mathrm{QT}}(n)$, in a first step were constructed the auxiliary series

$$\tilde{x}_{\mathrm{QT}}(n) = a\left(\sqrt{x_{\mathrm{RR}_{\mathrm{Re}}}(n)} + \sqrt{x_{\mathrm{RR}_{\mathrm{Ti}}}(n)}\right) + b \tag{2.31}$$

from which the reference model parameters are going to be extracted. The expression (2.31) is based in the classical static relation given by Bazett's QT correction formula (equation 2.2) and allows to obtain QTV series resulting nonlinearly from two uncorrelated sources: $x_{\mathrm{RR}_{\mathrm{Re}}}(n)$ and $x_{\mathrm{RR}_{\mathrm{Ti}}}(n)$.

Independent $x_{\mathrm{RR}}(n)$ realizations agreeing to spectra typically found at supine rest (Re) and head-up tilt (Ti) situations (Task Force, 1996) were considered (Figure 2.9). Those series were obtained using an Integral Pulse Frequency Modulation (IPFM) model (Mateo and Laguna, 2000), following AR_7 modulating signals with coefficient values a^r_{22}, residual standard deviation (λ^r_{RR}) and for simplicity sake $T_R = 1$ sec. The parameters values used in the simulation set-up can be found in Appendix C.

It should be remarked that the part of QTV uncorrelated with HRV does not need to have a RR like spectral shape, as has been here considered. However this choice assigns to the uncorrelated part a spectral behaviour which puts the method under evaluation in the more difficult situation: the spectral overlapping between the two QTV fractions forces the method to search for uncorrelations rather than just make frequency filtering.

The parameter b allows to set a zero mean; the parameter a allows to adjust the standard deviation (σ_{QT}) of $\tilde{x}_{\mathrm{QT}}(n)$ and therefore to consider distinct QTV levels. Six different QTV levels have been considered, corresponding to $\sigma_{\mathrm{QT}} = 17$, 13, 10, 8, 5 and 3 ms, covering the interval of values between extreme situations found in healthy subjects (Jensen *et al.*, 2004).

Parametric model identification in equations (2.26) and (2.27), considering $x_{\mathrm{RR}}(n) = x_{\mathrm{RR}_{\mathrm{Re}}}(n)$ and $x_{\mathrm{QT}}(n) = \tilde{x}_{\mathrm{QT}}(n)$ given by expression (2.31), provides the values for the reference coefficients values $a^r_{12}(k)$, $a^r_{11}(k)$, $d^r(k)$, and the residual noise standard deviation (λ^r_{QT}) for the simulation. This has been done for each of the considered QTV levels, allowing to construct six QTV reference models, denoted as models 1 to 6, which parameters values are presented in Appendix C.

To include similar memory on its own past for both $x_{\mathrm{QT}}(n)$ and $x_{\mathrm{RR}}(n)$, a value of $q = 4$ was chosen ($p = 7, 2q = 8$). As a consequence, $x_{\mathrm{QT}}(n)$ has a longer memory ($p + q$) on $x_{\mathrm{RR}}(n)$ past samples.

The *QT reference models construction* is summarized in the upper block of the diagram in Figure 2.9.

2.4.2 Clean Series Simulation

Once the QT reference model parameters were obtained, the clean test data were simulated, as outlined in the central block of Figure 2.9 and described in this Section.

The series $x_{\mathrm{RR}}(n)$ were obtained using modulating signals following the AR_7 model corresponding to the supine rest $x_{RR_{Re}}$ situation and the IPFM model.

The $x_{\mathrm{QT}}(n)$ fraction driven by RR, $x_{\mathrm{QT|RR}}(n)$, was obtained by filtering each simulated $x_{\mathrm{RR}}(n)$, i. e.

$$x_{\mathrm{QT|RR}}(n) = \sum_{k=0}^{q} a_{12}^{r}(k) x_{\mathrm{RR}}(n) - \sum_{k=1}^{q} a_{11}^{r}(k) x_{\mathrm{QT|RR}}(n-k), \tag{2.32}$$

which corresponds to follow the lower branch of the model in Figure 2.7. Analogously, $u_{\mathrm{QT}}(n)$ and the fraction uncorrelated with RR, $x_{\mathrm{QT|QT}}(n)$, were obtained following the upper branch of the model in Figure 2.7, that is filtering simulated white noise $w_{\mathrm{QT}}(n)$ with standard deviation $\lambda_{\mathrm{QT}}^{r}$

$$\begin{aligned} x_{\mathrm{QT|QT}}(n) &= u_{\mathrm{QT}}(n) - \sum_{k=1}^{q} a_{11}^{r}(k) x_{\mathrm{QT|QT}}(n-k); \\ u_{\mathrm{QT}}(n) &= -\sum_{k=1}^{q} d^{r}(k)\ u_{\mathrm{QT}}(n-k) + w_{\mathrm{QT}}(n). \end{aligned} \tag{2.33}$$

An example of simulated series can be found in Figures 2.10(a) and 2.10(b).

Three cases of possible *dependencies* were considered:

A) QT and RR fully correlated: $x_{\mathrm{QT}}(n) = x_{\mathrm{QT|RR}}(n)$,

B) QT and RR uncorrelated: $x_{\mathrm{QT}}(n) = x_{\mathrm{QT|QT}}(n)$,

C) mixture of the two dependencies: $x_{\mathrm{QT}}(n) = x_{\mathrm{QT|RR}}(n) + x_{\mathrm{QT|QT}}(n)$;

and A_c, B_c and C_c, the correspondent *clean* test data sets were generated.

2.4.3 Interactions model identification and performance evaluation

The identification of the adequate model for in each pair of simulated series is performed as described in Section 2.3.2 and it is represented in the lower block of the diagram in Figure 2.9. By applying the parametric methodology are estimated for each test data:

- the model coefficients $\hat{d}(k)$, $\hat{a}_{22}(k)$, $\hat{a}_{12}(k)$, $\hat{a}_{11}(k)$,
- the residual noises $\hat{w}_{\mathrm{RR}}(n)$, $\hat{w}_{\mathrm{QT}}(n)$,
- and their respective standard deviations $\hat{\lambda}_{\mathrm{RR}}$, $\hat{\lambda}_{\mathrm{QT}}$

From those were also calculated:

- the *variability measures* for each frequency band considered, $\hat{P}^{\mathcal{B}}_{\mathrm{QT|RR}}$, $\hat{P}^{\mathcal{B}}_{\mathrm{RR|RR}}$, $\mathcal{B} \in \{HF, LF\}$, according to equations (2.28) and (2.16);
- the *relative QTV fraction driven by RR*, for each frequency band, $\hat{R}^{\mathcal{B}}_{\mathrm{QT|RR}}$, $\mathcal{B} \in \{HF, LF\}$, using the values found for $\hat{P}^{\mathcal{B}}_{\mathrm{QT|RR}}$ and $\hat{P}^{\mathcal{B}}_{\mathrm{RR|RR}}$ and equation (2.29);
- the *signal* $\hat{x}_{RR}(n)$ *corresponding to the estimated AR model*, by filtering the residues $\hat{w}_{\mathrm{RR}}(n)$ with $\hat{A}_{22}(z)$;

- *the signals* $\hat{x}_{QT|RR}(n)$ *and* $\hat{x}_{QT|QT}(n)$*, corresponding to the two* $x_{QT}(n)$ *fractions*, following equations (2.32) and (2.33), by replacing the reference by the estimated coefficients and using as inputs $\hat{x}_{\mathrm{RR}}(n)$ and the residues $\hat{w}_{\mathrm{QT}}(n)$.

The spectral decomposition can be performed for each estimated QTV fraction as described in Section 2.3.1 and is illustrated in Figures 2.10(c) and 2.10(d).

The set of indexes used to evaluate the performance of the methods are summarized in the block on the right side of the diagram in Figure 2.9.

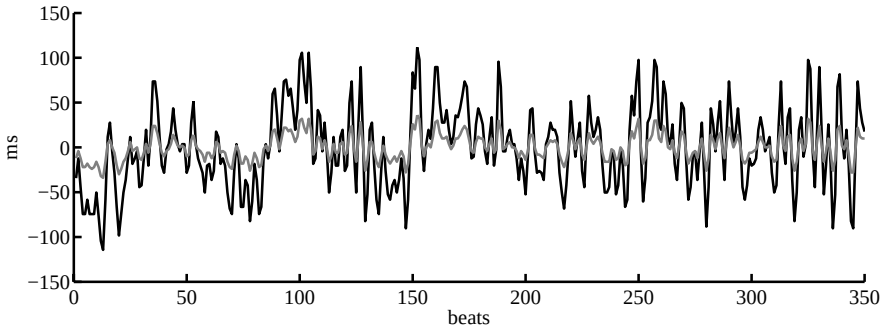

(a) $x_{\mathrm{RR}}(n)$ (black) and $x_{\mathrm{QT|RR}}(n)$ (grey)

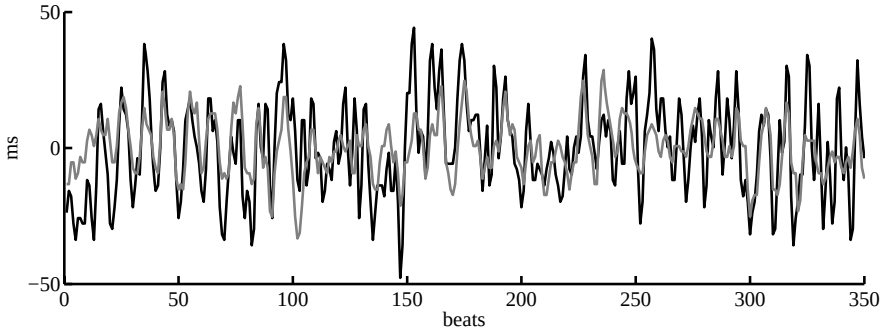

(b) $x_{\mathrm{QT}}(n)$ (black) and $x_{\mathrm{QT|QT}}(n)$ (grey)

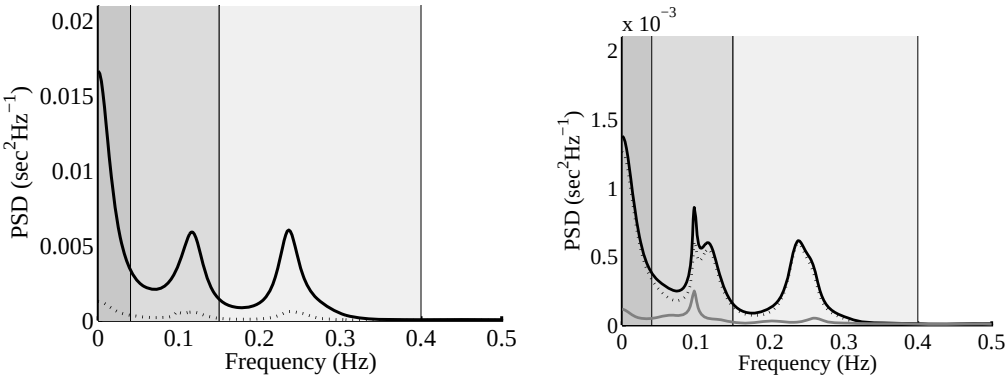

(c) $S_{\mathrm{RR}}(F)$ (full line) and $S_{\mathrm{QT|RR}}(F)$ (dashed line) (d) $S_{\mathrm{QT}}(F)$ (full black line), $S_{\mathrm{QT|QT}}(F)$ (full gray line) and $S_{\mathrm{QT|RR}}(F)$ (dashed line)

Figure 2.10: Examples of simulated series $x_{\mathrm{QT|RR}}(n)$, $x_{\mathrm{QT}}(n)$, $x_{\mathrm{QT|RR}}(n)$, $x_{\mathrm{QT|QT}}(n)$ and respective PSD functions. Simulation done following QT model 1 ($\sigma_{\mathrm{QT}} = 17$ ms).

The similarity between the estimated $\hat{x}_{\mathrm{QT|RR}}(n)$ and the corresponding simulated $x_{\mathrm{QT|RR}}(n)$ series was evaluated by the magnitude of the squared spectral coherence $K^2(F)$ and the phase of the cross-spectra $ph(F)$, obtained by bivariate modelling (Section 2.2.2), using an AR_4 model ($q = 4$). Analogously, $\hat{x}_{\mathrm{QT|QT}}(n)$ and $x_{\mathrm{QT|QT}}(n)$ were also compared using an AR_8 model ($2q = 8$).

The reference spectra of the simulated series were obtained directly from the reference parameters in the correspondent QT reference model used in simulation. The spectral decomposition was performed for each QTV fraction as described in Section 2.3.1. The reference variability measures ($P^{\mathcal{B}}_{\mathrm{QT|RR}}$ and $P^{\mathcal{B}}_{\mathrm{RR|RR}}$) and reference ratio ($R^{\mathcal{B}}_{\mathrm{QT|RR}}$) stand as references for all series derived from the correspondent QTV reference model. Performance indexes were evaluated with respect to these reference variability measures and ratios.

The QTV fraction driven by HRV is likely to give a preferential performance index, since it is more likely to be correctly estimated, due to the fact that any spurious QTV will be considered as part of the uncorrelated fraction. Thus two types of error were considered:

- *absolute errors* $\xi^{\mathcal{B}}$ in the estimated variability measures were computed with respect to the reference variability measures as

$$\xi^{\mathcal{B}} = \hat{P}^{\mathcal{B}}_{\mathrm{QT|RR}} - P^{\mathcal{B}}_{\mathrm{QT|RR}}, \tag{2.34}$$

- *percentage errors* $\varepsilon^{\mathcal{B}}$ in the quantification of the QTV fraction correlated with HRV were defined as the difference between the estimated and reference ratios, i. e.

$$\varepsilon^{\mathcal{B}} = \hat{R}^{\mathcal{B}}_{\mathrm{QT|RR}} - R^{\mathcal{B}}_{\mathrm{QT|RR}}. \tag{2.35}$$

It should be remarked that the percentage errors $\varepsilon^{\mathcal{B}}$ depend on both QTV fractions (equation (2.16)) and thus are performance indicators more sensitive than the absolute errors $\xi^{\mathcal{B}}$. As a matter of fact, overestimated $P^{\mathcal{B}}_{\mathrm{QT|QT}}$ leads to an artificial decrease on $\hat{R}^{\mathcal{B}}_{\mathrm{QT|RR}}$.

2.4.4 Clean simulated series results

For the *clean* test data sets A_c, B_c and C_c were considered segments of 350 beats from each pair of the 50 uncorrelated realizations (trials) of the series $x_{\mathrm{QT}}(n)$ simulated directly from each QT reference model and the correspondent $x_{\mathrm{RR}}(n)$. It should be noticed that for the mean HR considered in the simulation (60 bpm) 350 beats corresponds roughly to 6 min of ECG signal, what is not far from the 5 min duration recommended for HRV (Task Force, 1996). Also 350 is near the limit of data points required to avoid AIC overfit (Section 2.3.2), even in the extreme case of $p = q = 18$.

For each QT series realization in simulated data, the standard deviation (s_{QT}) was estimated and compared with the reference standard deviation (σ_{QT}) for the corresponding QT model. Table 2.1 summarizes the mean (m) and standard deviation (sd) across all trials obtained for each QTV level and data set; the reference standard deviation σ_{QT} values are presented in last row of the Table.

Table 2.1: Test data sets summary - number of valid segments (#), mean (m) and standard deviation (sd) of s_{QT} and reference standard deviation values for each QT model (σ_{QT}); units in ms.

		QT model 1		QT model 2		QT model 3		QT model 4		QT model 5		QT model 6	
	#	m	sd	m	sd	m	sd	m	sd	m	sd	m	sd
A_c	50	13.5	0.8	10.2	0.6	8.1	0.5	6.6	0.4	4.1	0.3	2.4	0.2
B_c	50	9.1	0.7	7.0	0.5	5.4	0.4	4.4	0.3	3.0	0.3	1.9	0.1
C_c	50	16.4	1.1	12.5	0.8	9.7	0.6	7.9	0.5	5.1	0.4	3.1	0.2
σ_{QT}	-	17.0	-	13.0	-	10.0		8.0	-	5.0	-	3.0	

In data set C_c, m was found to be near σ_{QT} for all QT reference models ($|m - \sigma_{\mathrm{QT}}| \leq 0.6$ ms). It should be remarked that only one of the QT dependencies (one QTV fraction) was included in the series generation for A_c and B_c, and $P^B_{\mathrm{QT}} = P^B_{\mathrm{QT|RR}}$ or $P^B_{\mathrm{QT}} = P^B_{\mathrm{QT|QT}}$, respectively. Thus, these data sets must present lower s_{QT} values.

For each QTV level, 49 valid estimated models were obtained. The selected orders p of the AR and q of the ARARX models are summarized in Figure 2.11.

The orders selected for modelling the majority of the clean simulated series are in accordance with the reference orders used in simulation ($p = 7$ and $q = 4$). It was found that for any QT reference model:

- $5 \leq p \leq 9$ in 82% of the $x_{\mathrm{RR}}(n)$ series;
- $3 \leq q \leq 7$ in more than 80% of the $x_{\mathrm{QT}}(n)$ series in data sets B_c and C_c;
- more spread values were selected for order q for series $x_{\mathrm{QT}}(n)$ in data set A_c.

In data set A_c the QTV fraction uncorrelated to HRV is null and therefore all the relevant memory effect was included in AR model part: the ARXAR part tries to model white noise and selects more spread out orders.

The estimated and reference QTV fractions were compared along frequency using the magnitude of the squared coherence ($K^2(F)$) and the phase of the cross-spectra ($ph(F)$). The minimum (min), 1^{st} quartile ($q1$), median ($q2$), 2^{nd} quartile ($q3$) and maximum (max) values of the functions $K^2(F)$ $ph(F)$ across trials were plotted for each QT reference model in Figures 2.12 and 2.13.

For both factions, the value of $K^2(F)$ reflects high degree of similarity found both in power as in the location of the peaks. Erroneous QTV introduced by delineation errors should be considered as not correlated with HRV, explaining the slightly inferior $K^2(F)$ values in this fraction, in particular for QT reference models corresponding to lower σ_{QT}. The negligible phase values confirm the absence of time delays in the dependence of $x_{\mathrm{QT}}(n)$ on $x_{\mathrm{RR}}(n)$. For QT reference models with lower σ_{QT}, $K^2(F)$ decreased, and both $K^2(F)$ and $ph(F)$ became more spread in both QTV fractions.

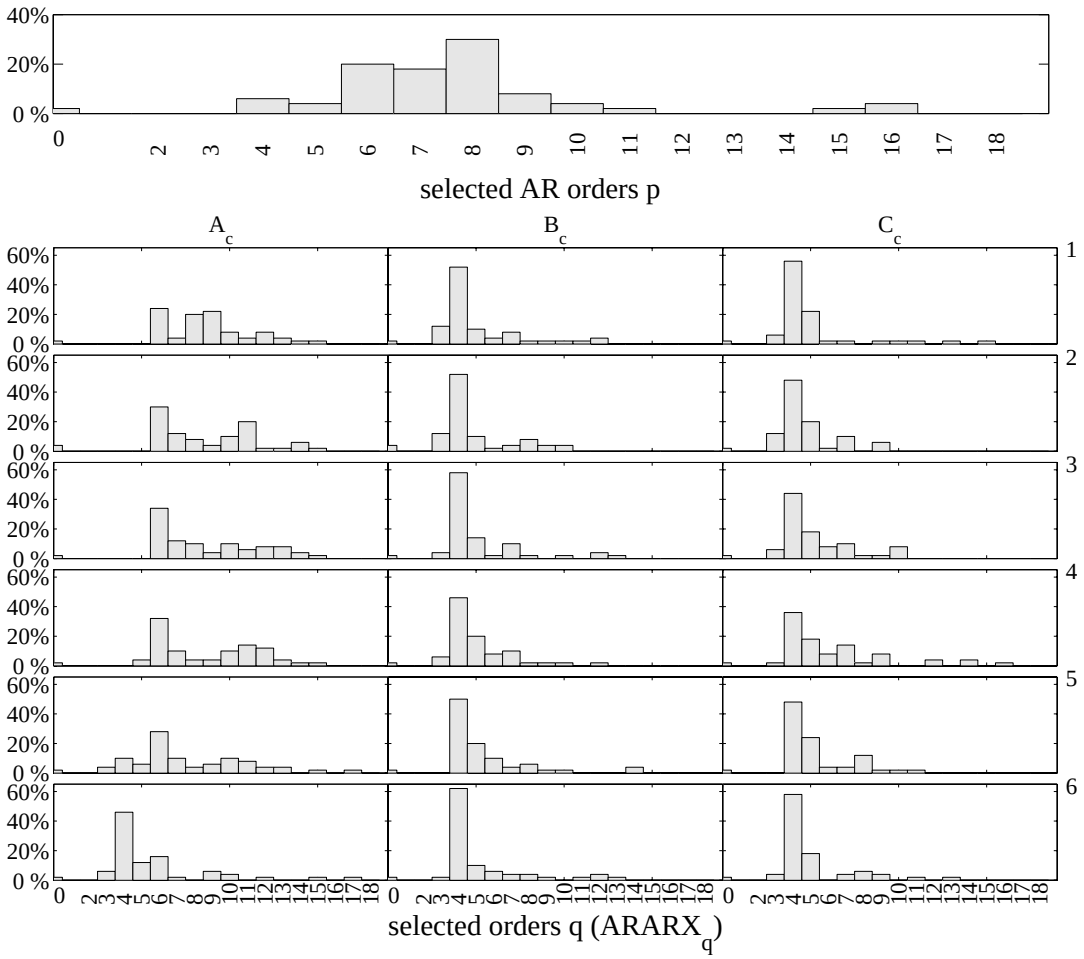

Figure 2.11: Orders p and q selected by AIC in model identification for clean simulated series for each QT reference model (model number 1 to 6 on the left corresponds to a reference QT standard deviation of $\sigma_{\mathrm{QT}} = 17$, 13, 10, 8, 5 and 3 ms, respectively, and order 0 stands for no model found).

The distributions of the absolute errors in each frequency band $\xi^{\mathcal{B}}$ for each QT reference model and data set are presented in Figure 2.14, in box-and whisker like plots (the sign + stands for values out of the quartiles box). In Table 2.2 are presented the mean and standard deviation values of the absolute errors in each frequency band ($\overline{\xi}^{\mathcal{B}}$, $s_{\xi}^{\mathcal{B}}$), along with the reference variability measure values $P_{\mathrm{QT|RR}}^{\mathcal{B}}$ and $P_{\mathrm{QT|QT}}^{\mathcal{B}}$ ($P_{\mathrm{QT}}^{\mathcal{B}} = P_{\mathrm{QT|RR}}^{\mathcal{B}} + P_{\mathrm{QT|QT}}^{\mathcal{B}}$) for the correspondent QT reference model. For the sake of comparison between different QTV levels, the normalized values of $\overline{\xi}^{\mathcal{B}}$ and $s_{\xi}^{\mathcal{B}}$ (normalization by the reference measure $P_{\mathrm{QT|RR}}^{\mathcal{B}}$) are also presented; for data set B_c no normalization is obviously done ($P_{\mathrm{QT|RR}}^{\mathcal{B}} = 0$).

Concerning the percentage errors $\varepsilon^{\mathcal{B}}$, the correspondent distributions are plotted in Figure 2.15. The reference measure for the QTV fraction driven by HRV in each frequency band and data set can be found in Table 2.3, along with the mean and standard deviation in $\varepsilon^{\mathcal{B}}$ ($\overline{\varepsilon}^{\mathcal{B}}$, $s_{\varepsilon}^{\mathcal{B}}$). Again it should be recalled that $R_{\mathrm{QT|RR}}^{\mathcal{B}} = 0$ for data set B_c.

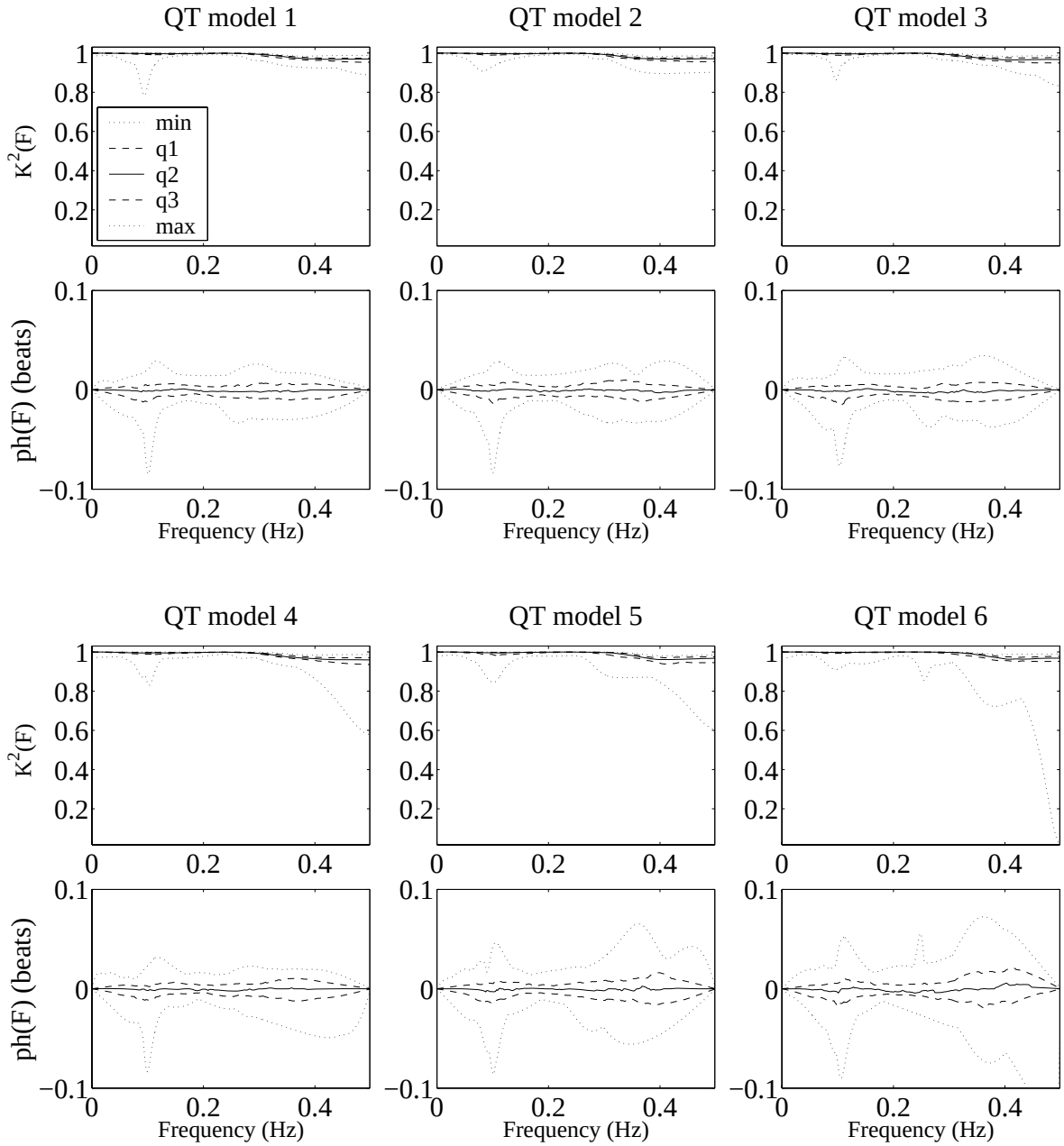

Figure 2.12: Similarity between estimated $\hat{x}_{\mathrm{QT|RR}}(n)$ and reference $x_{\mathrm{QT|RR}}(n)$ QTV fraction driven by HRV for each QTV level: magnitude of squared spectral coherence, $K^2(F)$, and phase of cross-spectra, $ph(F)$, in data set C_c. Frequency axis normalized by the sampling period (T_R).

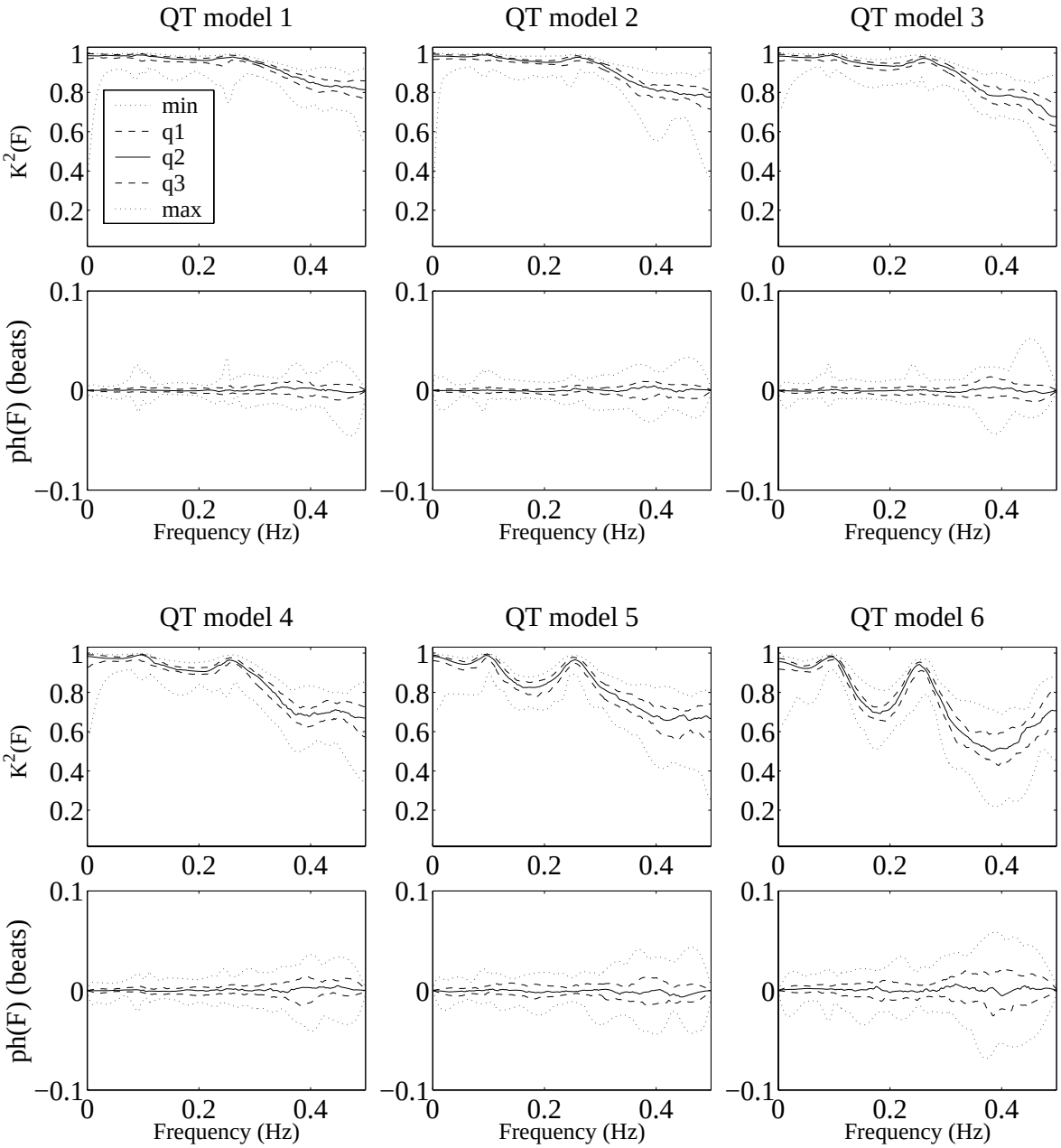

Figure 2.13: Similarity between $\hat{x}_{\mathrm{QT|QT}}(n)$ and reference $x_{\mathrm{QT|QT}}(n)$ QTV fraction uncorrelated with HRV for each QTV level: magnitude of squared spectral coherence, $K^2(F)$, and phase of cross-spectra, $ph(F)$, in data set C_c. Frequency axis normalized by the sampling period (T_R).

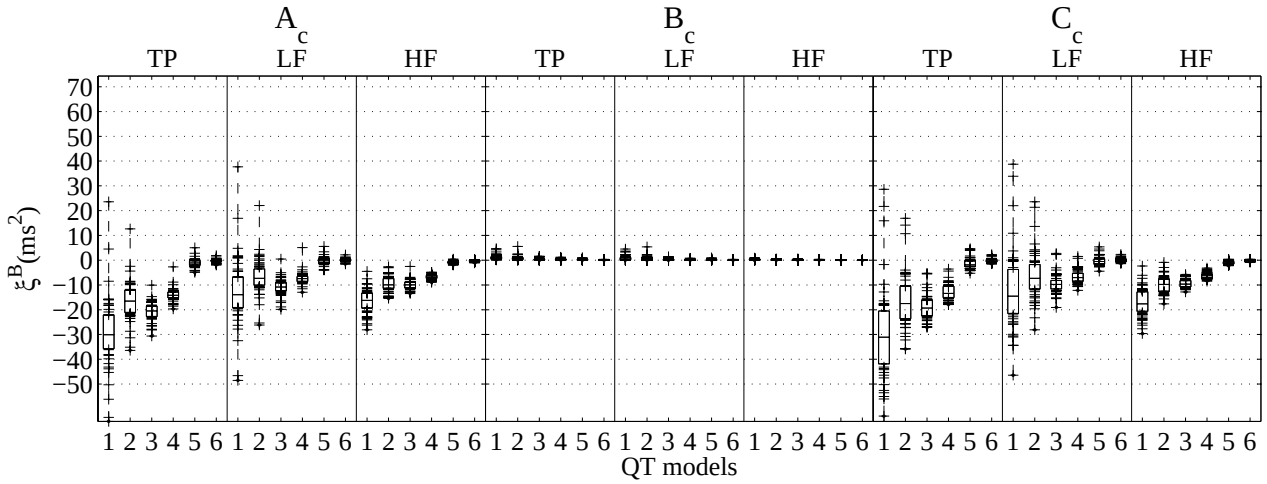

Figure 2.14: Distribution of percentage errors $\xi^{\mathcal{B}}$ in A_c, B_c, C_c datasets by frequency band ($\mathcal{B}$). In these charts, and in all similar ones in this thesis, the central box goes from 1^{st} to 2^{nd} quartiles, with a horizontal line marking the median, dashed vertical lines connecting the closest quartile to minimum and maximum values and + standing for values out of the quartiles box.

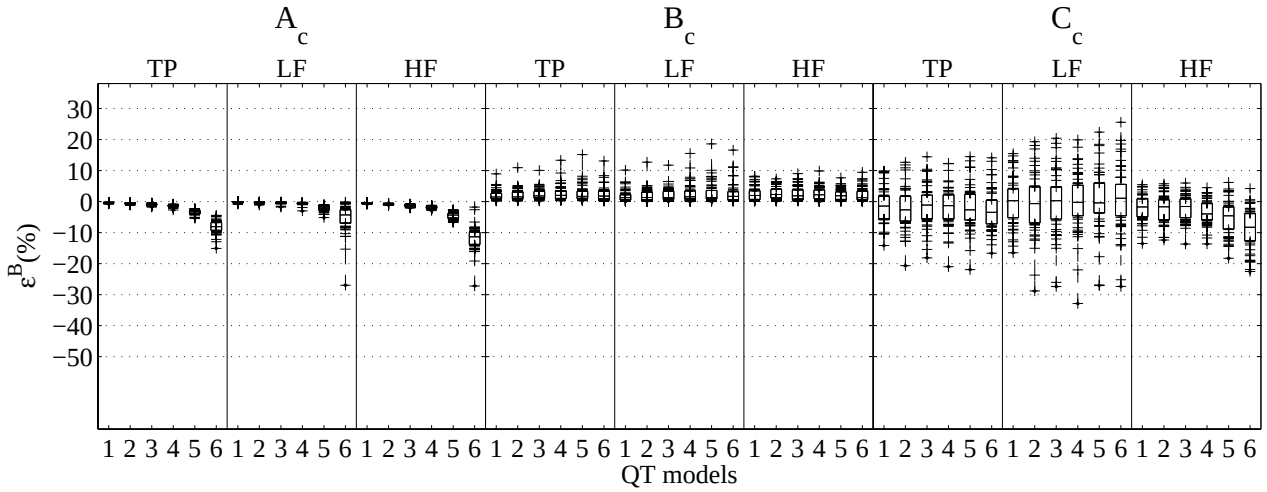

Figure 2.15: Distribution of absolute errors $\varepsilon^{\mathcal{B}}$ in A_c, B_c, C_c datasets by frequency band ($\mathcal{B}$). In this chart, and in all similar ones in this thesis, the central box goes from 1^{st} to 2^{nd} quartiles, with a horizontal line marking the median, dashed vertical lines connecting the closest quartile to minimum and maximum values and + standing for values out of the quartiles box.

Table 2.2: Mean and standard deviation of the absolute errors $\xi^{\mathcal{B}}$ in data sets A_c, B_c and C_c ($mean \pm sd$); number of valid models (#) and reference measures ($P^{\mathcal{B}}_{\mathrm{QT|RR}}$, $P^{\mathcal{B}}_{\mathrm{QT|QT}}$) are also presented for each data set.

QT model	$\mathcal{B}$	$P^{\mathcal{B}}_{\mathrm{QT\|RR}}$ ms^2	$P^{\mathcal{B}}_{\mathrm{QT\|QT}}$ ms^2	A_c #	A_c $\bar{\xi}^{\mathcal{B}} \pm s^{\mathcal{B}}_{\xi}$, ms^2	A_c $\frac{100\lvert\bar{\xi}^{\mathcal{B}}\rvert}{P^{\mathcal{B}}_{\mathrm{QT\|RR}}} \pm \frac{100\lvert s^{\mathcal{B}}_{\xi}\rvert}{P^{\mathcal{B}}_{\mathrm{QT\|RR}}}$	B_c #	B_c $\bar{\xi}^{\mathcal{B}} \pm s^{\mathcal{B}}_{\xi}$, ms^2	C_c #	C_c $\bar{\xi}^{\mathcal{B}} \pm s^{\mathcal{B}}_{\xi}$, ms^2	C_c $\frac{100\lvert\bar{\xi}^{\mathcal{B}}\rvert}{P^{\mathcal{B}}_{\mathrm{QT\|RR}}} \pm \frac{100\lvert s^{\mathcal{B}}_{\xi}\rvert}{P^{\mathcal{B}}_{\mathrm{QT\|RR}}}$
1	*TP*	109.0	64.2	49	-7.0 ± 18.9	-6.4 ± 17.4	49	1.4 ± 1.1	49	-4.3 ± 23.2	-4.0 ± 21.3
	LF	60.5	52.1	49	0.8 ± 17.2	1.3 ± 28.4	49	1.0 ± 1.1	49	2.8 ± 19.9	4.7 ± 33.0
	HF	48.5	12.2	49	-7.8 ± 6.4	-16.1 ± 13.3	49	0.3 ± 0.3	49	-7.2 ± 7.5	-14.9 ± 15.5
2	*TP*	62.5	38.4	49	-4.0 ± 10.9	-6.5 ± 17.5	49	0.9 ± 0.8	49	-2.8 ± 14.4	-4.5 ± 23.0
	LF	34.0	31.4	49	0.5 ± 10.1	1.5 ± 29.6	49	0.7 ± 0.7	49	1.7 ± 12.5	5.0 ± 36.7
	HF	28.5	7.0	49	-4.6 ± 3.8	-16.0 ± 13.5	49	0.2 ± 0.2	49	-4.5 ± 4.4	-15.9 ± 15.3
3	*TP*	38.2	22.3	49	-2.5 ± 6.5	-6.4 ± 17.1	49	0.5 ± 0.4	49	-1.3 ± 9.4	-3.3 ± 24.7
	LF	21.1	17.9	49	0.3 ± 5.9	1.2 ± 27.9	49	0.4 ± 0.4	49	1.1 ± 8.6	5.3 ± 40.5
	HF	17.1	4.4	49	-2.7 ± 2.3	-16.0 ± 13.6	49	0.1 ± 0.1	49	-2.4 ± 2.6	-14.0 ± 15.2
4	*TP*	25.1	14.9	49	-1.4 ± 4.6	-5.6 ± 18.3	49	0.4 ± 0.4	49	-1.2 ± 5.7	-4.9 ± 22.6
	LF	14.0	12.3	49	0.4 ± 4.2	2.7 ± 29.7	49	0.3 ± 0.4	49	0.4 ± 5.0	3.1 ± 35.4
	HF	11.1	2.6	49	-1.8 ± 1.6	-15.9 ± 14.0	49	0.1 ± 0.1	49	-1.7 ± 1.7	-15.2 ± 15.3
5	*TP*	9.6	7.2	49	-0.5 ± 1.7	-5.0 ± 17.8	49	0.2 ± 0.2	49	-0.3 ± 2.4	-3.2 ± 25.0
	LF	5.5	5.5	49	0.1 ± 1.6	2.2 ± 29.2	49	0.2 ± 0.2	49	0.3 ± 2.1	5.4 ± 38.0
	HF	4.1	1.6	49	-0.6 ± 0.5	-15.1 ± 13.3	49	0.0 ± 0.0	49	-0.6 ± 0.7	-14.9 ± 17.8
6	*TP*	3.3	2.7	49	-0.2 ± 0.6	-6.0 ± 19.3	49	0.1 ± 0.1	49	-0.1 ± 0.8	-3.6 ± 25.1
	LF	1.8	2.0	49	0.1 ± 0.6	4.0 ± 32.4	49	0.1 ± 0.1	49	0.1 ± 0.7	6.4 ± 40.1
	HF	1.5	0.7	49	-0.3 ± 0.3	-18.2 ± 16.7	49	0.0 ± 0.0	49	-0.2 ± 0.3	-15.8 ± 18.4

Table 2.3: Mean and standard deviation of the percentage errors $\varepsilon^{\mathcal{B}}$ in data sets A_c, B_c and C_c ($mean \pm sd$); reference values $R^{\mathcal{B}}_{\mathrm{QT|RR}}$ for each data set are also presented.

			$\overline{\varepsilon}^{\mathcal{B}} \pm s^{\mathcal{B}}_{\varepsilon}$, %		
QT model	$\mathcal{B}$	$R^{\mathcal{B}}_{\mathrm{QT|RR}}$, %	A_c	B_c	C_c
1	TP	109.0	-7.0 ± 18.9	1.4 ± 1.1	-4.3 ± 23.2
	LF	60.5	0.8 ± 17.2	1.0 ± 1.1	2.8 ± 19.9
	HF	48.5	-7.8 ± 6.4	0.3 ± 0.3	-7.2 ± 7.5
2	TP	62.5	-4.0 ± 10.9	0.9 ± 0.8	-2.8 ± 14.4
	LF	34.0	0.5 ± 10.1	0.7 ± 0.7	1.7 ± 12.5
	HF	28.5	-4.6 ± 3.8	0.2 ± 0.2	-4.5 ± 4.4
3	TP	38.2	-2.5 ± 6.5	0.5 ± 0.4	-1.3 ± 9.4
	LF	21.1	0.3 ± 5.9	0.4 ± 0.4	1.1 ± 8.6
	HF	17.1	-2.7 ± 2.3	0.1 ± 0.1	-2.4 ± 2.6
4	TP	25.1	-1.4 ± 4.6	0.4 ± 0.4	-1.2 ± 5.7
	LF	14.0	0.4 ± 4.2	0.3 ± 0.4	0.4 ± 5.0
	HF	11.1	-1.8 ± 1.6	0.1 ± 0.1	-1.7 ± 1.7
5	TP	9.6	-0.5 ± 1.7	0.2 ± 0.2	-0.3 ± 2.4
	LF	5.5	0.1 ± 1.6	0.2 ± 0.2	0.3 ± 2.1
	HF	4.1	-0.6 ± 0.5	0.0 ± 0.0	-0.6 ± 0.7
6	TP	3.3	-0.2 ± 0.6	0.1 ± 0.1	-0.1 ± 0.8
	LF	1.8	0.1 ± 0.6	0.1 ± 0.1	0.1 ± 0.7
	HF	1.5	-0.3 ± 0.3	0.0 ± 0.0	-0.2 ± 0.3

An apparent decrease in bias and dispersion of the errors $\xi^{\mathcal{B}}$ with the QTV level can be seen both in Table 2.2 and in Figure 2.14. However the normalized value of mean and standard deviation (obtained dividing by the reference measure $P^{\mathcal{B}}_{\mathrm{QT|RR}}$) did not change relevantly. Thus, there is no indication of different performance with respect to the quantification of the QTV driven by HR related with the amount to be quantified. The values obtained for HF band are higher than for LF band denoting a poorer performance for higher frequencies.

Regarding Figure 2.15, it is noticed that the values of the percentage error $\varepsilon^{\mathcal{B}}$ were mainly low ($\left|\varepsilon^{\mathcal{B}}\right| \leq 10\%$) for all data sets, indicating that the parametric method is able to estimate both QTV fractions correctly. In particular, the for QT reference models 1 to 5, with QTV level corresponding to $\sigma_{\mathrm{QT}} \geq 5$ ms, $\epsilon^{\mathcal{B}} < 10\%$:

- for 81% of the series, in TP band,
- for 65% of the series, in LF band,
- for 77% of the series, in HF band.

Also, it should be remarked from Table 2.3 that in all datasets for QT reference models corresponding to $\sigma_{\mathrm{QT}} \geq 5$ ms:

- $\left|\overline{\varepsilon}^{HF}\right| \leq 5.1\%$ ($s_{\varepsilon}^{HF} \leq 5.5\%$),
- $\left|\overline{\varepsilon}^{LF}\right| \leq 2.8\%$ ($s_{\varepsilon}^{LF} \leq 10.1\%$),
- $\left|\overline{\varepsilon}^{TP}\right| \leq 3.5\%$ ($s_{\varepsilon}^{TP} \leq 7\%$).

The dispersion and bias of the percentage errors were found to be higher for QT reference models with lower σ_{QT}. This effect was expected as the delineation errors proportionally assumed higher importance.

2.5 Concluding Remarks

The study of the VR/HR relations using the dynamic parametric approach over the series of QT and RR variabilities provided an adequate estimation of the QTV fraction driven by RR. As a matter of fact, validation over simulated series indicated that the absolute errors in the estimated measures are low, with mean error lower than 8 ms^2, which in the worse case represents less than 17% of the QTV.

The estimation of the QTV fractions presented a bias and error dispersion depending on the QTV level. Correct estimations for both QTV fractions, with percentage errors lower than 5%, were obtained for most of the series with QTV level corresponding to $\sigma_{QT} \geq 5$ ms.

The simulation strategy considered intends to be realistic, assuming that the linear model is adequate to describe QTV/HRV interrelations. This is well suited for the validation purpose, as the model used to explore those interactions only quantifies linear relations. Also, it is assumed that the variability series are available with no measurement error, which is not the case for ECG signals characterization.

The study of QTV and its dependencies from HRV in real signals requires the extraction of RR and QT sequences and therefore, the detection and location of the ECG waves. The uncertainty in the T end delineation is one of the main problems in measuring the QT interval with precision. In clinical practice, noise contamination increases delineation difficulty and can result in spurious QTV.

Thus, to make these methods applicable to real data, a precise and robust methodology to locate the fiducial ECG points is essential. This topic is discussed in the next Chapter of the thesis.

Chapter 3

Automatic ECG waves detection and delineation

The correct detection and delineation of the ECG characteristic points and waves is of extreme importance as it is the basis to study this signal. Namely, the detection of the R wave, taken as reference for the cardiac beat's location, is needed for the heart rate extraction. The study of rhythm and ventricular repolarization variabilities in real signals requires the detection of the QRS complex and the QT intervals delineation. For that it is essential to locate the QRS complex onset and the T wave end in each cardiac beat. Those, among other fiducial points, are provided by the ECG delineation.

In this Chapter is presented a single-lead based automatic system for ECG waves delineation using wavelet transforms, which was extended and improved in the framework of this thesis. In particular, regarding the study of QT interval variability, the boundaries location is particularly critic.

A novel multilead based methodology for boundaries location, established from the single-lead system, was also developed. It incorporates and combines the data, aiming to take advantage of the spacial information provided by orthogonal leads.

The delineation systems developed were evaluated over standard ECG databases and compared with other published approaches.

3.1 Introduction

The delineation of the ECG characteristic waves in each cardiac beat consists on detecting its peaks and boundaries (onset and end). It provides fundamental features to derive clinically useful information, namely about the duration and amplitude of the waves associated to the electrical phenomena involved and their beat-to-beat evolution.

Delineation of low-amplitude smooth waves, like P and T waves, is a particularly challenging task due to the low signal-to-noise ratio (SNR). Specially problematic is the delineation of flat boundaries as it is usually the case of the T wave end. Furthermore, there are not standard clear rules to locate the waves' boundaries, what makes more difficult the delineation systematization. Automatic methodologies allow to avoid intra/inter-observer variability and therefore developing accurate and robust methods for ECG automatic delineation is a topic of main interest, in particular for the analysis of long records.

The detection of the QRS complex is the first stage of any delineation system and the most straightforward one. The beat location is defined by the mark of the QRS complex main wave (usually the R wave) and a wide diversity of algorithms has been proposed. Literature revisions on this issue can be found in Pahlm and Sörnmo (1984), Gritzali (1988), Friesen *et al.* (1990) and Kohler *et al.* (2002).

The search for peaks and boundaries of the ECG waves is usually performed within temporal windows referred to the QRS position. Very different delineation approaches regarding some or all of the ECG waves and limits have also been proposed. As examples can be cited, among many others, the strategies based on ECG *slope* criteria (Algra *et al.*, 1987; de Chazal and Celler, 1996; Daskalov *et al.*, 1998; Daskalov and Christov, 1999*a*,*b*), *low-pass differentiation* (Laguna *et al.*, 1994; Speranza *et al.*, 1993; Meij *et al.*, 1994) and *wavelet transform* (Li *et al.*, 1995; Sahambi *et al.*, 1997; Bahoura *et al.*, 1997; Martínez *et al.*, 2000; Almeida *et al.*, 2003*c*; Martínez *et al.*, 2004).

Wavelet transform (WT) based methods have been proposed improving the results for ECG analysis and processing in several situations as signal compression, denoising, abnormalities/arrhythmias detection and waves delineation (Addison, 2005). The WT provides a description of the signal in the time-scale domain, allowing the representation of its temporal features at different resolutions according to their frequency content. This is illustrated in Figure 3.1 in which are presented an ECG segment and the correspondent WT at several scales. It must be remarked that the effect of QRS waves, which have higher frequency content, appears across scales being most visible in the lower ones, while smooth waves (like P and T only) affect mostly the higher scales. Thus, regarding the purpose of locating different waves with typical frequency characteristics, the WT is a suitable tool for ECG automatic delineation. More details in the WT and its application to ECG delineation problem will be presented in Section 3.2.

The system based on wavelet transforms proposed by Li *et al.* (1995) is of particular interest for the work developed in this thesis. It includes a QRS detector which was evaluated with a standard database. Li *et al.* (1995) also describes strategies for location of monophasic P and T waves and waves' boundaries, however did not validate them. This approach was generalized in Martínez *et al.* (2000), where was presented and validated a preliminary version of a system able to determine the

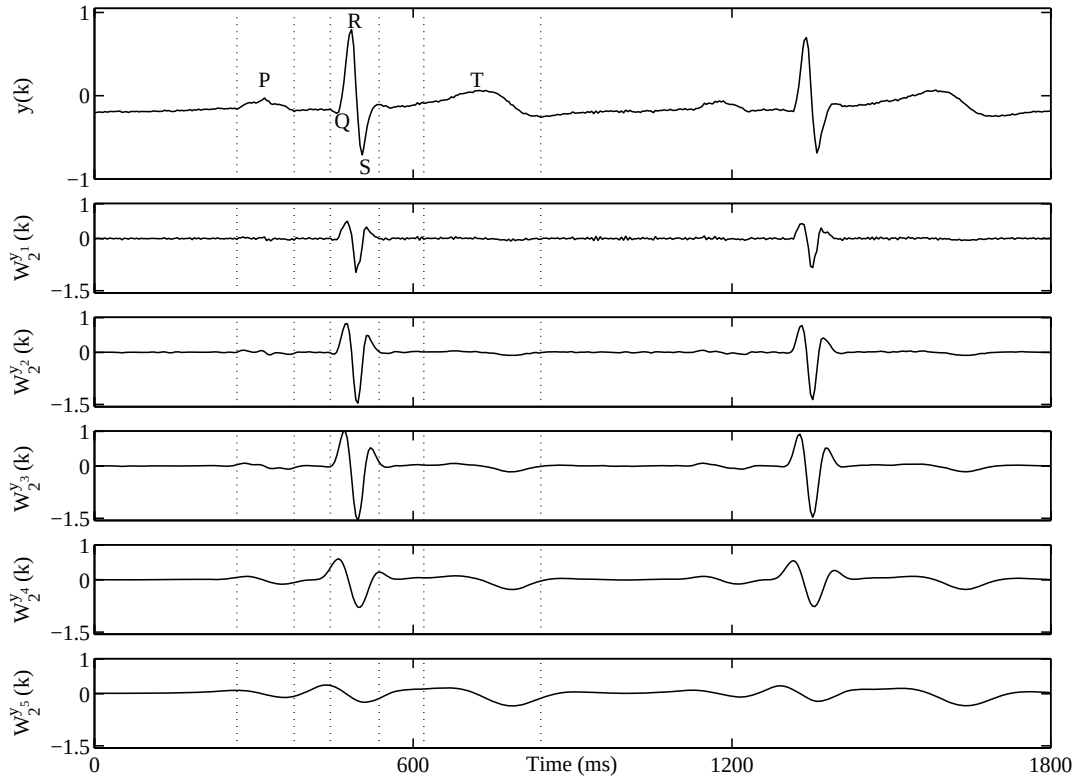

Figure 3.1: Example of and ECG segment $y(k)$, mV, and respective WT $W^y_{2^m}(k)$, arbitrary units, for scales $a = 2^m|_{m=1,..,5}$. The vertical dashed lines mark the boundaries of the QRS complex and P and T waves. The prototype wavelet used is a quadratic spline proposed by Mallat and Zhong (1992) which have been applied to ECG delineation by Li *et al.* (1995).

individual QRS waves and the boundaries of the five main waves, already accounting for different T wave morphologies.

The automatic delineation systems described in the literature are based on a single ECG lead. When multiple leads are available, some authors have proposed as a multilead strategy the use of post-processing rules to select one of the single-lead measurements (de Chazal and Celler, 1996; Laguna *et al.*, 1994). As a matter of fact, the availability of multiple simultaneous ECG leads allows to access more information, which can be used to increase the robustness of delineation. Moreover, the different view points (different leads) over the same electrical phenomena can be crucial to determine its true duration, as their beginning or end could be imperceptible in a particular lead.

The single-lead delineation system based on wavelet transform presented in Martínez *et al.* (2000) was improved during the framework of this thesis (Almeida *et al.*, 2003*c*; Martínez *et al.*, 2004). Namely, a novel multiscale strategy for detecting T and P waves was developed, the system was adapted for dealing with different P wave morphologies and several search windows and thresholds were adjusted using a trial and error approach (Almeida *et al.*, 2003*c*). The system is described in Section 3.4 and it includes post-processing decision rules to deal with multilead files, by choosing global marks based on the single-lead based sets of locations. In spite of the very satisfactory performance, the above referred system is not a true multilead delineation system.

An actual multilead methodology regarding boundaries location, which is presented in this Chapter, was developed and validated during this PhD research work (Almeida *et al.*, 2004*c*, 2006*a*). The multilead approach was established from the single-lead system and attends to the spatial characteristics of the different available leads, aiming to achieve a more robust delineation. The developed strategy is presented in Section 3.5.

The two delineation systems are comparatively evaluated over standard ECG databases and compared with other published approaches in Section 3.6. The main results and the global conclusions of this Chapter are summarized in Section 3.7.

3.2 General Considerations on the Wavelet Transform

A *wavelet* $\psi(t)$ is a small wave in the sense of having limited duration, as it is an oscillating function that goes quickly to zero. It has zero mean and finite energy concentrated around a point. A wavelet family is defined from a prototype wavelet $\psi(t)$ by means of dilations (a) and translations (b)

$$\psi_{a,b}(t) = \frac{1}{\sqrt{a}}\psi\left(\frac{t-b}{a}\right),\ a > 0. \tag{3.1}$$

The *continuous wavelet transform* $W_a^y(b)$ (CWT) decomposes a signal $y(t)$ as a combination of functions $\psi_{a,b}$, i. e.

$$W_a^y(b) = \frac{1}{\sqrt{a}}\int_{-\infty}^{+\infty} y(t)\,\psi_{a,b}^*(t)dt = \frac{1}{\sqrt{a}}\int_{-\infty}^{+\infty} y(t)\,\psi^*\left(\frac{t-b}{a}\right)dt, \tag{3.2}$$

where $\psi^*(t)$ denotes the complex conjugate of $\psi(t)$.

If a real $\psi(t) \in L^2$ is such that its Fourier Transform $\Psi(\omega)$ fulfils the *admissibility condition*

$$\int_0^{+\infty} \frac{|\Psi(\omega)|^2}{\omega}d\omega < \infty, \tag{3.3}$$

then the CWT satisfies energy conservation (Mallat, 1999).

The CWT presents clear advantages over the *short time Fourier transform* (STFT) for ECG characterization. As a matter of fact, in the case of STFT a sliding time window is applied, obtaining covering units with finite energy, what allows to add *some* time/frequency location to the Fourier transform. Each window corresponds to a time/frequency resolution that stands for the entire analysis. Nevertheless, in the case of non stationary signals a fixed resolution is hardly appropriated for the whole signal. The wavelet transform is specially adequate for describing non stationary signals, as is the case of the ECG. In fact, with the CWT the lower frequency components of the signal are characterized by the coefficients corresponding to wider $\psi_{a,b}(t)$ resulting from the higher scale factor a, and vice versa. This provides a time/scale domain description of $y(t)$ with higher temporal resolution at high frequencies and higher frequency resolution at low frequencies (Figure 3.1).

For the purpose of automatic computer analysis, a digitized signal $y(k)$ is considered and its *discrete wavelet transform* (DWT) is usually obtained following a dyadic grid on the time-scale plane ($a = 2^m$ and $b = 2^m l$, $m \in N, l \in Z$), denoted as $Wd_{2^m}{}^y(2^m l)$. With the dyadic grid the DWT is equivalent to an octave filter bank and can be implemented as a cascade of identical cells of low-pass and high-pass FIR filters, with a downsampling operation after each filter, as schematised in Figure 3.2(a). That is,

$$\begin{aligned} &Wd_{2^m}{}^y(2^m l) = c_{m-1}(2^{m-1} l) * \bar{g}(2^m l), \\ &c_m(2^m l) = c_{m-1}(2^{m-1} l) * \bar{h}(2^m l), \quad \text{(Mallat's algorithm)} \\ &\bar{g}(k) = g(-k);\ \bar{h}(k) = h(-k), \end{aligned} \tag{3.4}$$

where $g(k)$ and $h(k)$ are the impulse response functions of the associated low-pass and high-pass filters, respectively (Mallat, 1989).

The description in equation (3.4) is time-variant, with more reduced temporal resolution for increasing scales. This drawback can be overcome using the algorithm *à trous* (Cohen and Kovačević, 1996), in which each decimation stage is replaced by an interpolation of the filter impulse responses of the previous scale, as represented in Figure 3.2(b). In this way a redundant representation of $y(k)$ is obtained, but the temporal resolution is maintained at different scales, that is

$$\begin{aligned} &W^y_{2^m}(k) = c_{m-1}(k) * \bar{g}_m(k), \\ &c_m(k) = c_{m-1}(k) * \bar{h}_m(k), \quad \text{(algorithm } \textit{à trous}\text{)} \\ &\bar{g}_m(k) = g_m(-k);\ \bar{h}_m(k) = h_m(-k). \end{aligned} \tag{3.5}$$

for $g_m(k)$ and $h_m(k)$ denoting the impulse response obtained by inserting $2^m - 1$ zeros between every sample in the impulse response function $g(k)$ and $h(k)$, respectively. Using this algorithm, the equivalent frequency response for scale $a = 2^m$ is

$$Q_m\left(e^{jF}\right) = \begin{cases} G\left(e^{jF}\right) & m = 1 \\ G\left(e^{j2^{m-1}F}\right) \prod_{l=0}^{m-2} H\left(e^{j2^l F}\right) & m \geq 2. \end{cases} \tag{3.6}$$

where F stands for frequency in Hz ($F = \omega F_s / 2\pi$, for ω in rad and F_s the sampling frequency).

3.3 Prototype Wavelet

The frequency response of each scale derives from the prototype wavelet function used, thus it is of extreme importance that its choice attends to the specific frequency content of the signal of interest. It can be shown (Mallat and Zhong, 1992; Sahambi *et al.*, 1998) that taking as prototype wavelet $\psi(t)$, the derivative of a smoothing function $\theta(t)$, the CWT of a signal $y(t)$ at scale a is given by

$$W^y_a(b) = -a \left(\frac{d}{db}\right) \int_{-\infty}^{+\infty} x(t)\theta_a(t-b)dt, \tag{3.7}$$

where $\theta_a(t) = \frac{1}{\sqrt{a}}\,\theta\left(\frac{t}{a}\right)$ is the scaled version of the smoothing function.

Therefore, the wavelet transform at scale a is proportional to the derivative of the filtered version of the signal with a smoothing impulse response at scale a.

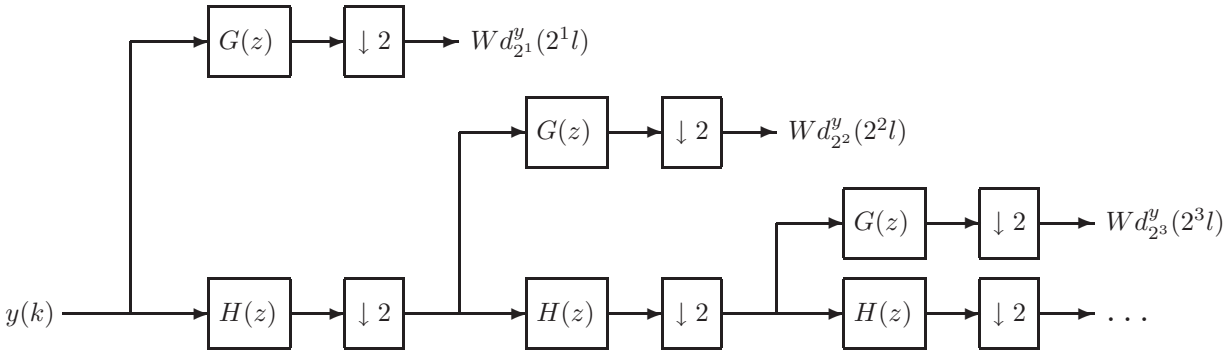

(a) Mallat's algorithm.

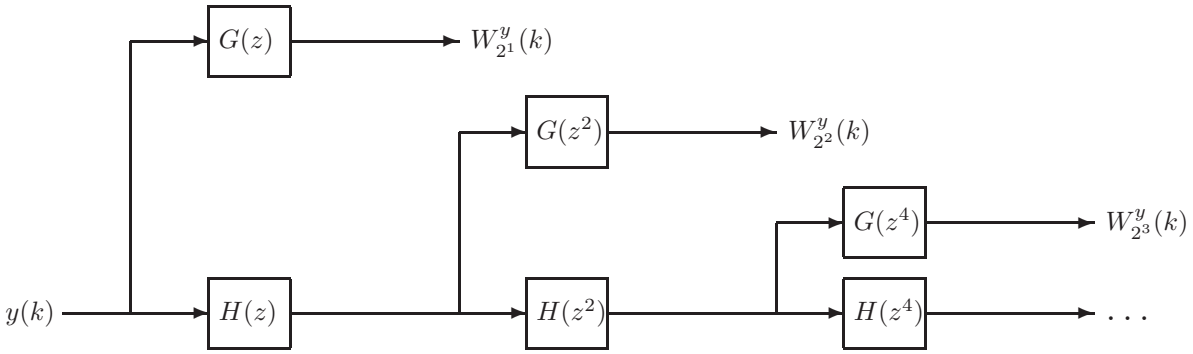

(b) Algorithm *à trous*.

Figure 3.2: Discrete wavelet transform implementation schemes (dyadic grid).

Regarding the ECG automatic delineation, this property is very convenient for the purpose of detecting ECG waves, which are composed of slopes and local maxima (or minima), as illustrated in Figure 3.1,

- wave peaks in the ECG correspond to zero crossings in the WT,
- slopes in ECG correspond to maxima and minima of the WT.

Mallat and Zhong (1992) proposed, as an example of a prototype wavelet with this property, a quadratic spline that matches the derivative of the convolution of four rectangular pulses. Its Fourier transform is given by

$$\Psi(\omega) = j\omega \left(\frac{\sin(\omega/4)}{\omega/4} \right)^4, \tag{3.8}$$

and the low-pass and high-pass FIR filters have transfer functions (Li *et al.*, 1995; Akay, 1996)

$$\begin{aligned} H\left(e^{j\omega}\right) &= e^{j\omega/2} \left(\cos\frac{\omega}{2} \right)^3, \\ G\left(e^{j\omega}\right) &= 4\, j\, e^{j\omega/2} \left(\sin\frac{\omega}{2} \right), \end{aligned} \tag{3.9}$$

with associated impulse responses

$$\begin{aligned} h[k] &= 1/8 \cdot \{\delta[k+2]+3\delta[k+1]+3\delta[k]+\delta[k-1]\}\,, \\ g[k] &= 2 \cdot \{\delta[k+1]-\delta[k]\}\,. \end{aligned} \tag{3.10}$$

This prototype wavelet has been applied to detection and delineation of ECG signals with good results (Li *et al.*, 1995; Bahoura *et al.*, 1997; Martínez *et al.*, 2000). As the analysis filters in equation (3.10) have linear phase (Li *et al.*, 1995), the outputs of the filters can be realigned in order to present the same delay with respect to the original signal $y(t)$. The equivalent frequency responses $Q_m\left(e^{jF}\right)$ for this prototype wavelet using the *algorithme à trous* can be calculated from equations (3.6) and (3.9). The frequency responses are plotted in Figure 3.3 for the first five scales $a = 2^m|_{m=1,2,...,5}$, considering a sampling frequency F_s of 250 Hz.

For a value of F_s different from 250 Hz the bands in Figure 3.3 would appear scaled in frequency. It is important to keep the scale fitting to the ECG features on the algorithms independent of F_s: for that purpose a new set of filters, having equivalent analogue frequency responses as close as possible to the ones of Figure 3.3 are constructed for each F_s. The new filters are obtained by resampling adequately the equivalent filter impulse responses at 250 Hz, as detailed described in Martínez *et al.* (2004). Such a procedure is required to construct a system able to handle equivalently ECG signals with different sampling frequencies.

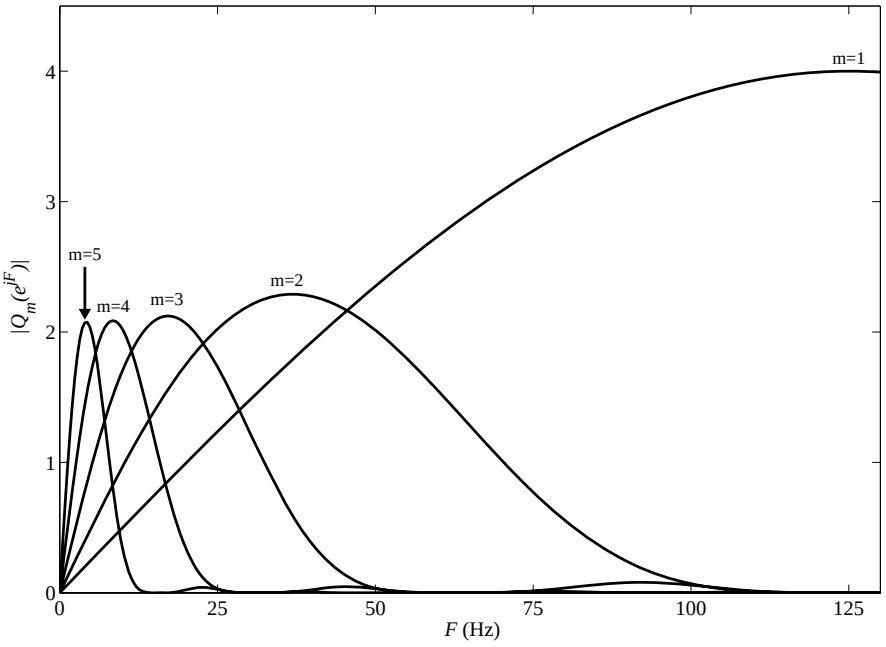

Figure 3.3: DWT equivalent frequency responses at scales $a = 2^m, m = 1, ..., 5$ (F_s = 250 Hz and $F = \omega/2\pi * F_s$, with F in Hz and ω in rad).

3.4 Single-lead based system

The single-lead based delineation system discussed in this section was described in Almeida *et al.* (2003*c*) and Martínez *et al.* (2004). As already referred, the extension and improvements included in the framework of this thesis were specially detailed in Almeida *et al.* (2003*c*).

Given the prototype wavelet used the local maxima, minima and zero crossings at different scales are considered (wave peaks in the ECG correspond to zero crossings in the WT signals and slopes in ECG correspond to maxima and minima of the WT). In spite of existing large variations with respect to the subject, lead and beat, each wave has some typical characteristics that facilitates its location. Detection of each fiducial point should be carried out across the adequate WT scales, attending to the dominant frequency components of each ECG wave. The characteristic spectrum of the waves is presented in Figure 3.4 and comparing with the equivalent frequency response of the several scales in Figure 3.3 it can be seen that:

- most of the ECG energy lies within the scales 2^1 to 2^5;
- for scales higher than 2^4 the QRS energy is very low;
- P and T waves produce important components at scales 2^4 and 2^5.

Therefore QRS waves correspond to a simultaneous effect in scales 2^1 to 2^4, while the T or P waves affect mainly scales 2^4 or 2^5. This can also be noticed very clearly in Figure 3.1, in which the different effects of each wave across the scales is illustrated. Noise and artifacts can be avoided by considering their different contribution at various scales.

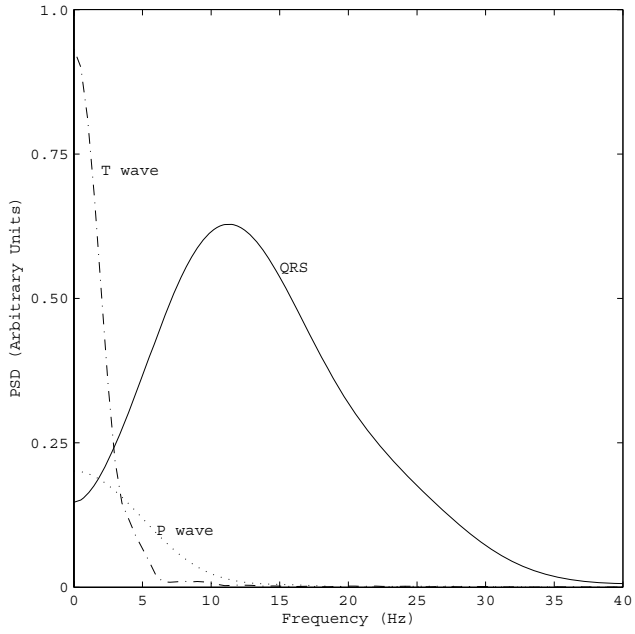

Figure 3.4: Indicative power spectrum of the QRS complex, P and T waves (reproduced from Sörnmo and Laguna (2005)).

The WT allowed to obtain an automatic system that does not require any prefiltering or preprocessing, being directly applicable to the digitized ECG signal. To allow dealing with long ECG recordings the algorithm segments the signal to be processed in excerpts of 2^{16} samples and automatically identifies the significant points in four steps, which are described in the next subsections, namely:

QRS complexes detection by finding the its main wave location,

QRS complexes delineation by locating of the *peaks* and complex boundaries (QRS *onset* and *end*) and identifying the individual waves (Q, R, S, R'),

T waves delineation by locating the wave *peak* and boundaries (T *onset* and *end*),

P waves delineation by locating the wave *peak* and boundaries (P *onset* and *end*).

3.4.1 QRS detection

The first step in any automatic ECG delineation system must be the beat detection, by locating the sample l^{QRS_n} that corresponds to the main wave peak in each beat n.

As illustrated in Figure 3.1 each wave of the QRS complex is reflected across scales as a zero crossing between two local maxima of opposite signs. The QRS complexes are detected using an algorithm based on the multiscale approach proposed by Li *et al.* (1995) and corresponds to the following sequence:

1. searching across the scales $a = 2^m|_{m=1,2,3,4}$ for candidate relevant maximum lines, defined as *"maximum modulus lines"* exceeding predefined thresholds γ_m^{QRS};
2. rejecting all isolated or redundant maximum lines;
3. identifying the pair of consecutive maximum lines with opposite polarity that has the biggest amplitude among the accepted candidates, as associated to main wave in the QRS complex of the beat n; taking that pair positions at scale 2^2 (samples $p_{\mathrm{pre}}^{\mathrm{QRS}_n}$ and $p_{\mathrm{post}}^{\mathrm{QRS}_n}$) ;
4. locating the *QRS position* in beat n, l^{QRS_n}, as the zero crossing of $W_{2^1}^y(k)$ between $p_{\mathrm{pre}}^{\mathrm{QRS}_n}$ and $p_{\mathrm{post}}^{\mathrm{QRS}_n}$.

Though based on Li *et al.* (1995) a slightly different implementation is here considered, namely:

- the thresholds are updated for each excerpt of 2^{16} samples (instead of updating then for each beat);
- only amplitude based criteria are considered (and not regularity analysis);
- the main wave of the QRS is not restricted to be an R wave, allowing the detection of both positive (positive maximum – negative minimum pair) and negative waves (negative minimum – positive maximum pair).

The thresholds regarding the detection of the QRS wave are defined proportional to the RMS as,

$$\gamma_m^{\mathrm{QRS}} = \mathrm{RMS}\left[W_{2^m}^y(k)\right] \text{ for } m = 1, 2, 3; \quad \gamma_4^{\mathrm{QRS}} = 0.5\mathrm{RMS}\left[W_{2^4}^y(k)\right] \tag{3.11}$$

Additional protection rules are taken, like a refractory period (in which no posterior QRS detection is admitted) or a search back with lowered thresholds if a relevant time has elapsed without detecting any QRS. A refractory period of 275 ms is considered, corresponding to a HR of more than 200 bpm. Search back is performed with thresholds reduced to half if no QRS complex was detected in a time interval corresponding to 1.5 of the median RR calculated from the 3 last RR intervals.

Examples of the detector's behavior and robustness dealing with motion artifacts, muscular noise, baseline wandering and changes in the QRS morphology can be found in Figure 3.5, reproduced from Martínez *et al.* (2004) for the sake of completeness.

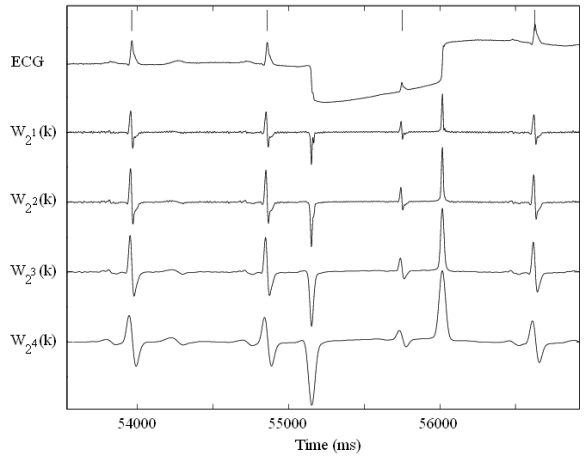

(a) Motion artifact.

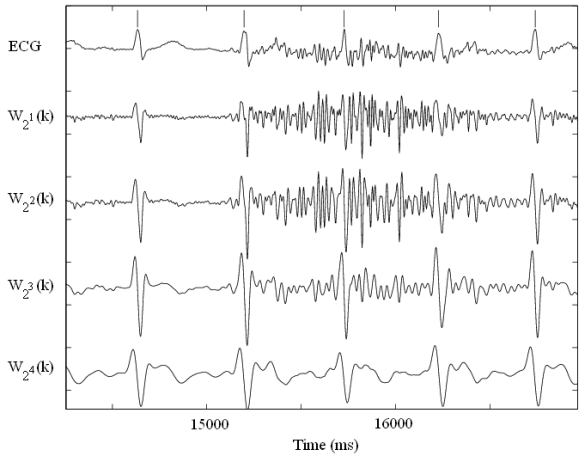

(b) Muscular noise.

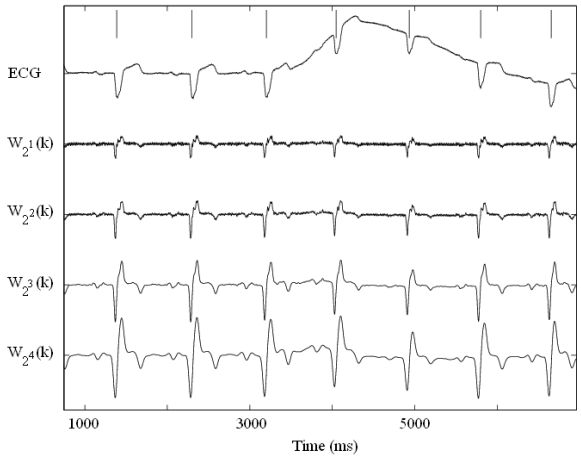

(c) Baseline wandering.

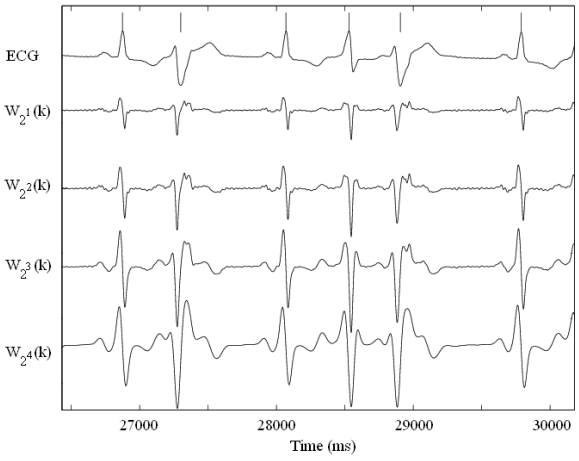

(d) QRS morphology changes.

Figure 3.5: Examples of the behavior of the QRS detector behavior dealing with different kinds of noise and morphology changes. The ECG signal, the WT's first four scales and the detected QRS complexes (vertical lines) are shown in each panel (Figure 6 of Martínez *et al.* (2004)).

3.4.2 QRS complex delineation

One of the novelties of this approach with respect to Li *et al.* (1995) is the location and identification of the QRS individual waves in each beat. Any QRS morphology with 3 or less waves (QRS, RSR', QR, RS, R and QS complexes) is admitted. The QRS complex detection and delineation is illustrated in Figure 3.6.

From the previous section, the two local maxima modulus produced before and after the QRS position (l^{QRS_n}) by the its main wave were located at samples $p_{\mathrm{pre}}^{\mathrm{QRS}_n}$ and $p_{\mathrm{post}}^{\mathrm{QRS}_n}$, respectively.

To account for other waves within the QRS complex, the algorithm looks for other significative modulus maxima at scale 2^2, rather than the ones associated to the main wave, in a search window QRS_{w_n} relative to the QRS position, defined as

$$QRS_{w_n} = [l^{\mathrm{QRS}_n} - 100 \text{ ms}\,, l^{\mathrm{QRS}_n} + 100 \text{ ms}] \tag{3.12}$$

A modulus maxima before $p_{\mathrm{pre}}^{\mathrm{QRS}_n}$ are considered to be significative if above a threshold γ_{pre}^{QRS}, while significative modulus maxima after $p_{\mathrm{post}}^{\mathrm{QRS}_n}$ are relative to a threshold γ_{post}^{QRS}. The thresholds used to decide the significance of the maximum modulus are given by

$$\begin{aligned} \gamma_{pre}^{\mathrm{QRS}} &= 0.06 Max\left[W_{2^2}^y(k)\right]|_{k\in QRS_{w_n}}, \\ \gamma_{post}^{\mathrm{QRS}} &= 0.09 Max\left[W_{2^2}^y(k)\right]|_{k\in QRS_{w_n}}, \end{aligned} \tag{3.13}$$

Peak's waves are taken as the zero-crossings of $W_{2^1}^y(k)$ between pairs of modulus maxima of $W_{2^2}^y(k)$ with opposite polarity. Time interval and sign rules were included to reject notches in waves and anomalous deflections in the ECG signal, as in the case of noise contamination. Depending of the number and polarity of the waves found, they are identified as Q, R, S or R' waves (Section 1.1).

The *boundaries* of the complex (QRS onset and QRS end) are located at scale 2^2 as described next, using thresholds $\gamma^{\mathrm{QRS_{on}}}$ and $\gamma^{\mathrm{QRS_{end}}}$. These thresholds are relative to the amplitude of the first or last maximum modulus at the QRS complex, located at samples $k = p_f^{QRS_n}$ and $k = p_l^{QRS_n}$, that is

$$\begin{aligned} \gamma^{\mathrm{QRS_{on}}} &= \begin{cases} \frac{1}{20} W_{2^2}^y\left(p_f^{\mathrm{QRS}_n}\right) & \text{if } W_{2^2}^y\left(p_f^{\mathrm{QRS}_n}\right) > 0 \\ \frac{1}{15} W_{2^2}^y\left(p_f^{\mathrm{QRS}_n}\right) & \text{if } W_{2^2}^y\left(p_f^{\mathrm{QRS}_n}\right) < 0, \end{cases} \\ \gamma^{\mathrm{QRS_{end}}} &= \begin{cases} \frac{1}{8} W_{2^2}^y\left(p_l^{\mathrm{QRS}_n}\right) & \text{if } W_{2^2}^y\left(p_{\mathrm{l}}^{\mathrm{QRS}_n}\right) > 0 \\ \frac{1}{14} W_{2^2}^y\left(p_l^{\mathrm{QRS}_n}\right) & \text{if } W_{2^2}^y\left(p_l^{\mathrm{QRS}_n}\right) < 0. \end{cases} \end{aligned} \tag{3.14}$$

QRS onset

The QRS onset for the n^{th} beat occurs before the *first* significant slope associated to the QRS complex, that is, before the *first* maximum of $\left|W^y_{2^2}(k)\right|$, at sample $k = p_f^{QRS_n}$.
The *location* of the *QRS onset* ($l^{\mathrm{QRS}_{on_n}}$) is identified by selecting the sample nearest to the *first* QRS peak where one of the following criteria is satisfied:

i) the sample where $\left|W^y_{2^2}(k)\right|$ is below a threshold $\gamma^{QRS_{on}}$ relative to the amplitude of $W^y_{2^2}\left(p_{\mathrm{f}}^{\mathrm{QRS}_n}\right)$;

ii) is a local minimum of $\left|W^y_{2^2}(k)\right|$ before $p_f^{QRS_n}$.

QRS end

The QRS end for the n^{th} beat occurs after the *last* significant slope associated to the QRS complex, that is, after the *last* maximum of $\left|W^y_{2^2}(k)\right|$, at the sample $k = p_l^{QRS_n}$.
The *location* of the *QRS end* ($l^{\mathrm{QRS}_{end_n}}$) is identified by selecting the sample nearest to the *last* QRS peak where one of the following criteria is satisfied:

i) the sample where $\left|W^y_{2^2}(k)\right|$ is below a threshold $\gamma^{QRS_{end}}$ relative to the amplitude of $W^y_{2^2}\left(p_l^{\mathrm{QRS}_n}\right)$;

ii) is a local minimum of $\left|W^y_{2^2}(k)\right|$ after $p_l^{QRS_n}$.

3.4.3 T wave delineation

In the framework of this thesis, a novel multiscale threshold based strategy was defined for T wave location. The T wave detection and delineation is also illustrated in Figure 3.6. For each beat n, is defined a search window $T_{w_n} = [t^b_{w_n},\ t^e_{w_n}]$ referred to the neighbour QRS positions and the S wave location $l^{\mathrm{S}n}$ (if it exists)

$$\begin{aligned} t^b_{w_n} &= Max\left\{l^{\mathrm{QRS}_n} + 100 \text{ ms}\ ,\ l^{\mathrm{S}n} + 50 \text{ ms}\right\}, \\ t^e_{w_n} &= Min\left\{l^{\mathrm{QRS}_{n+1}} - 240 \text{ ms}\ ,\ 0.6Max\left\{RR_n^{med},\ 1000 \text{ ms}\right\}\right\}. \end{aligned} \tag{3.15}$$

RR_{med} denotes a recursively computed median RR interval, that is

$$RR_n^{med} = \begin{cases} 0.8RR_{n-1}^{med} + 0.2RR(n) \text{ if } \begin{cases} RR(n) > 0.5RR_{n-1}^{med} \\ RR(n) < 1.5RR_{n-1}^{med} \end{cases} \\ RR_{n-1}^{med} \text{ otherwise.} \end{cases} \tag{3.16}$$

and the T wave is located in T_{w_n}:

- a T wave is considered to be present at scale 2^4 if at least two local maxima of $\left|W^y_{2^4}(k)\right|$ within the search window exceed a threshold γ_4^{T};
- if the T wave was found in scale 4, the local extrema of WT with amplitude greater than a threshold $\gamma_4^{\mathrm{T_{all}}}$ are considered as significant slopes of the wave and the zero crossings between them as the wave peaks.
- if the T wave was not found in the scale 2^4 the above process is repeated in the scale 2^5 over $\left|W^y_{2^5}(k)\right|$, with thresholds γ_5^{T} and $\gamma_5^{\mathrm{T_{all}}}$.

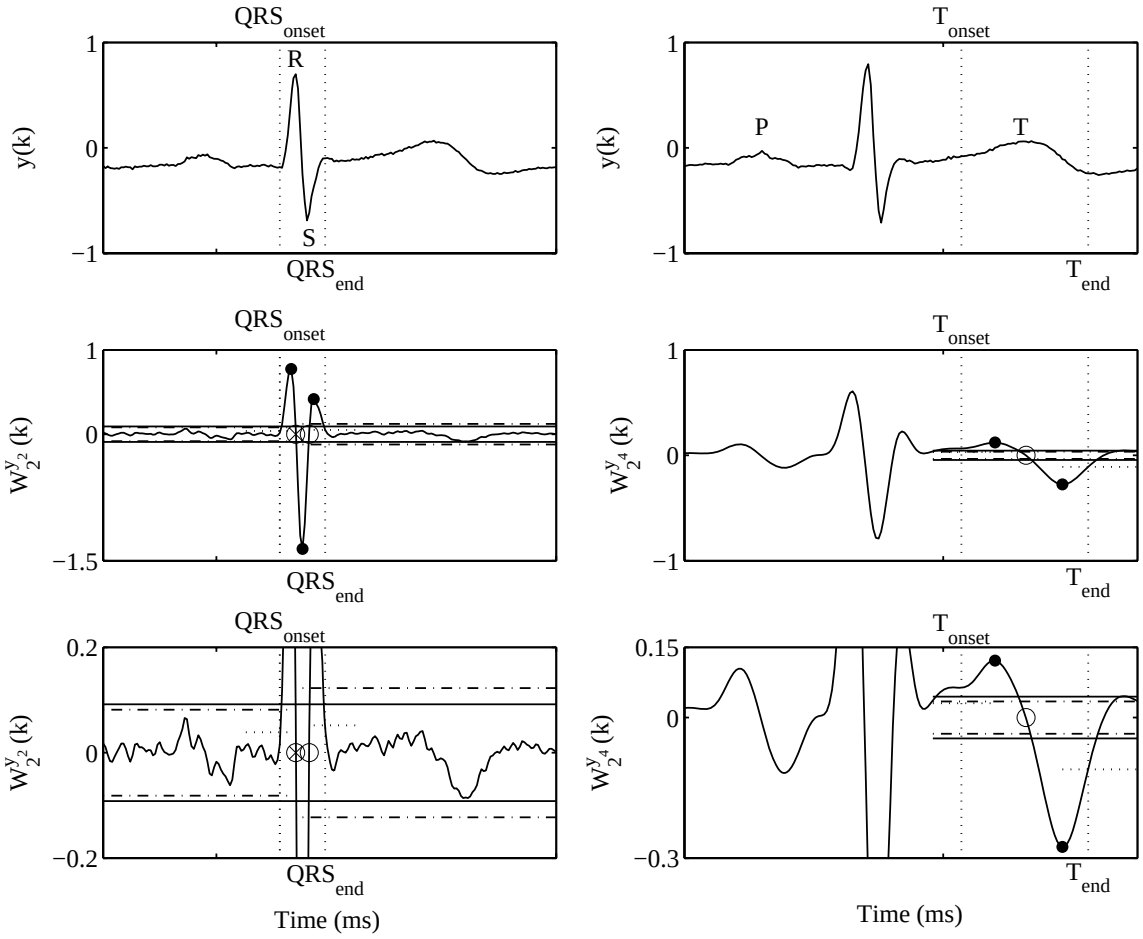

Figure 3.6: Single-lead based delineation example - QRS complex with only R and S waves (on the left) and positive T wave (on the right). Note that QRS boundaries and T wave end are marked using criterion i) while T onset satisfies criterion ii). The thresholds γ_2^{QRS} or γ_4^T correspond to the horizontal full lines, γ_{on}^{QRS}, γ_{end}^{QRS}, γ_{on}^T or γ_{end}^T to the horizontal dotted lines and γ_{pre}^{QRS} or γ_{post}^{QRS} or $\gamma_4^{T_{all}}$ to the horizontal dashed lines. The symbol ○ for zero crossing (wave peak),⊗ (on the left plot) for l^{QRS} and ● stands for modulus local maxima associated to the wave.

The *peak(s)* of the T wave correspond to the zero crossing(s) which, attending to the loss of time resolution in the growing scales are detected at scale 2^3, if they exist, or otherwise at the scale 2^m in which T wave was found. Once a T wave is found it is possible to proceed with its delineation. Depending on the number and polarity of the significant extrema found, it is assigned one out of six possible T wave morphologies (Figure 3.7): positive (+), negative (-), biphasic (+/- or -/+), only upwards and only downwards.

The thresholds used for T wave detection and to assign its morphology are defined as:

$$\begin{aligned} \gamma_m^{\mathrm{T}} &= 0.25\mathrm{RMS}\left[W_{2^m}^y(k)\right]|_{l^{\mathrm{QRS}_n}<k<l^{\mathrm{QRS}_{n+1}}}, m=4,5, \\ \gamma_m^{\mathrm{T_{all}}} &= 0.125 Max\left[W_{2^m}^y(k)\right]|_{k\in t_{w_n}}, m=4,5. \end{aligned} \tag{3.17}$$

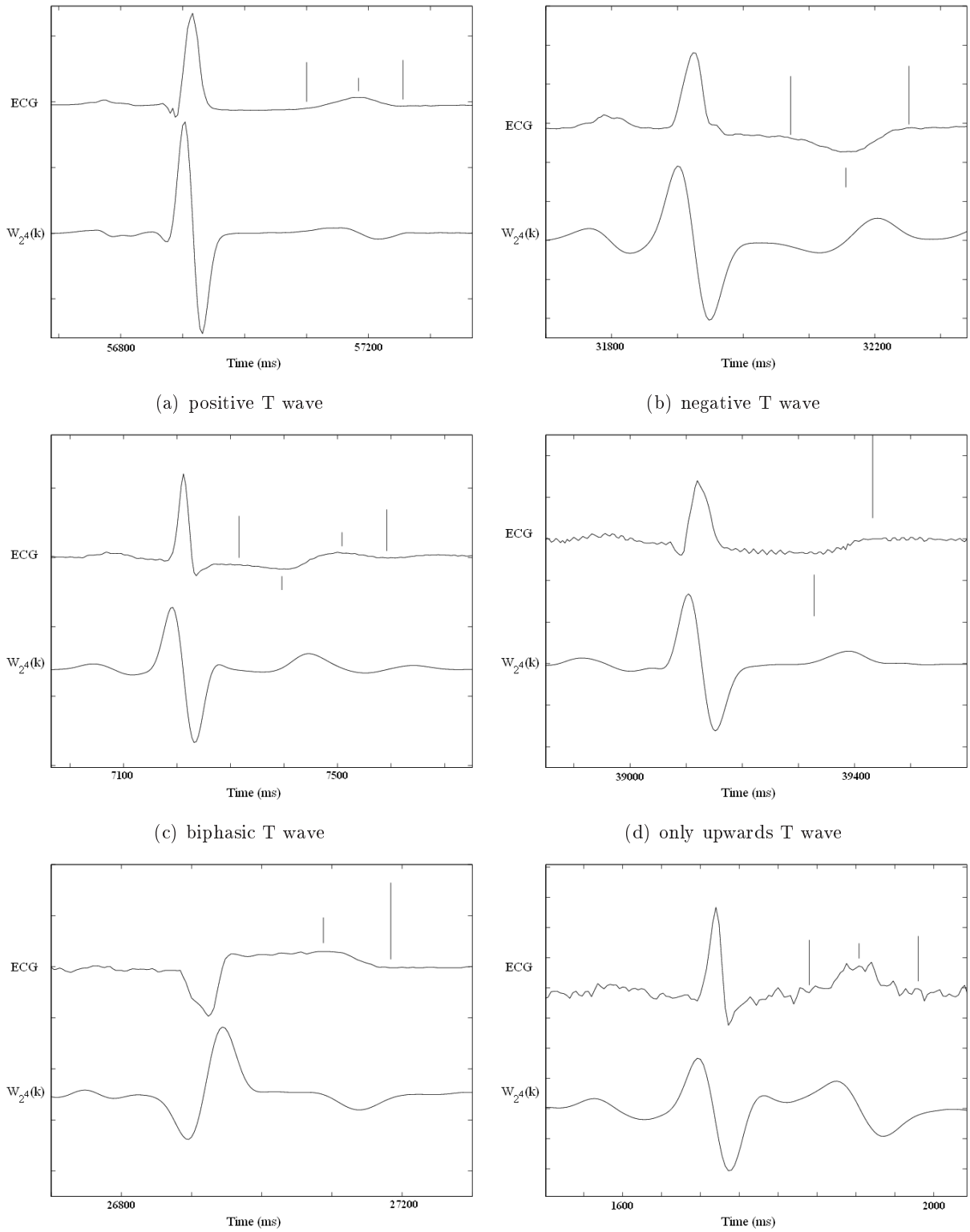

(a) positive T wave

(b) negative T wave

(c) biphasic T wave

(d) only upwards T wave

(e) only downwards T wave

(f) T wave with low SNR

Figure 3.7: Examples of different T wave morphologies, and their wavelet transform at scale 2^4. Short vertical lines show peak locations while long lines denote wave boundaries (Figure 8 of Martínez *et al.* (2004)).

The T wave *boundaries* $l^{\mathrm{T}on_n}$ and $l^{\mathrm{T}end_n}$ are located in the scale 2^m in which the T wave was found. As in the case of the QRS complex, thresholds used are relative to the amplitude of the first or last maximum modulus associated to the wave, located at samples $k = p_f^T$ and $k = p_l^T$

$$\begin{aligned} \gamma_m^{\mathrm{Ton}} &= 0.25 W_{2^m}^y(p_f^T), m = 4, 5, \\ \gamma_m^{\mathrm{Tend}} &= 0.4 W_{2^m}^y(p_l^T), m = 4, 5. \end{aligned} \tag{3.18}$$

T onset

The T wave initial limit $l^{\mathrm{T}on_n}$ occurs before the first $|W_{2^m}^y(k)|$ maximum, at the sample $k = p_f^T$. The same criteria as for the QRS onset is considered to locate $l^{\mathrm{T}on_n}$, with the threshold $\gamma_m^{\mathrm{Ton}}, m = 4, 5$.

T end

The T wave end $l^{\mathrm{T}end_n}$ occurs after the last $|W_{2^m}^y(k)|$ maximum, at the sample $k = p_l^T$. The same criteria as for the QRS end is considered to locate $l^{\mathrm{T}on_n}$, with the threshold γ_m^{Tend} applied to scale $2^m, m = 4, 5$..

3.4.4 P wave delineation

The algorithm for the P wave *peak(s)* and *boundaries* location is similar to the one described for T wave (Section 3.4.3), using an appropriate search window $P_{w_n} = [p_{w_n}^b,\ p_{w_n}^e]$ which depends on the QRS onset ($l^{\mathrm{QRS}on_n}$) and the T wave end in the previous beat ($l^{\mathrm{T}on_{n-1}}$),

$$\begin{aligned} p_{w_n}^b &= Max[l^{\mathrm{QRS}on_n} - 340ms\ ;\ l^{\mathrm{T}on_{n-1}}], \\ p_{w_n}^e &= l^{\mathrm{QRS}on_n} - 100ms, \end{aligned} \tag{3.19}$$

Four morphologies were admitted for P wave: positive (+), negative (-) and biphasic (+/- or -/+). The multiscale strategy for P wave detection and the extension to admit biphasic morphologies are novelties introduced in the framework of this thesis.

Adequate thresholds γ^{P}, γ^{Pall} were considered for wave detection and morphology assignment

$$\begin{aligned} \gamma_m^{\mathrm{P}} &= 0.02\mathrm{RMS}\left[W_{2^m}^y(k)\right]_{l^{\mathrm{QRS}_n} < k < l^{\mathrm{QRS}_{n+1}}}, m = 4, 5, \\ \gamma_m^{\mathrm{Pall}} &= 0.125 Max\left[W_{2^m}^y(k)\right]|_{k \in P_{w_n}}, m = 4, 5; \end{aligned} \tag{3.20}$$

thresholds γ^{Pon} and γ^{Pend} for boundaries location are relative to the amplitude of the first or last $|W_{2^m}^y(k)|$ maximum associated to the P wave, located at samples $k = p_f^P$ and $k = p_l^P$

$$\begin{aligned} \gamma_m^{\mathrm{Pon}} &= 0.5 W_{2^m}^y(p_f^P), m = 4, 5, \\ \gamma_m^{\mathrm{Pend}} &= 0.9 W_{2^m}^y(p_l^P), m = 4, 5. \end{aligned} \tag{3.21}$$

3.4.5 Rules for lead selection

The usual strategy for dealing with multilead signals is the inclusion of post-processing selection rules in the single-lead based delineation systems, as it was remarked in Section 3.1. The simplest rule consists in choosing the median mark; for example the main wave peak location corresponds to the median in the set of the main wave peak locations according to each lead considered.

However, the different spacial orientation of each lead allow the visibility of a phenomena in a lead before than in another and thus the median is not the best choice when dealing with boundaries. Thus, the best mark for a wave's begin (end) should be the earliest (latest) one, a choice that is strongly affected by erroneous marks (*"outliers"*).

Alternatives to reduce outliers effect in this kind of procedure have been proposed (de Chazal and Celler, 1996; Laguna *et al.*, 1994), consisting in sorting the single-lead annotations and selecting as boundary the first (last) annotation whose k nearest neighbours lay within a δ ms interval.
Laguna *et al.* (1994) considered $k = 3, \delta = 6$ ms for P wave limits and QRS onset, $\delta = 10$ ms for QRS end and $\delta = 12$ ms for T end, while de Chazal and Celler (1996) used $k = 2, \delta = 6$ ms for both QRS boundaries. This rule was included in the system here described for $k = 3$ nearest neighbours and

$$\delta = 12 \text{ ms for QRS onset and T end,}$$
$$\delta = 10 \text{ ms for QRS end,}$$
$$\delta = 4 \text{ ms for P wave boundaries.}$$

It should be remarked that, if no single-lead annotation satisfies this criteria, no mark is provided. Thus, these rules result quite well for choosing among a large set of single-lead annotations (for instance on a record acquired according the standard 12-lead system) but are hardly adequate for a record with just 2 or 3 leads. For records with a low number of leads available, a very low number of positive true detections should be expected for the more problematic characteristic points, for which missing annotations are more frequent even using a reduced value for k.

3.5 Multilead System

Choosing a particular lead for ECG delineation determines a point of view over the cardiac phenomena, and thus different latencies on the waves's onsets and ends are found in different leads (Section 1.2). Combining adequately the information provided by multiple leads is essential for the correct location of waves' boundaries.

To take advantage of the spacial information provided by multiple leads in the framework of this thesis a multilead extension of the WT based system described in Section 3.4 regarding the wave boundaries was developed, by considering simultaneously the orthogonal Frank leads (X, Y, Z). This constitutes an alternative to the application of post-processing lead selection as described in the previous Section.

Concerning the aim of application to the QTV study the efforts were concentrated in the location of the boundaries needed for QT interval measuring, in particular the QRS boundaries and the problematic of T wave end.

As previously described in Chapter 1, (X, Y, Z) define the vectocardiogram (VCG), which is a canonical representation of the electrical heart vector (EHV). An example is illustrated in Figure 3.8 for the T wave.

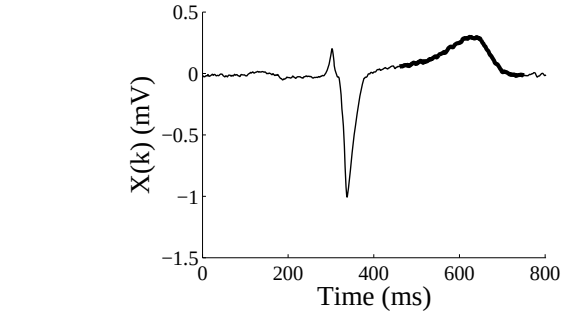

(a) Lead X

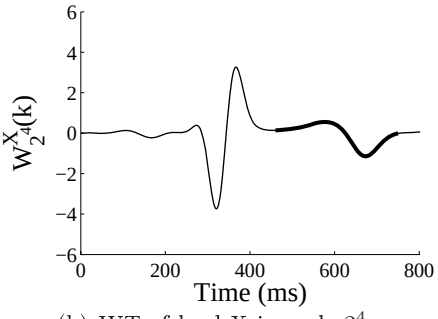

(b) WT of lead X in scale 2^4

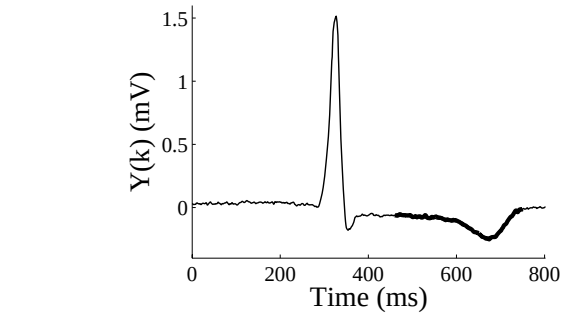

(c) Lead Y

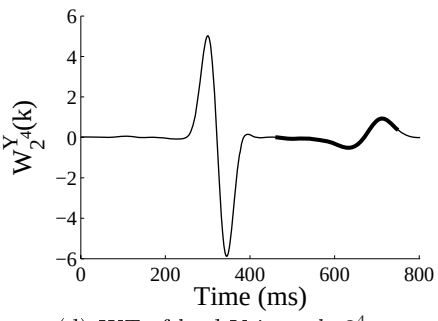

(d) WT of lead Y in scale 2^4

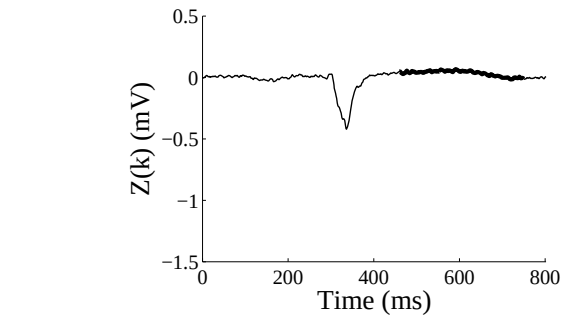

(e) Lead Z

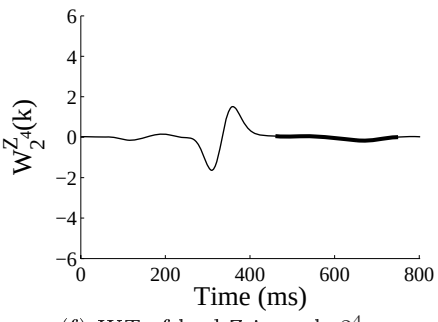

(f) WT of lead Z in scale 2^4

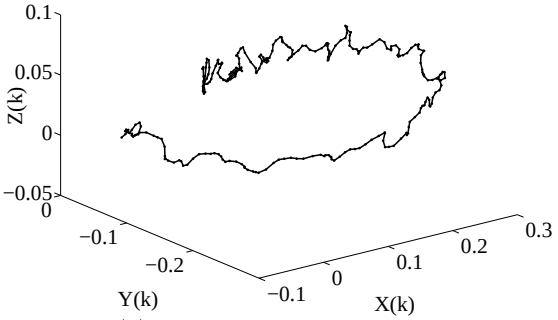

(g) VCG loop of the T wave

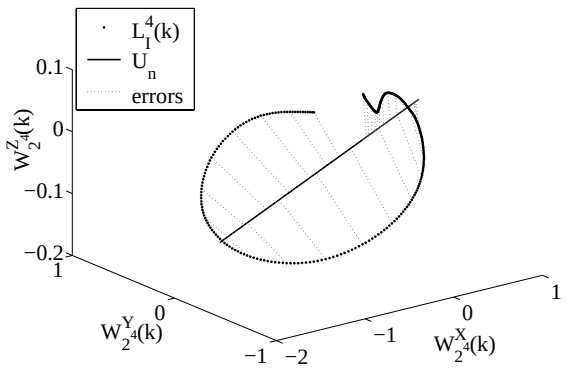

(h) W_{2^4} loop of the T wave, best line fit to the entire loop and some fitting residues in total least squares sense.

Figure 3.8: Examples of ECG and W_{2^4} signals corresponding to whole beat and VCG loop and WT loop corresponding to the T wave: (g) VCG loop corresponding to the thicker line in the ECG signals in (a), (c) and (e); (h) WT loop corresponding to the thicker line in the ECG signals in (b), (d) and (f) and the best line fit by total least squares (TLS) minimization.

A spatial WT *loop* in a time window w for scale $2^m, m \in \{1, 2, 3, ...\}$ is given by

$$\mathbf{L}_w^m(k) = [W_{2^m}^X(k), W_{2^m}^Y(k), W_{2^m}^Z(k)]', \ k \in w. \tag{3.22}$$

As a consequence of the WT prototype used in this work (Section 3.2) the wavelet loop $\mathbf{L}_w^m(k)$ is proportional to the VCG derivative and describes the EHV evolution in any time interval w. Therefore, regarding the n^{th} beat, the main direction $\mathbf{U_n} = [U_n^X, U_n^Y, U_n^Z]'$ of EHV variations in a scale 2^m on any time interval w_n is given by the director vector of the best straight line fit to all points in the WT loop $\mathbf{L}_{w_n}^m(k)$, $k \in w_n$.

Considering the VCG loop [X(k), Y(k), Z(k)] in any time interval I_n defined for the n^{th} beat, a *constructed ECG* lead $ECG_n(k)$ defined by axis $\mathbf{U_n}$, can be obtained by projecting the points of the VCG loop over the direction of $\mathbf{U_n}$, that is

$$ECG_n(k) = \frac{[X(k), Y(k), Z(k)]'_{k \in I_n}.\mathbf{U_n}}{||\mathbf{U_n}||}. \tag{3.23}$$

Instead, the WT loop $\mathbf{L}_{I_n}^m(k)$ can be projected and a *derived wavelet* signal $D_n(k)$, corresponding to the ECG lead defined by the axis $\mathbf{U_n}$ can be constructed, as:

$$D_n(k) = \frac{\mathbf{L}_{I_n}^m(k)'.\mathbf{U_n}}{||\mathbf{U_n}||}, \ k \in I_n. \tag{3.24}$$

It should be noticed that while the time intervals w_n, considered in the loop to find the best fitted direction, and I_n, defining the loop points to project, can be different, depending on each wave specificities. For each beat n, the new derived WT signal $D_n(k)$ based in the time window w_n, combines the information provided by the orthogonal original leads for the time interval I_n.

The strategy proposed for multilead boundary delineation using WT loops is based in a multi-step iterative search for a *better* spatial lead for delineation improvement (with *steeper* slopes). At each step, the vector $\mathbf{U_n}$ is determined separately for each beat and boundary, by adapting and updating the interval w_n in a way to increase the signal-to-noise ratio (SNR) and ensure steep slopes in $D_n(k)$. The goal is to construct a new lead $D_n(k)$ well suited for boundaries location, using the same detection criteria as in the single-lead delineator. Namely, for each beat n and boundary:

1. is defined a time interval w_n, adequate to find the EHV's main direction in the boundary;
2. the main direction of EHV variations $\mathbf{U_n}$, is estimated using the adequate scale 2^m as the best line fit to $\mathbf{L}_{w_n}^m(k)$, $k \in w_n$;
3. for $l_{[0]}^{\mathrm{QRS}_n}$ the location of the QRS complex in the n^{th} beat (location of the main wave peak), taken as the median mark of the 3 single-lead locations, a time interval I_n is defined as

$$I_n = [l_{[0]}^{\mathrm{QRS}_{n-1}} \ , \ l_{[0]}^{\mathrm{QRS}_{n+1}}], \tag{3.25}$$

4. the loop $\mathbf{L}_{I_n}^m(k)$, corresponding to the time interval I_n is projected according to equation (3.24) to construct the new derived WT signal $D_n(k)$;
5. SL delineation of the wave is performed as described in Section 3.4 over $D_n(k)$;

6. the time interval w_n is updated attending to the boundary location provided by the previous step; the procedure is repeated from Step 2, until no slope increase is obtained for $D_n(k)$ in Step 3; in that case the boundary location found in the previous iteration is adopted, as it corresponds to the best lead found for its delineation.

Note that for a best line fit the optimization process can provide any of two symmetric vectors and consequently the ECG lead produced will be one of two symmetric (with reversed polarity), as illustrated in Figure 3.9. This will not affect the delineation procedure as the single-lead system is prepared for several polarities of the ECG waves (Section 3.4).

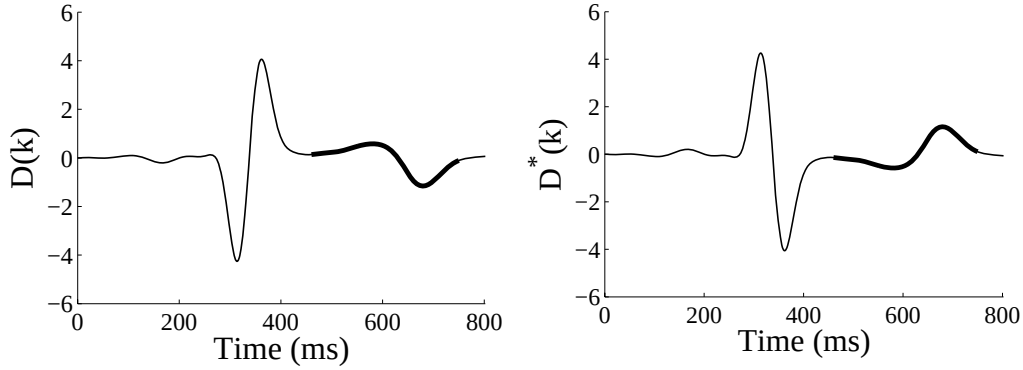

(a) Constructed WT signals

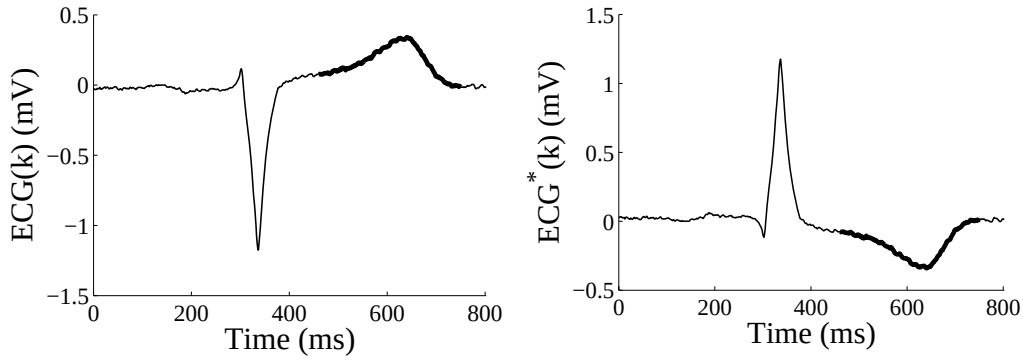

(b) Constructed ECG leads

Figure 3.9: Constructed WT and ECG signals $D(k)$ and $ECG(k)$, corresponding to the direction given by $\mathbf{U}_n$; $D^*(k)$ and $ECG^*(k)$ correspond to symmetric vector $-\mathbf{U}_n$.

The direction $\mathbf{U}_n$ of the EHV is taken as the best line fit in total least squares (TLS) sense.

In the traditional least squares criteria it is assumed that errors only occur in one *observed* variable, while the other variables are exactly known. However, all the 3 WT signals used for define the WT loop of equation (3.22) are representations of observed ECG leads that can contain errors, i.e. noise contamination. The TLS fitting does not assume that some variables are error free and minimizes the distance between each observation and the fitted line, that is, the deviations are orthogonal to the fitted line (Van Huffel and Vandewalle, 1991), as illustrated in Figure 3.8(h) [1].

[1]More details in the use of the total least squares fitting for finding the main loop direction can be found in the Appendix D

It must be also remarked that:

- the choice of *basing the lead direction* in the WT loop, instead of taking directly the VCG loop is of *extreme importance*, as it allows to avoid the high frequency noise contamination and thus produces a more accurate selection (Figure 3.8(h) and 3.8(g));
- Frank leads can also be synthesised from the standard 12-lead system, if they were not recorded [2];
- in spite of having been designed regarding the Frank lead system, the multilead delineation methodology can be applied over any set of three ECG orthogonal leads;
- considering WT loops in a 2D plane instead of in a 3D space is also possible, allowing to apply this methodology to any two ECG orthogonal leads, if the only available.

The time intervals w_n for multilead delineation were defined specifically for each wave and boundary, as will be detailed in the next sections; I_n should include the search window needed for SL delineation of each wave and thus was taken as the interval between QRS complexes in which the boundary is included. In this work, the information provided by each individual lead and the standard deviation tolerance values provided by The CSE Working Party (1985) were considered in the choice of the time intervals. The CSE reference tolerance values ($2s_{\text{CSE}}$) correspond to 2 standard deviations of the differences between the median of the interval manual annotations (which were used for constructing the CSE standard database) and the final referee marks included in the database. These tolerance values are given as a standard deviation error limit that should not be exceeded by an automatic delineation system (The CSE Working Party, 1985). They are widely accepted as tolerance for the delineation errors dispersion and are provided for the QRS onset, QRS end and T wave end, corresponding to:

- $s_{\text{CSE}}(\text{QRS}_{on}) = \frac{6.5}{2}$ ms;
- $s_{\text{CSE}}(\text{QRS}_{end}) = \frac{11.6}{2}$ ms;
- $s_{\text{CSE}}(T_{end}) = \frac{30.6}{2}$ ms.

No value was given for T wave onset, and thus in this work it was considered $s_{\text{CSE}}(T_{on}) = s_{\text{CSE}}(T_{end})$

The thresholds were adjusted by trial and error from the SL values, but advantage of tunning was only found for T wave end, with improved accuracy achieved by taking

$$\gamma_m^{\text{Tend}} = 0.25 W_{2^m}^y(p_{l_{D[1]}}^{T_n}),$$

The value for all other thresholds was taken equal to SL. The specific details of the strategy regarding each of the ECG boundaries are given in the next subsections.

[2] See Appendix A for more details

3.5.1 QRS boundaries

The multilead location of the QRS boundaries is performed using the WT loop in scale 2^2 using the locations given by the SL methods over each orthogonal lead.

QRS onset

The multilead delineation of QRS onset is illustrated in Figures 3.10 and 3.11. For QRS onset location, only the main direction of EHV on the earliest part of the first QRS wave is of interest. The multi-step iterative strategy for constructing a new lead, specially suited for QRS onset location, consists in the following steps, for each beat n:

Step 1 - initialization

- initial search window $Q[1]_n$ is defined as:

$$Q[1]_n = [l_{[0]}^{\mathrm{QRS}_{on_n}} - 4s_{\mathrm{CSE}}(\mathrm{QRS}_{on}) \ , \ p_{f_{[0]}}^{\mathrm{QRS}_n}] \tag{3.26}$$

  $l_{[0]}^{\mathrm{QRS}_{on_n}}$, the earliest QRS onset location given by the SL methods (over each orthogonal lead)

  $p_{f_{[0]}}^{\mathrm{QRS}_n}$, the earliest first significant maximum modulus location over the 3 orthogonal leads.

- the main direction $\mathbf{U}[1]_n$ of the EHV is found by TLS fitting in the WT *loop* $\mathbf{L}^2_{Q[1]_n}(k)$,
- a derived WT signal $D[1]_n(k)$ is constructed by projecting the WT *loop* $\mathbf{L}^2_{I_n}(k)$, $k \in I_n$ over $\mathbf{U}[1]_n$, where I_n is the interval given by equation (3.25);
- $l_{[1]}^{\mathrm{QRS}_{on_n}}$, the QRS onset position, is located by applying the SL delineation strategy to $D[1]_n(k)$;

Step g ≥ 2 - iteration

- the search window is actualized from the previous iteration as

$$Q[g]_n = [l_{[g-1]}^{\mathrm{QRS}_{on_n}} - 4s_{\mathrm{CSE}}(\mathrm{QRS}_{on}) \ ; \ p_{f_{D[g-1]}}^{\mathrm{QRS}_n}] \tag{3.27}$$

  $l_{[g-1]}^{\mathrm{QRS}_{on_n}}$, QRS onset position according to $D[g-1]_n(k)$

  $p_{f_{D[g-1]}}^{\mathrm{QRS}_n}$, location of the first significant maximum modulus of $D[g-1]_n(k)$.

- the direction $\mathbf{U}[g]_n$ is taken as the best line fit in the TLS sense to the WT *loop* $\mathbf{L}^2_{Q[g]_n}(k)$, $k \in Q[g]_n$;
- a derived wavelet signal $D[g]_n(k)$ is constructed by projecting the WT *loop* $\mathbf{L}^2_{I_n}(k)$, $k \in I_n$ over $\mathbf{U}[g]_n$, considering the same interval defined in equation (3.25);
- $l_{[g]}^{\mathrm{QRS}_{on_n}}$, the QRS onset position, is located by applying the SL delineation strategy to $D[g]_n(k)$;

- repeat for $g+1$, until one of the following occurs:

  i) $l_{[g]}^{\mathrm{QRS}_{onn}}$ differs less than one sample from $l_{[g-1]}^{\mathrm{QRS}_{onn}}$;

  ii) $l_{[g]}^{\mathrm{QRS}_{onn}} = l_{[g1]}^{\mathrm{QRS}_{onn}} = l_{[g2]}^{\mathrm{QRS}_{onn}}$ with $g > g1+1 > g2+1$,
  that is, same location was obtained for three non consecutive steps;

  iii) the 3 following conditions are fulfilled simultaneously

  $$\left|D[g]_n\left(p_f^{\mathrm{QRS}_{D[g]n}}\right)\right| \leq \left|D[g-1]_n\left(p_f^{\mathrm{QRS}_{D[g-1]n}}\right)\right|$$
  $$D[g-1]_n\left(p_f^{\mathrm{QRS}_{D[g-1]n}}\right) \text{ corresponds to a Q wave}$$
  $$D[g-1]_n\left(p_f^{\mathrm{QRS}_{D[g-1]n}}\right) \text{ have same sign than } D[g]_n\left(p_f^{\mathrm{QRS}_{D[g-1]n}}\right),$$

  meaning that the lead constructed at step g is not better for QRS onset location than the constructed in the step $[g-1]$;

  iv) no significant maximum of $|D[g]_n(k)|$ was found,
  meaning that the lead constructed at step g is not adequate for QRS onset location

- depending on the criteria applied to stop the iterative search:
  - if the criteria i) or ii) was fulfilled, then ML based QRS onset location is taken as $l_{[g]}^{\mathrm{QRS}_{onn}}$;
  - if the criteria the criteria iii) or iv) was fulfilled, then ML based QRS onset location is taken as $l_{[g-1]}^{\mathrm{QRS}_{onn}}$.

Examples of WT loops in space and the directions of the best line fit in the initial search window ($Q[1]_n$) and at the final step g ($Q[g]_n$) are presented in Figures 3.10(a) and 3.11(a), along with the respective best line fit ($\mathbf{U}[1]_n$ and $\mathbf{U}[g]_n$). As illustrated in the examples, the search window can be both enlarged or reduced along the iterations. The ECG constructed leads ($ECG[1]_n(k)$ and $ECG[g]_n(k)$) and derived WT signals ($D[1]_n(k)$ and $D[g]_n(k)$) are plotted in Figures 3.10(b) and 3.11(b). For comparison the original ECG signals in the orthogonal leads $X(k)$, $Y(k)$, $Z(k)$ and the WT signals $W_{2^2}^X(k)$, $W_{2^2}^Y(k)$ and $W_{2^2}^Z(k)$ for a neighborhood of the QRS complex are also plotted in Figures 3.10(b) and 3.11(b). In the first example a closer location to the reference mark is clearly achieved at step g compared to step 1 (Figure 3.10(b)). In the second example it is clear the steeper slope obtained for the first maximum modulus (Figure 3.11(b)). For both examples the mark found at step $g=2$ was adopted.

It must be stressed out that by applying consecutively the strategy defined in the **Step g**, a direction *closely* parallel to the begin of the first QRS wave can be found. Therefore a lead *more fitted* for QRS onset detection can be constructed.

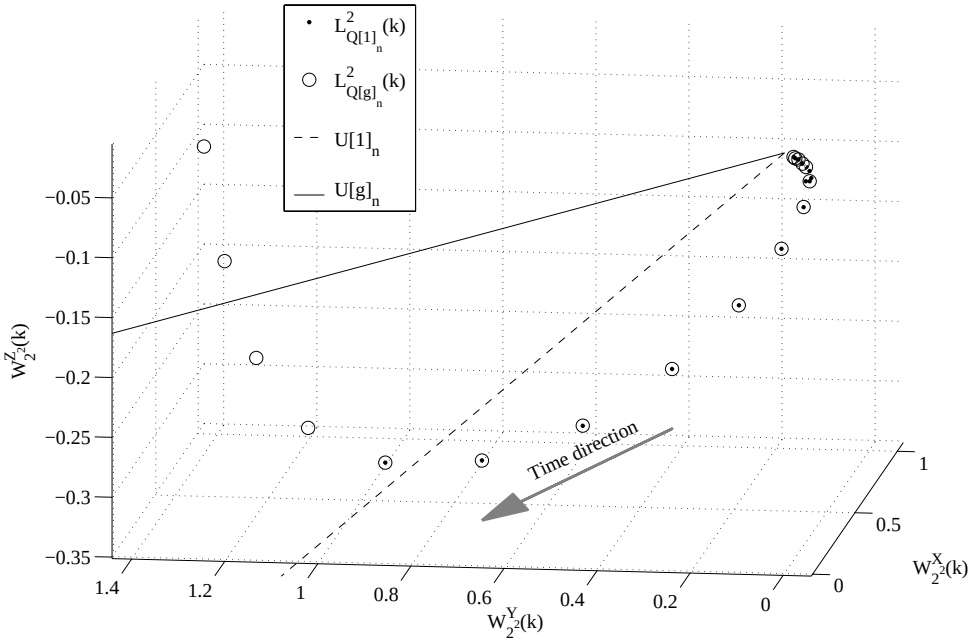

(a) WT VCG loops used for multilead QRS on set location (n^{th} beat) and the direction of the best line fit at the initial, $\mathbf{U}[1]_n$ and final step, $\mathbf{U}[g]_n$ ($g = 2$).

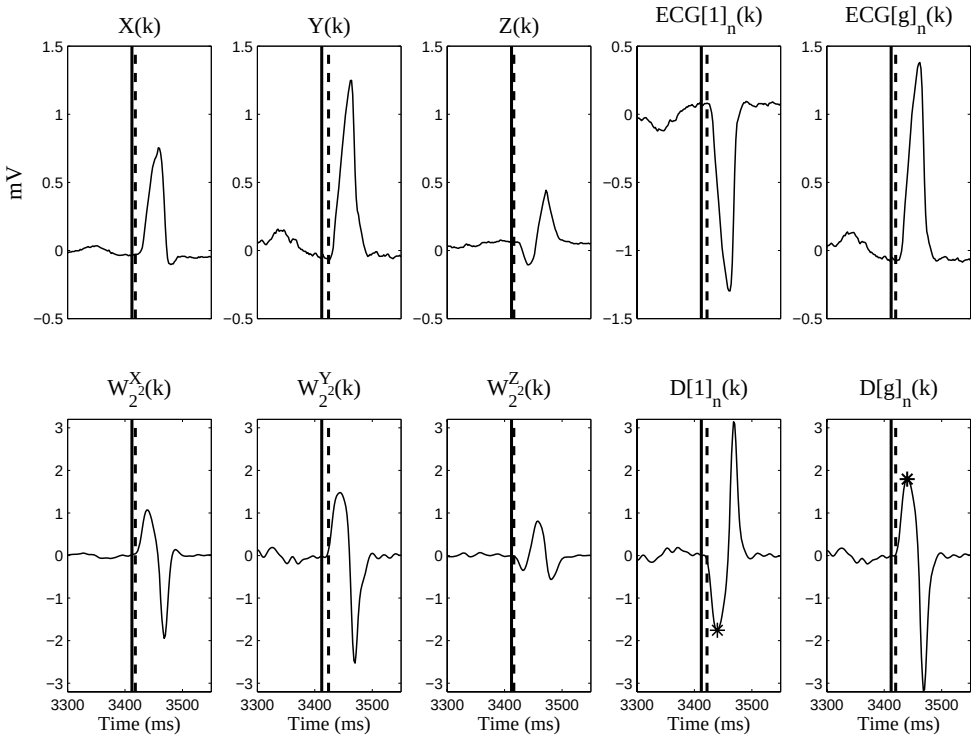

(b) ECG in orthogonal leads $X(k)$, $Y(k)$, $Z(k)$, the correspondent WT signals $W^X_{2^2}(k)$, $W^Y_{2^2}(k)$, $W^Z_{2^2}(k)$, the derived ECG signals $ECG[1]_n(k)$, $ECG[g]_n(k)$ and WT signals $D[1]_n(k)$, $D[g]_n(k)$, following the directions of vectors $\mathbf{U}[1]_n$ and $\mathbf{U}[g]_n$ (k in an arbitrary neighborhood of the QRS complex for the n^{th} beat). Vertical dashed line stands for the QRS onset mark found in the respective lead; solid line stands for *median referee* QRS onset mark and the star stands for the first significant maximum modulus in the constructed lead. ECG signals in mV and $g = 2$.

Figure 3.10: Example of multilead delineation of the QRS onset. **Step 1** (initial) and **Step g** (final step).

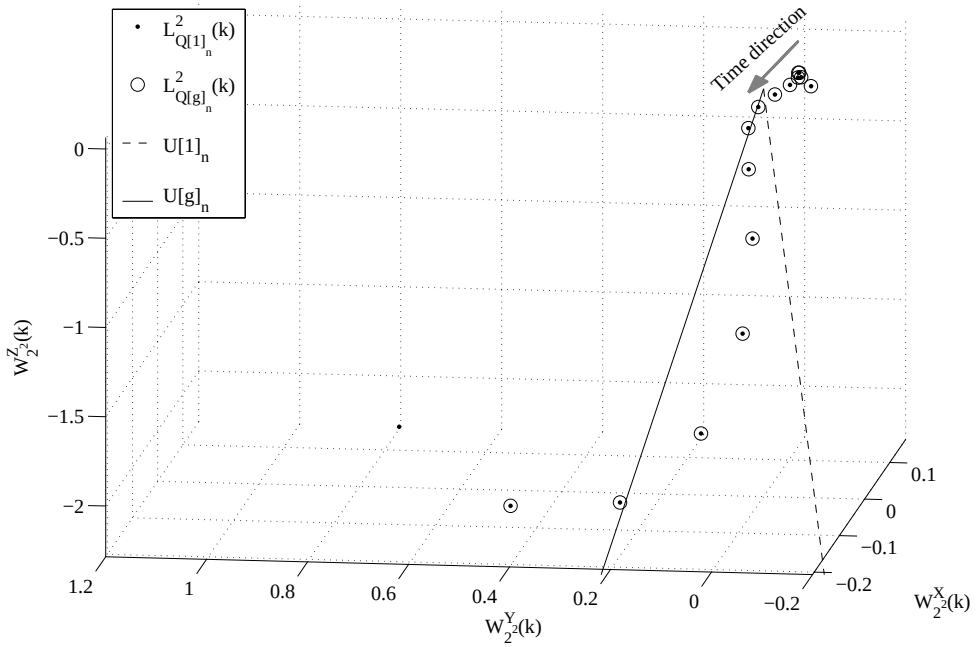

(a) WT VCG loops used for multilead QRS on set location (n^{th} beat) and the direction of the best line fit at the initial, $\mathbf{U}[1]_n$ and final step, $\mathbf{U}[g]_n$ ($g = 2$).

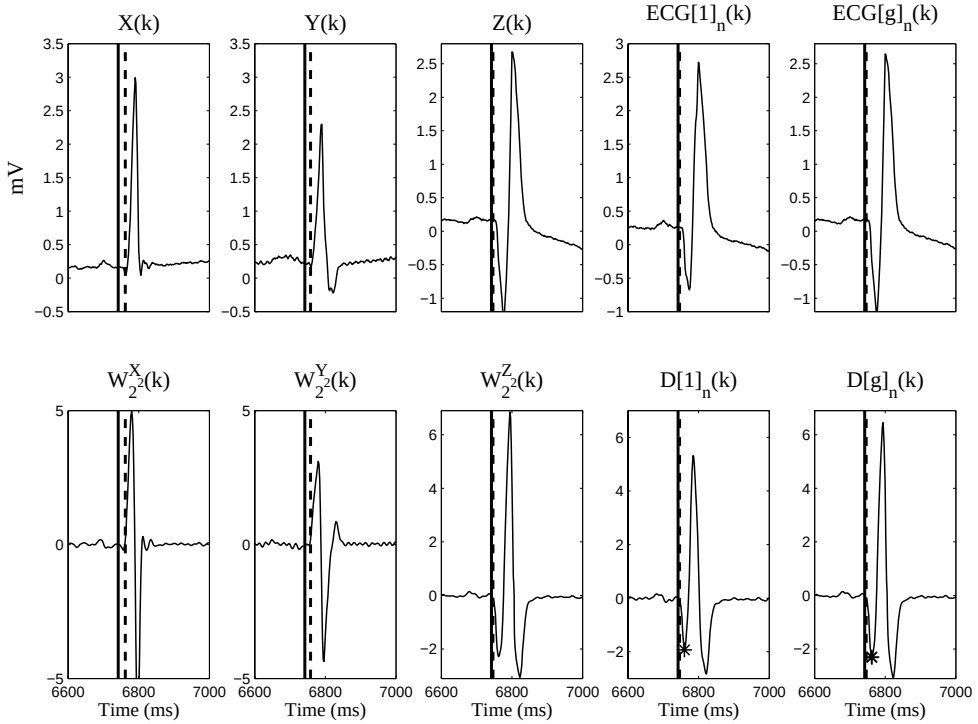

(b) ECG in orthogonal leads $X(k)$, $Y(k)$, $Z(k)$, the correspondent WT signals $W^X_{2^2}(k)$, $W^Y_{2^2}(k)$, $W^Z_{2^2}(k)$, the derived ECG signals $ECG[1]_n(k)$, $ECG[g]_n(k)$ and WT signals $D[1]_n(k)$, $D[g]_n(k)$, following the directions of vectors $\mathbf{U}[1]_n$ and $\mathbf{U}[g]_n$ (k in an arbitrary neighborhood of the QRS complex for the n^{th} beat). Vertical dashed line stands for the QRS onset mark found in the respective lead; solid line stands for *median referee* QRS onset mark and the star stands for the first significant maximum modulus in the constructed lead. ECG signals in mV and $g = 2$.

Figure 3.11: Example of multilead delineation of the QRS onset. **Step 1** (initial) and **Step g** (final step).

QRS end

The location of QRS end can be performed similarly to the described for the QRS onset, considering the fact than in this case, only the latest part of the last QRS wave is of interest. Thus, the iterative procedure is analogous to the defined for QRS onset noticing that, for each beat n,

- a initial search window is defined as:

$$S[1]_n = [p_{l_{[0]}}^{\text{QRS}_n} \ , \ l_{[0]}^{qrs_{on_n}} + 4s_{\text{CSE}}(\text{QRS}_{end})] \tag{3.28}$$

  $l_{[0]}^{\text{QRS}_{end_n}}$ is the latest QRS end location given by the SL methods

  $p_{l_{[0]}}^{\text{QRS}_n}$ is the latest significant maximum modulus location found in the orthogonal leads.

- at step $g \geq 2$ the search window is actualized as

$$S[g]_n = [p_{l_{[g-1]}}^{\text{QRS}_n} \ ; \ l_{[g-1]}^{\text{QRS}_{on_n}} + 4s_{\text{CSE}}(\text{QRS}_{end})] \tag{3.29}$$

  $l_{[g-1]}^{\text{QRS}_{end_n}}$ is the QRS end location found by applying the single-lead delineator to $D[g-1]_n(k)$

  $p_{l_{[g-1]}}^{\text{QRS}_n}$ is the last significant maximum modulus in the constructed new lead $D[g-1]_n(k)$.

- the criteria to stop the iterative search become:

  i) $l_{[g]}^{\text{QRS}_{end_n}}$ differs less than one sample from $l_{[g-1]}^{\text{QRS}_{end_n}}$;

  ii) $l_{[g]}^{\text{QRS}_{end_n}} = l_{[g1]}^{\text{QRS}_{on_n}} = l_{[g2]}^{\text{QRS}_{end_n}}$ with $g > g1 + 1 > g2 + 1$;

  iii) The 3 following conditions are fulfilled

$$\left|D[g]_n\left(p_{l_{[g]}}^{\text{QRS}_n}\right)\right| \leq \left|D[g-1]_n\left(p_{l_{[g-1]}}^{\text{QRS}_n}\right)\right|$$
$$D[g-1]_n\left(p_{l_{[g-1]}}^{\text{QRS}_n}\right) \text{ corresponds to a S wave}$$
$$D[g-1]_n\left(p_{l_{[g-1]}}^{\text{QRS}_n}\right) \text{ have same sign than } D[g]_n\left(p_{l_{[g-1]}}^{\text{QRS}_n}\right),$$

  iv) no significant maximum of $|D[g]_n(k)|$ was found;

- depending on the criteria applied to stop the iterative search:
  - if the criteria i) or ii) was fulfilled, then ML based QRS end location is taken as $l_{[g]}^{\text{QRS}_{end_n}}$;
  - if the criteria iii) or iv) was fulfilled, then ML based QRS end location is taken as $l_{[g-1]}^{\text{QRS}_{end_n}}$.

3.5.2 T wave boundaries

Multilead delineation of T wave boundaries is illustrated for the T end case in Figures 3.12 and 3.13. Scale $2^m = 2^5$ is considered for ML if in the SL delineation scale 2^5 was used for T wave detection for at least two out of the three leads, and $m = 4$ otherwise.

The T wave is typically more symmetric than the QRS complex, thus a single initial T wave search window $T[1]_n$, is considered for each beat, both regarding the onset and the end of the wave.

A very similar strategy, although with different threshoulds, is proposed for locating both T wave boundaries, consisting in the following steps, for each beat n:

Step 1 - initialization

- the initial T wave search window is defined as the union of the 3 single-lead based T wave search windows according to equation (3.15), that is

$$T[1]_n = [t^b_{w_n[0]};\ t^e_{w_n[0]}] \tag{3.30}$$
$$t^b_{w_n[0]} \text{ is the earliest } t^b_{w_n} \text{ in the orthogonal leads}$$
$$t^e_{w_n[0]} \text{ is the latest } t^e_{w_n} \text{ in the orthogonal leads}$$

- the main direction of EHV $\mathbf{U}[1]_n$, is found by TLS fitting to the WT *loop* $\mathbf{L}^m_{T[1]_n}(k)$;
- the derived WT signal $D[1]_n(k)$ is constructed by projecting the loop $\mathbf{L}^m_{I_n}(k)$ over $\mathbf{U}[1]_n$, considering the same interval defined for QRS boundaries (equation (3.25));
- $l^{T_{on_n}}_{[1]}$, the **T wave onset** position, is located by applying the same rules and threshold as in the SL delineator to $D[1]_n(k)$
- $l^{T_{end_n}}_{[1]}$, the **T wave end** position, is located by applying the same rules as in the SL delineator to $D[1]_n(k)$, with a threshold

$$\gamma^{\text{Tend}}_m = 0.25 W^y_{2^m}(p^{T_n}_{l_{D[1]}}), \tag{3.31}$$

where $p^{T_n}_{l_{D[1]}}$ is the last $|D[1]_n(k)|$ significant maximum associated to the T wave;

Step $g \geq 2$ - iteration

- the search window for **T onset** is actualized as

$$T[g]_n = [l^{T_{on_n}}_{[g-1]} - 4s_{\text{CSE}}(T_{on});\ p_{f^{T_n}_{D[g-1]}}];$$

where $l^{\text{T}on_n}_{[g-1]}$ is the T onset position according to $D[g-1]_n(k)$, $p^{\text{T}n}_{f_{D[g-1]}}$ is the location of the first significant maximum modulus, associated to the T wave, of $D[g-1]_n(k)$;
as a matter of fact, the T onset occurs before $p^{T_{D[g-1]_n}}_f$ thus only the main direction of EHV in the earliest part of the T wave is of interest;

- the search window for **T end** is actualized as

$$T[g]_n = [p^{T_n}_{l_{D[g-1]}};\ l^{T_{end_n}}_{[g-1]} + 4s_{\text{CSE}}(T_{end})];$$

where $l^{\text{T}end_n}_{[g-1]}$ is the T end position according to $D[g-1]_n(k)$, $p^{T_n}_{l_{D[g-1]}}$ is the location of the last maximum modulus, associated to the T wave, of $D[g-1]_n(k)$;
as a matter of fact, the T end occurs after $p^{T_{D[g-1]n}}_l$ thus only the main direction of EHV in the latest part of the T wave is of interest;

- the direction $\mathbf{U}[g]_n$ is taken as the best line fit in the TLS sense to the WT loop $\mathbf{L}^m_{T[g]_n}(k)$;
- a new wavelet signal $D[g]_n(k)$, corresponding to the direction $\mathbf{U}[g]_n$, is constructed by projecting all the points in the loop $\mathbf{L}^m_{I_n}(k)$ over $\mathbf{U}[g]_n$;
- the T onset position $l^{\mathrm{T}on_n}_{[g]}$ is located by applying the same rules as in the SL delineator to $D[g]_n(k)$;

- the direction $\mathbf{U}[g]_n$ taken as the best line fit in the TLS sense to the WT loop $\mathbf{L}^m_{T[g]_n}(k)$;
- a new wavelet signal $D[g]_n(k)$, corresponding to the direction $\mathbf{U}[g]_n$, is constructed by projecting all the points in the loop $\mathbf{L}^m_{I_n}$ over $\mathbf{U}[g]_n$;
- the T end position $l^{\mathrm{T}end_n}_{[g]}$ is located by applying the same rules as in the SL delineator to $D[g]_n(k)$ with threshold γ^{Tend}_m given in equation (3.31);

- repeat to g=g+1, until one of the following occur:

  i) $l^{T_n}_{[g]}$ differs less than one sample from $l^{T_n}_{[g-1]}$;

  ii) $D[g]_n\left(p^{T_n}_{l_{D[g]}}\right) \leq D[g-1]_n\left(p_{l^{T_n}_{D[g-1]}}\right)$,
  meaning that the lead constructed at g^{th} step is not better for T boundary location than the constructed in the step $[g-1]$

  iii) no significant maximum of $|D[g]_n(k)|$ was found,
  meaning that the lead constructed at g^{th} step is not adequate for T boundary location.

- depending on the criteria applied to stop the iterative search:
  - the criteria i) was fulfilled, then ML based T onset location is taken as $l^{\mathrm{T}on_n}_{[g]}$;
  - the criteria ii) or iii) was fulfilled, then ML based T onset location is taken as $l^{\mathrm{T}on_n}_{[g-1]}$.

- depending on the criteria applied to stop the iterative search:
  - the criteria i) was fulfilled, then ML based T end location is taken as $l^{\mathrm{T}end_n}_{[g]}$;
  - the criteria ii) or iii) was fulfilled, then ML based T end location is taken as $l^{\mathrm{T}end_n}_{[g-1]}$.

By applying consecutively the strategy defined in the **Step g**, a direction *closely* parallel to the T wave boundary can be found. Therefore, the final lead $D[g]_n(k)$ is likely to present a single slope, very steep, most fitted for T wave boundary detection.

Examples of T wave's loops and the directions of the best line fit in the initialization (Step 1) and at the final step (Step g) for T end location are presented in Figures 3.12(a) and 3.13(a). The original ECG and WT signals, the new derived signals and the ECG signals constructed by projecting the WT loop over the lead directions given by $\mathbf{U}[1]_n$ and $\mathbf{U}[g]_n$ are plotted in Figures 3.12(b) and 3.13(b). In both examples, the mark adopted was found in step 2 and the improvement in the location is reflected in a mark closer to the reference (Figures 3.12(b) and 3.13(b)).

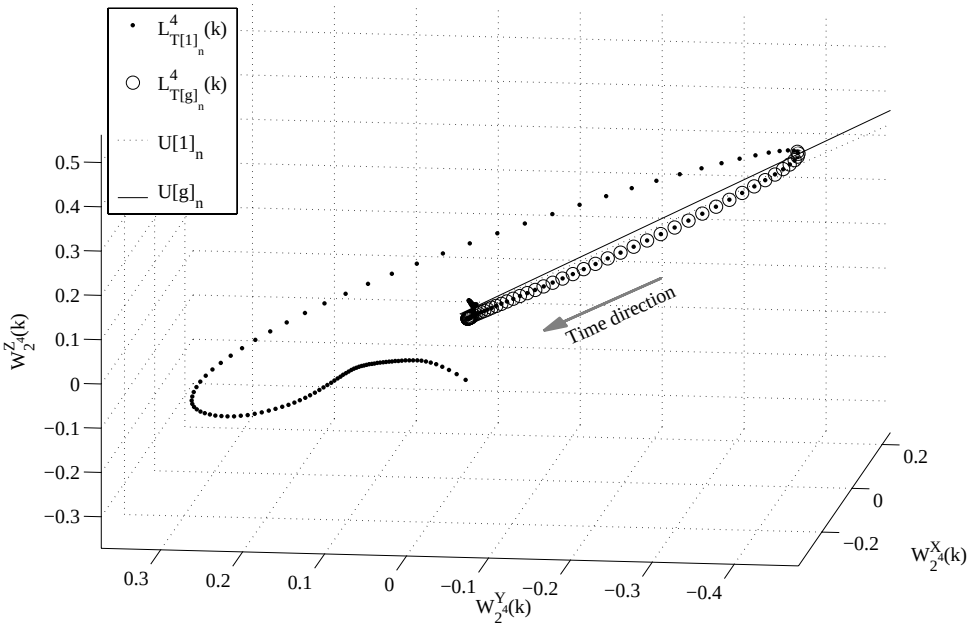

(a) WT VCG loops used for multilead T end location (n^{th} beat) and the direction of the best line fit at the initial, $\mathbf{U}[1]_n$, and final step, $\mathbf{U}[g]_n$ ($k \in T[1]_{w_n}$, $g = 2$).

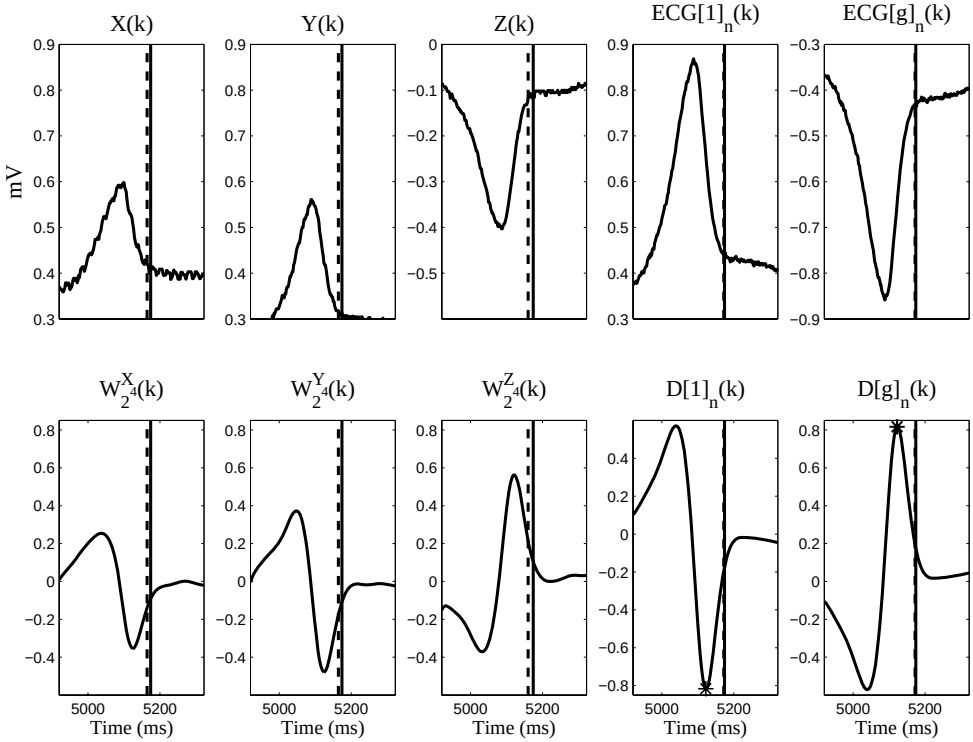

(b) ECG in orthogonal leads $X(k)$, $Y(k)$, $Z(k)$, the correspondent WT signals $W^X_{2^4}(k)$, $W^Y_{2^4}(k)$, $W^Z_{2^4}(k)$, the derived ECG signals signals $ECG[1]_n(k)$, $ECG[g]_n(k)$ and WT signals $D[1]_n(k)$, $D[g]_n(k)$, following the directions of vectors $\mathbf{U}[1]_n$ and $\mathbf{U}[g]_n$ found for the n^{th} beat ($k \in T[1]_{w_n}$). Vertical dashed line stands for the T end mark found in the respective lead; solid line stands for *median referee* T end mark and the star stands for the last significant maximum modulus in the constructed lead. ECG signals in mV and $g = 2$. (n^{th} beat)

Figure 3.12: Example of multilead delineation of the T end. **Step 1** (initial) and **Step g** (final step).

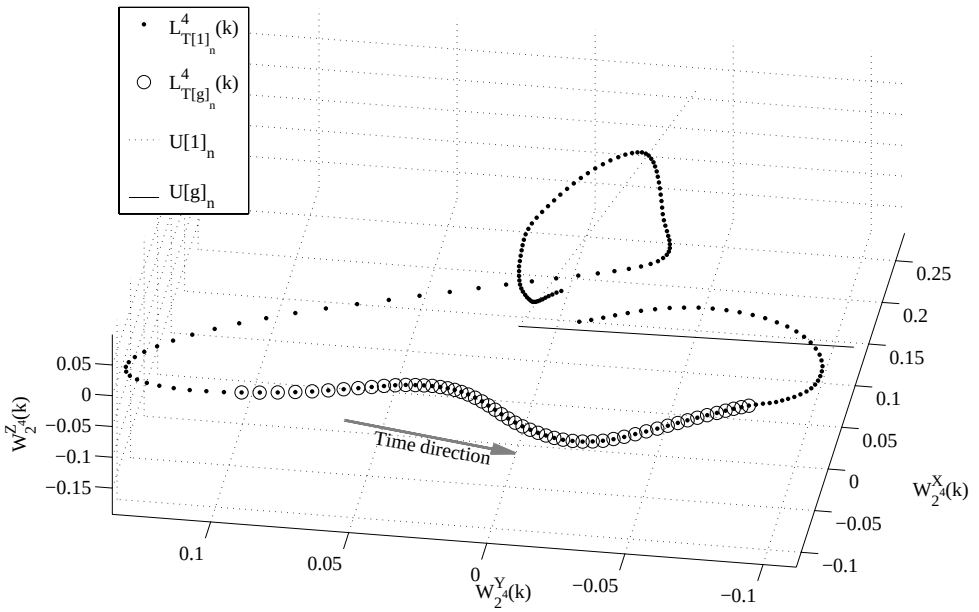

(a) WT VCG loops used for multilead T end location (n^{th} beat) and the direction of the best line fit at the initial, $\mathbf{U}[1]_n$, and final step, $\mathbf{U}[g]_n$ ($k \in T[1]_{w_n}$, $g = 2$).

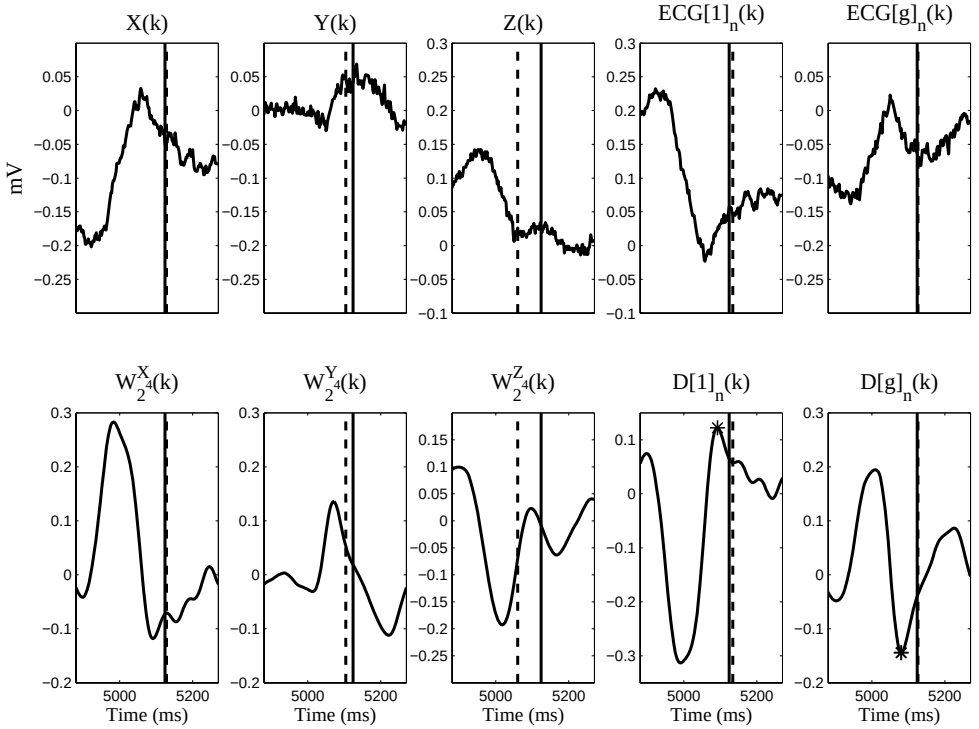

(b) ECG in orthogonal leads $X(k)$, $Y(k)$, $Z(k)$, the correspondent WT signals $W^X_{2^4}(k)$, $W^Y_{2^4}(k)$, $W^Z_{2^4}(k)$, the derived ECG signals signals $ECG[1]_n(k)$, $ECG[g]_n(k)$ and WT signals $D[1]_n(k)$, $D[g]_n(k)$, following the directions of vectors $\mathbf{U}[1]_n$ and $\mathbf{U}[g]_n$ found for the n^{th} beat ($k \in T[1]_{w_n}$). Vertical dashed line stands for the T end mark found in the respective lead; solid line stands for *median referee* T end mark and the star stands for the last significant maximum modulus in the constructed lead. ECG signals in mV and $g = 2$. (n^{th} beat)

Figure 3.13: Example of multilead delineation of the T end. **Step 1** (initial) and **Step g** (final step).

3.5.3 Other fiducial points

The multilead strategy here proposed aims to enhance boundaries location taking advantage of the spacial information. It developed regarding the particular application of the QT measurement, that is the location of the QRS complex onset and T wave end, and furthermore has been also extended to the QRS end and T wave onset.

Regarding wave peak detection is less relevant to consider different leads, as usually peaks are easier to locate than boundaries. For that reason no multilead strategy was developed for peak location and in this work the median mark between leads is assumed as multilead based peak location, namely for the R wave location.

With respect to the individual waves in the QRS complex morphologies, they are determined by the lead used (Section 1.2); therefore, it makes no sense to identify them in a ML base. Even so, it is possible to adapt the multilead strategy to locate the cardiac phase they reflect: for example the depolarization of the wall between the ventricles, no matter the wave that appears in each lead (negative small Q wave or a positive small R wave). This issue was not addressed in this thesis.

The P wave boundaries can also be located using the multilead approach, in spite of that implementation has not been done yet. With this approach a new direction closely parallel to the P wave boundary and optimally fitted for its detection can be found. As in the case of single-lead methods, a multilead strategy similar to the one for T wave boundaries would be appropriated. The criteria for the scale to use and the initial P wave search window for each beat can be chosen analogously; the iterative algorithm, the actualization of search windows at each step and the stop criteria would be the same, with adequate threshold tunning.

3.6 Validation of ECG automatic delineation

The evaluation of the automatic delineation strategies was performed over real files from ECG databases. Depending on the leads available, 3 different VCG systems were considered:

lead set F - defined by the orthogonal Frank leads X,Y and Z provided by the databases;

lead set M - defined by leads *V5*, *aVF* and *V2*, a subset of 3 mutually orthogonal leads out of the standard 12-lead system;

lead set D - defined by the synthesised orthogonal leads, by using the coefficients provided by the *Dower Matrix*.

The 12-lead system is the most used in the clinical practice, thus lead set *M* would be available much more frequently than lead set *F*. The leads *V5*, *aVF* and *V2* were chosen by their resemblance with the Frank leads. Nevertheless, *M* does not take into account the human torso's geometry. To include the needed corrections, the orthogonal Frank system should be synthesised as a linear combination

of the 12 recorded leads using the coefficients provided by the *Dower Matrix* [3] (lead set D).

The VCG systems here considered were chosen because they are defined by well known leads, which are likely to be familiar to clinicians, but any other combination of 3 orthogonal leads could be used instead and other transformations from 12 to 3 leads rather than Dower matrix can be considered.

Another possibility is, for each 12 lead record, to find the 3 orthogonal leads that maximize the explained variability from multidimensional ECG signal, that is, to find the first three principal components (PC). The PC are orthogonal ECG like signals which can be interpreted as synthesized leads that are not necessarily in the frontal or transverse plane used to define the standard lead system. Rather they could be any direction in space and change from record to record. The construction of PC does not take into account the spacial dependence between the original ECG leads and the first PC are likely to explain much more ECG variation than the other PC. Nevertheless, the resulting VCG loop is similar to the obtained using other VCG systems. PC have been used by (Tarvainen *et al.*, 2006, 2007) in a method for measuring QT variability directly from the ECG. In this work, the VCG obtained by PC was preliminary evaluated over CSEDB, but no improvement was achieved compared with the other VCG systems and this VCG was not here considered.

The SL delineation was evaluated over each available lead, while ML was evaluated over the above referred VCG systems F, M and D, whenever they were available. Additionally SL followed by post processing rules was used to combine SL marks (SLR) and was evaluated over one of more of the lead sets F, M and D. The decision rules described in Section 3.4.5 have been applied with $k = 3$ over 12 or 15 leads, and with $k = 1$ to the 3-lead sets that define F, M and D. The application of the ML strategy to in a 2D plane, by using 2 orthogonal leads only was also validated and compared with SL over each individual lead.

As the true marks on a real ECG signal are unknown, the validation of the automatic delineation systems was performed over available manually annotated databases. Standard databases are available for that purpose, some regarding only the beat detection (QRS location) others considering beat delineation by providing reference marks for several wave peaks and bands. Particularly, two standard databases have been repeatedly used for evaluation of ECG delineation systems: the CSE multilead measurement database (Willems *et al.*, 1987), with short signals in 15 leads, and the QT database (Laguna *et al.*, 1997), with 15 min long recordings in 2 leads only. Very recently, the PTB database has also been manually annotated in the context of the *"PhysioNet/Computers in Cardiology Challenge 2006: QT Interval Measurement"* competition [4] (Christov *et al.*, 2006; Moody *et al.*, 2006).

The delineation systems were validated over these three databases by comparing the marks found by the delineator with the provided referee marks. Other databases do not include reference marks regarding both QRS and T wave boundaries, and thus given the particular application of the QT measurement, were not here considered.

[3] See Appendix A for more details

[4] See http://www.physionet.org/challenge/2006/ for more details.

3.6.1 ECG Databases

The **CSE database** (CSEDB) includes 42 files, 10 sec long, at 500 Hz. Manual annotations were made by 5 cardiologists having in view all the available leads; *median referee* annotations (after outlier rejection) are provided for a beat per file. Two files present reference marks that were clearly miss located, possibly due to a technical problem.[5] The marks available differ for each annotated beat and can include the QRS location (R marks) and the boundaries for QRS, T and P waves. In particular, reference marks are provided for QRS onset in 32 beats and for T wave end in 27 beats.

The **PTB database** (PTBDB) consists in a set of 549 files of more than 30 sec at 1000 Hz. One file is unusable as it does not seem to be an ECG. A set of reference annotations was published in Christov *et al.* (2006), consisting in manual annotations for QRS onset and T wave end, done by four cardiologists and one biomedical engineer, and a *median referee* annotation (after outlier rejection). One beat per file in all usable files was chosen and annotated, following the recommendations of the *"PhysioNet/Computers in Cardiology Challenge 2006: QT Interval Measurement"* competition (Moody *et al.*, 2006). Briefly, the participants in that competition were asked to, *according to lead II, choose on each file the first representative non ectopic and not noisy beat and locate the QRS onset set and T wave end.* Christov *et al.* (2006) state that in more than 15% of the records in PTBDB no T wave could be definitely recognized in lead II and in such case the referees were instructed to mark the T wave end as a group, at one of the leads where the T wave was better manifested. For 6 files the reference annotations (Christov *et al.*, 2006) correspond to the first beat of the file, which is usually not annotated with the WT based automatic methods due to the border effect of the filters. Thus only 542 files were considered on the performance evaluation.

Both CSEDB and PTBDB consist in ECG files of 15 leads (12 standard plus 3 orthogonal Frank leads) and thus all 3 VCG systems (F, M and D) were considered in the validation.

The **QT database** (QTDB) consists in 105 records from other previously compiled 2-lead ECG databases (the European ST-T database and Arrhythmia, ST Change, Supraventricular Arrhythmia, Normal Sinus Rhythm, Sudden Death and Long Term MIT-BIH databases). QTDB includes segments of 15 minutes from each record, resampled at 250 Hz, corresponding to various 2-lead pairs. Cardiologist annotations (ref1) regarding QRS, P and T waves peaks and boundaries are provided for at least 30 beats per file, in a total of more than 3600 annotated beats.

Since QTDB only includes 2 leads, the described multilead delineation approach was applied using loops in the plane instead of in the space. Regarding the orthogonality of the available two leads, the QTDB was divided in four subgroups:

QTDB1 (7 files) records with orthogonal leads from the 12-lead standard system, in which the multilead delineation can be applied directly using a 2D approach;

QTDB2 (57 files) records with no identified leads (signal 1, signal 2), here assumed to be orthogonal; the files were treated as the ones in *QTDB1*;

[5] The CSEDB data available has been previously converted to MIT format (a standard ECG data storage format). An error in storage or in the conversion process should be the cause of this problem.

QTDB3 (34 files) records with no orthogonal and no parallel leads, which can be orthogonalized as described in the Appendix A, by constructing a new ECG lead orthogonal to one of the provided leads; the multilead delineation was applied using a 2D approach over the orthogonal pair (original lead, constructed lead);

QTDB4 records with parallel leads, that cannot be orthogonalized and will not be considered for the validation (7 files with leads *I* and *V5* from the 12 standard system) [5].

It should also be remarked that not all waves and boundaries are given for each annotated beat, in particular 3412 reference marks for QRS onset and 3331 for T end were provided for the 98 files included in the validation. QTDB also includes, for 11 out of its 105 records, an additional annotation performed by a second cardiologist (ref2), with a total of 404 QRS onset and 402 T end locations with a double reference annotation.

3.6.2 Performance evaluation

The automatic systems presented were evaluated with respect to the QRS onset and T wave end, boundaries which are illustrative of typical situations: a peaky and smooth wave. These boundaries are the ones with more reference marks provided by the available annotated databases and are of extreme importance due to the clinical relevance of the QT measurement. Furthermore, their automatic location is not yet established as a standard method (Moody *et al.*, 2006).

The improved single lead system described was previously validated with respect to the location of other fiducial points, using CSDDB, QTDB and other databases. Good results were obtained comparing with other published approaches and are presented with detail in Martínez *et al.* (2004). Most of them are not repeated here for simplicity, as the QRS onset and T wave end are considered to be illustrative of the 2 typical situations.

The two stages of any delineation automatic system, the detection of a wave and its delineation, were evaluated using different indexes. With respect to the *detection* performance, it is current in biostatistic applications to evaluate the *Sensitivity* (Se) of a method as:

$$Se = 100 \frac{true\ \ positive\ \ detections}{true\ \ positive\ \ detections + false\ \ negative\ \ detections}. \tag{3.32}$$

and the *Positive Predictivity* (P^+) as

$$P^+ = 100 \frac{true\ \ positive\ \ detections}{true\ \ positive\ \ detections + false\ \ positive\ \ detections}. \tag{3.33}$$

For the CSEDB only one bet per file is annotated, thus Se and P^+ cannot be calculated.

The large number of beats annotated in the PTBDB makes possible to evaluate the Se of the automatic system with respect to both QRS complex and T wave detection. On the other hand P^+ cannot be calculated, as only one beat per file (in which the T wave is present) is annotated and the number of *false positive detections* cannot be determined.

For the QTDB and for each boundary, Se was also calculated. Again, is impossible to evaluate P^+ in this kind of database as was already noted in Vila *et al.* (2000). The absence of an annotation in the reference marks could either be due to the decision of the cardiologist that no wave was present or that he could not confidently annotate the point (e.g. because of the noise). However, if it is assumed that all absent reference marks on an annotated beat result from the decision that no wave is present, a lower limit ($P^+_{\min}$) for the actual P^+ can be estimated for the T wave (Martínez *et al.*, 2004).

Regarding the delineation performance, an automatic detector should be accurate, robust and stable. In particular, for studying beat-to-beat variability it is crucial to ensure a low dispersion of the delineation error, in order to avoid introducing spurious variability in the series. Thus, reducing the errors' dispersion is even more important than reducing their bias.

The delineation error (ε) was taken as the*automatically detected boundary minus the respective referee mark* and in each database were evaluated the mean (m_ε) and standard deviation (s_ε) of ε; the mean $\left(m_{|\varepsilon|}\right)$ and standard deviation $\left(s_{|\varepsilon|}\right)$ of the absolute error $|\varepsilon|$ were also calculated. Concerning QT database, since several beats are annotated per file, the mean and standard deviation of the error ε and of the absolute error $|\varepsilon|$ were first calculated for each file i ($m_{\varepsilon_i},\ s_{\varepsilon_i}$) and then averaged. Thus, for this database, $\bar{s}_\varepsilon$ and $\bar{s}_{|\varepsilon|}$ stand for the mean standard deviation across files.

Additionally, the above mentioned parameters were calculated after *extreme cases* exclusion.
A file in CSEDB or PTBDB was considered as an extreme case if the correspondent error value ε didn't lie within the 3 standard deviation bounds, that is

$$\varepsilon \notin \left]\, m_\varepsilon - 3s_\varepsilon,\ m_\varepsilon + 3s_\varepsilon \,\right[\tag{3.34}$$

The values of the mean and standard deviation were updated after the exclusion of extreme cases, and the process was repeated until all files relied within $3s_\varepsilon$ bounds.

For the QT database, a file was considered as an extreme case with respect to its mean error m_{ε_i}, that is

$$m_{\varepsilon_i} \notin \left]\, m_\varepsilon - 3s_{m_\varepsilon},\ m_\varepsilon + 3s_{m_\varepsilon} \,\right[\tag{3.35}$$

$$s^2_{m_\varepsilon} = \frac{1}{N_i - 1}\sum_{i=1}^{N_i}(m_{\varepsilon_i} - m_\varepsilon)^2 \tag{3.36}$$

where N_i is the number of included files. The values of m_ε and s_{m_ε} were actualized after the exclusion of such files, and the process was repeated until all files satisfy equation (3.35).

According to The CSE Working Party (1985) recommendations *"the standard deviation of the differences from the reference should not exceed certain limits"*. These values ($2s_{CSE}$) correspond to 2 standard deviations of the differences between the median of the individual readers manual annotations used for constructing the standard database CSE. These CSE values were already referred in this thesis as they were used to define search windows in the multilead delineation system (Section 3.5). In spite of being widely accepted as a way for defining a tolerance for the automatic marks errors dispersion, is not consensual if an algorithm should accomplish the:

- loose criterion: $s < 2s_{CSE}$ (Laguna *et al.*, 1994; Sahambi *et al.*, 1997; Vullings *et al.*, 1998; Vila *et al.*, 2000);

- strict criterion: $s < s_{CSE}$ (de Chazal and Celler, 1996; Strumillo, 2002).

For CSEDB and PTBDB were evaluated and compared the following delineation strategies:

multilead delineation (ML) over

- the recorded Frank leads (X, Y, Z) - lead set F
- the recorded leads (V5, aVF, V2) - lead set M
- the constructed Frank leads using Dower matrix (X, Y, Z) - lead set D

single-lead delineation over

- each of the 15 recorded leads (SL);

single-lead delineation plus post-processing rules (SLR) over

- the recorded Frank leads (X, Y, Z) - lead set F;
- the recorded leads (V5, aVF, V2) - lead set M;
- the constructed Frank leads using Dower matrix (X, Y, Z) - lead set D;
- the recorded *12 standard leads*;
- all the recorded *15 leads* (12 standard leads plus the Frank leads).

In QTDB, the 2-dimensional version of the ML system was applied. Each lead was also processed using the SL delineation system and decision rules were applied over the 2 leads available with $k = 1$ (SLR approach), for the sake of comparison. Thus, the following delineation approaches were considered:

- **multilead** delineation (ML) over the two orthogonal (QTDB1), assumed to be orthogonal (QTDB2) or orthogonalized (QTDB3) leads (lead I and lead II);
- **single-lead** delineation (SL) over each of the 2 leads ;
- **single-lead delineation plus post-processing rules** (SLR) over the 2 leads;

Additionally, a combined mark was obtained by choosing for each fiducial point the location on the lead with less error (best mark). This last approach cannot be considered as a rule to apply in real practice where no reference marks exist, however it is a reasonable way to compare the two single-lead annotation sets with the manual annotations that are performed having in view all available leads.

3.6.3 QRS onset evaluation

A low number of iterations per beat was required for QRS onset multilead delineation and the marks were found at **Step1** or **Step2** of the algorithm for

- 80% in CSEDB and 72% in PTBDB, using lead set F ;
- 75% in CSEDB and 49% in PTBDB, using lead set M;
- 83% in CSEDB and 72% in PTBDB, using lead set D.

Moreover, the mean of iterations per beat was

- 2.2 both in CSEDB and in PTBDB, using lead sets F and M,;
- 2.1 in CSDB, 2.5 in PTBDB, using lead set D.

CSEDB results

In Figure 3.14(a) are plotted the values found in CSEDB for m_ε and $m_{|\varepsilon|}$ and the bands $m_\varepsilon \pm s_\varepsilon$ and $m_{|\varepsilon|} \pm s_{|\varepsilon|}$, considering *all true* QRS onset detections (#) and using ML, SL and SLR approaches. In Table 3.1(a) are presented the results of ML and SLR considering all true detections that can be compared with other published results also validated in CSEDB additionally presented in Table 3.1(e). The results reported by Laguna *et al.* (1994) and de Chazal and Celler (1996) used the described decision rules over the 15 sets of marks with the parameters referred in the Section 3.4.5, while Sahambi *et al.* (1997) did not provide information about what multilead rules were used.

The automatic procedures are marking the QRS onset latter than the referees, as can be seen from the *positive bias* found in most of the cases. This is likely to be due to non detected Q waves.

Also,

- better results are achieved by of SLR over the 12 or 15 leads, compared to the ones reported in Laguna *et al.* (1994);
- a performance decrease is evident when using SLR over 3 leads, compared with SLR over the 12 or 15 leads;
- considering all true detections (Figure 3.14(a) and Table 3.1(a)), the multilead approach shows clearly worse results.

Despite the apparent poor performance of ML considering all true detections, for results over the recorded Frank leads (F) it was found that 12.5% of the files (4 out of 32 files) were causing 58% of the mean error and 76% of the error standard deviation. Excluding the extreme files by appling the criterium in equation (3.34),

- the exclusion of 4 files for the lead set F reduces m_ε from 16.9 ms to 7.1 ms, and s_ε from 28.9 ms to 6.9 ms;
- over lead subset M a reduction of more that 25% in s_ε is obtained by excluding one single file.

The results after exclusion of extreme cases over each approach are plotted in Figure 3.14(b) and Table 3.1(b). For a better comparison are also presented the results obtained after excluding from all approaches the files found to be extreme cases in any of the approaches, considering SLR over 12 or 15 leads (Table 3.1(c)) and all SLR combinations (Table 3.1(d)).

After the exclusion of the extreme cases in each approach (Figure 3.14(b) and Table 3.1(b)), it can be concluded:

- ML over the lead sets F and M outperforms SL over any of the 15 leads;
- ML over F outperforms ML over M or D;
- ML over F achieved a s_ε value
  - similar to the obtained by SLR over 12 or 15 leads;
  - lower than in Laguna *et al.* (1994).

On the other hand, by excluding the extreme cases in any approach for all the cases (Table 3.1(c)) it is possible to compare errors considering exactly the same files and in that case:

- ML over F still outperforms ML over M or D;
- ML over F performs worse than SLR over 12 or 15 leads.

Given the reduced number of no extreme cases common to all ML and SLR approaches, it is hardly adequate to take conclusions from Table 3.1(d), but on those files ML over M or D performs better than ML over F.

With respect to the CSE error tolerance ($2s_{CSE}(QRS_{on}) = 6.5$ ms):

- considering all true detections, the loose criterion is at least nearly fulfilled by the SLR strategies using 12 or 15 leads, and also by Sahambi *et al.* (1997) and de Chazal and Celler (1996);
- after extreme cases exclusion, the loose criterion is at least nearly fulfilled by the previous and by multilead over the set F and SLR over D;
- the strict criterion is only accomplished by the results of Sahambi *et al.* (1997) (nearly accomplish by de Chazal and Celler (1996)).

It should be remarked that an exceptionally low standard deviation error was reported by Sahambi *et al.* (1997), nearly half of the reported by de Chazal and Celler (1996) (Table 3.1(e)). However, as Sahambi *et al.* (1997) did not provide information about the multilead rules used, it is not possible to take any conclusion.

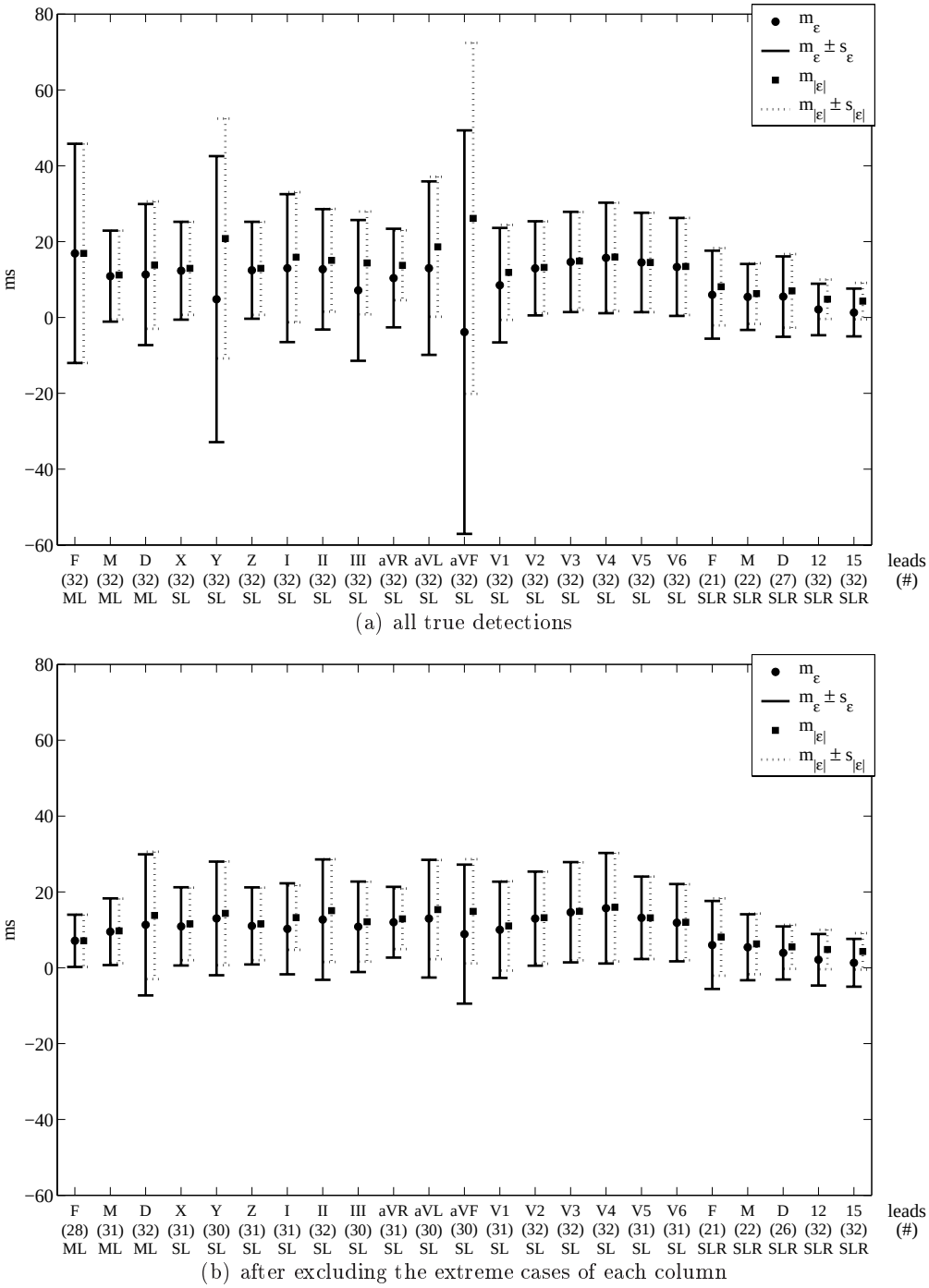

(a) all true detections

(b) after excluding the extreme cases of each column

Figure 3.14: QRS onset delineation results in CSEDB. Comparison between 3D multilead delineation (ML) over lead subsets F, M and D, single-lead delineation (SL) over each of the 15 available leads and single-lead delineation plus decision rules (SLR) over the 3 leads in each VCG system, the standard 12 leads or all 15 leads. The error ε is taken as the automatically detected location minus the *referee mark* and m_ε and s_ε ($m_{|\varepsilon|}$ and $s_{|\varepsilon|}$) stand for the mean and standard deviation of ε across files ($|\varepsilon|$); in (a) # denotes the number of true detections out of 32 reference marks provided, in (b) # denotes the number of true detections after excluding extreme cases in each approach.

Table 3.1: QRS onset delineation results in CSEDB. Comparison between 3D multilead (ML) and systems based in single-lead with selection rules (SLR); not reported (NR), number of true detections (#), errors in ms.

(a) ML and SLR considering all true detections files

method	ML			SLR				
lead set	F	M	D	F	M	D	12	12 + F
(#/32)	(32)	(32)	(32)	(21)	(22)	(27)	(32)	(32)
$m_\varepsilon \pm s_\varepsilon$	16.9 ± 28.9	10.9 ± 12.0	11.3 ± 18.6	6.0 ± 11.6	5.4 ± 8.7	5.5 ± 10.6	2.1 ± 6.8	1.3 ± 6.3
$m_{\lvert\varepsilon\rvert} \pm s_{\lvert\varepsilon\rvert}$	16.9 ± 28.9	11.2 ± 11.7	13.8 ± 16.8	8.1 ± 10.2	6.3 ± 8.0	7.0 ± 9.7	4.8 ± 5.2	4.3 ± 4.8

(b) ML and SLR after excluding extreme cases in each approach

method	ML			SLR				
lead set	F	M	D	F	M	D	12	12 + F
(#)	(28)	(31)	(32)	(21)	(22)	(26)	(32)	(32)
$m_\varepsilon \pm s_\varepsilon$	7.1 ± 6.9	9.5 ± 8.8	11.3 ± 18.6	6.0 ± 11.6	5.4 ± 8.7	3.9 ± 7.0	2.1 ± 6.8	1.3 ± 6.3
$m_{\lvert\varepsilon\rvert} \pm s_{\lvert\varepsilon\rvert}$	7.1 ± 6.9	9.7 ± 8.5	13.8 ± 16.8	8.1 ± 10.2	6.3 ± 8.0	5.5 ± 5.8	4.8 ± 5.2	4.3 ± 4.8

(c) ML and SLR over 12 or 15 leads after excluding extreme cases in any approach

method	ML			SLR	
lead set	F	M	D	12	12 + F
(#)	(28)	(28)	(28)	(28)	(28)
$m_\varepsilon \pm s_\varepsilon$	7.1 ± 6.9	7.8 ± 7.4	6.8 ± 13.5	0.4 ± 4.8	-0.2 ± 4.5
$m_{\lvert\varepsilon\rvert} \pm s_{\lvert\varepsilon\rvert}$	7.1 ± 6.9	8.1 ± 7.1	9.6 ± 11.6	3.6 ± 3.1	3.2 ± 3.1

(d) ML and SLR after excluding extreme cases in any approach

method	ML			SLR				
lead set	F	M	D	F	M	D	12	12 + F
(#)	(14)	(14)	(14)	(14)	(14)	(14)	(14)	(14)
$m_\varepsilon \pm s_\varepsilon$	8.9 ± 7.0	7.0 ± 5.2	6.9 ± 6.1	6.6 ± 13.1	2.3 ± 4.0	1.7 ± 4.1	-0.4 ± 5.0	-0.4 ± 5.0
$m_{\lvert\varepsilon\rvert} \pm s_{\lvert\varepsilon\rvert}$	8.9 ± 7.0	7.3 ± 4.8	7.1 ± 5.7	9.7 ± 10.8	3.7 ± 2.6	3.7 ± 2.3	3.6 ± 3.3	3.6 ± 3.3

(e) Other single-lead based with selection rules published approaches

	Laguna *et al.* (1994)	de Chazal and Celler (1996)	Sahambi *et al.* (1997)
(#/32)	(30)	(32)	(NR)
$m_\varepsilon \pm s_\varepsilon$	-2.1 ± 7.4	0.9 ± 3.6	$NR \pm 2.0$
$m_{\lvert\varepsilon\rvert} \pm s_{\lvert\varepsilon\rvert}$	$NR \pm NR$	$NR \pm NR$	$NR \pm NR$

For a better comparison of ML over the several VCG systems, the mean and standard deviation of the differences between the marks provided by each approach and its absolute value were also calculated, as summarized in Table 3.2 and:

- the mean differences are much lower than the bias reported in Table 3.1, but present high dispersion;
- more than an half of the dispersion reported is caused by only 6 extreme cases.

After the exclusion of these 6 extreme cases (Table 3.2(b))

- the mean differences are less than 1 ms;
- the differences dispersion is similar to the dispersion error.

Table 3.2: QRS onset delineation results in CSEDB. Comparison between 3D multilead using each VCG system; number of true detections (#), errors in ms.

(a) all available files

comparison	M vs F	D vs F	D vs M
(#)	(40)	(40)	(40)
$m_\varepsilon \pm s_\varepsilon$	-3.0 ± 24.3	-4.0 ± 23.9	-1.0 ± 15.7
$m_{\lvert\varepsilon\rvert} \pm s_{\lvert\varepsilon\rvert}$	11.7 ± 21.4	11.6 ± 21.2	7.9 ± 13.5

(b) after excluding extreme cases in all comparisons

comparison	M vs F	D vs F	D vs M
(#)	(34)	(34)	(34)
$m_\varepsilon \pm s_\varepsilon$	0.8 ± 8.6	0.2 ± 8.7	-0.6 ± 7.0
$m_{\lvert\varepsilon\rvert} \pm s_{\lvert\varepsilon\rvert}$	5.4 ± 6.7	5.2 ± 6.9	3.9 ± 5.8

PTBDB results

The results over PTBDB are presented in Figure 3.15 and Tables 3.3 and 3.4, making the same comparisons as for CSEDB.

The maximum Se (100%) is achieved by the SLR over 12 or 15 leads and ML in any VCG system, while SLR over 3 leads present a poor detection performance.

Since the reference marks are based in lead II, it was expected a better performance of the SL system over lead II, compared with SL over other leads. Surprisingly this is not the case, at least when considering all true detections (Figure 3.15(a)). As a matter of fact the automatic methodologies are prepared to deal with any hypothetical lead (even derived leads in ML) and are not optimized for a particular standard lead, as lead II. It can be the case that the thresholds are less fitted for this lead, producing a larger error.

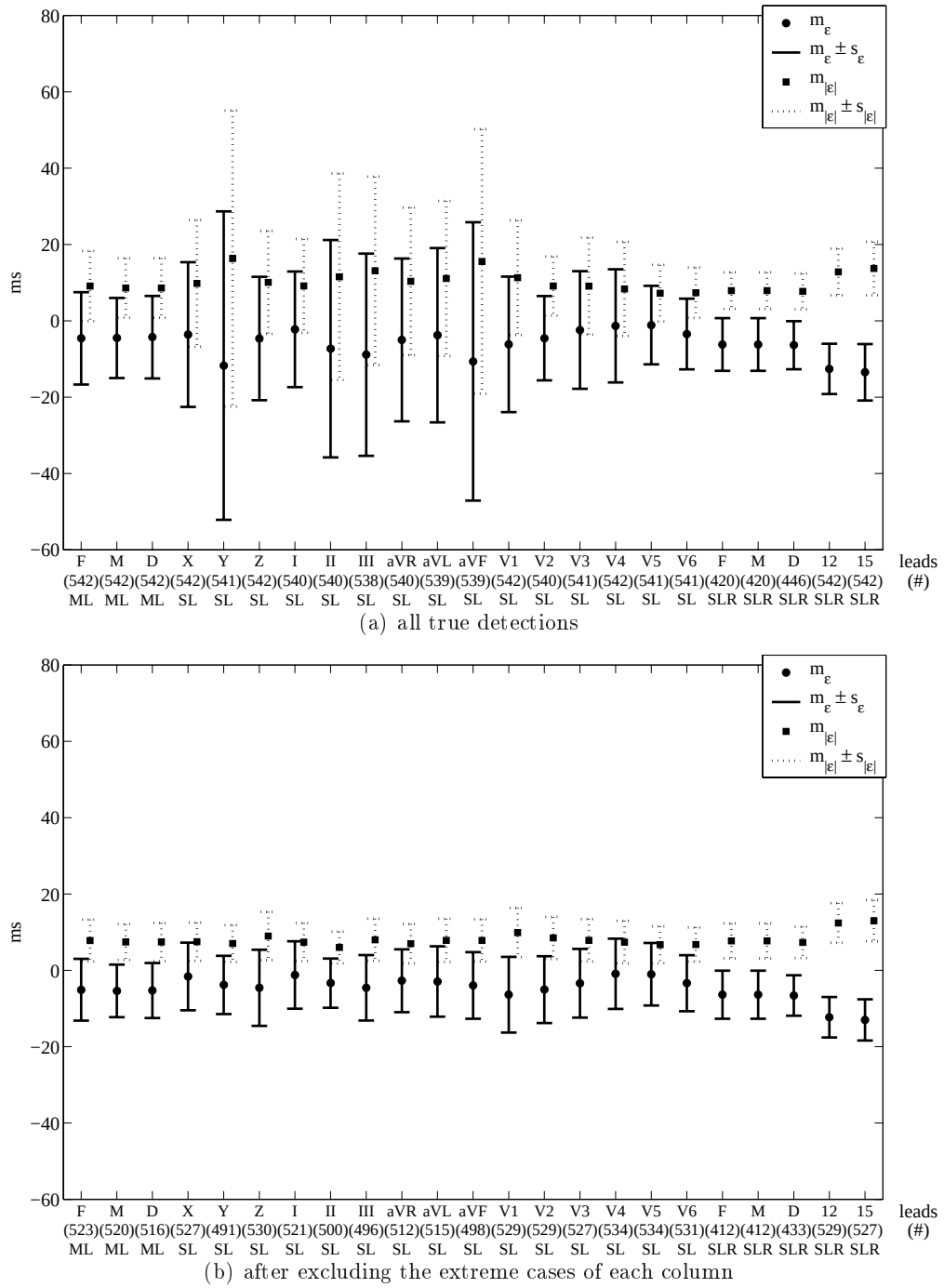

Figure 3.15: QRS onset delineation results in PTBDB. Comparison between 3D multilead delineation (ML) over lead subsets *F*, *M* and *D*, single-lead delineation (SL) over each of the 15 available leads and single-lead delineation plus decision rules (SLR) over the 3 leads in each VCG system, the standard 12 leads or all 15 leads. The error ε is taken as the automatically detected location minus the *referee mark* and m_ε and s_ε ($m_{|\varepsilon|}$ and $s_{|\varepsilon|}$) stand for the mean and standard deviation of ε across files ($|\varepsilon|$); in (a) # denotes the number of true detections out of 542 reference marks provided, in (b) # denotes the number of true detections after excluding extreme cases in each approach.

Table 3.3: QRS onset delineation results in PTBDB. Comparison between 3D multilead (ML) and single-lead with delineation rules (SLR); number of true detections (#), errors in ms.

(a) ML and SLR considering all true detections

method	ML		SLR				
lead set	F	M	D	F	M	D	12	$12+F$
(#/542)	(542)	(542)	(542)	(420)	(420)	(446)	(542)	(542)
Se (%)	100	100	100	77.5	77.5	77.5	100	100
$m_\varepsilon \pm s_\varepsilon$	-4.6 ± 12.2	-4.5 ± 10.7	-4.3 ± 10.8	-6.2 ± 6.9	-6.2 ± 6.9	-6.4 ± 6.3	-12.6 ± 6.6	-13.5 ± 7.4
$m_{\lvert\varepsilon\rvert} \pm s_{\lvert\varepsilon\rvert}$	9.1 ± 9.2	8.6 ± 7.8	8.6 ± 7.8	7.9 ± 4.8	7.9 ± 4.8	7.7 ± 4.7	12.8 ± 6.1	13.7 ± 7.0

(b) ML and SLR after excluding extreme cases in each approach

method	ML			SLR				
lead set	F	M	D	F	M	D	12	$12+F$
(#)	(523)	(520)	(516)	(412)	(412)	(433)	(529)	(527)
$m_\varepsilon \pm s_\varepsilon$	-5.0 ± 8.1	-5.4 ± 6.9	-5.3 ± 7.2	-6.4 ± 6.3	-6.4 ± 6.3	-6.6 ± 5.3	-12.3 ± 5.3	-13.0 ± 5.4
$m_{\lvert\varepsilon\rvert} \pm s_{\lvert\varepsilon\rvert}$	7.8 ± 5.5	7.4 ± 4.7	7.4 ± 5.0	7.7 ± 4.6	7.7 ± 4.6	7.3 ± 4.1	12.3 ± 5.2	13.0 ± 5.4

(c) ML and SLR over 12 or 15 leads after excluding extreme cases in any approach

method	ML			SLR	
lead set	F	M	D	12	$12+F$
(#)	(484)	(484)	(484)	(484)	(484)
$m_\varepsilon \pm s_\varepsilon$	-4.8 ± 7.8	-5.3 ± 6.7	-5.3 ± 7.0	-12.2 ± 5.2	-13.0 ± 5.4
$m_{\lvert\varepsilon\rvert} \pm s_{\lvert\varepsilon\rvert}$	7.6 ± 5.1	7.2 ± 4.6	7.3 ± 4.8	12.3 ± 5.1	13.0 ± 5.3

(d) ML and SLR after excluding extreme cases in any approach

method	ML			SLR				
lead set	F	M	D	F	M	D	12	$12+F$
(#)	(326)	(326)	(326)	(326)	(326)	(326)	(326)	(326)
$m_\varepsilon \pm s_\varepsilon$	-4.7 ± 7.2	-5.2 ± 6.2	-5.2 ± 6.4	-6.5 ± 5.8	-6.5 ± 5.8	-6.8 ± 5.1	-11.6 ± 4.7	-12.1 ± 4.9
$m_{\lvert\varepsilon\rvert} \pm s_{\lvert\varepsilon\rvert}$	7.2 ± 4.6	6.9 ± 4.1	7.0 ± 4.3	7.7 ± 4.1	7.7 ± 4.1	7.5 ± 4.1	11.7 ± 4.6	12.1 ± 4.9

From the results on PTBDB considering all true detections, it should be remarked that:

- the values found for m_ε in this database were all negative (automatic marks are earlier than reference marks);
- SLR approaches presented higher bias but lower dispersion than in CSEDB;
- ML produced values for the errors' dispersion lower than in CSEDB;
- ML errors dispersion in any VCG system is similar to the best SL, but with higher bias;
- SLR errors' dispersion in any lead set is lower than in any SL result, but with higher bias, in particular when considering 12 or 15 leads;
- a relative low number of files (around 4%) were responsable for a high percentage (more than 30%) of ML error standard deviation, but with lower impact in bias than for CSEDB;

The above mentioned remarks are still true after extreme cases exclusion. Furthermore, the exclusion of extreme cases allowed a relevant reduction on the bias dispersion in all approaches, with a slightly increase of the bias in some approaches.

Both considering all true detections (Table 3.3(b)) and after excluding the same files in all approaches (Table 3.3(d)

- SLR over 12 or 15 leads presented higher bias and but lower dispersion than the other approaches;
- ML and SLR based over the VCG systems have close performance with a maximum difference (worse to best) around 2 ms both in bias and dispersion;
- the loose criterion according to the error tolerances given by The CSE Working Party (1985) is nearly fulfilled by all SLR approaches except over 15 leads, and by ML over M and D after exclusion of extreme cases in any lead set.

As reference annotations in PTBDB are based on lead II the negative bias found is in accordance to the comment in Christov *et al.* (2006) referring that the marks based in lead II were found to be *"later than it would be if a group-QRS onset had to be considered"*. It should also be stressed out that the post-processing decision rules (Section 3.4.5) for wave onset try to find the first visible signs of the phenomena and thus they privilege the earlier locations. As the reference marks are single-lead based, these results can also indicate that delineation methods based in more than one lead are providing a different (earlier) location than SL.

Table 3.4: QRS onset delineation results in PTBDB. Comparison between 3D multilead using each VCG system; number of true detections (#), errors in ms.

(a) all available files

comparison	M vs F	D vs F	D vs M
(#/542)	(542)	(542)	(542)
$m_\varepsilon \pm s_\varepsilon$	0.0 ± 14.2	0.2 ± 13.8	0.2 ± 10.6
$m_{\lvert\varepsilon\rvert} \pm s_{\lvert\varepsilon\rvert}$	7.7 ± 11.9	7.1 ± 11.9	4.6 ± 9.5

(b) after excluding extreme cases in all comparisons

comparison	M vs F	D vs F	D vs M
(#)	(410)	(410)	(410)
$m_\varepsilon \pm s_\varepsilon$	-0.7 ± 5.7	-0.6 ± 5.6	-0.1 ± 1.5
$m_{\lvert\varepsilon\rvert} \pm s_{\lvert\varepsilon\rvert}$	3.8 ± 4.3	3.6 ± 4.3	1.0 ± 1.0

With respect to the comparison between the ML over the three VCG systems (Table 3.4):

- the mean differences are lower than 1 ms, much lower than the methods' bias (Table 3.3);
- excluding extreme cases allowed a reduction in the differences dispersion;
- the differences dispersion between ML over D and over M is less than 2 ms while over F and the other VCG systems is similar to the errors dispersion.

QTDB results

In Table 3.5(a) are presented the results for QRS onset delineation over the QTDB subgroups *QTDB1*, *QTDB2* and *QTDB3*, with respect to the first cardiologist (ref1). The results obtained after exclusion of the extreme files are presented in Table 3.5(b).

The *Se* values were found to be very high, with no relevant differences between approaches for subgroups *QTDB1* and *QTDB2*. For subgroup *QTDB3* ML presents lower *Se* than SL. However, it should be recalled that for *QTDB3* the leads processed by SL and ML are not the same, as an orthogonalization operation was performed.

The delineation errors with respect to the subset of annotations performed by the second cardiologist (ref2) are presented in Table 3.6. No ref2 annotations were available for files in subgroup *QTDB2*. The errors with respect to the first cardiologist (ref1) in these same 11 files and the intercardiologist differences (evaluating ref1 versus reference marks ref2) are also given. The differences between ML and any of the referees were found to be mainly higher than the intercardiologist differences.

Therefore, according to the results obtained there is not any advantage in using the multilead 2-dimensional approach for QRS onset delineation compared to the decision rule with $k = 1$ in any of the subgroups of files. This can partially be explained by the fact that the QRS waves are peaky rather than smooth, making the onset and end easier to locate in any lead, thus reducing the possibility of improvement by searching a lead presenting a steeper slope. On the other hand, Q and S waves have small duration what can difficults the search of the the main direction of EHV in the former (latter) part of the first (last) complex wave. Therefore, it is not surprising that two orthogonal leads do not provide enough spatial information to create an advantage compared to SLR.

Table 3.5: QRS onset delineation results in QTDB. Comparison between 3D multilead and single-lead in each subgroup of files. Last line (all files) corresponds to the reunion of the three subgroups.

(a) all true detections

		ML	SL		SLR	best
			lead I	lead II		mark
QTDB1	#files (#beats/312)	7 (312)	7 (312)	7 (312)	7 (312)	7 (312)
	$Se(\%)$	100	100	100	100	100
	$m_\varepsilon \pm \bar{s}_\varepsilon$ (ms)	7.1±12.3	4.7±10.8	12.3±11.5	6.4±10.7	5.3±6.7
	$m_{\lvert\varepsilon\rvert} \pm s_{\lvert\varepsilon\rvert}$ (ms)	10.9±10.2	10.5±8.6	14.4±9.9	10.6±8.4	8.0±7.1
QTDB2	#files (#beats/1908)	57 (1906)	57 (1907)	57 (1906)	57(1906)	57(1907)
	$Se(\%)$	99.9	99.9	99.9	99.9	99.9
	$m_\varepsilon \pm \bar{s}_\varepsilon (ms)$	6.0±12.1	5.5±10.5	6.7±11.2	4.2±9.6	4.5±7.8
	$m_{\lvert\varepsilon\rvert} \pm s_{\lvert\varepsilon\rvert}$ (ms)	12.7±9.7	13.0±8.1	13.2±8.5	10.2±7.2	7.4±6.1
QTDB3	#files (#beats/1192)	34 (1165)	34 (1179)	34 (1188)	34 (1175)	34 (1192)
	$Se(\%)$	97.7	98.9	99.7	98.6	100
	$m_\varepsilon \pm \bar{s}_\varepsilon$ (ms)	11.1±12.2	7.3±10.7	4.4±14.6	3.8±11.3	4.8±7.8
	$m_{\lvert\varepsilon\rvert} \pm s_{\lvert\varepsilon\rvert}$ (ms)	14.5±10.1	13.0±8.7	14.8±11.9	11.6±9.3	7.6±6.2
all	#files (#beats/3412)	98 (3383)	98 (3398)	98 (3436)	98 (3393)	98 (3411)
	$Se(\%)$	99.2	99.6	99.8	99.4	100
	$m_\varepsilon \pm \bar{s}_\varepsilon$ (ms)	7.8±12.2	6.6±10.6	6.2±12.4	4.2±10.3	4.6±7.9
	$m_{\lvert\varepsilon\rvert} \pm s_{\lvert\varepsilon\rvert}$ (ms)	13.2±9.9	11.8±8.3	13.9±9.8	10.7±8.0	7.5±6.2

(b) after exclusion of extreme cases

		ML	SL		SLR	best
			lead I	lead II		mark
QTDB1	#files	7	7	7	7	7
	(#beats/total beats)	(312/312)	(312/312)	(312/312)	(312/312)	(312/312)
	$m_\varepsilon \pm \bar{s}_\varepsilon$ (ms)	7.1±12.3	4.7±10.8	12.3±11.5	6.6±11.0	5.3±6.7
	$m_{\lvert\varepsilon\rvert} \pm s_{\lvert\varepsilon\rvert}$ (ms)	10.9±10.2	10.5±8.6	14.4±9.9	11.0±8.4	8.0±7.1
QTDB2	#files	55	57	56	56	56
	(#beats/total beats)	(1846/1848)	(1907/1908)	(1876/1878)	(1876/1878)	(1877/1878)
	$m_\varepsilon \pm \bar{s}_\varepsilon (ms)$	7.3±11.4	5.5±10.5	7.5±11.0	4.7±9.5	4.2±7.6
	$m_{\lvert\varepsilon\rvert} \pm s_{\lvert\varepsilon\rvert}$ (ms)	12.0±9.0	11.0±8.1	13.0±8.3	10.0±7.2	7.1±6.0
QTDB3	#files	33	33	33	33	33
	(#beats/total beats)	(1135/1162)	(1156/1143)	(1158/1162)	(1145/1162)	(1142/1142)
	$m_\varepsilon \pm \bar{s}_\varepsilon$ (ms)	10.2±12.2	8.3±11.0	6.3±12.0	4.8±10.0	4.2±7.2
	$m_{\lvert\varepsilon\rvert} \pm s_{\lvert\varepsilon\rvert}$ (ms)	13.8±10.0	13.0±8.7	13.0±9.6	11.0±8.2	7.1±5.6
all	#files	95	97	96	96	96
	(#beats/total beats)	(3293/3322)	(3362/3376)	(3346/3352)	(3333/3352)	(3331/3332)
	$m_\varepsilon \pm \bar{s}_\varepsilon$ (ms)	8.3±11.7	6.4±11.0	7.4±11.0	4.9±9.8	4.3±7.5
	$m_{\lvert\varepsilon\rvert} \pm s_{\lvert\varepsilon\rvert}$ (ms)	12.5±9.5	12.0±8.3	13.0±8.8	10.0±7.6	7.2±5.9

Table 3.6: QRS onset delineation results in QTDB. Comparison between multilead and both referees. Last line (all files) corresponds to the reunion of the subgroups.

comparison		multilead vs ref1	multilead vs ref2	ref1 vs ref2
QTDB1	#files (#beats)	3 (145)	3 (63)	3 (63)
	$m_\varepsilon \pm \bar{s}_\varepsilon$ (ms)	10.6±14.6	4.5±10.9	-8.4±10.6
	$m_{\lvert\varepsilon\rvert} \pm s_{\lvert\varepsilon\rvert}$ (ms)	14.2±11.9	8.9±7.3	14.0±8.2
QTDB3	#files (#beats)	8 (342)	8 (341)	8 (341)
	$m_\varepsilon \pm \bar{s}_\varepsilon$ (ms)	13.7±18.2	9.5±18.4	-4.2±11.3
	$m_{\lvert\varepsilon\rvert} \pm s_{\lvert\varepsilon\rvert}$ (ms)	16.8±15.8	17.5±14.2	10.8±7.8
all files	#files (#beats)	11 (487)	11(404)	11(404)
	$m_\varepsilon \pm \bar{s}_\varepsilon$ (ms)	12.9±17.3	8.2±16.4	-5.4±11.1
	$m_{\lvert\varepsilon\rvert} \pm s_{\lvert\varepsilon\rvert}$ (ms)	16.1±14.8	15.2±12.4	11.7±7.9

3.6.4 T end

Regarding the evaluation of the T wave end delineation, the number of iterations per beat required was also low and the marks were found at **Step1** or **Step2** of the algorithm for

- 92% in CSEDB and 83% in PTBDB, using lead set F ;
- 92% in CSEDB and 94% in PTBDB, using lead set M;
- 77% in CSEDB and 83% in PTBDB, using lead set D.

Moreover, the mean of iterations per beat was

- 1.6 in CSEDB and 1.7 in PTBDB using lead set F;
- 1.7 in CSEDB and 2.0 in PTBDB using lead set M;
- 2.0 in CSEDB and 1.8 in PTBDB, using lead sets D.

The mean error was found to be quite sensitive to the threshold γ^{Tend}, with best performance found by increasing the value used in single-lead delineation. In fact, SL delineation parameters need to be adequate to any possible lead, while in ML approach the boundaries are always detected in a potentially optimal signal, with a very steep slope before (after) the maximum modulus of interest, which allows a specific tunning of the thresholds.

CSEDB results

The values of m_ε and $m_{|\varepsilon|}$ and the bands $m_\varepsilon \pm s_\varepsilon$ and $m_{|\varepsilon|} \pm s_{|\varepsilon|}$ for all true detections (#) found for the T end delineation in CSEDB are plotted in Figure 3.16(a) considering ML, SL and SLR delineation

approaches (Section 3.6.2). In Figure 3.16(b) are represented the same parameters after excluding the extreme cases of each column, according to equation (3.34). The results of ML and SRL are also presented in Table 3.7, considering all beats, after exclusion of extreme cases in each one or in all approaches, together with the results of other published approaches also validated for the CSEDB.

The mean and standard deviation of the differences between the marks provided by ML over each VCG system and of its absolute error were also calculated (Table 3.8) to better compare between the approaches.

Considering all true detections found the ML results are :

- similar to the best SL performance in the 15 available leads;
- not far from the best SLR performance (over 15 leads).

The exclusion of two files reduces the value of s_ε for ML over the data set F to less than half of its initial value; one single file was causing 19% of the s_ε in D. As a matter of fact, ML delineation over the recorded Frank leads after the exclusion of the extreme files:

- presented better lower bias and errors' dispersion than ML over the other lead sets,
- attained a performance similar to the reported by Laguna *et al.* (1994), better than SL over any lead,
- presented an error dispersion lower than any other approach, including SLR over 15 leads.

In spite of the lower performance, ML over lead sets M and D attained much better results than SLR over these VCG systems, with around the double of true detections and lower s_ε (half of the s_ε value in lead set D).

Disregarding the reduced number in cases of Table 3.7(d), comparing the results over exactly the same files (excluding the same files for all the cases) these conclusions also stand, except for lower bias of ML over lead set D.

With respect to the CSE error tolerances for T end ($2s_{CSE}(T_{en}) = 30.6$ ms):

- loose criterion is fulfilled by all the strategies in Table 3.7, except by SLR over D ;
- the strict criterion is at least near accomplished by SLR over F, by Laguna *et al.* (1994), and after extreme cases exclusion, by ML over F and D, and SLR over F , 12 or 15 leads.

Comparing the marks provided by ML over each VCG system (Table 3.8), as for QRS onset location the differences are lower than the delineation errors. Again a small number of files were causing more than half of the differences dispersion and after their exclusion (Table 3.8(b)) the results in D and M are closer each other than to F results.

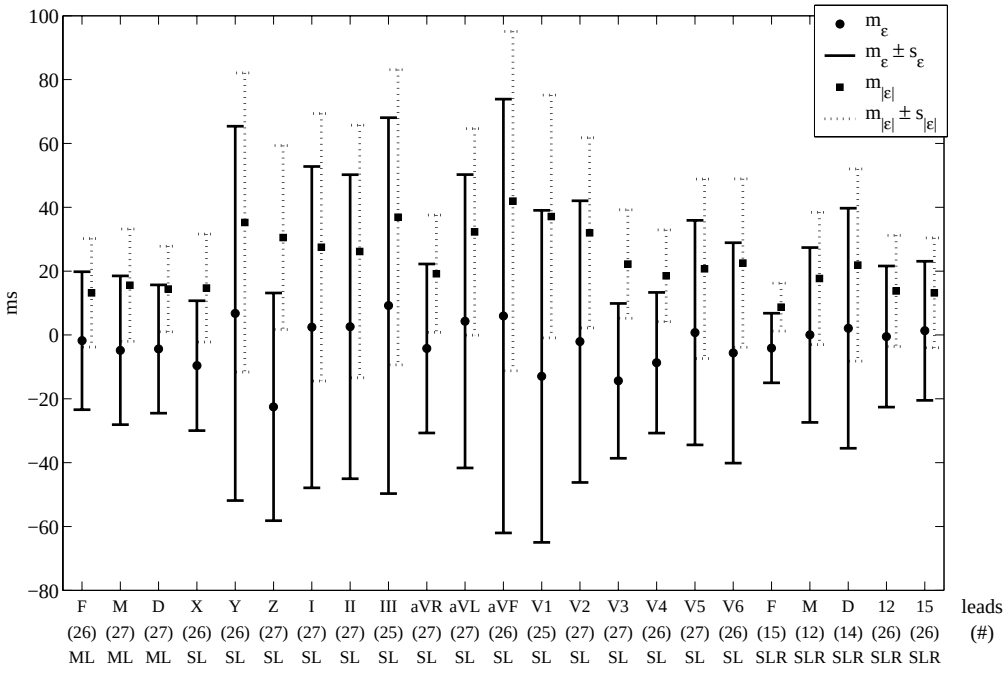

(a) all true detections

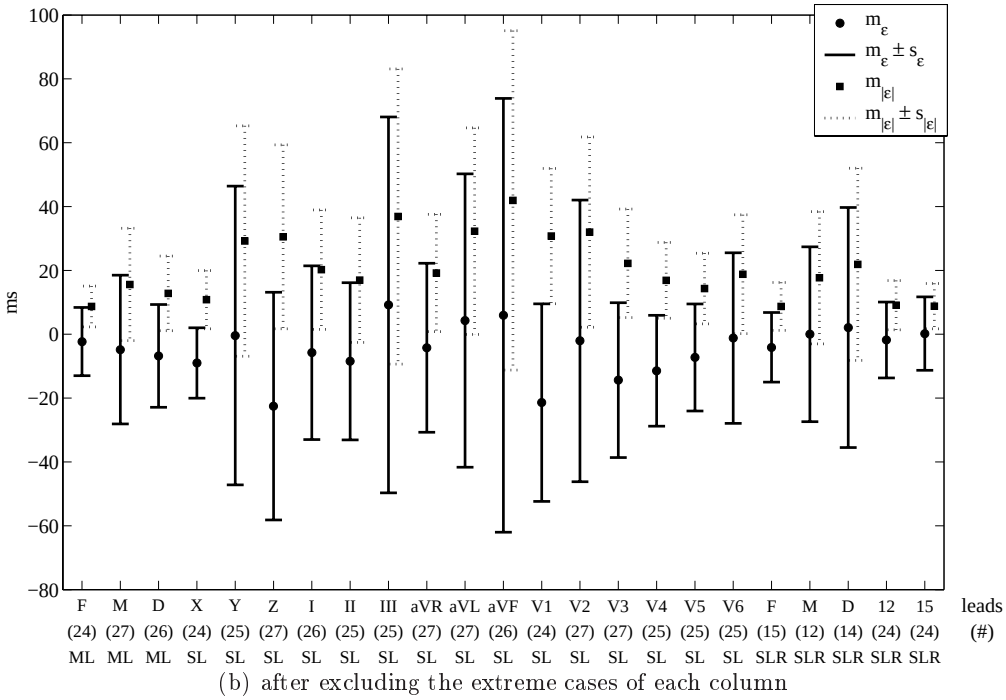

(b) after excluding the extreme cases of each column

Figure 3.16: T wave end delineation results in CSEDB. Comparison between 3D multilead delineation (ML) over lead subsets *F*, *M* and *D*, single-lead delineation (SL) over each of the 15 available leads and single-lead delineation plus decision rules (SLR) over the 3 leads in each VCG system, the standard 12 leads or all 15 leads. The error ε is taken as the automatically detected location minus the *referee mark* and m_ε and s_ε ($m_{|\varepsilon|}$ and $s_{|\varepsilon|}$) stand for the mean and standard deviation of ε across files ($|\varepsilon|$); in (a) # denotes the number of true detections out of 27 reference marks provided, in (b) # denotes the number of true detections after excluding extreme cases in each approach.

Table 3.7: T wave end delineation results in CSEDB. Comparison between 3D multilead and systems based in single-lead with selection rules (SLR); not reported (NR), number of true detections (#), errors in ms.

(a) ML and SLR considering all true detections

method	ML			SLR				
lead set	F	M	D	F	M	D	12	$12+F$
(#/27)	(26)	(27)	(27)	(15)	(12)	(14)	(26)	(26)
$m_\varepsilon \pm s_\varepsilon$	-1.8 ± 21.6	-4.8 ± 23.3	-4.4 ± 20.1	-4.1 ± 10.9	0 ± 27.4	2.1 ± 37.6	1.3 ± 21.8	-0.5 ± 22.1
$m_{\lvert\varepsilon\rvert} \pm s_{\lvert\varepsilon\rvert}$	13.2 ± 17.1	15.6 ± 17.6	14.4 ± 14.4	8.7 ± 7.5	17.7 ± 20.2	21.9 ± 30.1	13.2 ± 17.2	13.4 ± 17.4

(b) ML and SLR after excluding extreme cases in each lead set

method	ML			SLR				
lead set	F	M	D	F	M	D	12	$12+F$
(#)	(24)	(27)	(26)	(15)	(12)	(14)	(24)	(24)
$m_\varepsilon \pm s_\varepsilon$	-2.3 ± 10.7	-4.8 ± 23.3	-6.8 ± 16.1	-4.1 ± 10.9	0.0 ± 27.4	2.1 ± 37.6	-1.8 ± 11.9	0.2 ± 11.5
$m_{\lvert\varepsilon\rvert} \pm s_{\lvert\varepsilon\rvert}$	8.7 ± 6.4	15.6 ± 17.6	12.8 ± 11.7	8.7 ± 7.5	17.7 ± 20.2	21.9 ± 30.1	9.1 ± 7.7	8.8 ± 7.1

(c) ML and SLR over 12 or 15 leads after excluding extreme cases in any lead set

method	ML			SLR	
lead set	F	M	D	12	$12+F$
(#)	(23)	(23)	(23)	(23)	(23)
$m_\varepsilon \pm s_\varepsilon$	-2.1 ± 10.8	-7.7 ± 19.0	-5.2 ± 12.9	-0.9 ± 11.3	1.1 ± 10.7
$m_{\lvert\varepsilon\rvert} \pm s_{\lvert\varepsilon\rvert}$	8.7 ± 6.5	13.0 ± 15.7	10.6 ± 8.8	8.5 ± 7.3	8.3 ± 6.6

(d) ML and SLR after excluding extreme cases in any lead set

method	ML			SLR				
lead set	F	M	D	F	M	D	12	$12+F$
(#)	(8)	(8)	(8)	(8)	(8)	(8)	(8)	(8)
$m_\varepsilon \pm s_\varepsilon$	-3.3 ± 5.4	-4.0 ± 7.3	-2.8 ± 5.7	-4.8 ± 10.4	-9.3 ± 7.0	-7.3 ± 8.0	-3.5 ± 7.4	-1.8 ± 7.4
$m_{\lvert\varepsilon\rvert} \pm s_{\lvert\varepsilon\rvert}$	4.8 ± 4	7.0 ± 4.0	5.3 ± 3.0	8.8 ± 6.8	9.3 ± 7.0	8.3 ± 6.8	6.5 ± 4.5	5.8 ± 4.5

(e) Other single-lead based with selection rules published approaches

	Laguna *et al.* (1994)	Sahambi *et al.* (1997)
(#/27)	(26)	(NR)
$m_\varepsilon \pm s_\varepsilon$	2.6 ± 10.5	$NR \pm 20.0$
$m_{\lvert\varepsilon\rvert} \pm s_{\lvert\varepsilon\rvert}$	$NR \pm NR$	$NR \pm NR$

Table 3.8: T wave end delineation results in CSEDB. Comparison between 3D multilead using each VCG system; results after exclusion of extreme cases are presented in a second sub column; not reported (NR), number of true detections (#), errors in ms.

(a) all available files

comparison	M vs F	D vs F	D vs M
(#/40)	(39)	(39)	(40)
$m_\varepsilon \pm s_\varepsilon$	-2.8 ± 35.5	-3.8 ± 22.0	-1.6 ± 23.3
$m_{\lvert\varepsilon\rvert} \pm s_{\lvert\varepsilon\rvert}$	16.9 ± 31.2	11.5 ± 19.1	10.3 ± 20.9

(b) after excluding extreme cases in all comparisons

comparison	M vs F	D vs F	D vs M
(#)	(33)	(33)	(33)
$m_\varepsilon \pm s_\varepsilon$	-1.4 ± 8.8	-2.1 ± 6.4	-0.7 ± 5.5
$m_{\lvert\varepsilon\rvert} \pm s_{\lvert\varepsilon\rvert}$	6.4 ± 6.2	4.9 ± 4.5	3.8 ± 4.0

PTBDB results

The results for T end delineation on PTBDB are presented in Figure 3.17 and Tables 3.9 and 3.10, with same comparisons that in the QRS onset case.

The highest Se in T wave detection is achieved by ML over F or D , outperforming SLR over 12 or 15 leads, while SLR over 3 leads presents a poor T wave detection performance.

SL over lead II presented the lowest bias values found, in accordance to the fact that 85% of the T end locations were done regarding only this lead (Christov *et al.*, 2006).

Furthermore, considering all true detections:

- ML and SLR approaches presented higher bias in PTBDB than in CSEBD, what can result from the different latency of the leads with respect to lead II;
- m_ε in ML and SLR approaches are all positive denoting that T end location based in several leads result in later boundary mark;
- any of ML or SLR based approaches present lower dispersion than the best SL results.

As a matter of fact, both the post-processing decision rules (Section 3.4.5) and the ML strategy for the wave end try to find the latest visible signs of the phenomena and thus they privilege the latter locations.

As before, a low number of files (no more than 5%) were responsable for a considerable part (more than 30% in some cases) of the error standard deviation.

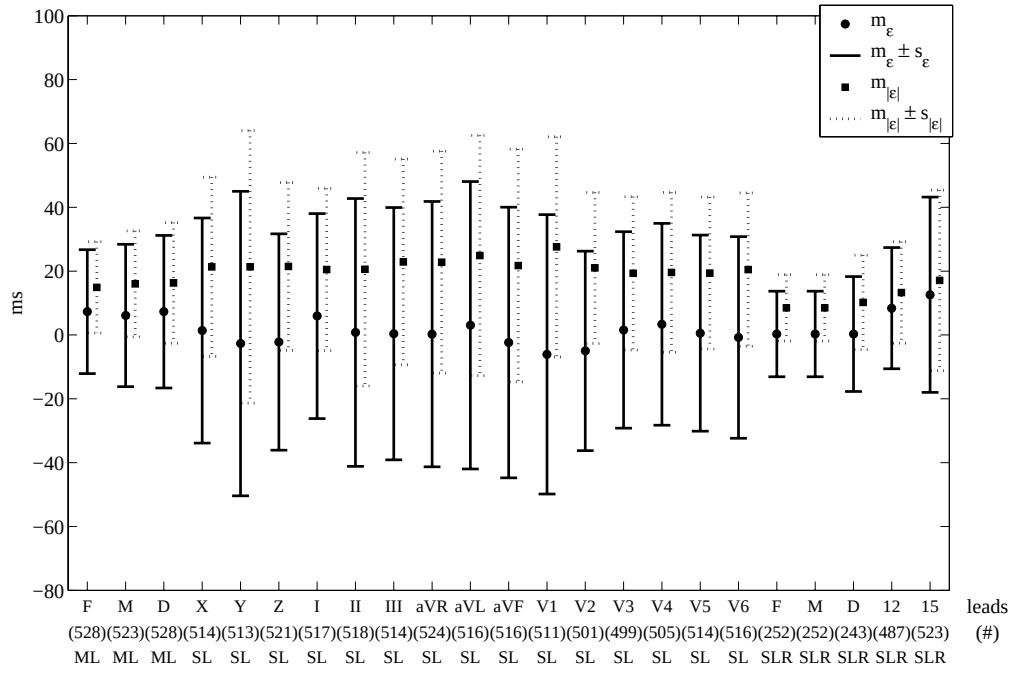

(a) all true detections

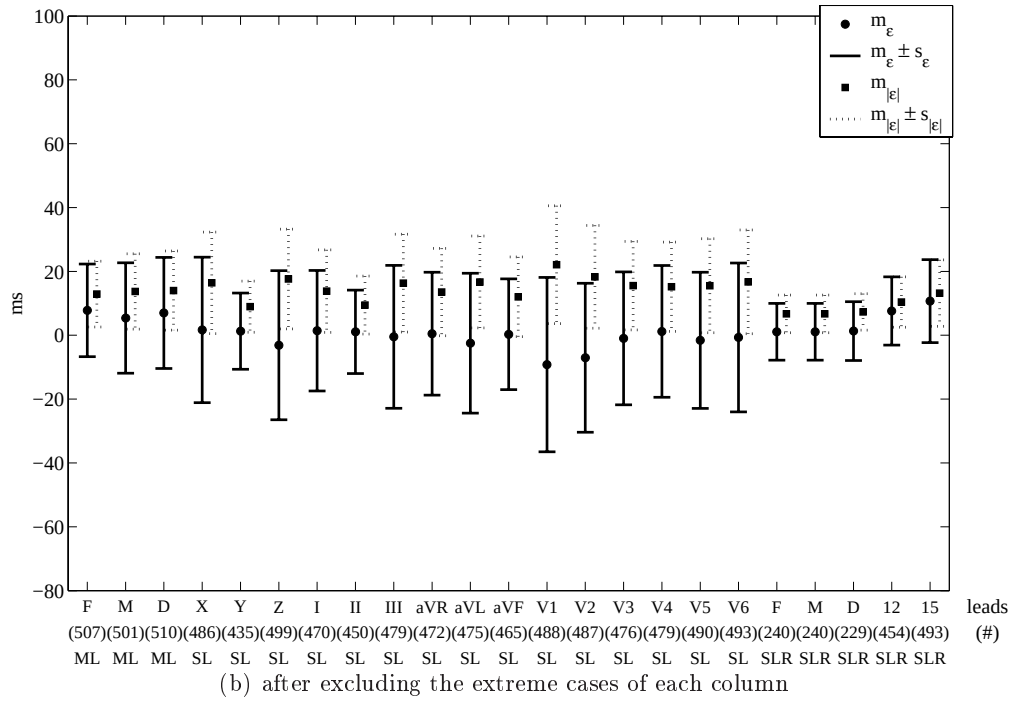

(b) after excluding the extreme cases of each column

Figure 3.17: T end delineation results in the PTBDB. Comparison between 3D multilead delineation (ML) over lead subsets F, M and D, single-lead delineation (SL) over each of the 15 available leads and single-lead delineation plus decision rules (SLR) over the 3 leads in each VCG system, the standard 12 leads or all 15 leads. The error ε is taken as the automatically detected location minus the *referee mark* and m_ε and s_ε ($m_{|\varepsilon|}$ and $s_{|\varepsilon|}$) stand for the mean and standard deviation of ε across files ($|\varepsilon|$); in (a) # denotes the number of true detections out of 542 reference marks provided, in (b) # denotes the number of true detections after excluding extreme cases in each approach.

Table 3.9: T end delineation results in the PTBDB. Comparison between 3D multilead (ML) and single-lead with delineation rules (SLR); number of true detections (#), errors in ms.

(a) ML and SLR considering all true detections

method	ML			SLR				
lead set	F	M	D	F	M	D	12	12 + F
(#/542)	(528)	(523)	(528)	(252)	(252)	(243)	(487)	(523)
Se (%)	97.4	96.5	97.4	46.6	46.6	44.9	90.0	96.7
$m_\varepsilon \pm s_\varepsilon$	7.3 ± 19.3	6.0 ± 22.3	7.3 ± 23.9	0.3 ± 13.4	0.3 ± 13.4	0.3 ± 18.0	8.4 ± 18.9	12.6 ± 30.5
$m_{\lvert\varepsilon\rvert} \pm s_{\lvert\varepsilon\rvert}$	14.9 ± 14.3	16 ± 16.6	16.3 ± 18.9	8.5 ± 10.4	8.5 ± 10.4	10.2 ± 14.8	13.3 ± 15.9	17.1 ± 28.3

(b) ML and SLR after excluding extreme cases in each lead set

method	ML			SLR				
lead set	F	M	D	F	M	D	12	12 + F
(#)	(507)	(501)	(510)	(240)	(240)	(229)	(454)	(493)
$m_\varepsilon \pm s_\varepsilon$	7.8 ± 14.5	5.3 ± 17.3	7.0 ± 17.4	1.0 ± 8.9	1.0 ± 8.9	1.3 ± 9.2	7.6 ± 10.7	10.7 ± 13.0
$m_{\lvert\varepsilon\rvert} \pm s_{\lvert\varepsilon\rvert}$	12.9 ± 10.3	13.7 ± 11.8	14 ± 12.5	6.7 ± 5.9	6.7 ± 5.9	7.3 ± 5.7	10.4 ± 7.9	13.2 ± 10.4

(c) ML and SLR over 12 or 15 leads after excluding extreme cases in any lead set

method	ML			SLR	
lead set	F	M	D	12	12 + F
(#)	(419)	(419)	(419)	(419)	(419)
$m_\varepsilon \pm s_\varepsilon$	7.9 ± 12.2	6.3 ± 14.0	6.9 ± 13.6	7.6 ± 10.3	10.2 ± 11.1
$m_{\lvert\varepsilon\rvert} \pm s_{\lvert\varepsilon\rvert}$	11.5 ± 8.9	11.7 ± 10.0	11.5 ± 9.9	10.2 ± 7.8	12.1 ± 9.0

(d) ML and SLR after excluding extreme cases in any lead set

method	ML			SLR				
lead set	F	M	D	F	M	D	12	12 + F
(#)	(147)	(147)	(147)	(147)	(147)	(147)	(147)	(147)
$m_\varepsilon \pm s_\varepsilon$	8.2 ± 8.4	7.2 ± 10.0	7.7 ± 9.0	1.4 ± 7.1	1.4 ± 7.1	1.5 ± 8.1	6.5 ± 7.6	8.1 ± 7.7
$m_{\lvert\varepsilon\rvert} \pm s_{\lvert\varepsilon\rvert}$	9.7 ± 6.7	9.1 ± 8.3	9.0 ± 7.6	6.4 ± 5.1	7.9 ± 6.2	9.2 ± 6.5	5.5 ± 4.7	5.5 ± 4.7

Table 3.10: T end delineation results in PTBDB. Comparison between 3D multilead using each VCG system; number of true detections (#), errors in ms.

(a) all available files

comparison	M vs F	D vs F	D vs M
(#)	(516)	(520)	(518)
$m_\varepsilon \pm s_\varepsilon$	-1.0 ± 22.1	0.1 ± 21.0	-1.0 ± 17.3
$m_{\lvert\varepsilon\rvert} \pm s_{\lvert\varepsilon\rvert}$	11.4 ± 19.0	10.2 ± 18.3	6.8 ± 16.0

(b) after excluding extreme cases in all comparisons

comparison	M vs F	D vs F	D vs M
(#)	(410)	(410)	(410)
$m_\varepsilon \pm s_\varepsilon$	-1.4 ± 6.9	-1.7 ± 6.2	0.3 ± 3.1
$m_{\lvert\varepsilon\rvert} \pm s_{\lvert\varepsilon\rvert}$	5.2 ± 4.7	4.6 ± 4.5	2.3 ± 2.1

Nevertheless, after excluding the extreme cases:

- both ML and SLR approaches performed worse than best SL results, but with much more files evaluated for ML and SLR over 12 or 15 leads (Figure 3.17(b));
- considering exactly the same files ML presented results close to SLR over 12 or 15 leads (Tables 3.9(c));
- considering exactly the same files in all approaches similar results were attained in all, except for a lower bias for SLR over 3 leads.

The loose criterion according to the error tolerances given by The CSE Working Party (1985) was fulfilled by all ML and SLR approaches and the strict criteria was fulfilled by SLR over F or M and after extreme cases exclusion by all SLR cases and ML over F .

With respect to the comparison between the ML over the three VCG systems (Table 3.10) it should be noted:

- the mean differences are much lower than the bias of the methods (Table 3.9);
- the exclusion of the extreme cases reduced the differences dispersion;
- after excluding extreme cases, the dispersion of the differences between ML over D and over M is near 3 ms, while in the other comparisons are close to 7 ms and 6 ms.

QTDB results

In Table 3.11(a) are presented the results for the T wave end delineation over the QTDB subgroups *QTDB1*, *QTDB2* and *QTDB3*, relative to the first cardiologist annotations (ref1). The results obtained after exclusion of the extreme files are presented in Table 3.11(b).

The delineation errors with respect to the subset of annotations performed by the second cardiologist (ref2) are presented in Table 3.12. It should be recalled that no ref2 annotations were available for files in subgroup *QTDB2*. The errors with respect to the first cardiologist (ref1) in these same 11 files and the intercardiologist differences (evaluating ref1 versus reference marks ref2) are given, as well as the number of T waves detected by ML (# beats) on the beats with double annotation (total beats).

The ML approach presents a higher Se value and a similar P^{+}_{min} value than SLR over the two annotation sets. Considering all true positive detections (Table 3.11(a)):

- ML attains an errors' dispersion lower or similar to the obtained for SL or SLR, considering all three subgroups, in spite of a larger bias in some comparisons;
- the global standard deviation (all files) fulfils the loose criterion in all the considered approaches;
- none of the approaches accomplishes the strict criterion, not even the *best mark* approach.

Table 3.11: T wave end delineation results in QTDB. Comparison between 3D multilead and single-lead in each subgroup of files. Last line (all files) corresponds to the reunion of the three subgroups.

(a) all true detections

		ML	SL		SLR	best
			lead I	lead II		mark
QTDB1	#files (#beats/312)	7 (309)	7 (311)	7 (312)	7 (312)	7 (312)
	$Se(\%)$ - $P^{+}_{\min}(\%)$	$99-100$	$99.7-100$	$100-100$	$99.7-100$	$100-100$
	$m_\varepsilon \pm \bar{s}_\varepsilon$ (ms)	-8.1±24.4	-18.1±28.5	3.7±37.6	-6.1±27.6	-12.2±17.8
	$m_{\lvert\varepsilon\rvert} \pm s_{\lvert\varepsilon\rvert}$ (ms)	20.2±20.9	29.4±25.4	45.4±35.6	35.1±24.8	18.2±15.0
QTDB2	#files (#beats/1827)	55 (1775)	55 (1798)	55 (1789)	55 (1768)	55(1819)
	$Se(\%)$ - $P^{+}_{\min}(\%)$	$97.2-95.7$	$98.4-95.7$	$97.9-96.1$	$96.8-96.0$	$99.6-95.8$
	$m_\varepsilon \pm \bar{s}_\varepsilon (ms)$	11.5±24.4	3.1±26.9	0.3±26.8	3.5±23.5	1.7±20.1
	$m_{\lvert\varepsilon\rvert} \pm s_{\lvert\varepsilon\rvert}$ (ms)	32.8±17.4	32.8±18.9	31.2±20.7	29.6±17.8	22.3±15.0
QTDB3	#files (#beats/1192)	34 (1159)	34 (1179)	34 (1159)	34 (1146)	34 (1192)
	$Se(\%)$ - $P^{+}_{\min}(\%)$	$97.2-100$	$98.9-100$	$97.2-100$	$96.1-100$	$100-100$
	$m_\varepsilon \pm \bar{s}_\varepsilon$ (ms)	8.8±21.6	-8.5±18.9	-7.3±29.0	-6.3±21.7	-4.0±16.3
	$m_{\lvert\varepsilon\rvert} \pm s_{\lvert\varepsilon\rvert}$ (ms)	28.3±17.4	28.7±15.2	29.3±23.3	26.5±17.2	17.9±13.1
all files	#files (#beats/3331)	96 (3243)	96 (3288)	96 (3260)	96 (3225)	96 (3323)
	$Se(\%)$ - $P^{+}_{\min}(\%)$	$97.4-97.6$	$98.7-97.6$	$97.9-97.89$	$96.8-97.8$	$99.8-97.6$
	$m_\varepsilon \pm \bar{s}_\varepsilon$ (ms)	9.1±23.4	-2.5±24.2	-2.1±28.4	-0.7±23.2	-1.3±18.6
	$m_{\lvert\varepsilon\rvert} \pm s_{\lvert\varepsilon\rvert}$ (ms)	30.3±17.6	31.1±18.0	31.6±22.7	28.9±18.1	20.4±14.3

(b) after exclusion of extreme cases

		ML	SL		SLR	best
			lead I	lead II		mark
QTDB1	#files	6	7	6	5	5
	(#beats/total beats)	(235/235)	(311/312)	(282/282)	(205/205)	(205/205)
	$m_\varepsilon \pm \bar{s}_\varepsilon$ (ms)	-0.1±13.7	18.1±28.5	-14.7±28.4	-6.1±16.3	-12.2±17.8
	$m_{\lvert\varepsilon\rvert} \pm s_{\lvert\varepsilon\rvert}$ (ms)	13.0±10.3	29.4±25.4	33.9±26.3	22.1±13.2	18.2±15.0
QTDB2	#files	48	514	51	48	48
	(#beats/total beats)	(1588/1614)	(1678/1706)	(1668/1706)	(1561/1614)	(1607/1614)
	$m_\varepsilon \pm \bar{s}_\varepsilon$ (ms)	10.0±19.3	-0.7±26.3	-0.4±25.0	2.5±20.8	3.9±15.5
	$m_{\lvert\varepsilon\rvert} \pm s_{\lvert\varepsilon\rvert}$ (ms)	20.3±14.6	24.6±18.4	21.9±18.6	18.7±14.5	18.8±11.9
QTDB3	#files	30	32	31	30	28
	(#beats/total beats)	(1048/1071)	(1118/1131)	(1083/1102)	(1039/1071)	(1011/1011)
	$m_\varepsilon \pm \bar{s}_\varepsilon (ms)$	3.1±17.9	-8.0±18.8	-8.2±23.3	-6.0±18.9	-4.0±16.3
	$m_{\lvert\varepsilon\rvert} \pm s_{\lvert\varepsilon\rvert}$ (ms)	18.1±13.3	24.1±14.9	22.3±18.0	18.9±14.4	17.9±13.1
all files	#files	84	90	88	83	81
	(#beats/total beats)	(2872/2920)	(3107/3149)	8(3033/3090)	8(2805/2890)	(2823/2830)
	$m_\varepsilon \pm \bar{s}_\varepsilon$ (ms)	6.8±18.4	4.6±23.8	-3.7±24.6	-1.1±19.8	-0.3±16.0
	$m_{\lvert\varepsilon\rvert} \pm s_{\lvert\varepsilon\rvert}$ (ms)	19.0±13.8	24.8±17.7	272.9±18.9	19.0±14.4	18.4±12.6

After the exclusion of extreme cases (between 6% and 16% of the files in each approach), as present in Table 3.11(b):

- ML in *QTDB1* and *QTDB3* files outperforms SL and SLR;
- ML is better than the *best mark* in *QTDB1* files;
- ML in *QTDB2* files errors presents a dispersion lower than SL or SLR, but with a much higher bias;
- loose criterion is fulfilled by all the approaches;
- ML accomplish the strict criterion over *QTDB1*, while the best mark nearly accomplish it in other two subgroups.

The slightly worse result of ML over *QTDB2* can be related to the possibility that no orthogonal leads are being considered. It should be recalled that in this subgroup the recorded leads are unknown, and they are treated as if they were orthogonal.

From Table 3.12 is possible to conclude that the differences between ML and any of the referees has a lower or equivalent standard deviation than the intercardiologist differences.

Table 3.12: T wave end delineation results in QTDB. Comparison between multilead and both referees. Last line (all files) corresponds to the reunion of the subgroups.

comparison		multilead vs ref1	multilead vs ref2	ref1 vs ref2
QTDB1	#files (#beats/total beats)	3 (145/145)	3 (62/62)	3 (62/62)
	$Se(\%)$ - $P^{+}_{\min}(\%)$	$100 - 100$	$100 - 98.4$	$100 - 98.4$
	$m_{\varepsilon} \pm \bar{s}_{\varepsilon}$ (ms)	-4.9±14.6	-10.2±13.9	-3.9±13.4
	$m_{\lvert\varepsilon\rvert} \pm s_{\lvert\varepsilon\rvert}$ (ms)	11.7±10.4	13.0±12.0	11.6±10.3
QTDB3	#files (#beats/total beats)	8 (340/340)	8 (338/340)	8 (340/340)
	$Se(\%)$ - $P^{+}_{\min}(\%)$	$99.4 - 100$	$99.4 - 99.7$	$100 - 99.7$
	$m_{\varepsilon} \pm \bar{s}_{\varepsilon}$ (ms)	-6.7±19.5	-8.3±25.3	-1.5±25.8
	$m_{\lvert\varepsilon\rvert} \pm s_{\lvert\varepsilon\rvert}$ (ms)	27.5±13.8	18.9±20.5	26.1±22.1
all files	#files (#beats/total beats)	11 (485/487)	11(400/402)	11(402/402)
	$Se(\%)$ - $P^{+}_{\min}(\%)$	$99.6 - 100$	$99.5 - 99.5$	$100 - 99.5$
	$m_{\varepsilon} \pm \bar{s}_{\varepsilon}$ (ms)	-6.2±18.1	-8.8±22.2	-2.1±22.4
	$m_{\lvert\varepsilon\rvert} \pm s_{\lvert\varepsilon\rvert}$ (ms)	23.2±12.9	17.3±18.2	22.0±18.9

3.7 Concluding Remarks

The WT based automatic systems for ECG delineation here proposed were evaluated with respect to the QRS onset and T wave end boundaries.

The single-lead delineator outperforms other published approaches in detecting ECG waves and locating their peaks and boundaries, namely by considering post-processing rules to deal with multiple leads (Martínez *et al.*, 2004). Furthermore, it shows a very satisfactory performance both in QRS onset and T wave end delineation, thus it can be considered an adequate tool to measure the QT interval and to study its beat-to-beat variations.

Using different leads can be crucial to determine the ECG interval true duration, as its beginning or end could be imperceptible in a particular lead. The automatic multilead approach proposed allows to deal with multiple leads, taking advantage of their availability to further improve the delineation.

Once a QRS complex is detected, both the multilead and the single-lead automatic delineation always give a location for the QRS onset. Thus, the sensitivity of the QRS onset corresponds in fact to the sensitivity of QRS complex detection, which is very high. The use of post-processing rules over a large number of leads also guaranties good sensitivity, nevertheless in case where only 3 leads are available the number of false negatives is quite high, and sensitivity value decreases.

For the T wave end, the sensitivity also corresponds to the T wave detection rates, but this is a much more complex problem and as expected lower values were found. Even so:

- in PTBDB the worse sensitivity value (96.5%) was not far from the best case in single-lead or post-processing rules over 15 leads (96.7%), ouperforming largely the other post-processing rules based delineation strategies;
- in QTDB both the sensitivity and minimum positive predictivity were higher or similar to using post-processing rules, and not far from the best mark strategy, in any subgroup.

Considering the multilead approach over the VCG system given by recorded Frank leads, both for QRS onset and T wave end, it:

- outperformed any single-lead based delineation, by comparing with reference marks made having in sight all the available leads (data from CSEDB);
- after extreme cases exclusion, allowed to perform the delineation with error dispersion similar to the ones obtained using decision rules over the 12 leads or all the 15 leads together, including other published approaches;
- after extreme cases exclusion, outperformed single-lead delineation with decision rules over 3 leads in any at lead set.

Either multilead or single-lead followed by decision rules combine information from different leads and when compared with single-lead based reference marks (PTDB) show biased values in the location of both the boundaries, than can be relevant. This bias,

- was found to be negative for QRS onset and positive for T wave end;
- was lower in SLR over 3 leads than in ML;
- had the highest value for SLR over 12 or 15 leads.

These results are in clear accordance with the strategy of using information from multiple leads in order to locate the earliest and the latest signs of ventricular activity. Also, they denote that *multilead delineation over 3 leads* achieves better this goal than *decision rules over 3 leads.*

The higher bias found by single lead with post processing rules over 12 or 15 leads does not agree with the results in CSEDB, in which strategies based in 12 or 15 leads presented lower bias than multilead methods, comparing with multilead based reference marks. Attending to this fact, the *higher bias* relative to the *single-lead based reference marks* of PTBDB can be understood as *corresponding to an effective lower bias* relative to an hypothetical *multilead based reference marks.*

With respect to the validation on the PTBDB data it should also be referred that both automatic delineation systems here described have taken part of the *"PhysioNet/Computers in Cardiology Challenge 2006: QT Interval Measurement"* competition, in which the measuring of the QT interval in a representative beat per file was evaluated. Comparisons were made considering 15 manually-reviewed entries and 28 fully automatic strategies. The single-lead delineation approach presented in this thesis achieved a global error of 19.22 ms, while the multilead strategy. considering respectively leads sets F, M and D, committed errors of 27.04 ms, 27.81 ms and 28.96 ms. It should be remarked that only 5 more out of the 28 fully automatic strategies presented global errors between 20 ms and 30 ms, and only 2 more presented errors under 20 ms (Moody *et al.*, 2006).

The multilead methods over the VCG were able to provide from only 3 ECG leads, boundaries locations as stable as the ones provided by other methods using many more leads. It should be remarked that the proposed method requires the WT calculation of 3 leads, with delineation procedures involving a variable number of signals. Thus, even considering fitting and projecting features, the multilead strategy is likely to be more efficient that applying single-lead to 12 or 15 leads, as the number of steps needed is not very high. The number of iterations for QRS onset and T end was low, with mean values lower or equal to 2.5. Thus, the results presented denote a clear performance improvement.

The approaches based in decision rules over leads set F and M performed similarly over PTBDB for both boundaries, but in CSEDB lead set M allowed the least error on QRS onset, while for T end lead set F should be preferred. Using multilead methods, lead set F was clearly better than the others in both boundaries, except for QRS onset over PTBDB in which lead set M performed slightly better.

Thus, among the VCG systems considered, *lead set* F *was the one that achieved the best global performance*. It should be recalled that the direct comparison between the delineation using each VCG system showed a *clear accordance between the three lead sets*, indicating that the stability of the measure does not depend on the VCG system used.

The results also indicated that using a 2 dimensional approach over 2 orthogonal leads (QTDB files) is not adequate for QRS onset delineation and a decision rule should be used instead. On the contrary, the multilead delineation of the T end in files with two orthogonal (or orthogonalized) leads, achieved higher performance than choosing the channel with less error for each mark. Thus a multilead approach over 2 orthogonal leads is better than any possible selection rule for T end delineation.

The VCG systems here considered were chosen because they are defined by well known leads, which are likely to be familiar to clinicians, but any other combination of 3 orthogonal leads could be used instead. One alternative is to consider the VCG defined by the first three principal components (PC). According to the preliminary evaluation done during this research did using PC did not allowed an improvement compared with the other VCG systems and this system was not considered in this thesis. Nevertheless, many aspects of that possibility remains to be studied. Namely, alternative initial lead sets (sub sets of the 12-lead systems) can be used for the PC calculation and adequate tunning of the methods can be required. The performance of single-lead based delineation over the first PC should also be evaluated.

Alternative transformations from the 12 for 3 orthogonal leads can also be considered. There are works supporting that an individual matrix transformation from 12 to 3 leads is more effective than an universal transformation matrix applied to every individual, as in Dower transformation or other proposed in the literature (de Chazal and Celler, 1994). Furthermore, it is possible to obtain VCG systems optimized for the study of a particular phenomena or wave (Guillem *et al.*, 2006). Constructing an individual matrix transformation would require extra computational effort but could reduce the differences between lead set F and the synthesized Frank leads. That study was not here considered, but should be explored in the future.

Globally, good results were obtained in the delineation of both boundaries, with methods that are quite robust against noise and morphological variations.

In particular, the low error dispersion and the ML improvement allow accurate measuring of the beat-to-beat variabilities and the improvement obtained using multilead delineation when only 3 leads are available could represent an advantage in the quantification of variability. The methodology using single-lead delineation followed by decision rules is likely to be the strategy more close to what a cardiologist does when annotating a multilead record. Nevertheless the multilead approach is potentially more stable and then more suited for variability analysis.

The stability of the measures guaranties that the measured QT intervals are appropriate to explore the relation between HRV and QTV, as described in Chapter 2 of this thesis. The joint performance of automatic delineation and QTV fractions quantification is studied in the next Chapter.

Chapter 4

QT variability and HRV interactions in ECG: Quantification and Reliability

The methodology presented and evaluated in Chapter 2 provides an adequate estimation of the QTV fraction driven by HRV. The method was evaluated over simulated *"clean"* variability series which are free of measurement errors.

In real signals noise contamination is frequent and can produce errors in the measured intervals. The use of a precise and robust delineation methodology, as the one presented in Chapter 3, is essential to reduce the errors in the location of the wave's boundaries, however it cannot eliminate them. For the measurement of reduced variability, even very low errors can result in important spurious data.

The goal of this Chapter is to quantify these effects by joint validation of the automatic delineation and parametric methodology applied to the QTV and HRV interactions.

To evaluate the methodology in a more realistic context were constructed artificial *3-lead* ECG signals matching the simulated series of the clean test data sets "*c*". Along with morphologic beat-to-beat variability, real ECG signals are also affected by extra cardiac factors, such as respiration or muscular activity, and those factors have also been considered in the simulation.

4.1 Introduction

The data sets for joint systems validation were derived by automatic delineation of artificial ECG signals at 500 Hz, constructed by concatenation of modified template beats, in way to match the previously "clean" simulated variability series (Section 2.4.1). Contamination with "*respiratory like*" and real recorded noises (baseline wandering - *bw*, electrode movement - *em* and muscular artifacts - *ma*) were considered, as well as noise extracted from a real ECG file. Automatic delineation over these artificial signals provides fiducial marks for measuring the variability series $x_{\mathrm{RR}}(n)$ and $x_{\mathrm{QT}}(n)$, defining new data sets as described in Section 4.2.

Different test data sets were obtained, corresponding to the different dependency cases, contamination approaches and the automatic delineation used (single or multilead based), as summarized in Table 4.1. These data sets were constructed for each QT reference model 1 to 6, corresponding respectively to to $\sigma_{\mathrm{QT}} = 17$, 13, 10, 8, 5 and 3 ms (QTV levels).

In Section 4.3, the error in the estimation of the power spectral density measures in each fraction is quantified as a function of the QTV level and noise contamination. The main conclusions of this analysis are summarized in Section 4.4.

Table 4.1: Simulated data sets: the clean simulated data sets were described in Section 2.4 (nc stands for not considered, $SNR \in \{30dB, 25dB, 20dB, 15dB, 10dB\}$, *bw* - baseline wandering, *em* - electrode movement, *ma* - muscular artifacts).

Dependency case	A: RR and QT fully correlated		B: RR and QT uncorrelated		C: mixture of two dependencies	
Clean simulated series	A_c		B_c		C_c	
Signal derived series	lead X	Frank leads	lead X	Frank leads	lead X	Frank leads
no noise contamination	A_s^X	A_s^F	B_s^X	B_s^F	C_s^X	C_s^F
respiratory effect	nc		nc		C_r^X	C_r^F
MIT pre-recorded noise	nc		nc		$C_{bw}^X(SNR)$ $C_{em}^X(SNR)$ $C_{ma}^X(SNR)$	nc
3-lead extracted noise	nc		nc		$C_v^X(SNR)$	$C_v^F(SNR)$

4.2 Signal derived data sets

The simulation of signal derived variability series from the original "clean" variability series is outlined in the central block of Figure 4.1. The identification of the QTV/HRV interactions model and the performance evaluation are analogous to the ones used in Chapter 2 and are summarized in the lowest and right blocks of the diagram. The several ECG simulation approaches considered are detailed in the following sections.

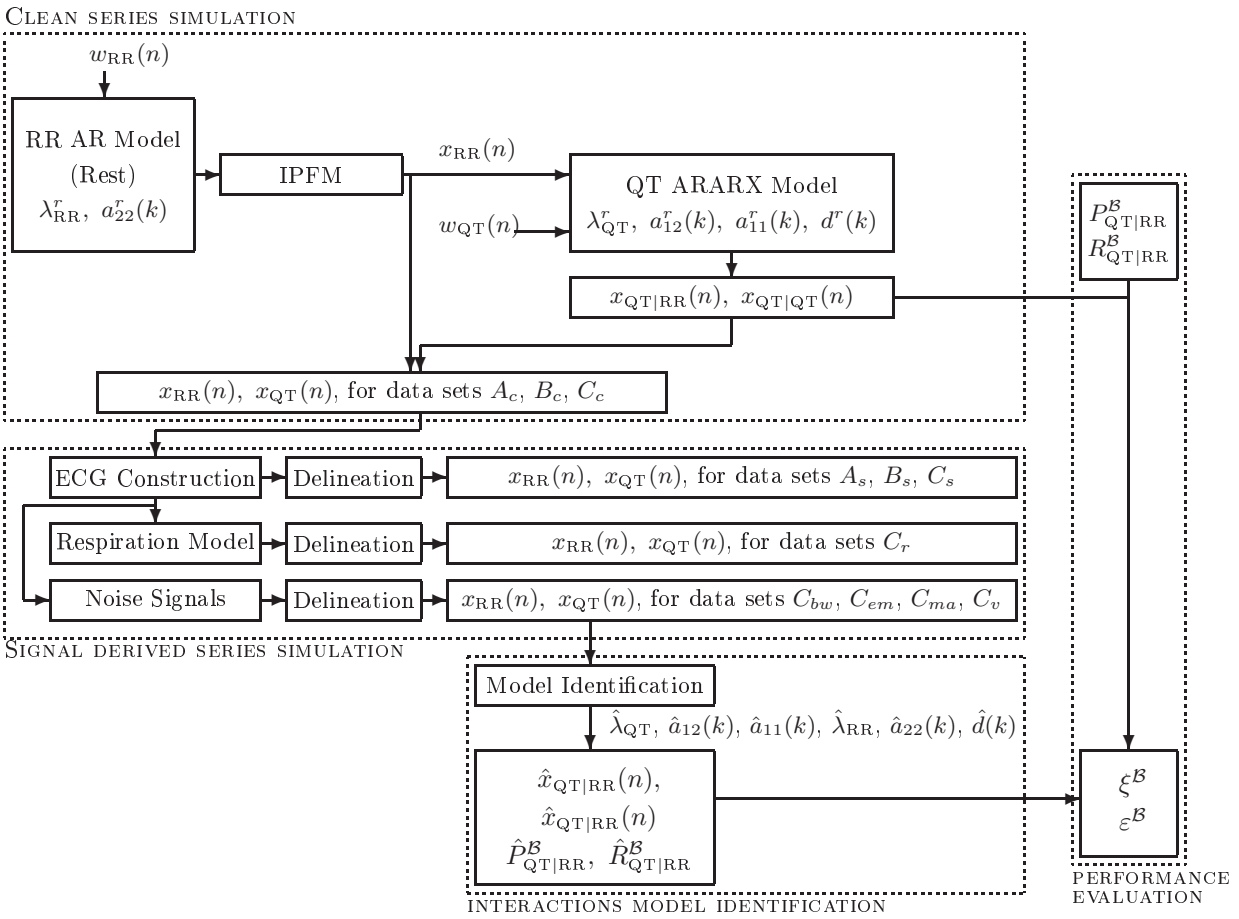

Figure 4.1: Methods block Diagram - signal derived test data sets simulation (central block), QTV versus HRV interactions model estimation (lower block) and performance evaluation (right side).

4.2.1 Signal derived series without noise contamination

A 3-lead artificial ECG signal $\{y^X(k), y^Y(k), y^Z(k)\}$, following each clean series $x_{RR}(n)$, was obtained by concatenation of beats modified from a template as illustrated in Figure 4.2 and described below.

A clean and well defined template beat (Figure 4.3(a)) was chosen from a real 12-lead ECG of the *STAFF III database* (Garcia *et al.*, 2000), and the correspondent (X, Y, Z) leads were synthesized using *Dower* transformation [1]. Automatic single-lead delineation of the template beat on (X, Y, Z) was used to obtain the locations of the R peak, the onset and the end of the QRS complex and the end of T wave. The reference mark for the R peak was arbitrary taken as the single-lead based location corresponding to the largest signal amplitude among the 3 single-lead marks. The reference marks for the boundaries were taken as the earliest/latest marks for the onset/end given by single-lead delineation. The baseline corrected 3-lead template beat, the single-lead based marks and the reference marks are presented in Figure 4.3(a).

[1] See Appendix A for more details

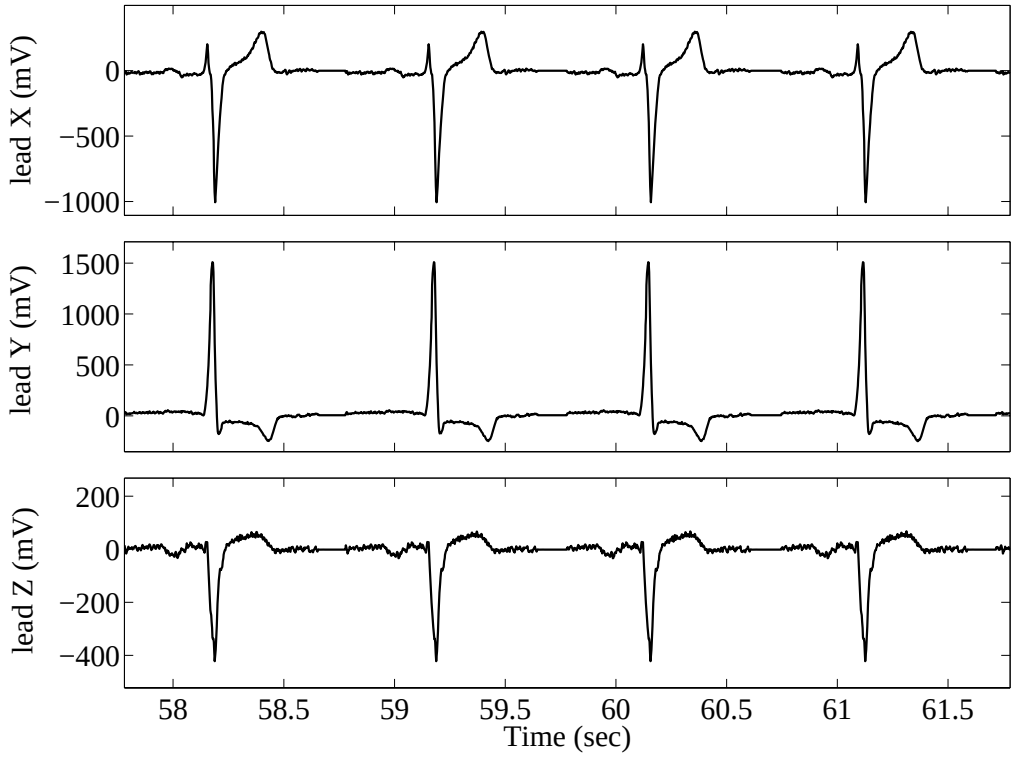

Figure 4.2: Example of a simulated ECG signal.

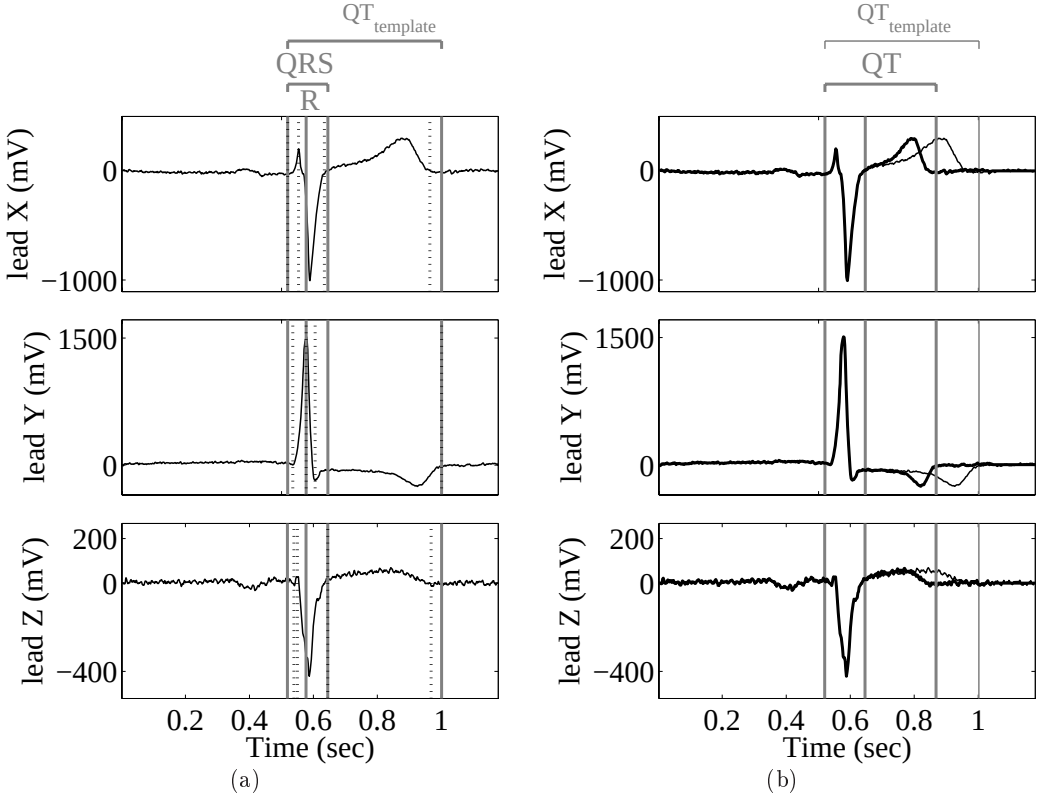

Figure 4.3: Template beat on the three leads, reference marks and scaling - (a) dashed lines correspond to the single-lead based marks and full line to the adopted reference marks; (b) original beat and reference T wave end in thinner line and rescaled and new T wave end location in thicker line.

To reflect the variability inherent to the correspondent clean series $x_{\mathrm{QT}}(n)$, the template beat was properly scaled from the QRS end to the T wave end reference marks. As it is illustrated in Figure 4.3(b), this scaling allows to create beats with the target QT interval, keeping a realistic slope in each wave. By applying the same scaling to each orthogonal lead X, Y and Z, artificial 3-lead ECG signals with same QTV and HRV in all leads can be obtained.

Automatic delineation over the simulated ECG signals provided the fiducial marks and the corresponding *signal derived* ("s") variability series were obtained for each dependency case and QTV level. The set of series corresponding to single-lead delineation over $y^X(k)$ are denoted as data sets A_s^X, B_s^X and C_s^X; other leads were not considered for single-lead delineation. Multilead delineation was used to obtain data sets A_s^F, B_s^F and C_s^F.

4.2.2 Respiratory like effect

The respiratory activity has several effects over the ECG signal, namely induces changes in the cardiac cycle length and in the waves' morphology. As the location of the R peak is quite straightforward, changes in cycle length should not increase the delineation error. However, lungs expansion and contraction during the respiratory cycle change the heart electric axis within the chest and result also in scaling and rotation on the ECG. This is likely to cause errors in the T end delineation and thus to introduce spurious QTV in the analysis. To measure the robustness of the methodology, this *respiratory-like* electrical axis rotation effect was simulated over the artificial ECG signals.

The angular variation around a lead axis is usually assumed to be a function of the air volume in the lungs at each time, which was modelled as a sinusoid. The rotation angle around each orthogonal lead $E \in \{X, Y, Z\}$ is given by (Aström *et al.*, 1998)

$$\varphi^E(k) = 0.5\phi^E\left(sin\left(2\pi k\frac{F_r}{F_s}\right)+1\right), \tag{4.1}$$

where k is sample number, ϕ^E is the maximum amplitude for the rotation angle around lead E, and F_r and F_s denote respectively respiratory and sampling frequency. The rotation matrix $Q(k)$ can be computed as the product of the planar rotations with angles $\varphi^X(k), \varphi^Y(k), \varphi^Z(k)$, as

$$Q(k) = Q_X(k).Q_Y(k).Q_Z(k) \tag{4.2}$$

$$Q_X(k) = \begin{bmatrix} 1 & 0 & 0 \\ 0 & cos\left(\varphi^X(k)\right) & sin\left(\varphi^X(k)\right) \\ 0 & -sin\left(\varphi^X(k)\right) & cos\left(\varphi^X(k)\right) \end{bmatrix}, Q_Y(k) = \begin{bmatrix} cos\left(\varphi^Y(k)\right) & 0 & sin\left(\varphi^Y(k)\right) \\ 0 & 1 & 0 \\ -sin\left(\varphi^Y(k)\right) & 0 & cos\left(\varphi^Y(k)\right) \end{bmatrix},$$

$$Q_Z(k) = \begin{bmatrix} cos\left(\varphi^Z(k)\right) & sin\left(\varphi^Z(k)\right) & 0 \\ -sin\left(\varphi^Z(k)\right) & cos\left(\varphi^Z(k)\right) & 0 \\ 0 & 0 & 1 \end{bmatrix}. \tag{4.3}$$

The effect of a three lead rotation over automatic delineation should not be different of the rotation effect along one single-lead. For the sake of simplicity, only the rotation around the Z axis was considered, with $\phi^Z = 15\pi/180$ rad (Aström *et al.*, 2000), affecting leads X and Y. The lead choice is arbitrary, except for the fact that lead X is being used for the single-lead delineation comparisons and for that reason it should be avoided.

The respiratory frequency was set to $F_r = 0.24$ Hz, corresponding to the central frequency of the highest variability peak on the Rest model spectra used in the series simulation (Figure 2.9). The ECG signals affected by respiration $\left[y_r^X(k), y_r^X(k), y_r^Z(k)\right]$ were constructed as the product of $Q(k)$ matrix by the 3-lead ECG vector $\left[y^X(k), y^Y(k), y^Z(k)\right]$.The *respiratory-like effect* ("r") was simulated for the case of mixture of dependencies (case C) and the correspondent data set C_r^F was constructed from the series of multilead delineated intervals over the ECG signal $\left[y_r^X(k), y_r^X(k), y_r^Z(k)\right]$; the series resulting from single-delineation over lead $y_r^X(k)$ are denoted as data set C_r^X.

An illustrative segment of a simulated 3-lead ECG signal with this kind of contamination is presented in Figure 4.4. As the rotation considered is around lead Z, this particular lead is unchanged, and therefore only leads X and Y are presented.

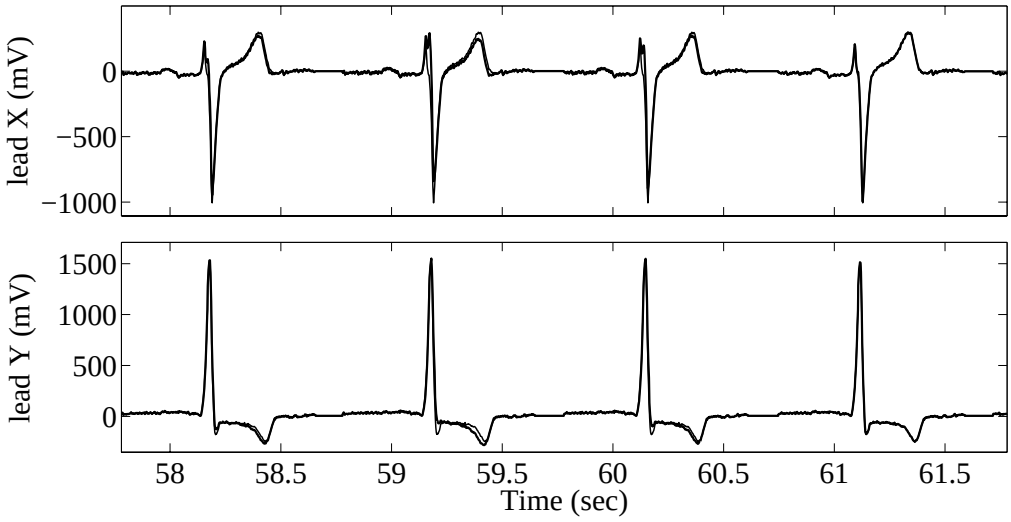

Figure 4.4: Example of a simulated ECG signal contaminated with respiratory effect (grey), superimposed to the signal without contamination (black). Same segment as in Figure 4.2.

4.2.3 MIT pre-recorded Noise

Other contamination types were considered over the fist lead of the simulated ECG ($y^X(k)$), by adding pre-recorded noise corresponding to baseline wandering (bw), electrode movement (em) and muscular (ma) artifacts. Noise records at 360 Hz from the MIT-BIH Noise Stress Test Database (Moody and Mark, 1990) was used to create a noise contamination to be added to $y^X(k)$ according to predefined set of SNR values $SNR \in \{30dB, 25dB, 20dB, 15dB, 10dB\}$. The first lead of the noise records ($v^{\mathcal{N}}(k)$, $\mathcal{N} \in \{bw, em, ma\}$) was resampled at 500 Hz and rescaled by a constant a to get the each SNR values

$$a = \frac{\text{RMS}\left[y^X(k)\right]}{\text{RMS}\left[v^{\mathcal{N}}(k)\right]} * \left(10^{\frac{-SNR}{20}}\right), \mathcal{N} \in \{bw, em, ma\}. \tag{4.4}$$

It should be remarked that according to equation (4.4), the entire signals were considered for calculating the power of signal and noise. This approach is only possible since both the clean and noise signals are known. An illustrative segment of a simulated ECG with different noise contaminations is presented in Figure 4.5.

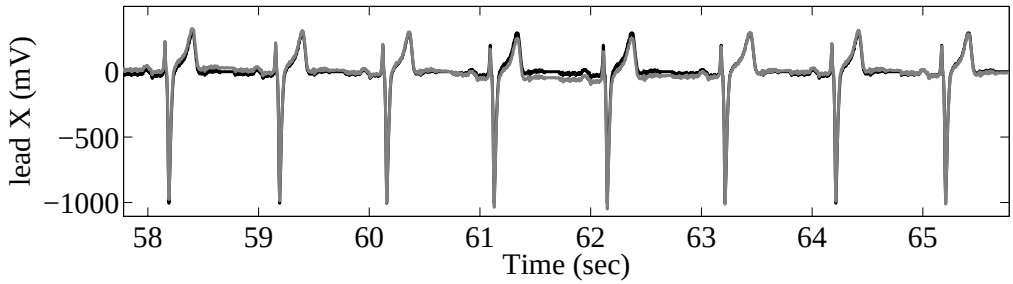

(a) baseline wandering contamination: SNR=15dB

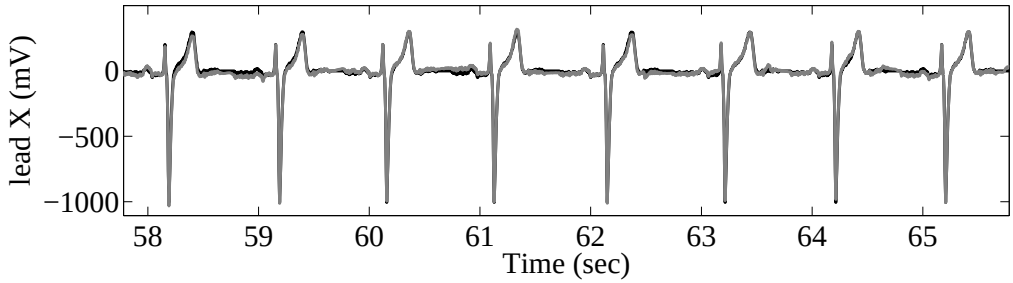

(b) electrode movement contamination: SNR=15dB

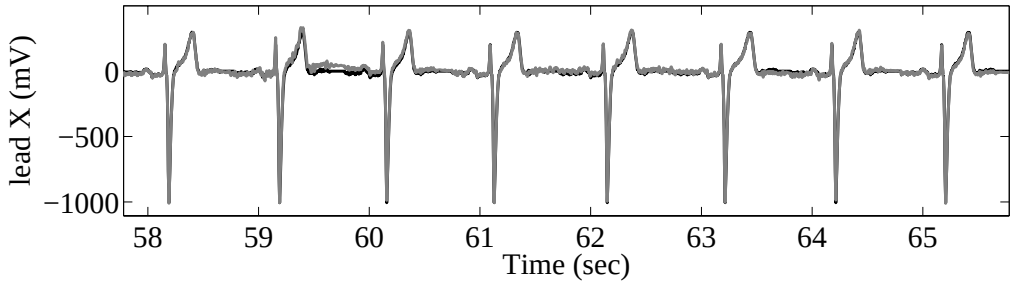

(c) muscular artifacts: SNR=20dB

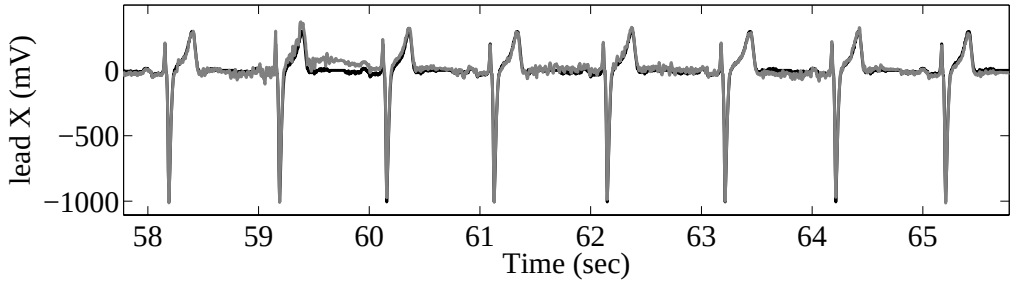

(d) muscular artifacts: SNR=15dB

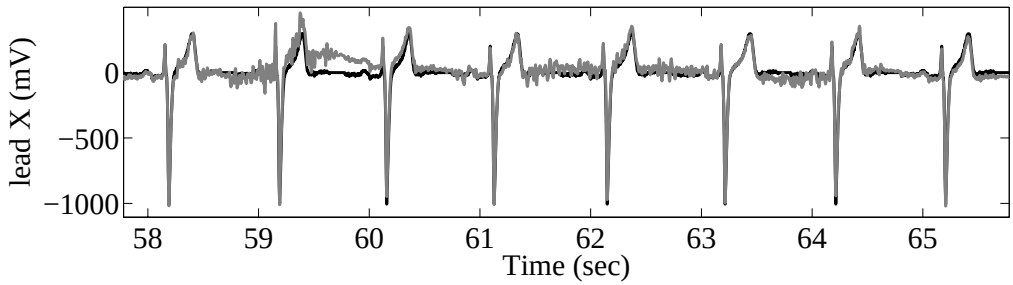

(e) muscular artifacts: SNR=10dB

Figure 4.5: Example of a simulated ECG signal contaminated with MIT pre-recorded noise (grey), superimposed to the signal without contamination (black).

Noise was added to the simulated series corresponding to the mixture of dependencies (case C) and data sets $C^X_{\mathcal{N}}(SNR), \mathcal{N} \in \{bw, em, ma\}$ were defined as the series obtained from automatic delineation over the single-lead *noisy* ECGs corresponding to a certain SNR value.

4.2.4 3-lead extracted Noise

The noise is likely to have some spacial structure, thus the noise recorded in one lead has some dependence on the noise on the other leads. To obtain a 3-lead realistic noise effect to be added to the simulated clean ECG, the following strategy was considered (Figure 4.6):

- a real 3-lead file was delineated using the multilead based automatic system
- a centered average of beats was calculated separately for each lead and the averaged beats were stretched in amplitude to fit to the original beats
- an artificial clean ECG file was constructed following the original RR series, by concatenating the amplitude stretched beats,
- finally, the 3-lead noise was taken as the difference between the real ECG and the artificial clean ECG

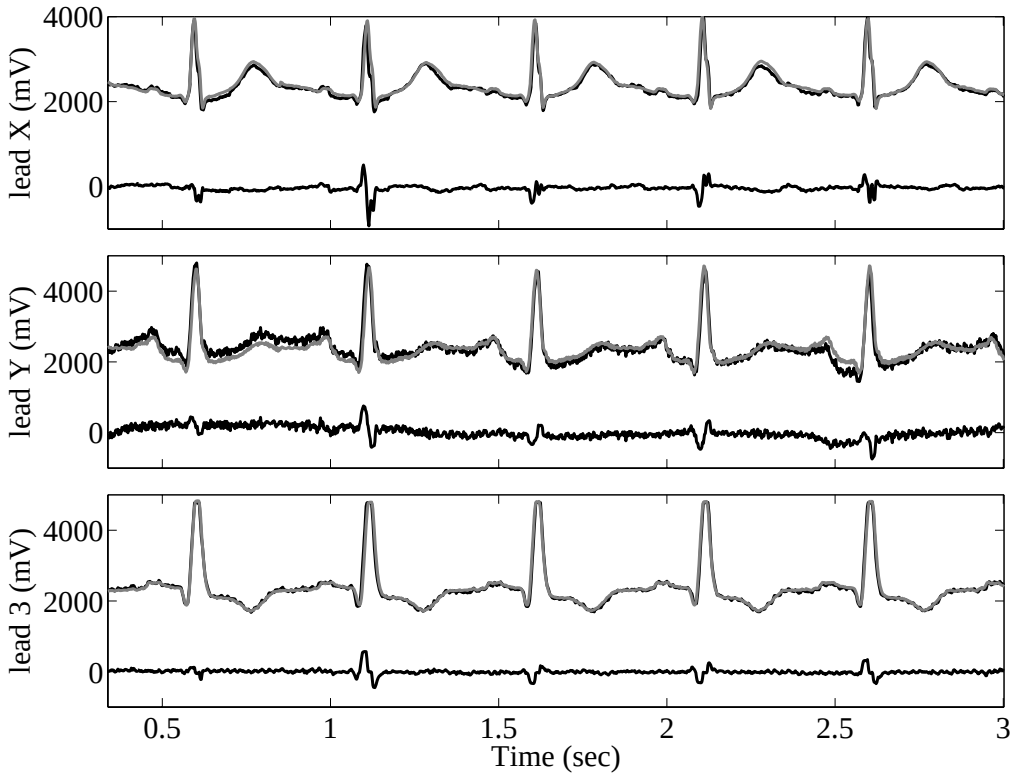

Figure 4.6: Extraction of a 3-lead noise from the real file *ra1* from the POLI/MEDLAV database. The lower signal in each axis corresponds to the 3-lead noise signal and the auxiliary artificial clean ECG (grey) is superimposed to the original ECG (black).

The file *ra1* from POLI/MEDLAV database (Pinciroli *et al.*, 1998)[2] was used to extract the noise $\left(v^E(k), E \in \{X, Y, Z\}\right)$.

By trial and error it was found that an acceptable noise estimation was obtained using an average of 7 beats. The extraction of the 3-lead noise is illustrated in Figure 4.6. As it is notorious in the Figure, some residual forms from the QRS complex remain visible in the extracted noise. Despite that, adding this noise to the artificial ECG it is unlikely that these forms coincide with the QRS waves, otherwise the delineation procedure should be able to consider them as artifacts.

The 3-lead noise file was multiplied by a constant factor a to get a predefined global SNR when added to the artificial ECG $\left(y^E(k)\right)$.

$$a = \frac{\text{RMS}\left[y^X(k)\right] + \text{RMS}\left[y^Y(k)\right] + \text{RMS}\left[y^Z(k)\right]}{\text{RMS}\left[v^X(k)\right] + \text{RMS}\left[v^Y(k)\right] + \text{RMS}\left[v^Z(k)\right]} * (10^{\frac{-SNR}{20}}). \tag{4.5}$$

As in the MIT recorded noise case, the entire clean artificial ECG and noise signals were considered for calculating the power of signal and noise, respectively. An example of an artificial ECG signal contaminated with the extracted realistic noise can be found in Figure 4.7.

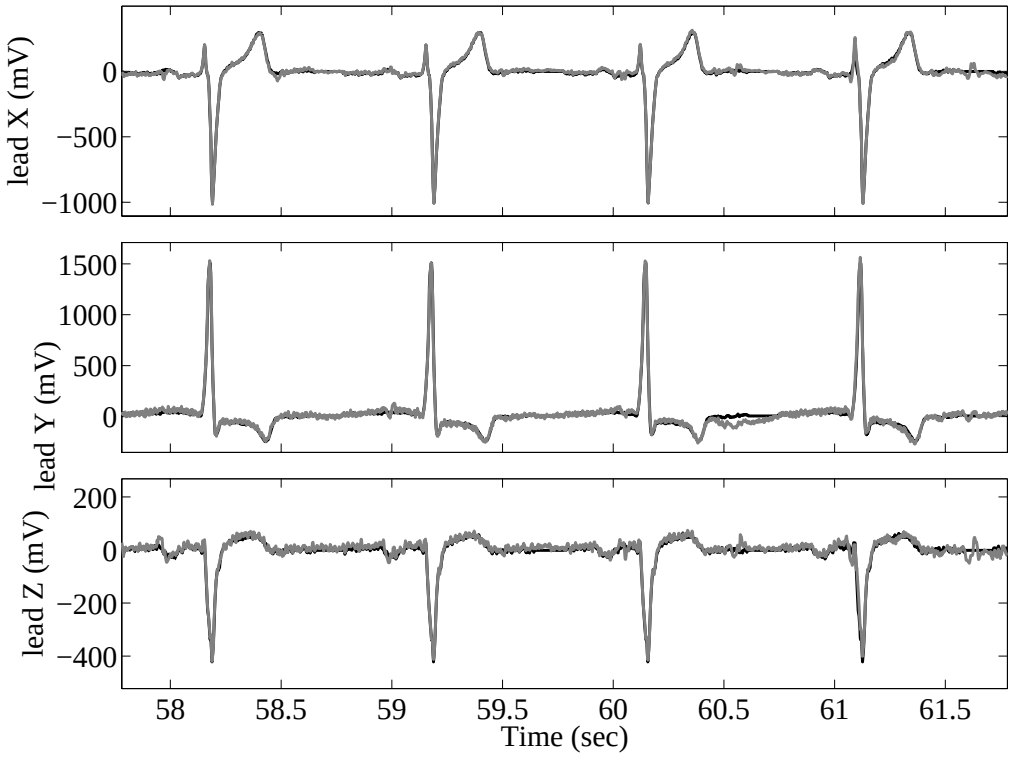

Figure 4.7: Example of a simulated ECG signal contaminated with 3-lead extracted noise with SNR=15dB (grey) superimposed to the simulated signal with no contamination (black, same segment as in Figure 4.2).

[2]More details on this database can be found in Section 5.2.

Again, only the mixture of dependencies (case C) was considered and the data sets $\{C_v^F(SNR)\}$ and $\{C_v^X(SNR)\}$ were defined from the series obtained applying, respectively, multilead or single-lead based delineation over each *noisy* ("v") ECGs corresponding to the values $SNR \in \{30dB, 25dB, 20dB, 15dB, 10dB\}$ value. Again, only segments of consecutive 350 valid beats measures after exclusion of missing QT values and RR outliers were considered.

4.3 Performance Results

The ECG simulated signals were constructed for 50 realizations (trials) for each QT reference model and the correspondent series $x_{\mathrm{RR}}(n)$ and $x_{\mathrm{QT}}(n)$ were checked for RR outliers (Mateo and Laguna, 2003) and missing QT values. In this study were considered to be *adequate segments* 350 consecutive beats with no potential RR outliers or missing QT intervals.

Delineation errors can produce outliers in the variability series, therefore to allow a large enough data set large, more than 1000 intervals were initially simulated, and only adequate segments in the data sets. It should be noticed that the test data sets "c" considered in Section 2.4 are in fact subsegments (350 beats long) of these longer trials.

The number of adequate segments obtained are reported in Table 4.2, along with the mean and standard deviation found for $\hat{\sigma}_{\mathrm{QT}}$. The reference standard deviation (σ_{QT}) for each QT model is presented in last row.

For all QT reference models adequate segments were found in all 50 trials of each data set:

- for which $SNR > 10$ dB, using single-lead delineation (SL);
- for which $SNR > 20$ dB, using multilead delineation (ML).

For each data set with $SNR \geq 20$ dB, a minimum number of 31 trials with an adequate segment were found, while for lower SNR a reduced number of segments were found for some QT models. For $SNR \leq 15$, the data sets derived using ML delineation was found to be very small or empty, as result of the high number of *false negatives*.

Mean s_{QT} values found in data sets C_s^X and C_s^F are mainly lower than the reference value σ_{QT} for all QT reference models, indicating that the considered automatic delineation methods do not allow to measure the total amount of QTV. The differences between measured and reference QT standard deviation correspond to:

- 21% to 15% of the QTV using SL delineation;
- 15% of the QTV, for QT models 1 or 2, using ML delineation
- 27% or 25% of the QTV, for QT models 3 or 4, using ML delineation
- less than 5% of the QTV, for QT models 5 or 6 using ML delineation.

Table 4.2: ECG derived test data sets summary - number of valid segments (#), mean (m) and standard deviation (sd) of s_{QT} and reference standard deviation values for each QT model (σ_{QT}); units in ms.

	QT model 1			QT model 2			QT model 3			QT model 4			QT model 5			QT model 6		
	#	m	sd	#	m	sd	#	m	sd	#	m	sd	#	m	sd	#	m	sd
A_s^X	50	11.2	0.7	50	8.5	0.5	50	6.8	0.4	50	5.5	0.3	50	3.3	0.2	50	1.8	0.1
A_s^F	50	11.9	0.7	50	9.1	0.5	50	6.1	0.4	50	5.0	0.3	50	4.0	0.2	50	2.4	0.1
B_s^X	50	7.6	0.6	50	5.8	0.4	50	4.5	0.3	50	3.7	0.3	50	2.3	0.2	50	1.3	0.1
B_s^F	50	8.1	0.6	50	6.2	0.5	50	4.2	0.2	50	3.8	0.2	50	3.0	0.2	50	1.9	0.1
C_s^X	50	13.7	0.9	50	10.4	0.7	50	8.2	0.5	50	6.7	0.4	50	4.2	0.3	50	2.4	0.2
C_s^F	50	14.4	0.9	50	11.0	0.7	50	7.3	0.5	50	6.0	0.4	50	4.8	0.3	50	3.1	0.2
C_r^X	50	14.5	0.9	50	11.7	0.7	50	10.0	0.6	50	8.8	0.5	50	7.0	0.3	50	6.1	0.2
C_r^F	50	14.5	0.9	50	11.1	0.7	50	8.2	0.5	50	6.7	0.4	50	4.8	0.3	50	3.1	0.2
$C_{bw}^X(30dB)$	50	14.4	0.8	50	11.4	0.6	50	9.4	0.5	50	8.1	0.4	50	6.2	0.3	50	5.2	0.2
$C_{bw}^X(25dB)$	50	14.4	0.9	50	11.4	0.7	50	9.4	0.5	50	8.2	0.4	50	6.3	0.3	50	5.3	0.2
$C_{bw}^X(20dB)$	50	14.4	0.8	50	11.4	0.6	50	9.4	0.5	50	8.1	0.4	50	6.2	0.3	50	5.3	0.2
$C_{bw}^X(15dB)$	50	14.5	0.8	50	11.5	0.6	50	9.6	0.5	50	8.3	0.4	50	6.4	0.3	50	5.4	0.2
$C_{bw}^X(10dB)$	50	14.7	0.8	50	11.8	0.6	50	10.2	0.5	50	9.0	0.4	50	7.0	0.3	50	6.2	0.3
$C_{em}^X(30dB)$	50	13.7	0.9	50	10.5	0.7	50	8.3	0.5	50	6.8	0.4	50	4.5	0.3	50	2.8	0.2
$C_{em}^X(25dB)$	50	13.9	0.8	50	10.7	0.6	50	8.5	0.5	50	7.1	0.4	50	4.8	0.3	50	3.4	0.2
$C_{em}^X(20dB)$	50	14.1	0.8	50	11.0	0.6	50	9.2	0.8	50	7.9	0.9	50	5.5	0.3	50	4.3	0.2
$C_{em}^X(15dB)$	50	16.0	1.5	50	13.6	1.9	50	13.0	2.4	50	12.0	2.5	50	9.3	2.1	50	8.6	2.2
$C_{em}^X(10dB)$	50	22.2	2.4	50	20.7	2.5	50	21.3	2.7	50	20.7	2.9	50	18.0	3.4	50	17.8	3.3
$C_{ma}^X(30dB)$	50	14.1	0.8	50	11.0	0.6	50	8.9	0.5	50	7.5	0.4	50	5.5	0.3	50	4.2	0.2
$C_{ma}^X(25dB)$	50	14.4	0.9	50	11.4	0.7	50	9.5	0.5	50	8.2	0.4	50	6.3	0.3	50	5.3	0.2
$C_{ma}^X(20dB)$	50	14.9	0.9	50	12.0	0.7	50	10.2	0.5	50	9.0	0.4	50	7.3	0.3	50	6.4	0.2
$C_{ma}^X(15dB)$	50	15.4	1.0	50	12.8	1.0	50	11.1	1.0	50	10.0	1.0	50	8.2	0.4	50	7.4	0.3
$C_{ma}^X(10dB)$	50	17.3	1.2	50	14.8	1.2	50	13.7	1.3	50	12.9	1.4	50	11.2	1.3	50	10.5	1.3
$C_v^X(30dB)$	50	13.9	0.9	50	10.8	0.7	50	8.7	0.6	50	7.3	0.5	50	5.1	0.3	50	3.7	0.3
$C_v^F(30dB)$	50	14.5	0.9	50	11.1	0.7	50	8.3	0.5	50	7.0	0.4	50	5.0	0.3	50	3.3	0.2
$C_v^X(25dB)$	50	14.2	0.9	50	11.2	0.7	50	9.1	0.5	50	7.8	0.4	50	5.8	0.3	50	4.6	0.3
$C_v^F(25dB)$	50	14.7	0.9	50	11.3	0.7	50	8.9	0.5	50	7.6	0.5	50	5.3	0.3	50	3.9	0.2
$C_v^X(20dB)$	50	14.6	0.9	50	11.7	0.7	50	9.8	0.6	50	8.6	0.5	50	6.8	0.3	50	5.8	0.3
$C_v^F(20dB)$	33	15.2	1.1	33	11.9	0.8	50	9.7	0.7	50	8.5	0.6	31	6.2	0.5	32	5.0	0.4
$C_v^X(15dB)$	50	15.7	1.3	50	12.9	1.1	50	11.6	1.3	50	10.5	1.4	50	8.4	1.1	50	7.7	1.1
$C_v^F(15dB)$	1	15.3	-	0	-	-	46	11.9	1.1	47	10.8	0.9	0	-	-	0	-	-
$C_v^X(10dB)$	45	21.1	2.2	47	19.0	2.3	50	18.7	2.4	50	18.1	2.6	48	15.9	2.7	49	15.6	2.7
$C_v^F(10dB)$	0	-	-	2	22.0	4.2	16	23.3	3.9	19	22.9	3.6	1	23.9	-	0	-	-
σ_{QT}		17.0			13.0			10.0			8.0			5.0			3.0	

Thus, the QTV amount missed is lower with ML than with SL delineation, for all except QT models 3 and 4. Analogously to the results presented in Section 2.4.4 of this thesis (Table 2.1), lower s_{QT} values were found when only one of the QT dependencies (one QTV fraction) was included in the series generation (data sets A_s^X, A_s^F, B_s^X and B_s^F).

The s_{QT} mean value (m) progressively increased with SNR reduction, strongly indicating that delineation errors that resulted from noise had introduced spurious variability in the measured series. The values found for m in data sets obtained using SL or ML delineation over the same ECG simulated files present close values, differing by more than 1 ms only for respiratory like effect in QT models 3 to 6, and for 3-lead extracted noise contamination with $SNR = 10$ dB. The value of the bias $[m - \sigma_{\mathrm{QT}}]$ increases when the amount of QTV considered decreases. So σ_{QT} was:

- underestimated for most of data sets with QT reference models 1 and 2 ($\sigma_{\mathrm{QT}} > 10$ ms),
- overestimated in many data sets for QT reference models 5 and 6 ($\sigma_{\mathrm{QT}} < 8$ ms).

This can result from delineation inaccuracies, as errors present increasing relative importance. However, once the differences in values are low for data sets that only differ in delineation strategy, it should be considered the hypothesis of an effect from the simulation itself.

Facing respiratory like effect, SL delineation introduces more spurious QTV than ML in QTV models corresponding to $\sigma_{\mathrm{QT}} \leq 13$ ms. This indicates that the multilead method is able to take advantage of the differences on the respiratory effect over each lead. With respect to noise level, the values of both m and sd does not differ much between data sets corresponding to the same simulation strategy with $SNR > 10$ dB.

The consequences of reducing the QTV level and increasing noise need to be taken into consideration in the analysis of the parametric methodology results, that are presented in the next sections.

4.3.1 Signal derived series

A minimum of 48 (out of 50) valid estimated models were found in each signal derived data set (A_s^X, B_s^X, C_s^X, A_s^F, B_s^F and C_s^F) for every QT reference models used and any of the delineation approaches. Results are summarized in Tables 4.3 and 4.4, both considering the absolute errors ($\xi^{\mathcal{B}}$) and the percentage errors ($\varepsilon^{\mathcal{B}}$). These Tables are similar to Tables 2.2 and 2.3 presented in Section 2.4.4 of this thesis, relative to the clean simulated series (data sets A_c, B_c and C_c). For the sake of comparison between different QTV levels are also presented the relative values of $\overline{\xi}^{\mathcal{B}}$ and $s_{\xi}^{\mathcal{B}}$, normalized by the reference measures $P^{B}_{\mathrm{QT|RR}}$, that can be found in Table 2.2. It must be remembered that for data set B_c no normalization is required ($P^{B}_{\mathrm{QT|RR}} = 0$). The distributions of $\xi^{\mathcal{B}}$ and $\varepsilon^{\mathcal{B}}$ are presented in Figures 4.8 and 4.9, respectively, in plots similar to the ones presented in Section 2.4.4 (Figures 2.14 and 2.15).

As it should be expected, the bias and dispersion of errors $\xi^{\mathcal{B}}$ in the signal derived data sets decrease with the QTV amount to be measured. Nevertheless, its relative value remains unchanged or increases with the QTV decrease when considering SL delineation, moreover decreases for QTV models 5 and 6 (lowest QTV levels) with ML. The signal derived data sets present greater errors than the clean simulated series, in particular in dependency case A. For QT models 3 and 4, data sets for ML delineation present greater errors than SL data sets.

Table 4.3: Mean and standard deviation of the absolute errors $\xi^{\mathcal{B}}$ in data sets A_s^X, B_s^X, C_s^X,A_s^F, B_s^F and $C_s^F(ms^2, mean \pm sd)$; number of valid models (#) are also presented for each data set; reference measures ($P^{\mathcal{B}}_{\mathrm{QT|RR}}$, $P^{\mathcal{B}}_{\mathrm{QT|QT}}$) can be found in Table 2.2.

QT model	$\mathcal{B}$	A_s^X #	A_s^X $\overline{\xi}^{\mathcal{B}} \pm s_\xi^{\mathcal{B}}$	A_s^X $\frac{100\lvert\overline{\xi}^{\mathcal{B}}\rvert}{P^{\mathcal{B}}_{\mathrm{QT|RR}}} \pm \frac{100\lvert s_\xi^{\mathcal{B}}\rvert}{P^{\mathcal{B}}_{\mathrm{QT|RR}}}$	B_s^X #	B_s^X $\overline{\xi}^{\mathcal{B}} \pm s_\xi^{\mathcal{B}}$	C_s^X #	C_s^X $\overline{\xi}^{\mathcal{B}} \pm s_\xi^{\mathcal{B}}$	C_s^X $\frac{100\lvert\overline{\xi}^{\mathcal{B}}\rvert}{P^{\mathcal{B}}_{\mathrm{QT|RR}}} \pm \frac{100\lvert s_\xi^{\mathcal{B}}\rvert}{P^{\mathcal{B}}_{\mathrm{QT|RR}}}$
1	TP	49	-38.1 ± 13.1	-34.9 ± 12.1	49	1.1 ± 0.8	48	-36.5 ± 16.6	-33.5 ± 15.2
	LF	49	-17.9 ± 12.0	-29.6 ± 19.8	49	0.8 ± 0.8	48	-16.5 ± 14.1	-27.3 ± 23.4
	HF	49	-20.2 ± 4.5	-41.7 ± 9.2	49	0.2 ± 0.2	48	-20.0 ± 5.3	-41.3 ± 10.9
2	TP	49	-21.8 ± 7.3	-34.8 ± 11.6	49	0.7 ± 0.7	49	-21.0 ± 10.0	-33.5 ± 15.9
	LF	49	-10.0 ± 6.6	-29.3 ± 19.3	49	0.5 ± 0.7	49	-9.2 ± 8.8	-27.1 ± 25.9
	HF	49	-11.8 ± 2.7	-41.5 ± 9.4	49	0.2 ± 0.2	49	-11.7 ± 3.1	-41.2 ± 10.9
3	TP	49	-12.8 ± 4.5	-33.4 ± 11.9	49	0.4 ± 0.4	49	-11.9 ± 6.2	-31.1 ± 16.2
	LF	49	-5.9 ± 4.1	-27.8 ± 19.3	49	0.4 ± 0.4	49	-5.1 ± 5.4	-24.4 ± 25.7
	HF	49	-6.9 ± 1.7	-40.5 ± 9.7	49	0.1 ± 0.1	49	-6.8 ± 1.9	-39.5 ± 10.9
4	TP	49	-8.4 ± 2.7	-33.3 ± 10.8	49	0.3 ± 0.3	49	-8.0 ± 4.0	-31.9 ± 16.0
	LF	49	-3.9 ± 2.5	-27.7 ± 17.6	49	0.2 ± 0.3	49	-3.6 ± 3.5	-25.9 ± 24.7
	HF	49	-4.5 ± 1.1	-40.5 ± 9.8	49	0.0 ± 0.0	49	-4.4 ± 1.2	-39.6 ± 11.1
5	TP	49	-3.8 ± 1.1	-39.5 ± 11.7	49	0.1 ± 0.1	49	-3.2 ± 1.7	-33.6 ± 17.3
	LF	49	-1.9 ± 1.0	-34.2 ± 18.6	49	0.1 ± 0.1	49	-1.5 ± 1.4	-27.2 ± 25.8
	HF	49	-1.9 ± 0.4	-46.9 ± 9.7	49	0.0 ± 0.0	49	-1.7 ± 0.5	-42.1 ± 12.4
6	TP	49	-1.8 ± 0.3	-56.0 ± 9.2	49	0.0 ± 0.0	49	-1.5 ± 0.5	-43.9 ± 15.1
	LF	49	-0.9 ± 0.2	-51.2 ± 13.5	49	0.0 ± 0.0	49	-0.7 ± 0.4	-37.4 ± 21.7
	HF	49	-0.9 ± 0.1	-61.9 ± 9.2	49	0.0 ± 0.0	49	-0.8 ± 0.2	-52.1 ± 12.4

QT model	$\mathcal{B}$	A_s^F #	A_s^F $\overline{\xi}^{\mathcal{B}} \pm s_\xi^{\mathcal{B}}$	A_s^F $\frac{100\lvert\overline{\xi}^{\mathcal{B}}\rvert}{P^{\mathcal{B}}_{\mathrm{QT|RR}}} \pm \frac{100\lvert s_\xi^{\mathcal{B}}\rvert}{P^{\mathcal{B}}_{\mathrm{QT|RR}}}$	B_s^F #	B_s^F $\overline{\xi}^{\mathcal{B}} \pm s_\xi^{\mathcal{B}}$	C_s^F #	C_s^F $\overline{\xi}^{\mathcal{B}} \pm s_\xi^{\mathcal{B}}$	C_s^F $\frac{100\lvert\overline{\xi}^{\mathcal{B}}\rvert}{P^{\mathcal{B}}_{\mathrm{QT|RR}}} \pm \frac{100\lvert s_\xi^{\mathcal{B}}\rvert}{P^{\mathcal{B}}_{\mathrm{QT|RR}}}$
1	TP	49	-29.2 ± 14.9	-26.8 ± 13.7	49	1.1 ± 1.0	49	-29.2 ± 18.6	-26.8 ± 17.0
	LF	49	-12.6 ± 13.7	-20.8 ± 22.7	49	0.8 ± 1.0	49	-12.2 ± 16.0	-20.2 ± 26.4
	HF	49	-16.7 ± 4.9	-34.5 ± 10.1	49	0.3 ± 0.2	49	-17.0 ± 5.7	-35 ± 11.8
2	TP	49	-16.4 ± 8.1	-26.3 ± 13.0	49	0.8 ± 0.9	49	-16.2 ± 11.2	-25.9 ± 17.9
	LF	49	-6.8 ± 7.4	-20.0 ± 21.8	49	0.6 ± 0.9	49	-6.4 ± 9.9	-18.7 ± 29.1
	HF	49	-9.7 ± 3.1	-34.1 ± 10.7	49	0.2 ± 0.1	49	-9.8 ± 3.3	-34.5 ± 11.7
3	TP	48	-20.7 ± 3.8	-54.1 ± 9.8	49	0.4 ± 0.3	49	-18.9 ± 4.8	-49.6 ± 12.6
	LF	48	-10.8 ± 3.4	-51.3 ± 16.3	49	0.3 ± 0.3	49	-9.5 ± 4.0	-45.1 ± 18.8
	HF	48	-9.9 ± 1.8	-57.6 ± 10.7	49	0.1 ± 0.1	49	-9.4 ± 1.7	-55.0 ± 9.8
4	TP	49	-14 ± 2.6	-55.7 ± 10.4	49	0.3 ± 0.2	49	-12.8 ± 3.3	-51.1 ± 13.1
	LF	49	-7.3 ± 2.5	-51.9 ± 18.1	49	0.2 ± 0.2	49	-6.6 ± 2.8	-47.2 ± 19.9
	HF	49	-6.7 ± 0.9	-60.5 ± 7.9	49	0.1 ± 0.1	49	-6.2 ± 1.2	-56.2 ± 10.4
5	TP	49	-1.1 ± 1.7	-11.2 ± 17.3	49	0.2 ± 0.2	49	-1.4 ± 2.1	-14.4 ± 21.9
	LF	49	-0.2 ± 1.5	-3.8 ± 28.0	49	0.2 ± 0.2	49	-0.3 ± 1.8	-6.3 ± 33.5
	HF	49	-0.9 ± 0.5	-21.3 ± 12.5	49	0.0 ± 0.0	49	-1.0 ± 0.6	-25.5 ± 15.0
6	TP	49	-0.2 ± 0.6	-6.1 ± 19.2	49	0.1 ± 0.1	49	-0.2 ± 0.8	-5.2 ± 23.8
	LF	49	0.1 ± 0.6	4.1 ± 32.4	49	0.1 ± 0.1	49	0.1 ± 0.7	4.5 ± 38.3
	HF	49	-0.3 ± 0.3	-18.7 ± 16.7	49	0.0 ± 0.0	49	-0.3 ± 0.3	-17.1 ± 17.8

Table 4.4: Mean and standard deviation of the percentage errors $\varepsilon^{\mathcal{B}}$ in data sets A_c, B_c, C_c, A_s, B_s and C_s in data sets A_s^X, B_s^X, C_s^X,A_s^F, B_s^F and C_s^F $(\%, mean \pm sd)$; the reference value of $R^{\mathcal{B}}_{\mathrm{QT|RR}}$ can be found in Table 2.3.

QT model	$\mathcal{B}$	A_s^X $\overline{\varepsilon}^{\mathcal{B}} \pm s_\varepsilon^{\mathcal{B}}$	B_s^X $\overline{\varepsilon}^{\mathcal{B}} \pm s_\varepsilon^{\mathcal{B}}$	C_s^X $\overline{\varepsilon}^{\mathcal{B}} \pm s_\varepsilon^{\mathcal{B}}$	A_s^F $\overline{\varepsilon}^{\mathcal{B}} \pm s_\varepsilon^{\mathcal{B}}$	B_s^F $\overline{\varepsilon}^{\mathcal{B}} \pm s_\varepsilon^{\mathcal{B}}$	C_s^F $\overline{\varepsilon}^{\mathcal{B}} \pm s_\varepsilon^{\mathcal{B}}$
1	TP	-0.8 ± 0.2	2.2 ± 1.8	-1.7 ± 5.9	-0.9 ± 0.3	2.0 ± 1.6	-2.3 ± 6.4
	LF	-0.4 ± 0.2	2.0 ± 2.2	-0.2 ± 8.5	-0.5 ± 0.3	1.9 ± 1.9	-0.7 ± 9.1
	HF	-1.1 ± 0.3	2.9 ± 2.5	-2.1 ± 4.1	-1.3 ± 0.3	2.9 ± 2.2	-2.9 ± 4.3
2	TP	-1.3 ± 0.3	2.4 ± 2.1	-2.1 ± 6.5	-1.4 ± 0.3	2.5 ± 2.8	-2.5 ± 6.6
	LF	-0.6 ± 0.3	2.3 ± 2.5	-0.6 ± 10.0	-0.7 ± 0.3	2.4 ± 3.4	-0.9 ± 10.2
	HF	-1.7 ± 0.4	3.0 ± 2.5	-3.0 ± 4.5	-1.8 ± 0.4	2.8 ± 2.2	-3.3 ± 4.4
3	TP	-2.1 ± 0.5	2.7 ± 2.7	-1.6 ± 6.2	-19.4 ± 4.4	2.6 ± 2.2	-7.6 ± 6.2
	LF	-1.2 ± 0.6	2.9 ± 3.5	0.4 ± 9.5	-14.0 ± 9.0	2.7 ± 2.8	-2.8 ± 9.3
	HF	-2.7 ± 0.6	2.3 ± 2.0	-3.3 ± 4.1	-23.7 ± 8.2	2.4 ± 2.1	-15.6 ± 6.0
4	TP	-2.9 ± 0.5	2.6 ± 2.5	-2.2 ± 6.3	-27.3 ± 6.9	2.3 ± 1.9	-10.4 ± 6.5
	LF	-1.5 ± 0.7	2.7 ± 3.1	-0.2 ± 9.5	-19.3 ± 13.4	2.3 ± 2.2	-3.5 ± 9.5
	HF	-4.0 ± 1.0	2.3 ± 2.0	-5.0 ± 4.3	-34.7 ± 10.1	2.4 ± 2.2	-23.2 ± 6.7
5	TP	-8.2 ± 2.0	2.8 ± 2.5	-2.4 ± 7.1	-4.3 ± 1.0	2.8 ± 2.7	-2.2 ± 7.2
	LF	-6.1 ± 3.8	2.9 ± 3.3	0.7 ± 10.0	-2.8 ± 1.7	2.9 ± 3.4	0.4 ± 10.0
	HF	-10.1 ± 3.2	2.3 ± 2.2	-7.7 ± 5.8	-5.6 ± 1.4	2.4 ± 2.2	-6.5 ± 6.3
6	TP	-22.1 ± 6.5	2.4 ± 1.7	-5.4 ± 6.9	-8.3 ± 2.0	2.5 ± 2.4	-3.2 ± 6.6
	LF	-16.7 ± 11.2	2.3 ± 2.4	0.1 ± 9.9	-5.4 ± 4.5	2.7 ± 3.3	0.4 ± 10.1
	HF	-26.9 ± 6.5	2.7 ± 2.2	-14.0 ± 6.8	-11.6 ± 3.9	2.3 ± 2.3	-9.2 ± 6.2

In percentage errors $\varepsilon^{\mathcal{B}}$:

- $\epsilon^{\mathcal{B}} < 10\%$ for SL delineation, QT models corresponding to $\sigma_{\mathrm{QT}} \geq 5$ ms (QT models 1 to 5)
  - for 95% of the series, in TP band,
  - for 87% of the series, in LF band,
  - for 85% of the series, in HF band,
- $\epsilon^{\mathcal{B}} < 15\%$ for ML delineation, QT models corresponding to $\sigma_{\mathrm{QT}} \in \{17, 13, 5, 3\}$ ms (models 1, 2, 5 and 6),
  - for 71% of the series, in TP band,
  - for 83% of the series, in LF band,
  - for 79% of the series, in HF band.

Using multilead delineation, it is difficult to establish the degree of performance decrease with QTV level reduction, since QT models 5 and 6, with the lowest σ_{QT}, present less percentage error than QT models 3 and 4, both for dependency cases A and C, in all frequency bands.

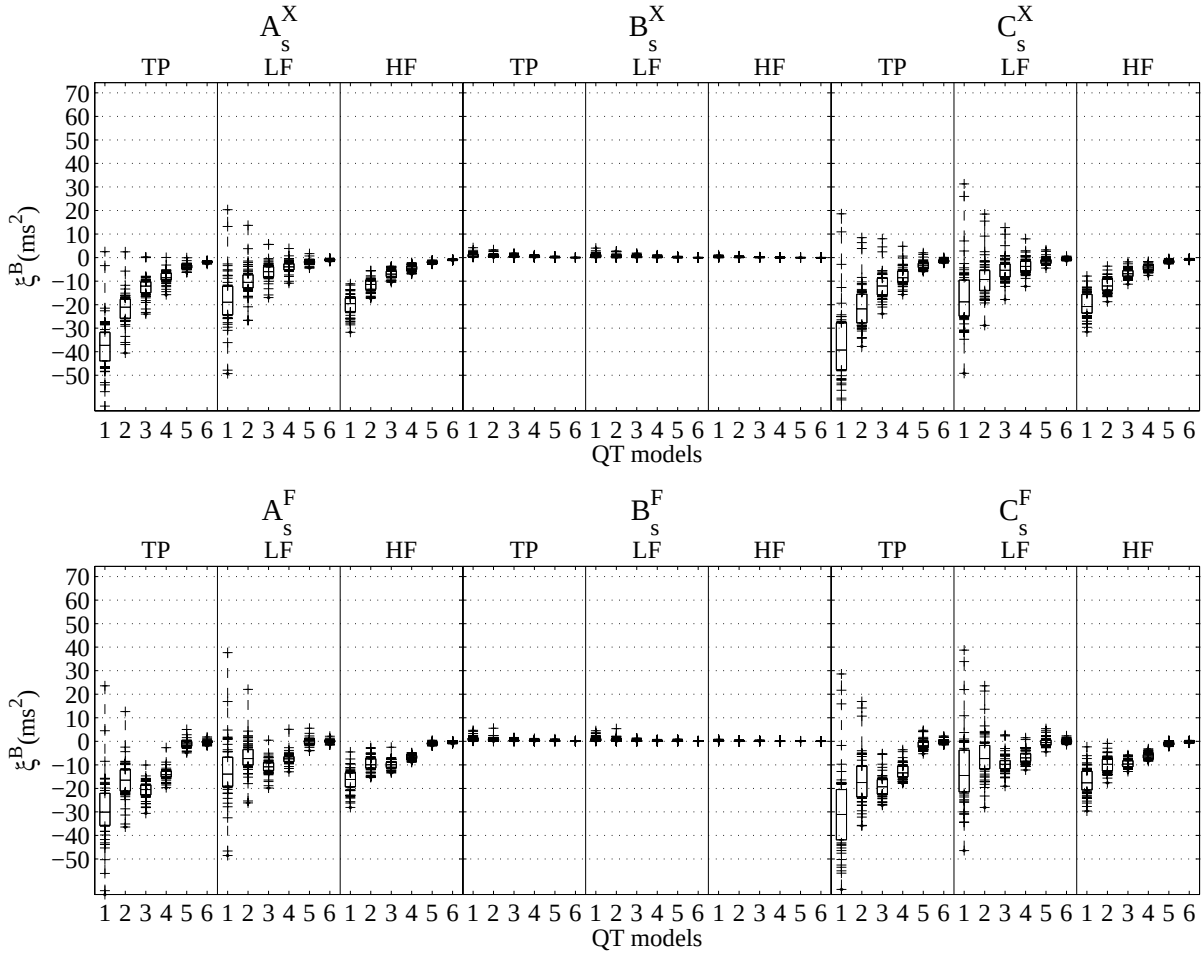

Figure 4.8: Distributions of the absolute errors ξ in data sets A_s^X, B_s^X,C_s^X,A_s^F, B_s^F,C_s^F: box-and-whisker plot by frequency band (+ stands for values out of the quartiles box).

It should also be remarked from Table 4.4 that:

- in all cases for every QT reference models using single-lead delineation
  - $\left|\overline{\varepsilon}^{HF}\right| \leq 10.1\%$ ($s_\varepsilon^{HF} \leq 6.8\%$),
  - $\left|\overline{\varepsilon}^{LF}\right| \leq 2.9\%$ ($s_\varepsilon^{LF} \leq 11.2\%$),
  - $\left|\overline{\varepsilon}^{TP}\right| \leq 8.2\%$ ($s_\varepsilon^{TP} \leq 7.1\%$).
- in all cases for QT models with $\sigma_{\mathrm{QT}} \in \{17, 13, 5, 3\}$ ms (models 1, 2, 5, 6), using multilead delineation
  - $\left|\overline{\varepsilon}^{HF}\right| \leq 11.6\%$ ($s_\varepsilon^{HF} \leq 6.2\%$),
  - $\left|\overline{\varepsilon}^{LF}\right| \leq 5.4\%$ ($s_\varepsilon^{LF} \leq 10.2\%$),
  - $\left|\overline{\varepsilon}^{TP}\right| \leq 8.3\%$ ($s_\varepsilon^{TP} \leq 7.2\%$).

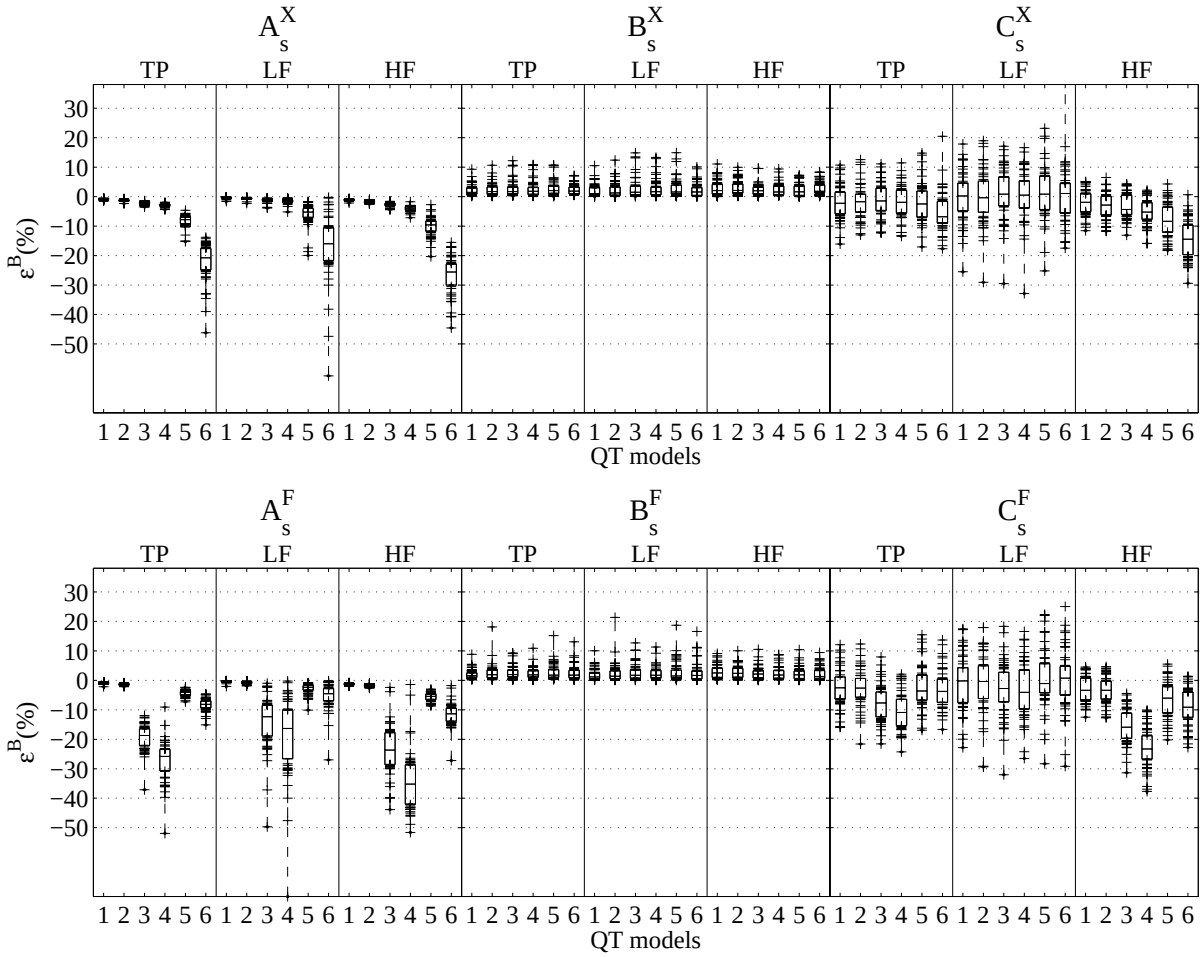

Figure 4.9: Distributions of the percentage errors ε in data sets A_s^X, B_s^X,C_s^X,A_s^F, B_s^F,C_s^F: box-and-whisker plot by frequency band (+ stands for values out of the quartiles box).

Again, for models with $\sigma_{\mathrm{QT}} \in \{17, 13\}$ ms (QT models 3 and 4) a greater error is denoted with multilead delineation. The worse performance over multilead based data sets, in particular for dependency case A, should not be related with the QTV level, as the results for QT models 5 and 6 ($\sigma_{\mathrm{QT}} \in \{5, 3\}$ ms) are better than for QT models 3 and 4. It should also be noticed that for dependency cases A or B, one of the fractions to be quantified is zero, which is unrealistic and make the estimation more difficult.

4.3.2 Noise contamination

Respiratory like effect contamination

The results over ECG signals with respiratory like effect contamination (data sets C_r^X and C_r^F) are summarized in Tables 4.5 and 4.6, with correspondent distributions of $\xi^{\mathcal{B}}$ and $\varepsilon^{\mathcal{B}}$ in Figures 4.10 and 4.11, respectively.

Table 4.5: Mean and standard deviation of the absolute errors $\xi^{\mathcal{B}}$ in data sets C_r^X and C_r^F $(ms^2, mean \pm sd)$; ; number of valid models (#) are also presented for each data set; reference measures ($P^{\mathcal{B}}_{\mathrm{QT|RR}}$, $P^{\mathcal{B}}_{\mathrm{QT|QT}}$) can be found in Table 2.2.

QT model	$\mathcal{B}$	C_r^X #	C_r^X $\bar{\xi}^{\mathcal{B}} \pm s_\xi^{\mathcal{B}}$	C_r^X $\frac{\lvert\bar{\xi}^{\mathcal{B}}\rvert}{P^{\mathcal{B}}_{\mathrm{QT\lvert RR}}} \pm \frac{\lvert s_\xi^{\mathcal{B}}\rvert}{P^{\mathcal{B}}_{\mathrm{QT\lvert RR}}}$	C_r^F #	C_r^F $\bar{\xi}^{\mathcal{B}} \pm s_\xi^{\mathcal{B}}$	C_r^F $\frac{\lvert\bar{\xi}^{\mathcal{B}}\rvert}{P^{\mathcal{B}}_{\mathrm{QT\lvert RR}}} \pm \frac{\lvert s_\xi^{\mathcal{B}}\rvert}{P^{\mathcal{B}}_{\mathrm{QT\lvert RR}}}$
1	TP	48	-37.8 ± 14.8	-34.7 ± 13.6	48	-29.3 ± 17.1	-26.9 ± 15.7
	LF	48	-18.3 ± 12.7	-30.2 ± 21	48	-12.4 ± 14.9	-20.5 ± 24.7
	HF	48	-19.6 ± 6.6	-40.4 ± 13.7	48	-16.9 ± 5.4	-34.9 ± 11.1
2	TP	48	-21.2 ± 9.7	-34 ± 15.5	48	-17.2 ± 10.1	-27.6 ± 16.2
	LF	48	-10.5 ± 8.4	-31 ± 24.6	48	-7.2 ± 9.4	-21.2 ± 27.6
	HF	48	-10.7 ± 4.9	-37.6 ± 17	48	-10 ± 3.1	-35.3 ± 11
3	TP	48	-11.6 ± 5.8	-30.5 ± 15.2	48	-14 ± 5.6	-36.7 ± 14.7
	LF	48	-6.8 ± 4.3	-32.1 ± 20.6	48	-6.5 ± 4.9	-30.6 ± 23.3
	HF	48	-4.9 ± 4.2	-28.5 ± 24.8	48	-7.6 ± 1.8	-44.2 ± 10.5
4	TP	48	-6.4 ± 4.9	-25.6 ± 19.6	48	-9.5 ± 3.7	-38 ± 14.8
	LF	48	-4.4 ± 3.6	-31.2 ± 25.8	48	-4.6 ± 3.3	-33 ± 23.3
	HF	48	-2.1 ± 3.8	-18.5 ± 34.2	48	-4.9 ± 1.2	-44.4 ± 10.5
5	TP	48	-0.9 ± 3.4	-9.4 ± 35.7	48	-2 ± 1.8	-21.3 ± 19.1
	LF	48	-1.7 ± 1.3	-30.5 ± 24.2	48	-0.8 ± 1.6	-14.7 ± 28.9
	HF	48	0.8 ± 3.1	18.8 ± 75.5	48	-1.2 ± 0.6	-30.3 ± 13.6
6	TP	48	1.3 ± 2.6	38.1 ± 79.3	48	-0.5 ± 0.6	-16.5 ± 19.5
	LF	48	-0.6 ± 0.4	-34.4 ± 21.5	48	-0.2 ± 0.6	-9.3 ± 31.8
	HF	48	1.9 ± 2.6	125 ± 176.1	48	-0.4 ± 0.3	-25.1 ± 17.2

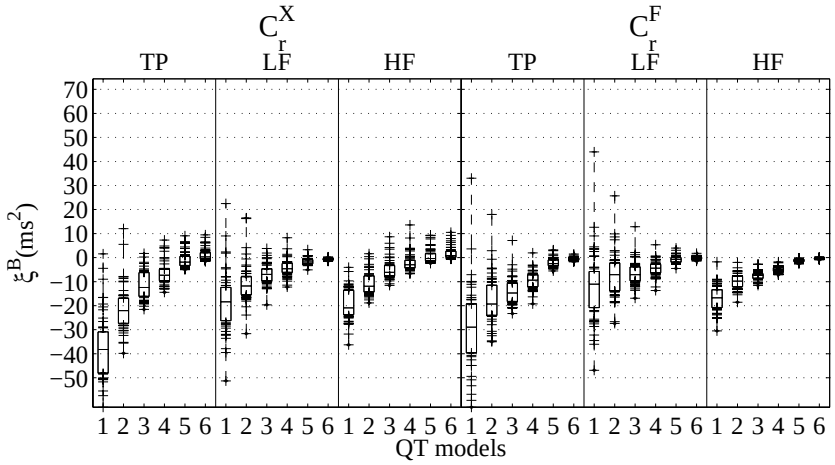

Figure 4.10: Distributions of the absolute errors ξ in data sets C_r^X and C_r^F - box-and-whisker plot by frequency band (+ stands for values out of the quartiles box).

Table 4.6: Mean and standard deviation of the percentage errors $\varepsilon^{\mathcal{B}}$ in data sets C_r^X and C_r^F $(\%, mean \pm sd)$; the reference value of $R^{\mathcal{B}}_{\mathrm{QT|RR}}$ can be found in Table 2.3.

		C_r^X	C_r^F
QT model	$\mathcal{B}$	$\overline{\varepsilon}^{\mathcal{B}} \pm s_\varepsilon^{\mathcal{B}}$, %	$\overline{\varepsilon}^{\mathcal{B}} \pm s_\varepsilon^{\mathcal{B}}$, %
1	TP	-14.19 ± 5.71	-2.69 ± 5.97
	LF	2.27 ± 9.31	-0.65 ± 8.77
	HF	-39.23 ± 6.03	-5.06 ± 4.22
2	TP	-21.18 ± 6.27	-3.2 ± 6.04
	LF	1.1 ± 10.9	-0.94 ± 9.86
	HF	-49.35 ± 5.69	-6.65 ± 3.91
3	TP	-30.6 ± 5.31	-4.51 ± 5.88
	LF	-1.75 ± 10.37	0.73 ± 8.71
	HF	-57.36 ± 5.65	-14.68 ± 4.97
4	TP	-35.75 ± 5.51	-6.72 ± 6.66
	LF	-1.46 ± 12.1	-0.62 ± 12
	HF	-63.36 ± 5.22	-19.95 ± 4.5
5	TP	-40.6 ± 5.8	-7.06 ± 6.88
	LF	0.93 ± 10	-0.8 ± 9.9
	HF	-60.98 ± 6.12	-19.03 ± 5.92
6	TP	-45.29 ± 4.95	-13.48 ± 5.82
	LF	-3.66 ± 10.44	-2.31 ± 10.07
	HF	-62.09 ± 5.37	-30.68 ± 5.83

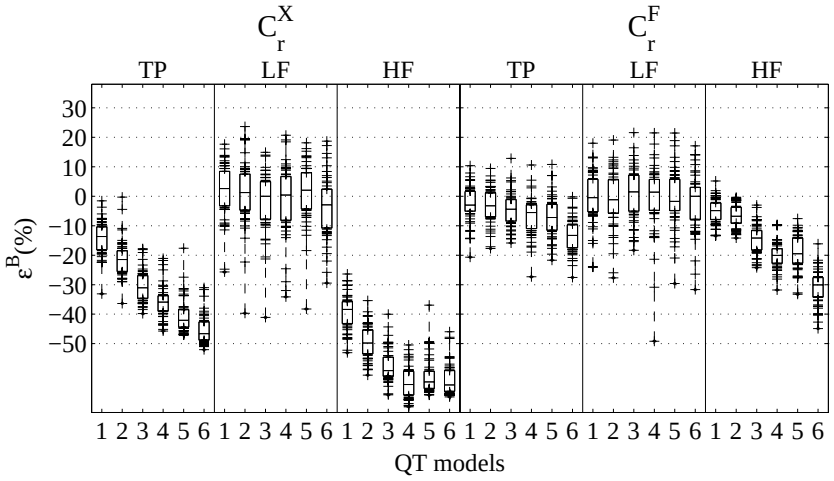

Figure 4.11: Distributions of the percentage errors ε in data sets C_r^X and C_r^F - box-and-whisker plot by frequency band (+ stands for values out of the quartiles box).

For any QT reference model and delineation approaches 48 (out of 50) valid estimated models were found. Comparing with the results on signal derived data sets with no noise contamination (previous section), there were no relevant effects on the absolute error ($\xi^{\mathcal{B}}$) distributions as result of the respiratory like noise, rather than a slightly increase of dispersion in HF band. Again its relative value does not increase with the QTV. The percentage errors ($\varepsilon^{\mathcal{B}}$) presented an important bias for HF band with the SL delineation , that increases with the QTV level reduction. This effect is much attenuated considering multilead delineation (data set C_r^F).

MIT pre-recorded Noise

The results over the data sets corresponding to each type of MIT pre-recorded noise (bw - baseline wandering, em - electrode movement, ma - muscular artifacts) were analysed separately.

The distributions of the absolute errors $\xi^{\mathcal{B}}$ and percentage errors $\varepsilon^{\mathcal{B}}$, for $\mathcal{B} \in= \{LF, HF\}$, are plotted in Figures 4.12, 4.13 and 4.14, respectively for bw, em and ma type of contamination. For the sake of comparison, the distributions of $\xi^{\mathcal{B}}$ over data sets C_c and C_s^X were also included. For the sake of completeness, the results are also summarized in Appendix E of this thesis, regarding $\xi^{\mathcal{B}}$ (Tables E.1, E.2 and E.3) and with respect to $\varepsilon^{\mathcal{B}}$ (Tables E.4, E.5 and E.6).

From those tables, it can be conclude that a minimum of 48 (out of 50) valid estimated models for each QT reference model were found for every data set and noise type in data set.

Both bias and dispersion of $\xi^{\mathcal{B}}$ were found to be increased compared with the values found with single-lead delineation with dependency case C without noise contamination (Table 4.3 and Figure 4.9), however only the error dispersion increases with the noise level. Again it was noticed an apparent reduction in $\xi^{\mathcal{B}}$ bias and dispersion resulting from QTV level decrease that become smaller or disappears when relative values are considered.

A negative bias of $\varepsilon^{\mathcal{B}}$, specially marked in for $\mathcal{B} = HF$, was noticed with progressive increase with noise contamination. This performance decay was more evident with QT reference models corresponding to lower σ_{QT}, presenting important levels in HF for baseline contamination even with $SNR = 30$ dB (QT models 3 to 6). The method is slightly more robust to other contamination types with intermediate SNR levels, in particular to electrode movement artifacts contamination.

Globally, $\left|\varepsilon^{\mathcal{B}}\right| \leq 25\%$ for:

- over 82% of segments in data sets with SNR > 15 dB and $\sigma_{\mathrm{QT}} > 5$ ms, in the LF band;
- over 56% of segments in data sets with SNR > 20 dB and $\sigma_{\mathrm{QT}} > 10$ ms, in the HF band.

Therefore, it can be concluded that LF band is clearly less affected in all data sets.

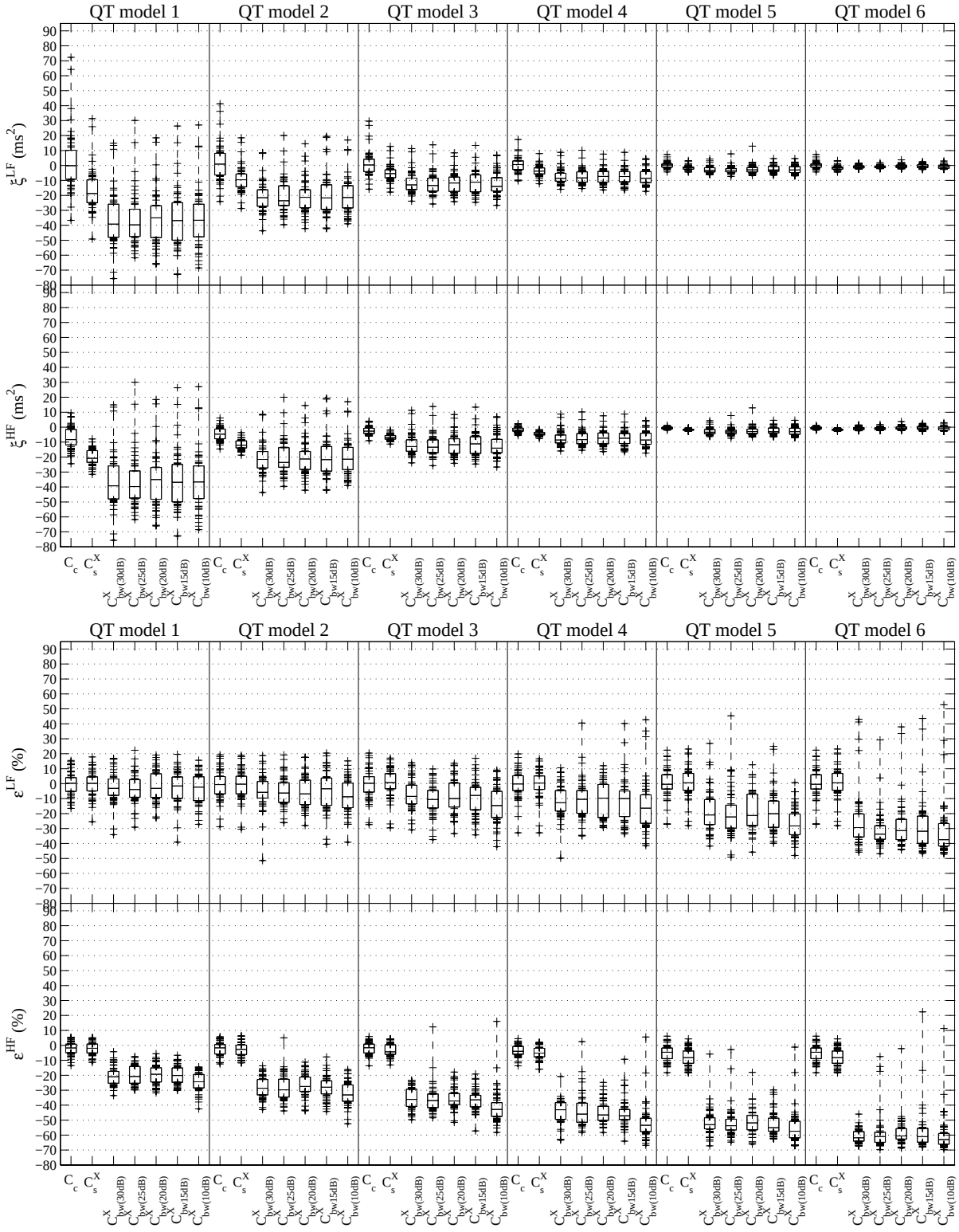

Figure 4.12: Distributions of the errors $\varepsilon^{\mathcal{B}}$ and $\xi^{\mathcal{B}}$ in data sets with baseline wandering contamination (*bw* MIT pre-recorded Noise) - box-and-whisker plot by data set and frequency band.

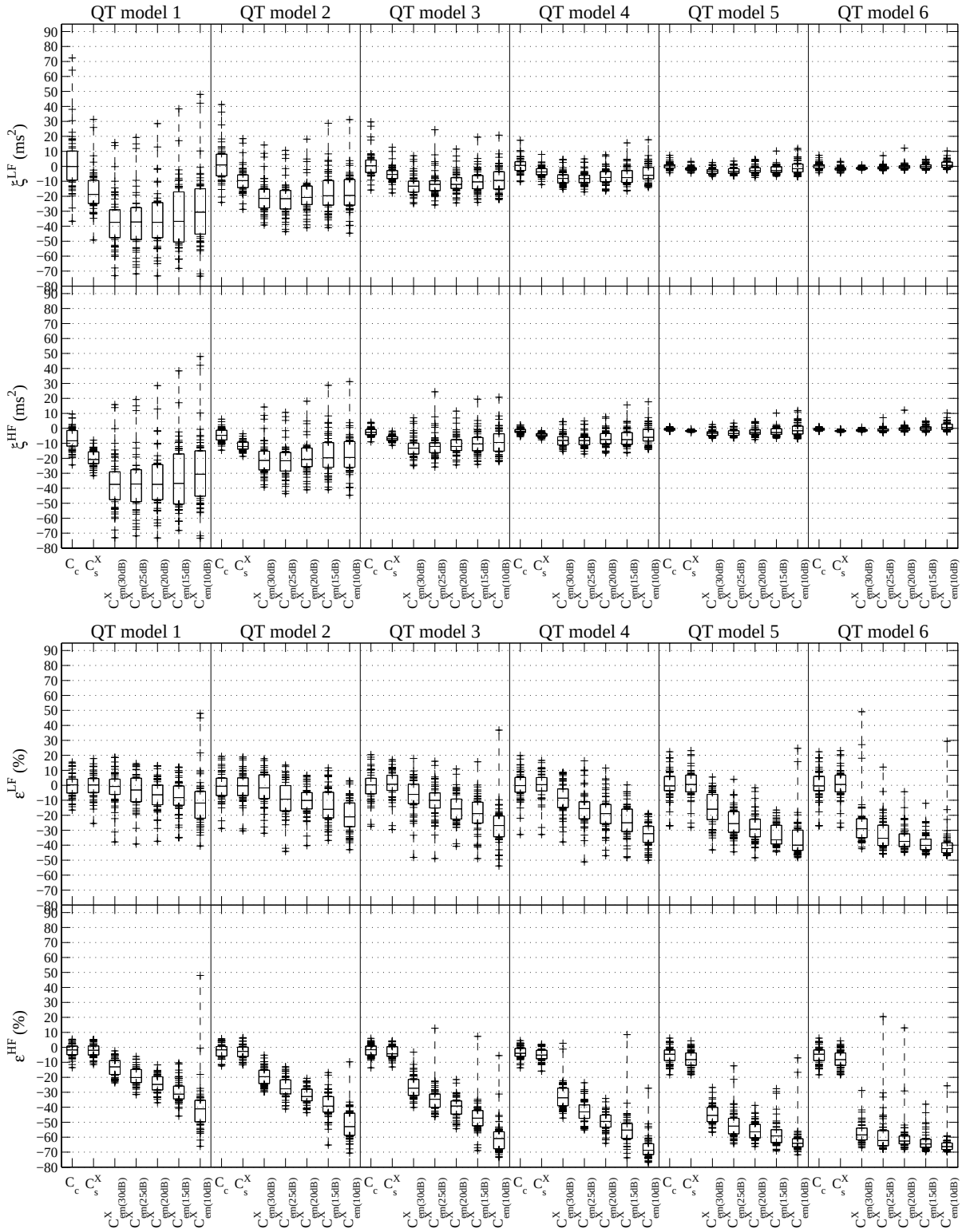

Figure 4.13: Distributions of the errors $\varepsilon^{\mathcal{B}}$ and $\xi^{\mathcal{B}}$ in data sets with electrode movement contamination (*em* MIT pre-recorded Noise) - box-and-whisker plot by data set and frequency band.

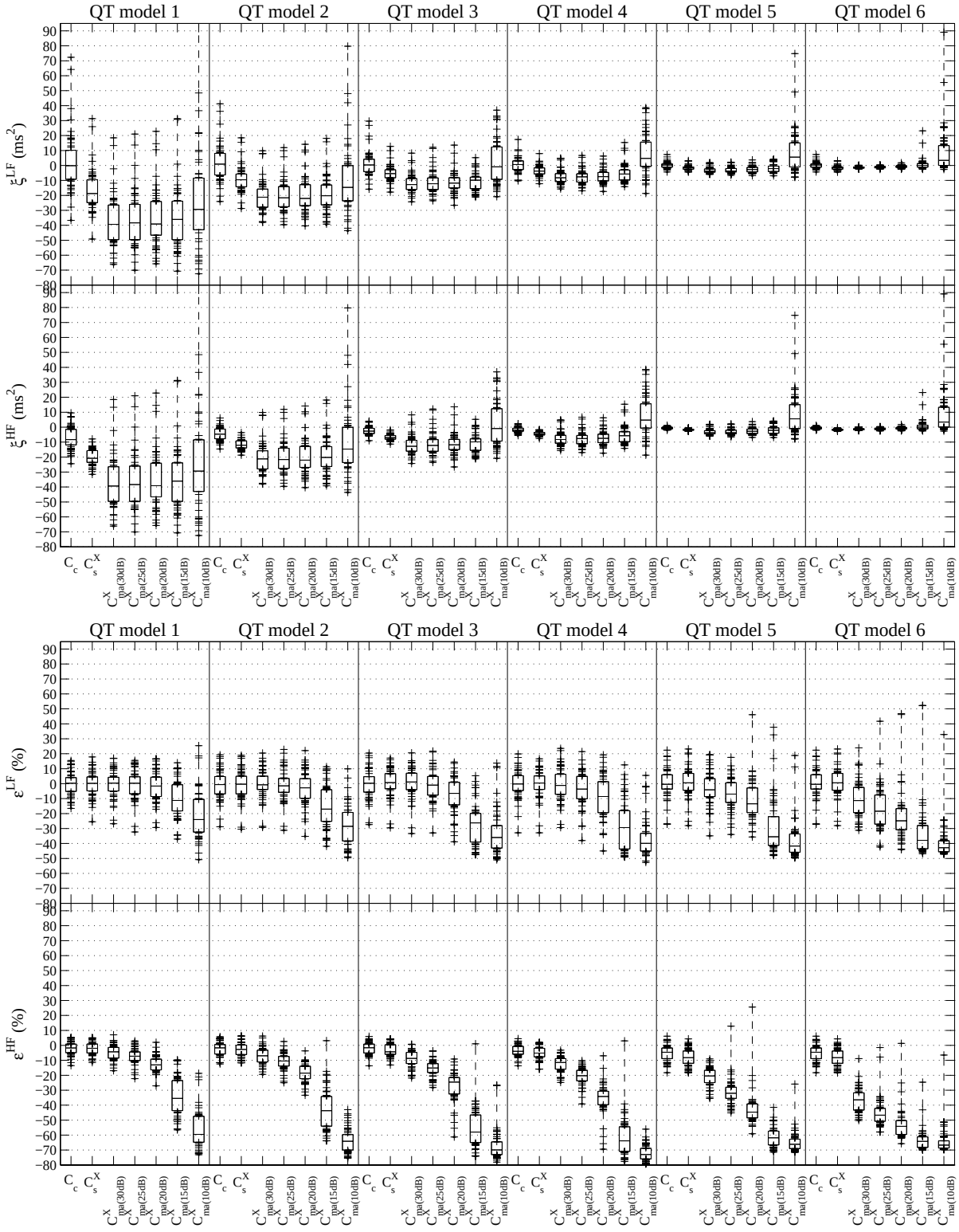

Figure 4.14: Distributions of the errors $\varepsilon^{\mathcal{B}}$ in data sets with muscular artifacts contamination (*ma* MIT pre-recorded Noise) - box-and-whisker plot by data set and frequency band.

3-lead extracted Noise

The distributions of $\varepsilon^{\mathcal{B}}$ and $\xi^{\mathcal{B}}$ obtained over simulated ECG with 3-lead extracted noise are plotted in Figures 4.15 and 4.16. Again the errors distribution found in data sets C_c and C_s^X were also included, for the sake of comparison. The results over these data sets are summarized in Tables E.7, E.9, E.8 and E.10, all presented in Appendix E.

Valid estimated models were found for more than 97% of the segments, considering single or multilead delineation, with a minimum of 94% segments with valid models found in each data set. The results relative to SL delineation are very similar to the ones obtained for the MIT recorded noise, reflecting the much poorer performance in HF than in LF. As was already noticed over the results without noise contamination (Section 4.3.1), using ML the performance decrease with QTV level reduction is not clear (as QT models 5 and 6, with the lowest σ_{QT} present less percentage error than QT models 3 and 4).

The errors found in the LF band were fund to be $\left|\varepsilon^{\mathcal{LF}}\right| \leq 25\%$:

- in over 75% of segments in data sets with SNR > 20 dB and $\sigma_{\mathrm{QT}} > 3$ ms, for SL delineation;
- in over 74% of segments in data sets with SNR > 15 dB and $\sigma_{\mathrm{QT}} > 3$ ms, for ML delineation;

The errors found in the HF band were fund to be $\left|\varepsilon^{\mathcal{HF}}\right| \leq 25\%$:

- in over 67% of segments in data sets with SNR > 20 dB and $\sigma_{\mathrm{QT}} > 10$ ms, for SL delineation;
- in over 95% of segments in data sets with SNR > 20 dB and $\sigma_{\mathrm{QT}} > 10$ ms, for ML delineation.

The use of ML delineation allows an error reduction in the intermediate SNR levels, both in LF and HF, increasing the robustness of the methodology.

For lower SNR (≤ 15 dB), the data sets derived from ML delineation are very small or empty, and thus no results are available. It should be remarked that using SL delineation the results for very low SNR indicate that the parametric methodology is not applicable due to the large errors involved.

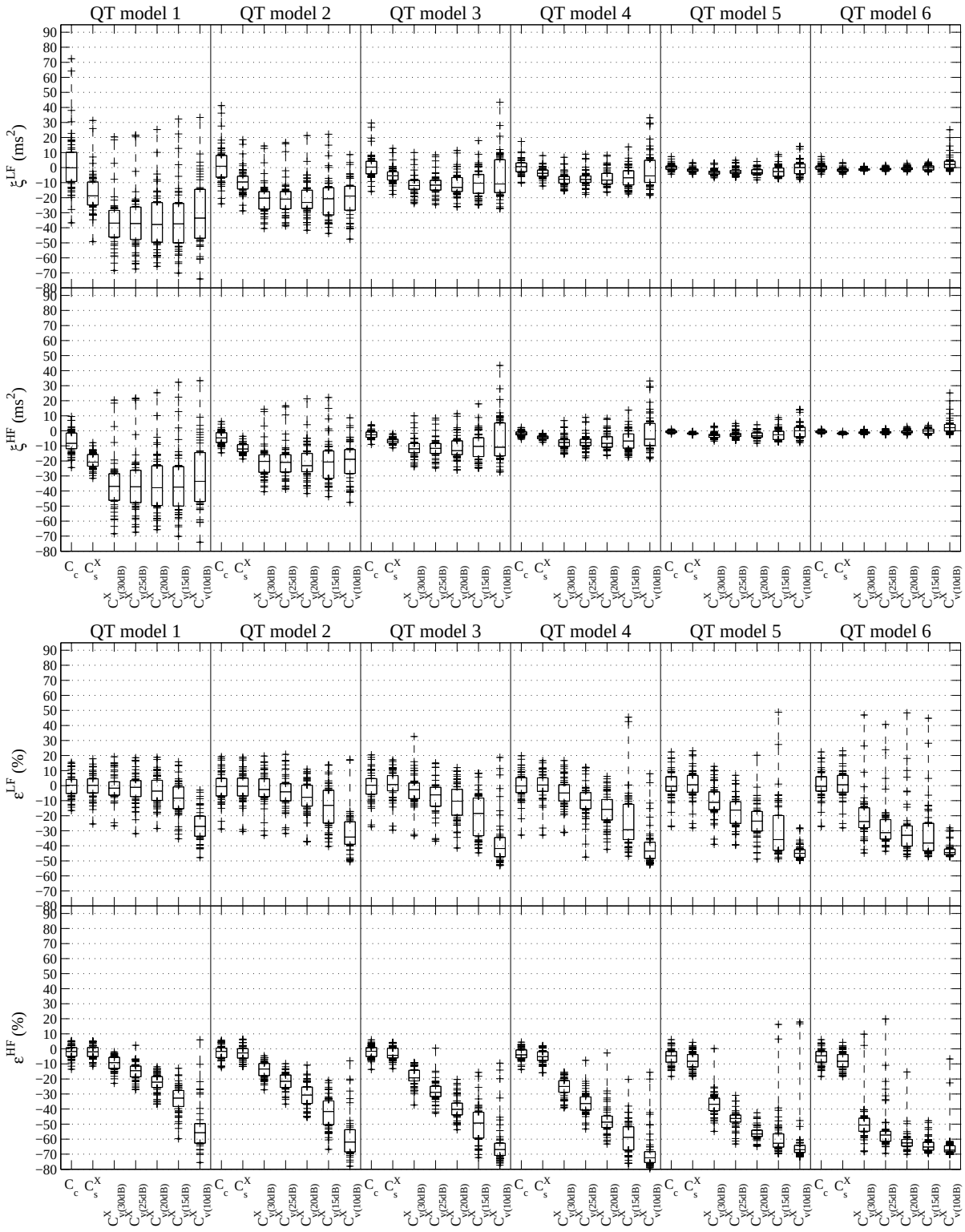

Figure 4.15: Distributions of the errors $\varepsilon^{\mathcal{B}}$ and $\xi^{\mathcal{B}}$ in data sets corresponding to single-lead based delineation of ECG contaminated with real 3-lead extracted Noise - box-and-whisker plot by data set and frequency band.

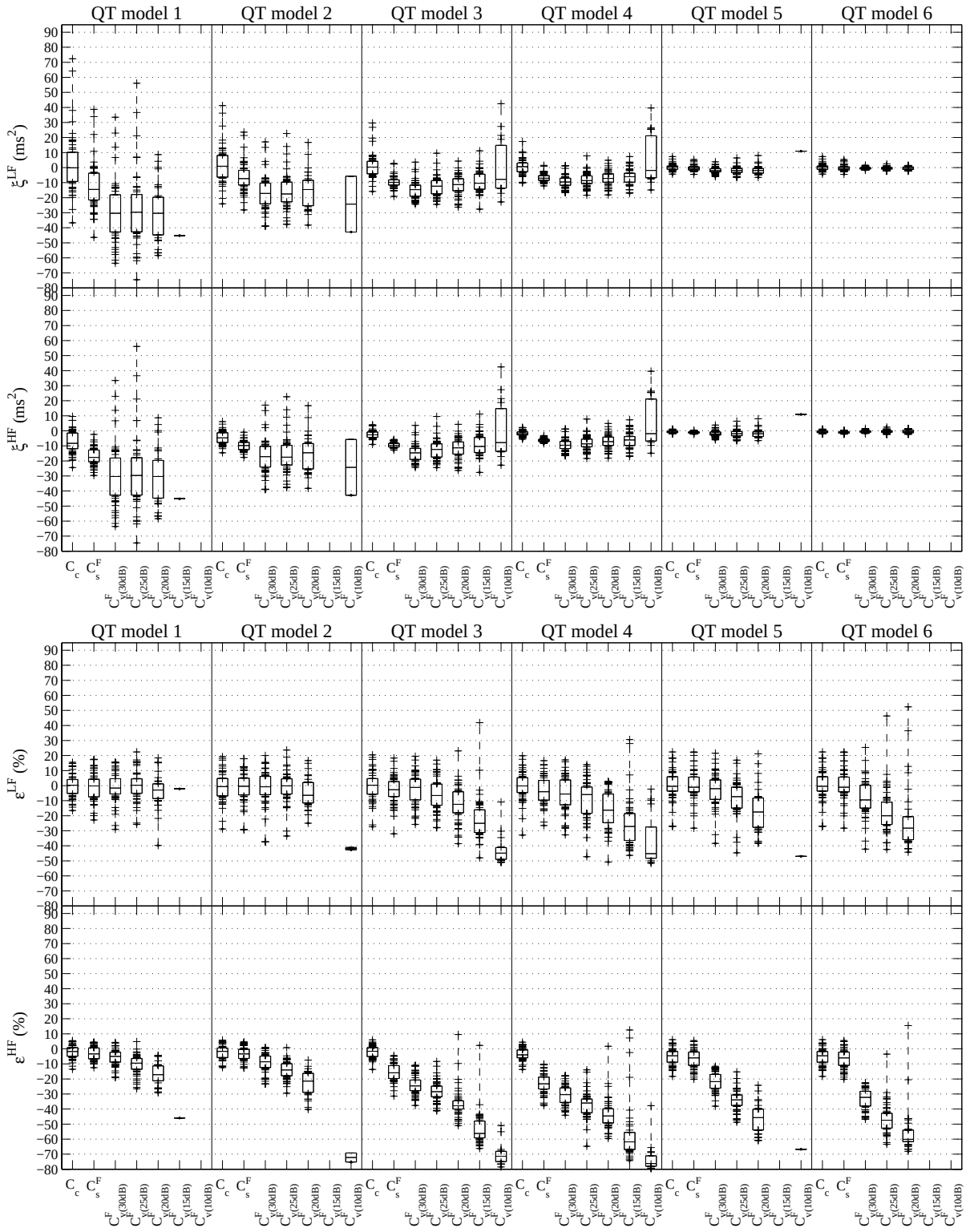

Figure 4.16: Distributions of the errors $\varepsilon^{\mathcal{B}}$ and $\xi^{\mathcal{B}}$ in data sets corresponding to multilead based delineation of ECG contaminated with real 3-lead extracted Noise - box-and-whisker plot by data set and frequency band.

4.4 Concluding Remarks

The strategy used for simulating the artificial ECG signals aims to keep realistic features in which the automatic delineators are based on, such as slopes and time intervals. Nevertheless a small amount of QTV was missed using any of the automatic delineation strategies. As should be expected, the noise effects increased delineation errors, introducing spurious QTV.

The results allow to conclude that over the simulated data:

- the multilead strategy missed less QTV, in most of the data sets with no noise contamination;
- the multilead strategy introduced less spurious QTV, facing respiratory noise;
- no relevant differences were noticed between single-lead/multilead delineation methods, facing noise regarding 3-lead extracted noise SNR $>$ 10 dB.

Adequate model identification was possible for more than 95% of the qualified segments. As expected, the joint performance of the delineation and parametric approaches depended both on the QTV level and on the noise level.

Nevertheless, using multilead delineation, it is difficult to establish the degree of performance decrease with QTV level reduction, as QT models 5 and 6, corresponding to the lowest σ_{QT}, present repeatedly less percentage error than QT models 3 and 4. This result can be related with the specific models parameters used in simulation, rather than with the aspects here under consideration (QTV and SNR level). To further clarify this point a different simulation approach or using different reference models should be considered.

The power of the QTV fraction correlated with HRV was underestimated for most of the data sets, what can be related with the global QTV missed by delineation. Moreover,

- in the presence of *moderate noise* (SNR$\geq$ 20 dB):
  - the quality of the $P^{\mathcal{B}}_{\mathrm{QT|RR}}$ estimation decreased with SNR level, but not to unusable levels, as far as the level of QTV to be measured is not too low ($\sigma_{\mathrm{QT}} \geq 10$ ms);
  - a better performance of multilead delineation is noticed (3-lead extracted noise).
- for noise contamination corresponding to $SNR \leq 15dB$
  - delineation errors produced more $x_{\mathrm{RR}}(n)$ outliers and QT intervals are more frequently missed, which difficult the finding of adequate segments of data, especially using multilead delineation;
  - even in qualified segments, the parametric method is hardly applicable (except maybe for the highest QTV level).

It should also be noticed that for QT reference models with $\sigma_{\mathrm{QT}} \leq 5$ ms, a worse performance can be related not only with the lower QTV levels but also with insufficient ECG time resolution (2 ms) resulting from the sampling frequency used in this study.

The spurious QTV resulting from noise should be quantified as not related with RR. Thus, the ratio underestimated the importance of $P^{\mathcal{B}}_{\mathrm{QT|RR}}$ in total QTV and the bias of the fraction of QTV driven by RR ($R^{\mathcal{B}}_{\mathrm{QT|RR}}$) increases with SNR decrease in a more marked way than the bias of the error in the power measures.

Finally it should be stressed that, considering both the data sets with MIT recorded and 3-lead extracted noise:

the joint performance of single-lead delineation plus variability analysis achieved less than 25% error

- in over 82% of segments in data sets with SNR > 15 dB and $\sigma_{\mathrm{QT}} > 5$ ms in LF band;
- in over 59% of segments in data sets with SNR > 20 dB and $\sigma_{\mathrm{QT}} > 10$ ms in HF band.

the joint performance of multilead delineation plus variability analysis achieved less than 25% error

- in over 74% of segments in data sets with SNR > 15 dB and $\sigma_{\mathrm{QT}} > 3$ ms in LF band;
- in over 95% of segments in data sets with SNR > 20 dB and $\sigma_{\mathrm{QT}} > 10$ ms in HF band.

Thus, for the LF band, the methods were able to estimate satisfactory both QTV fractions in most of the files, using any of the delineation approaches. Nevertheless, multilead delineation allowed the quantification in data sets corresponding to lower QTV levels.

With respect to HF band, single-lead delineation performed unsatisfactory in a large number of segments, and thus this band should only be studied when multilead delineation is possible and, even so, in a critical way.

Chapter 5

Studies in Real data

The automatic methodology proposed in this thesis, ECG delineation and the study of QTV versus HRV relations, was jointly evaluated in Chapter 4 in a realistic context by using artificial simulated *3-lead* ECG signals.

The robustness of the methods was further tested by adding noise to the simulated ECG signals considering different noise types and levels. An indicative framework of applicability was obtained, as function of QTV and noise levels. The adequateness of the methods proposed in this thesis for studying QTV versus HRV relations on ECG files with moderate noise contamination was confirmed and the application to real ECG files can be faced.

This Chapter illustrates the application of the automatic methods proposed to clinical signals, namely ECG Holter recordings.

The results obtained over real ECG recordings from POLI/MEDLAV database and ECG HOLTER recordings are detailed presented. Namely, the methods were illustrated over ECG files from pediatric patients of an intensive care unit.

5.1 Introduction

The validation of the methods presented in this thesis over simulated data allowed to conclude their adequateness for studying QTV/HRV relations, particularly on the framework of applicability described. This Chapter aims to illustrate the application of the methods in real ECG data.

To fully illustrate the methodology it is essential to have access to multilead ECG data including 3 orthogonal leads (preferentially with Frank leads or 12-leads) and with an adequate sampling frequency (F_s). Risk *et al.* (2005) recommended $F_s > 300$ Hz for QT measurement, moreover no relevant differences were reported for 300 Hz $< F_s <$ 500 Hz.

Among the standard multilead ECG databases presently available, only the **POLI/MEDLAV** (POLItecnico/MEDicina del LAVoro) database (Pinciroli *et al.*, 1998), here denoted as PMDB, fulfils the requirements. Other databases either do not include 3 orthogonal leads, present a too low F_s value or the records are too short for studying variability.

To reduce the possibility of spurious QTV the sampling frequency should be as high as possible, allowing a high time resolution. The acquisition of Mortara H12+ Holter Recorders and high resolution 1000 Hz flash cards in the framework of ongoing research projects allowed to begin the collection of clinical data in early 2006. Also experimental software for research purposes, provided by the equipment supplier (*Mortara Rangoni Italy*), made possible the 12-lead ECG signal extraction.

The real data considered and the approaches used (namely the delineation strategy) are described in the next Sections.

5.2 Real data description

The **POLI/MEDLAV** database (PMDB) on respiratory and ECG recordings was constructed for the evaluation of interactions between ECG and respiration on young subjects (Pinciroli *et al.*, 1998). Files from this database were already used to motivate and illustrate the work presented in previous Chapters in this thesis.

The database consists in 20 ECG recordings with Frank leads (X, Y, Z), plus 2-channels with respiratory signals: respiratory air flow and body volume variation. The recordings are from 20 young normal subjects, have 24 minutes of duration at 500 Hz (the file *ra1* was excluded from the analysis, since $F_s = 250$ Hz for this one file). PMDB only contains reference annotations for the QRS complex position which were not used in this work.

The **Holter** ECG recordings were made according the standard 12-lead system, using the *Mortara H12+* Holter Recorders with high resolution 1000 Hz 512Mb flashcards (Mortara 11018-002-50). The ECG signals were extracted using the software specially provided for research purposes from *Mortara*.

Using this equipment, an illustrative 24-hour Holter recording from a 21 years volunteer was collected and the first 30 min of each hour taken to illustrate the methods application for ambulatory data.

An Holter data set comprising recordings from children admitted in the pediatric intensive care unit of Hospital de S. João, Porto (PICU) was also gathered. The pediatric data was collected under the project *"Análise de variabilidade cardiovascular em doença crítica: seguimento e prognóstico"* [1]. This project was approved by the ethic commission of Hospital de S. João and by the Portuguese data protection authority (*Comissão Nacional de Protecção de Dados*).

Critically ill patients with acute central nervous system pathology also exhibit a number of changes in HR and cardiovascular control, which reflect ANS dysfunctions. Also, there are under the influence of several drugs that have direct an indirect effect over the ANS and cardiac function. Thus, the QTV and its HRV dependence are likely to be affected by the ANS dysfunctions and the intense pharmacologic therapy.

From each PICU patient, an Holter recording was taken within 24h of the admission time, and successive follow-up every 24h until clinical discharge. The data herein analysed corresponds to a total of 36 recordings collected from 9 patients, distributed as summarized in Table 5.1. Patients 6 to 9 had suffered a traumatic brain injury (TBI) while patients 1 to 5 were admitted at PICU for diverse non TBI related causes. In particular the patient 3 had suffered an airway obstruction due to a foreign object and brain death outcome. All the other patients have survived.

The typical length of each recording is between 45 and 60 min, with longer recordings for patients 7 and 9 (one recording for patient 7, 12 h long; five recordings for patient 9, with 6 h at admission, 2 h, 14 h, 1 h and 2 h of successive follow-up). The first 30 min of each hour recorded were considered in the data set, with a total of 67 ECG excerpts.

5.3 Data processing

The ECG recordings described in the previous section were delineated using the automatic systems presented in this thesis and considering lead sets previously discussed (Chapter 3).

- For PMDB data, each of the ECG leads (X, Y and Z) was processed using the single-lead based automatic delineation system (SL). The multilead automatic system (ML) described was applied over lead set F (Frank leads).
- For Holter data, the multilead delineation system (ML) was applied over lead set D (synthesised orthogonal Frank system using Dower transformation), and lead set M (leads $V5$, aVF and $V2$).

In analogy with the simulated data processing, the time series of RR and QT intervals obtained after delineation were carved up in *admissible segments* as previously stated, i.e. 350 consecutive beats with valid RR and QT intervals measurements. Several non-overlapping segments were admitted for the same ECG recording, constituting the data to be used in subsequent variability analysis.

[1]Project with participation of Faculdade de Ciências da Universidade do Porto, Faculdade de Medicina da Universidade do Porto and Unidade de Cuidados Intensivos Pediátricos do Hospital de S. João, Porto; funding from Projectos pluridisciplinares Universidade do Porto / Caixa Geral de Depósitos, Investigação Científica na pré graduação.

Table 5.1: Summary of recordings from PICU patients.

patient	1	2	3	4	5	6	7	8	9
age (years)	6	11	2	1	3	8	11	3	11
# recordings	2	2	4	9	5	4	1	4	5

Each segment is identified by an *id* of the form i_E, where i stands for the segment number and E stands for the lead ($E \in \{X, Y, Z\}$) or lead set ($E \in \{F, D, M\}$), in which the segment is based. The segment number i is sequential in time and along each data set. For the sake of comparison between lead sets, segments within 60% overlapping were considered to be simultaneous and the same segment segment number i was attributed.

5.3.1 Segments description

For each qualified segment were calculated the mean QT interval (T_{QT}), the QT standard deviation (s_{QT}) and the coefficient of variation ($CV = 100 s_{\mathrm{QT}}/T_{\mathrm{QT}}$). The SNR was also estimated from the ECG signal corresponding to the segment. The QT variability level is evaluated from the estimated s_{QT} value in each segment.

Moreover, the s_{QT} and SNR values were confronted with the limits of applicability established for simulated data as function of frequency band, QTV and SNR levels (Section 4.4). The qualification of applicability ("yes" or "no") obtained should be considered as indicative.

SNR estimation

In real ECG the clean and noise signals are unknown. In this work the SNR level was estimated in each segment as follows.

- For each lead $E \in \{X, Y, Z\}$ (Figure 5.1), a clean version of each beat, $y_n^E(k)$, was first obtained (Figure 5.2(a)), calculating a centered average of beats, which was stretched in amplitude to fit the current beat. Only the interval $QT(n)$, from the QRS onset ($l^{\mathrm{QRS}_{on_n}}$) to the T wave end ($l^{\mathrm{T}_{end_n}}$), was considered (lighter rectangle in Figure 5.1), in order to use the signal intervals in which the ECG signal predominates over the noise.
- The noise ($v_n^E(k)$, $E \in \{X, Y, Z\}$) in the current beat (Figure 5.2(b)) was estimated on the interval between QRS complexes ($QRS_{end\_onset}(n+1) =]\, l^{\mathrm{QRS}_n}, l^{\mathrm{QRS}_{n+1}}\, [$), in which the information of ECG signal is reduced and noise predominates (darker rectangle in Figure 5.1). A fifth-order Butterworth filter with cut-off frequency 10 Hz was used to further reduce the ECG related contribution (Thakor *et al.*, 1984) and better estimate the noise signal.

It was found that SNR can be adequately estimated if an average of 7 beats is considered in order to obtain the clean beat.

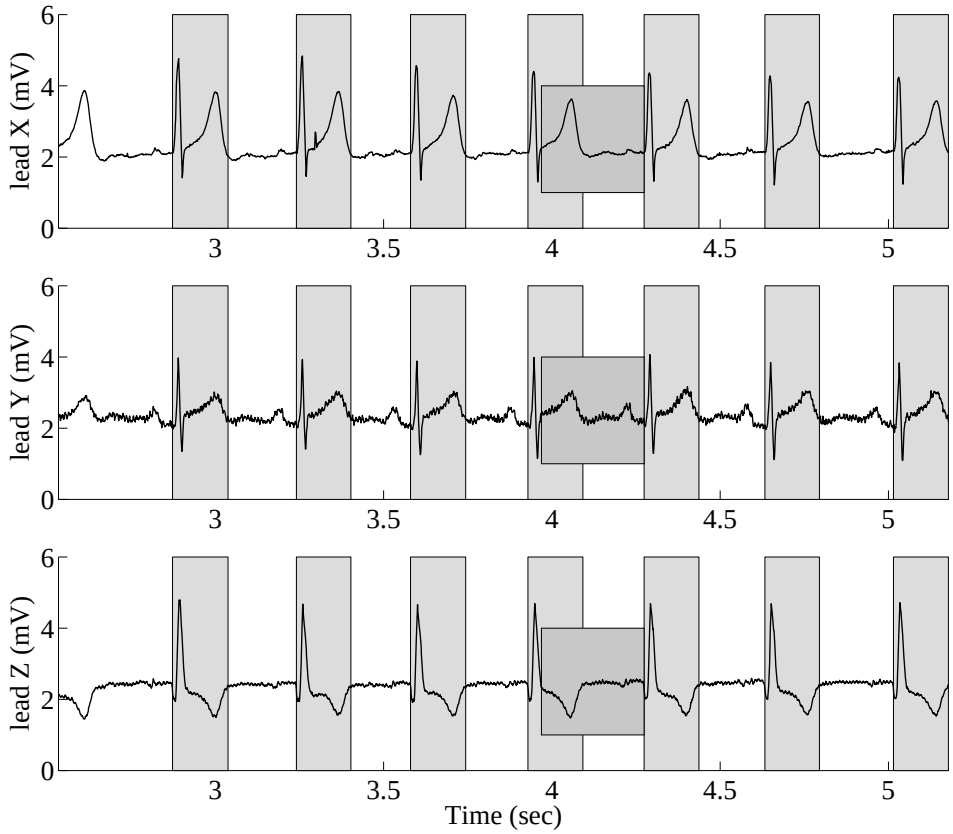

Figure 5.1: Intervals used in SNR estimation on a real ECG signal beat in each lead (X, Y and Z). Regarding the central complete beat on the figure (4^{th} beat), the construction of a clean beat considers the average of the 7 intervals $QT(n)$ in the lighter rectangles while the noise estimation considers the signal in the darker rectangle $QRS_{end\_onset}(n+1)$. Estimated clean beat and noise presented in Figure 5.2.

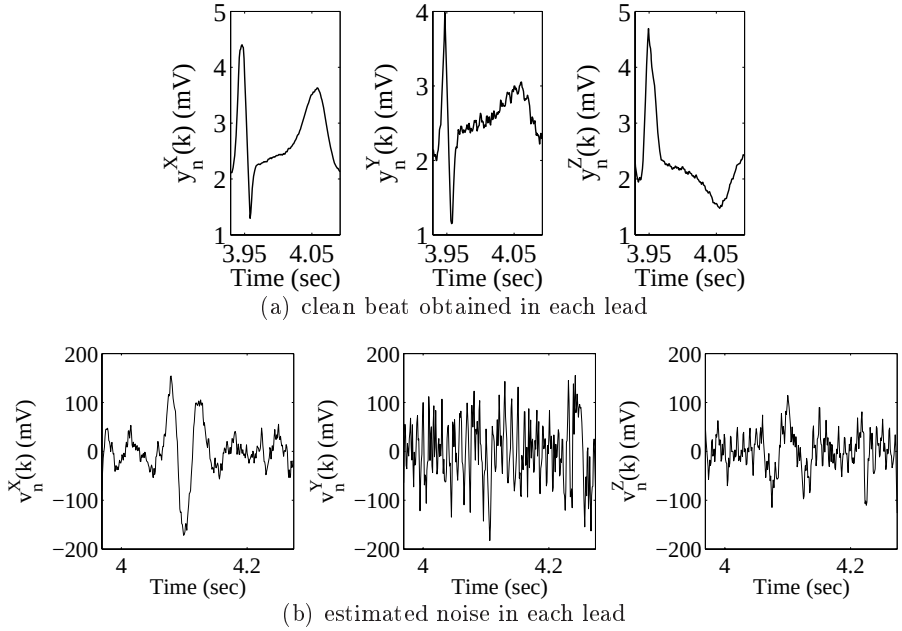

(a) clean beat obtained in each lead

(b) estimated noise in each lead

Figure 5.2: Estimated clean beat and noise in each lead (central complete beat in ECG from Figure 5.1).

The single-lead SNR value for each lead $E \in \{X, Y, Z\}$ considers the 350 beats in the segment and the marks provided for each beat n by the respective SL delineation

$$SNR = 20log_{10}\left(\frac{\sum_n \text{RMS}\left[y_n^E(k)\right]\sqrt{QT(n)}}{\sum_n \text{RMS}\left[v_n^E(k)\right]\sqrt{QRS_{end\_onset}(n+1)}}\right), E \in \{X, Y, Z\}; \quad (5.1)$$

The global multilead based SNR (SNR_{ML}) uses the marks provided by ML delineation for each beat n on the segment and the power in all three leads

$$SNR_{\text{ML}} = 20log_{10}\left(\frac{\sum_n \left(\text{RMS}\left[y_n^X(k)\right] + \text{RMS}\left[y_n^Y(k)\right] + \text{RMS}\left[y_n^Z(k)\right]\right)\sqrt{QT(n)}}{\sum_n \left(\text{RMS}\left[v_n^X(k)\right] + \text{RMS}\left[v_n^Y(k)\right] + \text{RMS}\left[v_n^Z(k)\right]\right)\sqrt{QRS_{end\_on}(n+1)}}\right) \quad (5.2)$$

The estimation of the SNR over real data is very different from the process to getting a target SNR level used in the simulation study (Sections 4.2.3 and 4.2.4). As a matter of fact, the whole available clean artificial ECG and noise signals were considered for calculating the power of signal and noise in the simulation, rather than selected ECG intervals.

5.3.2 Study of QTV/HRV relation

After automatic delineation of the ECG data, selection and characterization of the adequate segments as described before, the QTV/HRV relation was explored by the parametric methodology presented in Chapter 2.

The parametric methodology was applied over the optimally adequate orders selected according to AIC, as described in Section 2.3.2. The estimated QTV fraction correlated with HRV in each frequency band $\mathcal{B}$ ($\hat{R}^{\mathcal{B}}_{\text{QT|RR}}$) was calculated and the uncorrelated fraction ($\hat{R}^{\mathcal{B}}_{\text{QT|QT}}$) assumed as the remaining QTV.

For the segments that fulfilled the indicative limits of applicability, was also quantified how many presented a *relevant* QTV fraction not linearly driven by HRV, corresponding to $\hat{R}^{\mathcal{B}}_{\text{QT|QT}} \geq 40\%$. Thus, for each segment, it was arbitrary considered that a relevant QTV fraction not linearly driven by HRV to be present if $\hat{R}^{\mathcal{B}}_{\text{QT|RR}} < 60\%$. In this case the uncorrelated fraction would be large enough to be considered important.

5.4 POLI/MEDLAV database results

The admissible segments found in PMDB files are presented and described in Tables 5.2 to 5.4. Each segment obtained using SL is identified by an ID of the form i_E where i stands for the segment number and E the lead in which it is based on ($E \in X, Y, Z$); ML based segments have ID of the form i_F. The recordings names for which the valid segments were found are also indicated in the Tables. In Table 5.5 are presented the *minimum*, *mean*, *standard deviation (sd)* and *maximum* values found for s_{QT}, CV, and SNR for all the segments found for each lead system.

Using SL, respectively 29, 20 and 17 admissible segments were found over leads X, Y and Z, while 24 ML based segments were obtained. It should be noticed that for some recordings more than one segment was found. ML allowed to find admissible segments for 9 files (out of 19), and every segments were found simultaneously using SL in all least one lead (20 segments in at least two leads, 4 segments in only one lead). In 3 of these 9 files, one additional segment was also found in each file in only one lead (SL); in other 3 files segments were found using SL but not ML. For 7 files no segments were found by any delineation approach.

It should also be noticed that for some segments $s_{\mathrm{QT}} < 5$ ms and therefore, attending to the indicative limits of applicability, the QTV quantification may be not reliable in some of these files, in particular for the band HF no matter its SNR value.

Table 5.2: Description of PMDB segments on lead X ($CV = 100 s_{\mathrm{QT}}/T_{\mathrm{QT}}$). Last line indicates the number of: qualified segments, subjects, and segments in the indicative limits of applicability for each frequency band.

segment	recording	segment, beats		$x_{\mathrm{QT}}(n)$		SNR	Applicability	
id	name	begin	end	$T_{\mathrm{QT}} \pm s_{\mathrm{QT}}$, ms	CV, %	dB	LF	HF
1_X	ra2	248	597	328.4 ± 3.3	1.0	34	no	no
2_X	ra2	1157	1506	326.0 ± 3.1	1.0	34.2	no	no
3_X	ra2	1507	1856	320.6 ± 2.9	0.9	33.7	no	no
4_X	rb2	83	432	294.2 ± 9.1	3.1	35.3	yes	no
5_X	rb2	893	1242	302.1 ± 7.8	2.6	35.8	yes	no
7_X	rb2	433	782	296.0 ± 8.6	2.9	36.1	yes	no
8_X	rb2	1243	1592	302.5 ± 8.1	2.7	36.3	yes	no
9_X	rc2	2	351	345.1 ± 3.6	1.0	37.6	no	no
10_X	rc2	720	1069	347.4 ± 2.5	0.7	38.6	no	no
11_X	re1	530	879	377.7 ± 9.4	2.5	40.1	yes	no
13_X	re2	2	351	309.2 ± 4.8	1.5	32.9	no	no
14_X	re2	668	1017	305.5 ± 2.3	0.8	33.2	no	no
15_X	re2	1018	1367	303.3 ± 2.2	0.7	33.3	no	no
16_X	rf1	2	351	336.8 ± 3.5	1.0	36.9	no	no
17_X	rf1	410	759	339.5 ± 2.5	0.7	37.5	no	no
18_X	rf1	1222	1571	335.6 ± 2.4	0.7	37.5	no	no
19_X	rf2	2	351	359.5 ± 15.7	4.4	38.4	yes	yes
20_X	rf2	762	1111	349.7 ± 2.3	0.7	39.0	no	no
21_X	rf2	1179	1528	348.5 ± 3.4	1.0	38.8	no	no
22_X	rg1	368	717	348.1 ± 2.9	0.8	33.7	no	no
23_X	rg1	799	1148	347.4 ± 3.2	0.9	34.0	no	no
24_X	rg1	1322	1671	349.4 ± 2.9	0.8	34.4	no	no
25_X	rg2	2	351	339.7 ± 10.4	3.1	34.9	yes	yes
26_X	rg2	659	1008	339.5 ± 9.5	2.8	34.6	yes	no
27_X	rg2	1246	1595	339.2 ± 10.3	3.1	34.6	yes	yes
28_X	rg2	1596	1945	341.8 ± 10.2	3.0	34.7	yes	yes
31_X	rh1	114	463	400.3 ± 11.8	3.0	41.4	yes	yes
32_X	rl1	679	1028	360.2 ± 4.9	1.4	36.1	no	no
33_X	rl1	1029	1378	364.2 ± 7.1	1.9	36.1	yes	no
#	11	29				# (yes)	12	5

Table 5.3: Description of PMDB segments ($CV = 100 s_{\mathrm{QT}}/T_{\mathrm{QT}}$). Last line indicates the number of qualified segments, subjects, and segments in the indicative limits of applicability for each frequency band.

(a) PMDB segments on lead Y

segment	recording	segment, beats		$x_{\mathrm{QT}}(n)$		SNR	Applicability	
id	name	begin	end	$T_{\mathrm{QT}} \pm s_{\mathrm{QT}}$, ms	CV, %	dB	LF	HF
1_Y	ra2	248	597	335.2 ± 14.2	4.2	33.2	yes	yes
2_Y	ra2	1157	1506	334.4 ± 14.8	4.4	33.0	yes	yes
3_Y	ra2	1507	1856	330.9 ± 19.2	5.8	32.1	yes	yes
9_Y	rc2	2	351	340.8 ± 27.6	8.1	32.9	yes	yes
10_Y	rc2	720	1069	342.4 ± 20.3	5.9	33.0	yes	yes
12_Y	re1	609	958	397.4 ± 30.5	7.7	30.6	yes	yes
16_Y	rf1	2	351	355.6 ± 8.1	2.3	28.2	yes	no
17_Y	rf1	410	759	360.9 ± 13.3	3.7	28.6	yes	yes
18_Y	rf1	1221	1570	359.4 ± 15.7	4.4	29.1	yes	yes
19_Y	rf2	2	351	378.2 ± 21.8	5.8	29.1	yes	yes
20_Y	rf2	762	1111	376.0 ± 24.9	6.6	26.4	yes	yes
22_Y	rg1	368	717	363.8 ± 4.4	1.2	30.8	no	no
23_Y	rg1	799	1148	363.3 ± 4.2	1.2	31.1	no	no
24_Y	rg1	1322	1671	366.5 ± 7.9	2.2	31.2	yes	no
25_Y	rg2	2	351	352.3 ± 19.3	5.5	28.0	yes	yes
26_Y	rg2	659	1008	353.5 ± 20.4	5.8	28.3	yes	yes
27_Y	rg2	1246	1595	355.0 ± 22.2	6.3	28.7	yes	yes
28_Y	rg2	1596	1945	356.4 ± 20.4	5.7	29.0	yes	yes
32_Y	rl1	678	1027	397.5 ± 38.4	9.7	26.0	yes	yes
33_Y	rl1	1028	1377	398.2 ± 37.0	9.3	26.3	yes	yes
#	8	20				# (yes)	18	16

(b) PMDB segments on lead Z

segment	recording	segment, beats		$x_{\mathrm{QT}}(n)$		SNR	Applicability	
id	name	begin	end	$T_{\mathrm{QT}} \pm s_{\mathrm{QT}}$, ms	CV, %	dB	LF	HF
1_Z	ra2	248	597	339.1 ± 4.5	1.3	34.9	no	no
2_Z	ra2	1157	1506	337.0 ± 4.6	1.4	34.9	no	no
3_Z	ra2	1507	1856	330.4 ± 4.3	1.3	33.4	no	no
4_Z	rb2	83	432	293.9 ± 5.2	1.8	35.4	yes	no
5_Z	rb2	433	782	295.3 ± 4.2	1.4	35.6	no	no
6_Z	rb2	783	1132	297.0 ± 4.7	1.6	35.3	no	no
8_Z	rb2	1133	1482	300.5 ± 4.4	1.5	35.3	no	no
10_Z	rc2	720	1069	361.0 ± 5.5	1.5	36.5	yes	no
16_Z	rf1	2	351	335.1 ± 7.1	2.1	39.0	yes	no
17_Z	rf1	410	759	340.2 ± 7.9	2.3	39.5	yes	no
18_Z	rf1	1220	1569	345.0 ± 15.4	4.5	39.0	yes	yes
19_Z	rf2	76	425	341.4 ± 27.0	7.9	33.3	yes	yes
22_Z	rg1	367	716	353.3 ± 2.9	0.8	36.2	no	no
23_Z	rg1	798	1147	354.1 ± 3.1	0.9	36.2	no	no
24_Z	rg1	1321	1670	356.5 ± 3.1	0.9	36.5	no	no
29_Z	rg3	1123	1472	349.9 ± 34.3	9.8	34.9	yes	yes
30_Z	rg3	1553	1902	366.6 ± 47.0	12.8	33.4	yes	yes
#	7	17				# (yes)	8	4

Table 5.4: Description of PMDB segments from multilead delineation ($CV = 100 s_{\mathrm{QT}}/T_{\mathrm{QT}}$). Last line indicates the number of: qualified segments, subjects, and segments in the indicative limits of applicability for each frequency band.

segment	recording	segment, beats		$x_{\mathrm{QT}}(n)$		SNR_{ML}	Applicability	
id	name	begin	end	$T_{\mathrm{QT}} \pm s_{\mathrm{QT}}$, ms	CV, %	dB	LF	HF
1_F	ra2	248	597	349.5 ± 5.2	1.5	33.2	yes	no
2_F	ra2	1157	1506	346.6 ± 5.4	1.6	32.9	yes	no
3_F	ra2	1507	1856	339.3 ± 6.1	1.8	32.1	yes	no
4_F	rb2	83	432	308.8 ± 5.0	1.6	33.2	yes	no
5_F	rb2	433	782	310.0 ± 4.1	1.3	33.4	yes	no
6_F	rb2	783	1132	312.3 ± 5.7	1.8	33.5	yes	no
8_F	rb2	1133	1482	317.6 ± 4.4	1.4	33.5	yes	no
9_F	rc2	2	351	364.4 ± 5.2	1.4	34.9	yes	no
10_F	rc2	720	1069	366.3 ± 5.2	1.4	35.3	yes	no
11_F	re1	530	879	405.8 ± 19.1	4.7	33.2	yes	yes
13_F	re2	245	594	325.4 ± 4.6	1.4	32.1	yes	no
14_F	re2	595	944	321.7 ± 4.8	1.5	32.2	yes	no
16_F	rf1	2	351	362.0 ± 5.7	1.6	34.0	yes	no
17_F	rf1	410	759	366.6 ± 5.2	1.4	34.5	yes	no
18_F	rf1	1221	1570	363.6 ± 4.2	1.2	34.7	yes	no
22_F	rg1	368	717	371.9 ± 5.3	1.4	33.4	yes	no
23_F	rg1	799	1148	371.8 ± 5.5	1.5	33.6	yes	no
24_F	rg1	1322	1671	374.3 ± 5.1	1.4	34.0	yes	no
25_F	rg2	2	351	361.4 ± 6.2	1.7	31.4	yes	no
26_F	rg2	755	1104	361.1 ± 7.0	1.9	31.2	yes	no
27_F	rg2	1246	1595	364.2 ± 8.9	2.5	31.5	yes	no
28_F	rg2	1596	1945	364.8 ± 8.1	2.2	31.6	yes	no
32_F	rl1	678	1027	389.7 ± 20.6	5.3	30.7	yes	yes
33_F	rl1	1028	1377	392.3 ± 21.1	5.4	30.9	yes	yes
#	9	24				# (yes)	24	3

Table 5.5: Minimum, mean, standard deviation (sd) and maximum values found for s_{QT}, CV and SNR for the all segments found in PMDB by lead set. For ML segments SNR_{ML} was considered.

	lead set	X	Y	Z	F
s_{QT}	*maximum*	15.7	38.4	64.5	21.1
	mean $\pm$ *sd*	5.3 ± 3.6	19.2 ± 9.5	13.9 ± 17.8	7.4 ± 5.1
	minimum	2.2	4.2	2.9	4.1
CV, %	*maximum*	4.4	9.7	12.8	5.4
	mean $\pm$ *sd*	1.6 ± 1.1	5.3 ± 2.4	3.5 ± 3.8	2 ± 1.2
	minimum	0.7	1.2	0.8	1.2
SNR, dB	*maximum*	40.1	33.2	39.5	35.3
	mean $\pm$ *sd*	35.9 ± 2.2	29.8 ± 2.3	35.7 ± 2.3	33 ± 1.3
	minimum	32.9	26.0	32.0	30.7

The noisiest lead was found to be lead Y, as it should be expected due to the electrode standard positions. Lead Y also presents the highest mean values for s_{QT} and CV, possibly due to spurious QTV resulting from noise. Even so, the minimum SNR value found was 26.0 dB. Thus all SNR values found are in the described framework of applicability. Specifically, the methodology was found applicable (Tables 5.2 to 5.4):

- for LF band variability in
  - 12 segments (lead X);
  - 18 segments (lead Y);
  - 8 segments (lead Z);
  - all 24 segments (ML);
- for HF band variability in
  - 5 segments (lead X);
  - 16 segments (lead Y);
  - 4 segments (lead Z);
  - 3 segments (ML).

Thus, according to the indicative limits of applicability in LF band, less than 60% of the SL based segments would be considered, while all admissible segments found in ML approach fulfilled the limits. Regarding HF band the number of segments in the frame of applicability is low, except for lead Y.

No valid model was found in segments 11_X, 28_Y, 06_F and 11_F, which were excluded from the analysis. The orders selected by AIC in identification (Figures 5.3 to 5.4) were found to be:

- $8 \leq p \leq 12$, for 48 out of 64 models (75%) with SL; for 15 out of 22 models (68%) with ML;
- $4 \leq q \leq 8$, for 52 models (81%) with SL; for 15 models (68%) with ML;
- $q > p$, for 8 models (13%) with SL; for 2 models (9%) with ML;
- $q = p$, for 2 models (3%) with SL; none with ML.

The estimated QTV fractions in LF and HF bands are presented in Figures 5.5 and 5.6. Admissible segments for which no valid model was found are listed on the axis with no correspondent bar plotted.

The QTV fractions found for simultaneous segments depend on the lead set, which reinforces the importance of the delineation approach. For simultaneous segments, the QTV fraction uncorrelated with HRV found in both bands ($\hat{R}^{LF}_{\mathrm{QT|QT}}$ and $\hat{R}^{LF}_{\mathrm{QT|QT}}$) for lead Y are mainly higher than in the other leads or lead set F. It must be recalled that lead Y has the lowest SNR and that spurious QTV is unrelated with HRV, thus artificially increases the uncorrelated fraction. Also, for most of the segments in all lead sets, $\hat{R}^{HF}_{\mathrm{QT|QT}}$ is higher than $\hat{R}^{LF}_{\mathrm{QT|QT}}$, what can be a consequence of the lower performance of the QTV quantification in the HF band, as noticed for simulated data (Chapter 4).

From the segments within the indicative frame of applicability for which an adequate model was found, a relevant QTV uncorrelated with HRV ($\hat{R}^{LF}_{\mathrm{QT|RR}} < 60\%$) was found for:

- all 36 models with SL;
- 19 out of 22 models with ML (86.4%);

and $\hat{R}^{HF}_{\mathrm{QT|RR}} < 60\%$ for all models (24 in SL and 2 in ML).

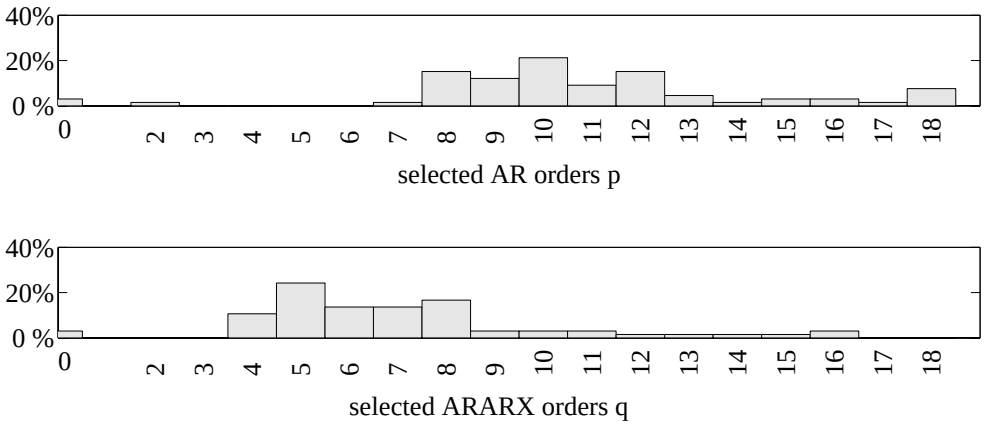

Figure 5.3: Histograms of orders p and q selected by AIC in model identification for PMDB segments relative to single-lead delineation (0 stands for no model found).

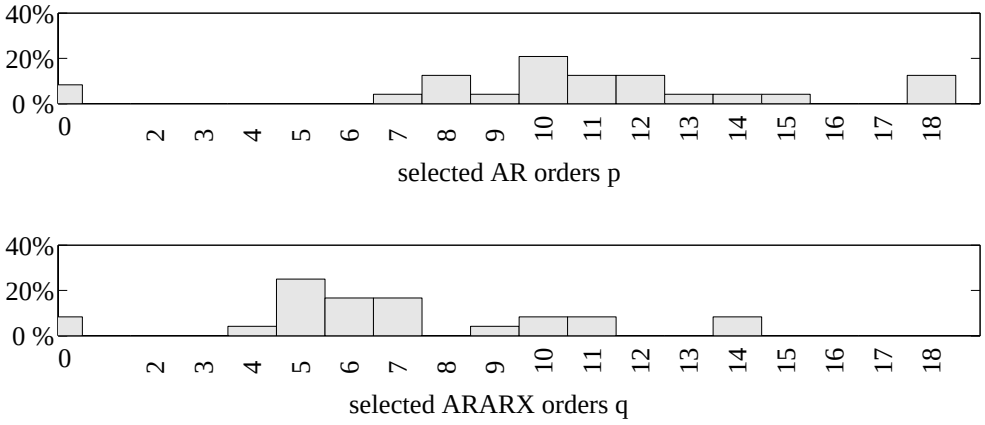

Figure 5.4: Histograms of orders p and q selected by AIC in model identification for PMDB segments relative to multilead delineation (0 stands for no model found).

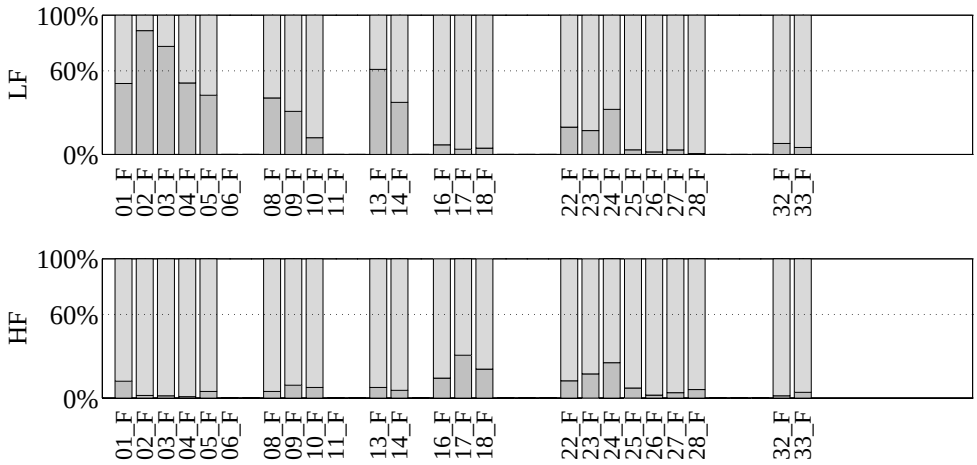

Figure 5.5: Multilead delineation (ML) QTV fractions estimated in PMDB segments. HRV driven fraction in dark grey, uncorrelated fraction in light grey.

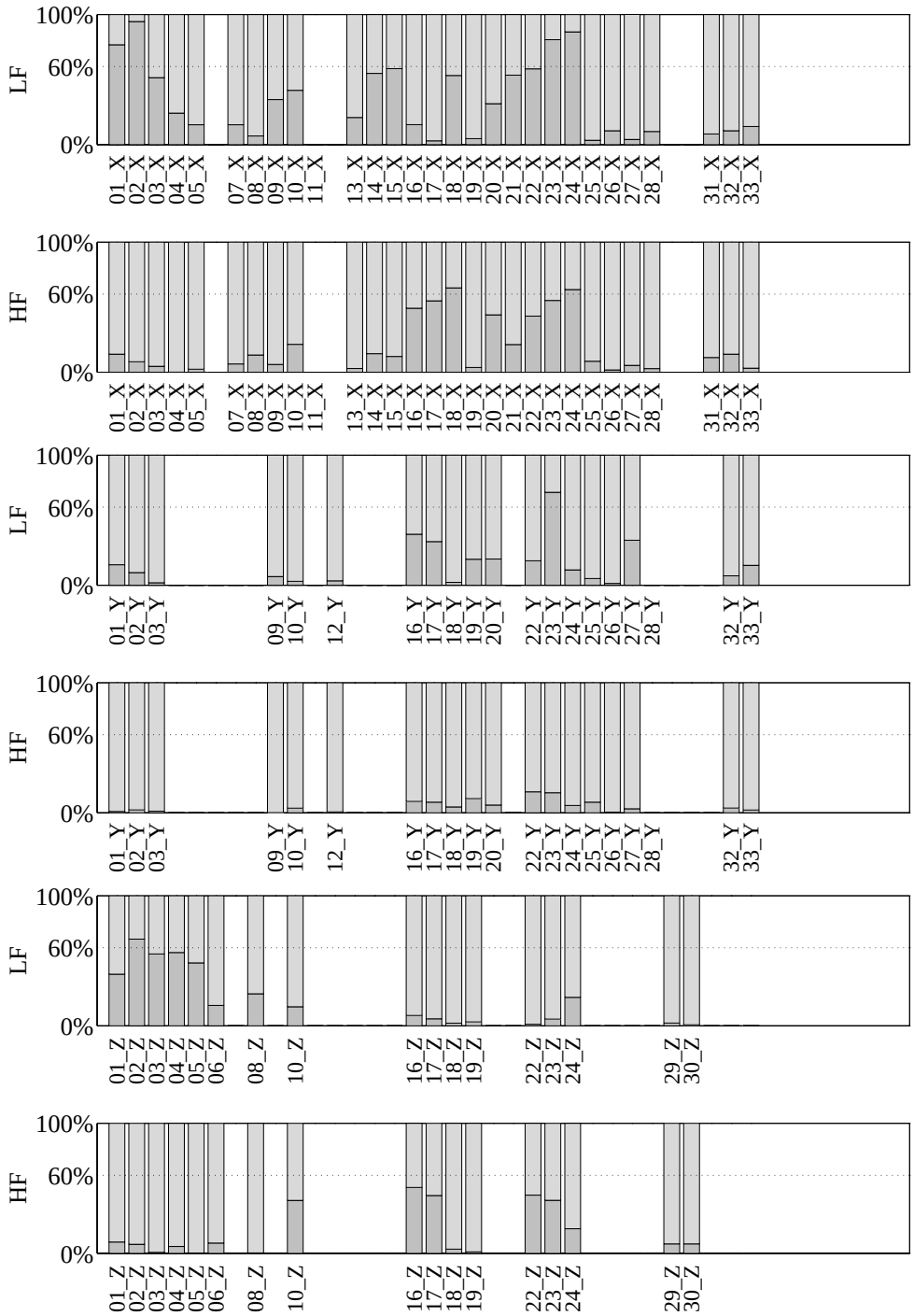

Figure 5.6: Single-lead delineation (SL) based QTV fractions estimated in PMDB segments. HRV driven fraction in dark grey, uncorrelated fraction in light grey.

5.5 Holter recordings results

The **24-hour Holter of the adult** volunteer, started at 16:30 and the subject indicated the period in which he was sleeping, here denoted as *night* period. The remaining period was denoted as *day*. The subject has also referred to have got-up during night at a unknown time, fact that was disregarded in this analysis. The tachogram of the 24-hour is plotted in Figure 5.7, with the *night* period marked in grey. The RR series was obtained using single-lead delineation over lead II with some manual verification to correct false positive occurrences.

During the ECG extraction process using the software provided by *Mortara* the Holter recording is fragmented in partial files corresponding to each hour of the recording. In some of those partial files, segments of signal are missing in the beginning or end of the hour and are lost. This is a limitation of the extraction software presently available. As a consequence, the tachogram in Figure 5.7 present some discontinuities.

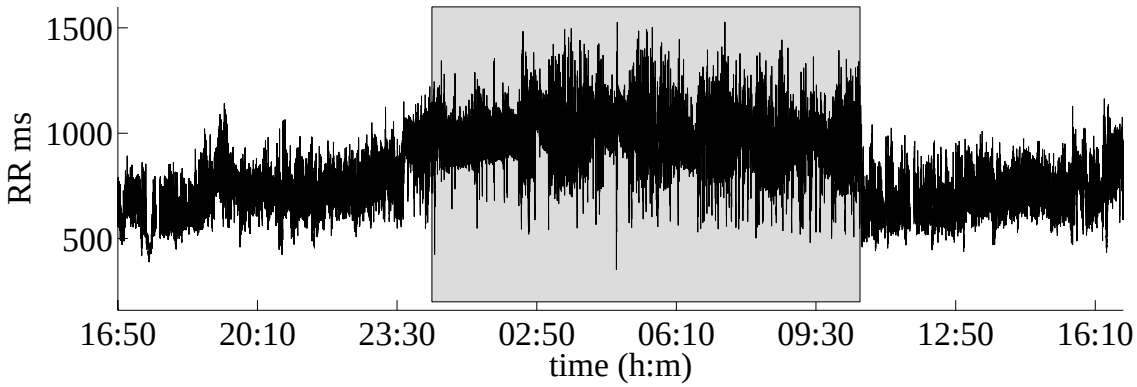

Figure 5.7: Tachogram of the 24-hour Holter file. Darker area corresponds to the time in which the subject indicated to be sleeping (*night* period).

Regarding the fist 30 min of each hour in this recording, 25 segments from 12 different partial files were obtained using lead set D. From those segments, 12 simultaneous segments were found using lead set M (Table 5.6). The range of variation of s_{QT}, CV and SNR for the day and night periods are summarized in Table 5.7, with no relevant differences noticed between the lead sets. Also, $s_{\mathrm{QT}} > 3$ ms in 11 segments based on lead system D and in 3 based on lead system M, and $s_{\mathrm{QT}} < 10$ ms in all segments. The minima SNR value found was 23 dB.

Thus, the methodology was found to be:

- applicable to LF band in
  - 11 segments with lead system D;
  - 3 segments with lead system M;
- not applicable to HF band in all segment with both lead systems.

Table 5.6: 24-hour Holter data segments description; segments have ID of the form i_D or i_M, depending of the lead system considered (D or M, respectively), for i the segment number.

(a) lead system D

segment id	recording hour	period	segment, beats		x_{QT}		SNR	Applicability	
			begin	end	$mean \pm s_{QT}$, ms	CV, %	dB	LF	HF
1_D	1	day	392	741	324.6 ± 8.0	2.5	23.8	yes	no
2_D	1	day	1109	1458	342.4 ± 4.3	1.3	25.8	yes	no
3_D	1	day	2087	2436	339.6 ± 3.6	1.1	23.0	yes	no
4_D	3	day	1548	1897	364.2 ± 5.5	1.5	27.6	yes	no
5_D	4	day	301	650	356.5 ± 2.6	0.7	29.2	no	no
6_D	4	day	800	1149	357.6 ± 2.1	0.6	30.8	no	no
7_D	4	day	1150	1499	358.8 ± 2.3	0.7	29.7	no	no
8_D	4	day	1888	2237	356.2 ± 2.0	0.6	31.3	no	no
9_D	5	day	190	539	355.5 ± 2.2	0.6	28.8	no	no
10_D	6	day	708	1057	352.9 ± 4.2	1.2	24.6	yes	no
11_D	7	day	825	1174	366.2 ± 6.6	1.8	24.2	yes	no
12_D	7	day	1247	1596	370.6 ± 4.0	1.1	26.0	yes	no
13_D	8	day	970	1319	405.4 ± 7.0	1.7	27.1	yes	no
14_D	9	night	191	540	412.9 ± 1.9	0.5	28.8	no	no
15_D	9	night	541	890	413.3 ± 2.1	0.5	28.8	no	no
16_D	9	night	891	1240	414.1 ± 3.0	0.7	28.8	no	no
17_D	9	night	1434	1783	415.8 ± 2.3	0.5	28.7	no	no
18_D	10	night	2	351	416.7 ± 2.4	0.6	29.0	no	no
19_D	10	night	352	701	414.2 ± 1.8	0.4	29.0	no	no
20_D	10	night	1186	1535	419.4 ± 2.0	0.5	28.9	no	no
21_D	11	night	244	593	432.3 ± 3.1	0.7	29.1	yes	no
22_D	11	night	594	943	427.7 ± 2.8	0.6	28.5	no	no
23_D	13	night	2	351	426.0 ± 2.2	0.5	29.9	no	no
24_D	24	day	1533	1882	351.5 ± 4.5	1.3	27.6	yes	no
25_D	24	day	2107	2456	351.9 ± 3.1	0.9	28.9	yes	no
#	12		25				# (yes)	11	0

(b) lead system M

segment id	recording hour	period	segment, beats		x_{QT}		SNR	Applicability	
			begin	end	$mean \pm s_{QT}$, ms	CV, %	dB	LF	HF
4_M	3	day	1548	1897	366.3 ± 6.8	1.8	25.1	yes	no
6_M	4	day	795	1144	360.7 ± 2.2	0.6	27.9	no	no
8_M	4	day	1888	2237	359.7 ± 2.2	0.6	28.3	no	no
14_M	9	night	191	540	414.7 ± 2	0.5	26.4	no	no
15_M	9	night	541	890	414.8 ± 2.5	0.6	26.5	no	no
16_M	9	night	891	1240	415.7 ± 3.1	0.8	26.5	yes	no
17_M	9	night	1434	1783	417.4 ± 2.5	0.6	26.4	no	no
18_M	10	night	2	351	418.4 ± 2.5	0.6	27.1	no	no
19_M	10	night	352	701	415.8 ± 1.9	0.5	27	no	no
20_M	10	night	1186	1535	421.2 ± 2.1	0.5	26.2	no	no
23_M	13	night	2	351	429.3 ± 2.6	0.6	27	no	no
25_M	24	day	2110	2459	356 ± 3.7	1	25.9	yes	no
#	6		12				# (yes)	3	0

Table 5.7: Minimum, mean, standard deviation (sd) and maximum values found for s_{QT}, CV and SNR_{ML} for the segments corresponding to 24-hour Holter data segments (both lead sets).

	lead set	D		M	
	period	day	night	day	night
s_{QT}	*maximum*	8.0	3.1	6.8	3.1
	$m \pm sd$	4.1 ± 1.9	2.4 ± 0.5	3.7 ± 2.1	2.4 ± 0.4
	minimum	2.0	1.8	2.2	1.9
CV, %	*maximum*	2.5	0.7	1.8	0.8
	$mean \pm sd$	1.2 ± 0.5	0.6 ± 0.1	1.0 ± 0.6	0.6 ± 0.1
	minimum	0.6	0.4	0.6	0.5
SNR_{ML}, dB	*maximum*	31.3	29.9	28.3	3.1
	$mean \pm sd$	27.0 ± 2.6	29.0 ± 0.4	27.0 ± 1.5	2.4 ± 0.4
	minimum	23.0	28.5	25.1	1.9

No valid model was found for segment 1_D. The orders selected by AIC are presented in Figures 5.8 and 5.9. Using lead set M the minimum order $q = 2$ is mainly selected. Also:

- $8 \leq p \leq 12$, for 15 out of 24 models (63%) found with lead set D; for 10 out of 12 models (83%) with lead set M;
- $4 \leq q \leq 8$, for 20 models (83%) with lead set D; for 1 model (8%) with lead set M;
- $q > p$, for 2 models (8%) with lead set D; for none with lead set M;
- $q = p$, for 2 models (8%) with lead set D; for none with lead set M.

The estimated QTV fractions in LF and HF bands are presented in Figure 5.10. During the night period most of the segments found present lower uncorrelated fraction (lighter grey) than segments during day, specially for HF band. This can be related with the dominant effect of the **parasympathetic** system during sleep, in particular with the modulation of respiration.

Considering only segments that fulfill the indicative limits of applicability, a relevant QTV fraction not driven by HRV for LF band (corresponding to $\hat{R}^{LF}_{\mathrm{QT|RR}} < 60\%$) was found for:

- 6 out of 11 models using lead set D (54.5%),
- 2 out of 3 models using lead set M (66.6%).

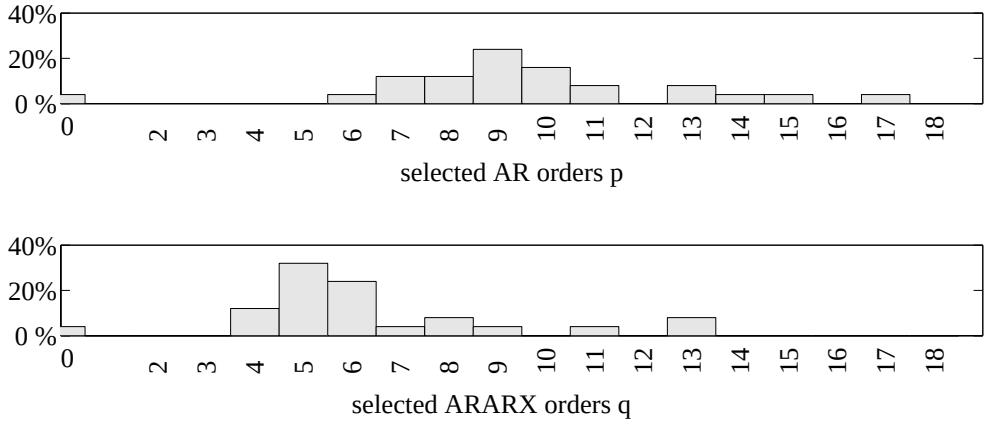

Figure 5.8: Histograms of orders p and q selected by AIC in model identification segments from 24-hour Holter example with lead set D (0 stands for no model found).

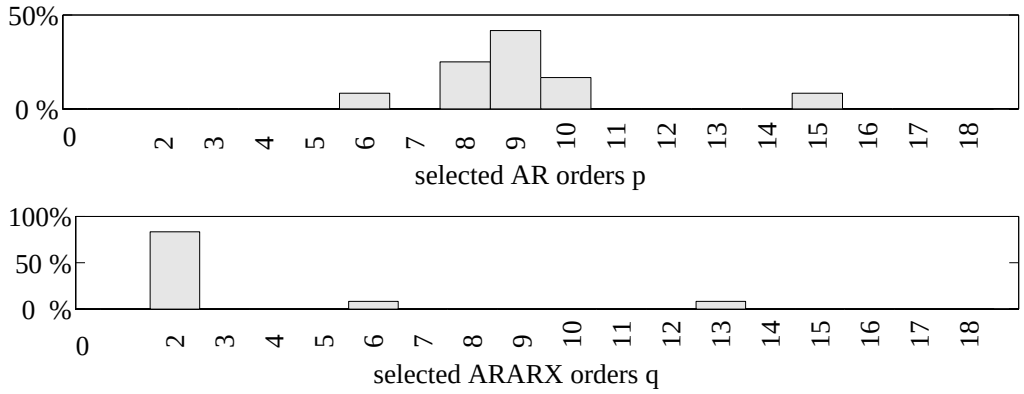

Figure 5.9: Histograms of orders p and q selected by AIC in model identification segments from 24-hour Holter example with lead set M (0 stands for no model found).

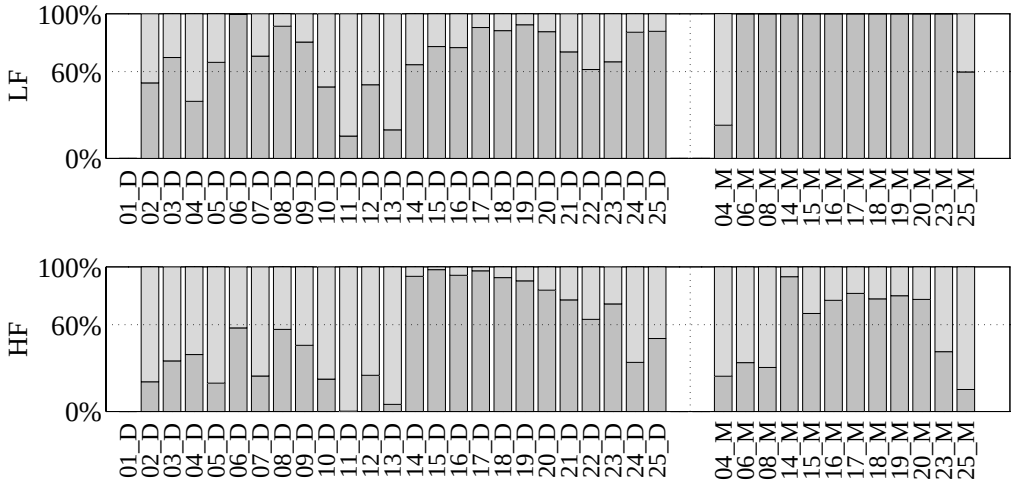

Figure 5.10: QTV fractions estimated in segments from 24-hour Holter example. HRV driven fraction in darker grey, uncorrelated fraction in lighter.

The valid segments were found in the **pediatric data** are denoted as i_D or i_M. The segments are described in Tables E.11 to E.20, all presented in the Appendix E of this thesis. Admissible segments were found for 40 out of the 67 ECG excerpts, in a total of 157 segments using lead set D and 148 segments using lead set M. From those, 125 segments were simultaneously present in the two lead sets. Only for patient 2, no valid segments were obtained in any of the files, using both lead sets, due to disperse not detected T waves. The minimum and maximum values found for s_{QT}, CV and SNR_{ML} for the segments corresponding to each patient are summarized in Table 5.8.

According to the indicative framework of applicability described for the simulated data, the automatic methodology was found to be applicable to:

- to LF band in
  - 108 segments with lead set D,
  - 85 segments with lead set M
- to HF band in
  - 32 segments with lead set D,
  - 18 segments with lead set M.

Valid models were found for a total of 274 segments (out of 305), corresponding to 89.8% of the segments. A third of the segments for which no valid models were found correspond to recordings from patient 3 which corresponds to the brain death outcome. Considering all the other patients, valid models were found for 92.7% of the adequate segments (267 out of 288 segments).

The AIC orders selected from the ones providing valid models are presented in Figures 5.11 and 5.12. The model orders p for the HRV models are higher in these segments than in the POLI/MEDLAV database or the 24-hour Holter, while the orders q are similar. As a matter of fact:

- for the 142 valid models found using lead set D
  - $8 \leq p \leq 12$, for 50 models (35%),
  - $p > 12$, for 81 models (58%),
  - $4 \leq q \leq 8$, for 83 models (57%),
  - $q > p$, for 21 models (15%),
  - $q = p$, for 8 models (6%),
- for the 132 valid models found using lead set M
  - $8 \leq p \leq 12$, for 47 models (36%),
  - $p > 12$, for 77 models (61%),
  - $4 \leq q \leq 8$, for 80 models (58%),
  - $q > p$, for 19 models (14%),
  - $q = p$, for 8 models (6%).

Table 5.8: Minimum and maximum values found for s_{QT}, CV and SNR_{ML} for the segments corresponding to each patient on pediatric Holter data segments (patient 2, for which no admissible segments were found with both lead systems are not presented).

(a) segments corresponding to lead set D

	patient	1	3	4	5
s_{QT}, ms	*maximum*	7	7.4	10.3	21.8
	mean $\pm$ *sd*	5.1 ± 2.7	4.8 ± 1.7	8.2 ± 1.3	7.2 ± 5.7
	minimum	3.2	3	6.8	1.6
V, %	*maximum*	2.2	2	3.4	6.7
	mean $\pm$ *sd*	21.4 ± 0.6	21.8 ± 2	24.2 ± 0.2	23.3 ± 1.5
	minimum	1	0.7	2.2	0.5
SNR_{ML}, dB	*maximum*	21.8	24.2	24.4	25.1
	mean $\pm$ *sd*	1.6 ± 0.9	1.2 ± 0.5	2.7 ± 0.4	2.2 ± 1.8
	minimum	20.9	19.8	23.9	20.1

	patient	6	7	8	9
s_{QT}, ms	*maximum*	25.9	23.3	16.2	14.8
	mean $\pm$ *sd*	19.1 ± 6.3	6.1 ± 7.5	11 ± 3.2	5.4 ± 3.7
	minimum	8.2	1.4	7.3	1.1
V, %	*maximum*	9.1	7.4	5.2	4.4
	mean $\pm$ *sd*	21.9 ± 0.9	17.6 ± 0.7	23.1 ± 0.6	25.8 ± 1.9
	minimum	3.2	0.4	2.6	0.3
SNR_{ML}, dB	*maximum*	23.5	19	24.4	29.9
	mean $\pm$ *sd*	6.5 ± 2.1	1.7 ± 2.2	3.8 ± 1	1.5 ± 1.1
	minimum	20.9	16.3	22.5	20.6

(b) segments corresponding to lead set M

	patient	1	3	4	5
s_{QT}, ms	*maximum*	-	12.3	-	20
	mean $\pm$ *sd*	-	4.1 ± 3.2	-	6.2 ± 5.6
	minimum	-	1.5	-	1.4
V, %	*maximum*	-	3	-	6.2
	mean $\pm$ *sd*	-	1 ± 0.8	-	1.9 ± 1.7
	minimum	-	0.4	-	0.4
SNR_{ML}, dB	*maximum*	-	26.9	-	27.5
	mean $\pm$ *sd*	-	26 ± 1	-	25.4 ± 3
	minimum	-	24.4	-	19.7

	patient	6	7	8	9
s_{QT}, ms	*maximum*	-	16.7	14.9	16.8
	mean $\pm$ *sd*	-	4.6 ± 4.1	10.3 ± 2.9	4.2 ± 3.3
	minimum	-	1.6	7.1	1.2
V, %	*maximum*	-	4.5	4.8	4.9
	mean $\pm$ *sd*	-	1.3 ± 1.1	3.5 ± 0.9	1.2 ± 0.9
	minimum	-	0.5	2.3	0.3
SNR_{ML}, dB	*maximum*	-	30.7	27.4	31.4
	mean $\pm$ *sd*	-	26.2 ± 4.1	26.3 ± 0.4	29.4 ± 1.4
	minimum	-	19.2	26	24.8

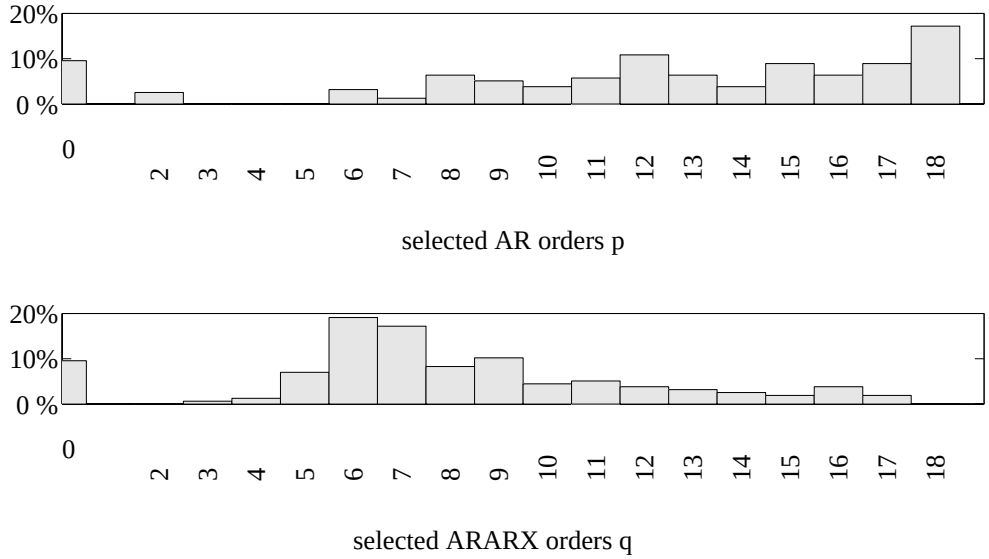

Figure 5.11: Histograms of AIC orders p and q in segments from Holter PICU files using lead set D (0 stands for no model found).

Figure 5.12: Histograms of AIC orders p and q in segments from Holter PICU files using lead set M (0 stands for no model found).

Higher orders p were found compared to the previous results in data from PMDB and the 24-h Holter recording. It should be recalled that results obtained over adults and children data are being compared. For instance, a higher respiratory frequency in children than in adults has been reported (Goldstein *et al.*, 1993). Also, at PICU patients can be artificially ventilated, are always lying down and under the effect of many drugs; which can have a combined effect over the HR that may also contributes to these results.

The estimated QTV fractions in LF and HF bands over pediatric files are presented in Figures 5.13 to 5.17. Considering only segments within the indicative limits of applicability, $\hat{R}^{\mathcal{B}}_{\mathrm{QT|RR}} < 60\%$ was found in the band LF:

- for 69 out of 95 models (73%), using lead set D,
- for 63 out of 85 models (74%), using lead set M,

and in the band HF,

- for 26 out of 27 models (96%), using lead set D,
- for 15 out of 18 models (83%), using lead set M.

5.6 Concluding Remarks

The application of the parametric methodology in this thesis was restricted to segments of consecutive 350 beats without RR outliers or missing QT values (*admissible segments*), attending both to the goal of short time variability study and to the difficulty of QT measurement. Globally, finding this kind of segments either in research, Holter and clinical ECG data has proved to be feasible.

As expected, a relative low number of segments were found in Holter recordings with respect to the amount of data, due to the noise contamination and the difficulties in T wave detection. Even so, a reasonable number of segments qualified for the analysis. The difference in the number of segments obtained using single-lead and multilead based delineation over the same files (PMDB data) was not relevant. Using lead set D allowed to obtain a larger number of segments than using lead set M (Holter data), what can result from a better delineation performance according to the results of Chapter 3.

Adequate model identification was possible for more than 90% of the real data set analysed segments. This number is slightly lower than the one found in the simulated data (Chapters 2 and 4). AIC selected mainly $p > q$ (for more than 80%) reinforcing the adequacy of allowing different orders for AR and ARARX models. In fact, there is no reason to constrain QT and RR sequences to attached memories of its own past.

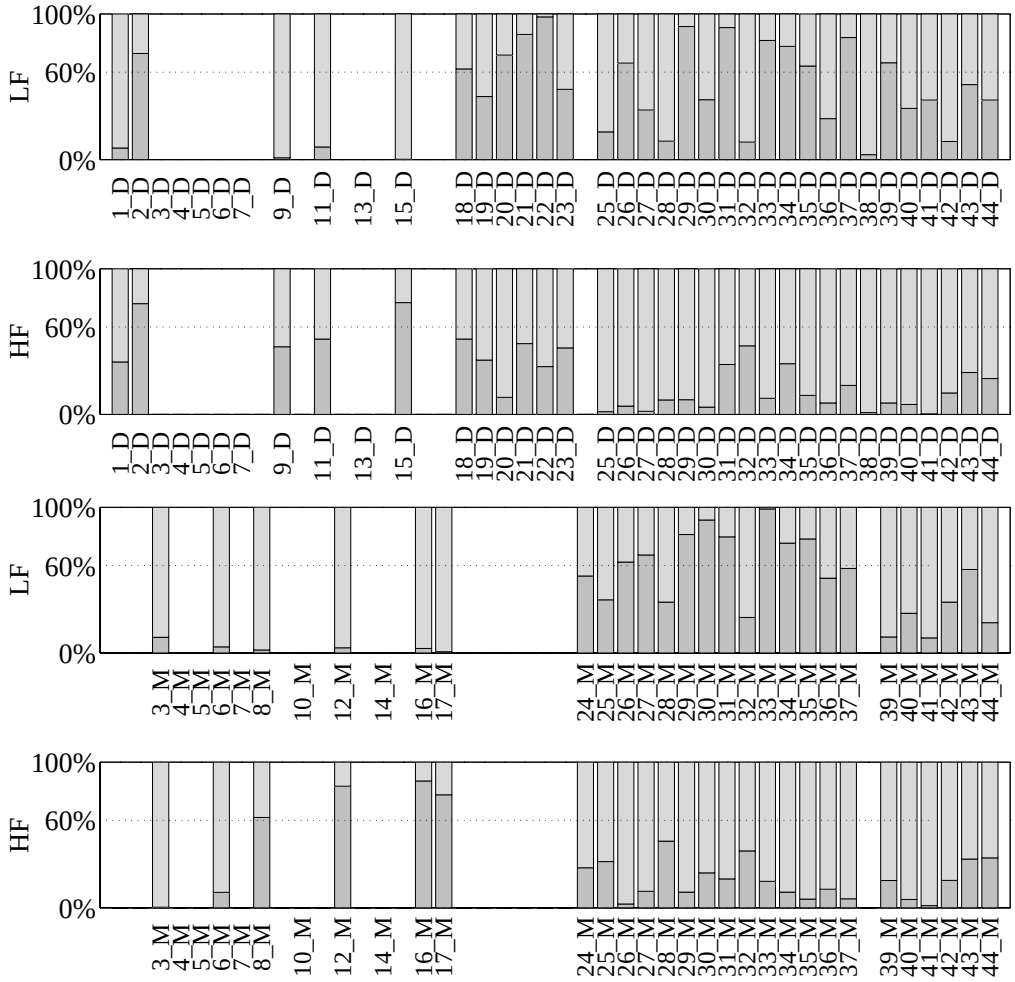

Figure 5.13: QTV fractions estimated in segments from Holter PICU files that correspond to 1h recordings (continues in Figure 5.14). HRV driven fraction in darker grey, uncorrelated fraction in lighter.

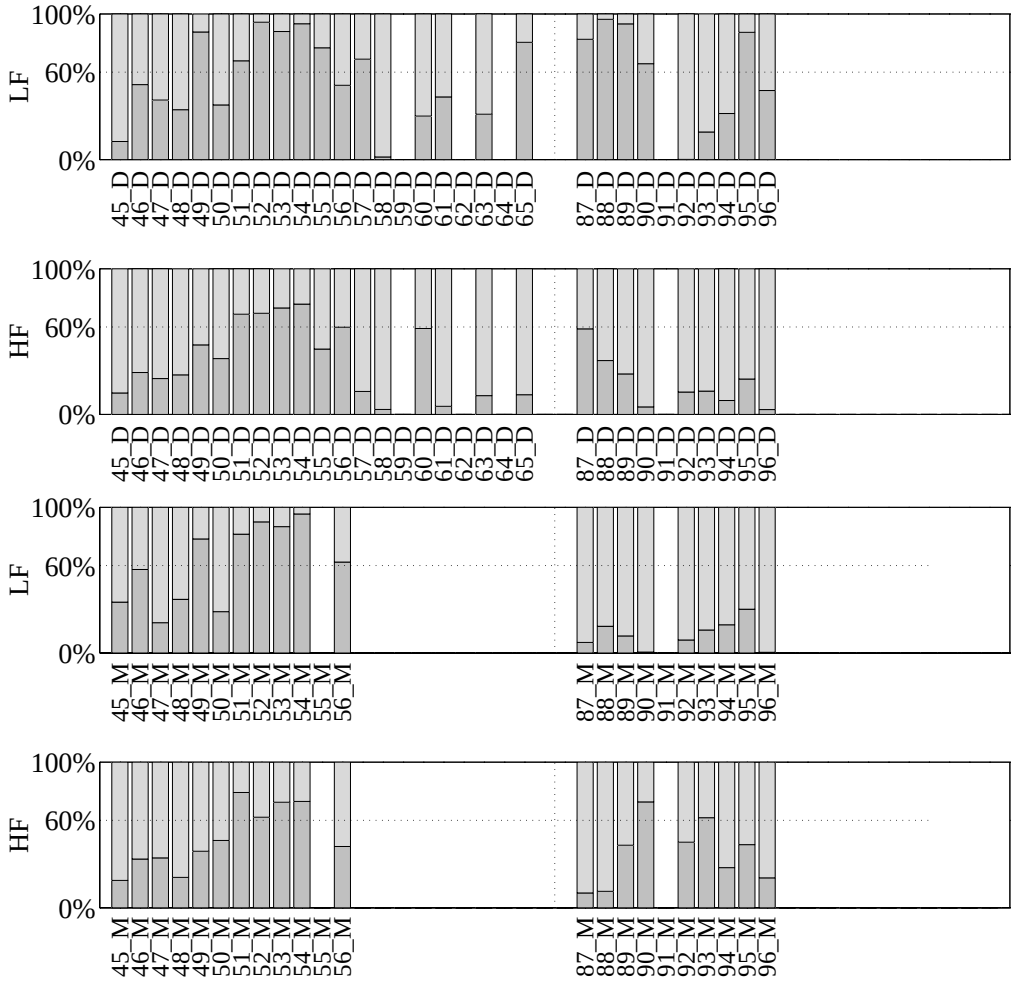

Figure 5.14: QTV fractions estimated in segments from Holter PICU files that correspond to 1h recordings (continued from Figure 5.13). HRV driven fraction in darker grey, uncorrelated fraction in lighter.

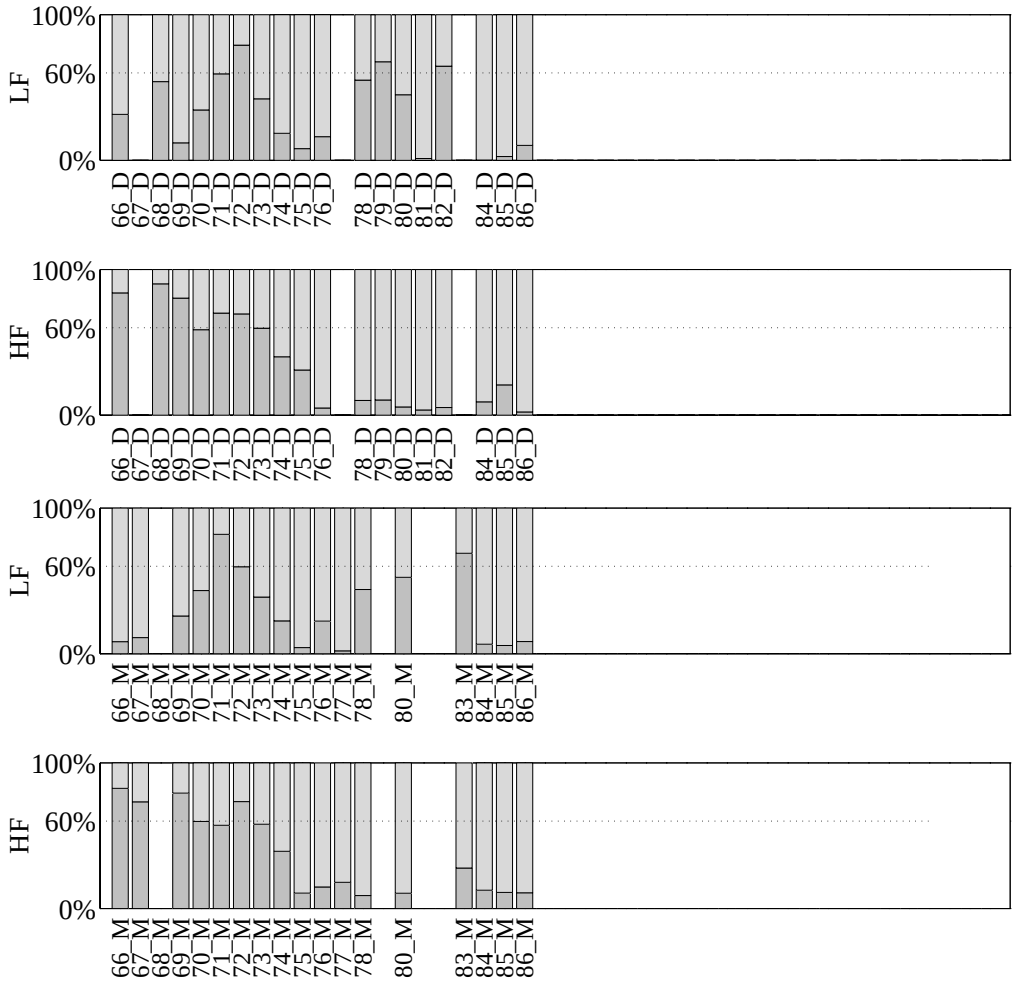

Figure 5.15: QTV fractions estimated in segments from the 12-hour PICU example. HRV driven fraction in darker grey, uncorrelated fraction in lighter.

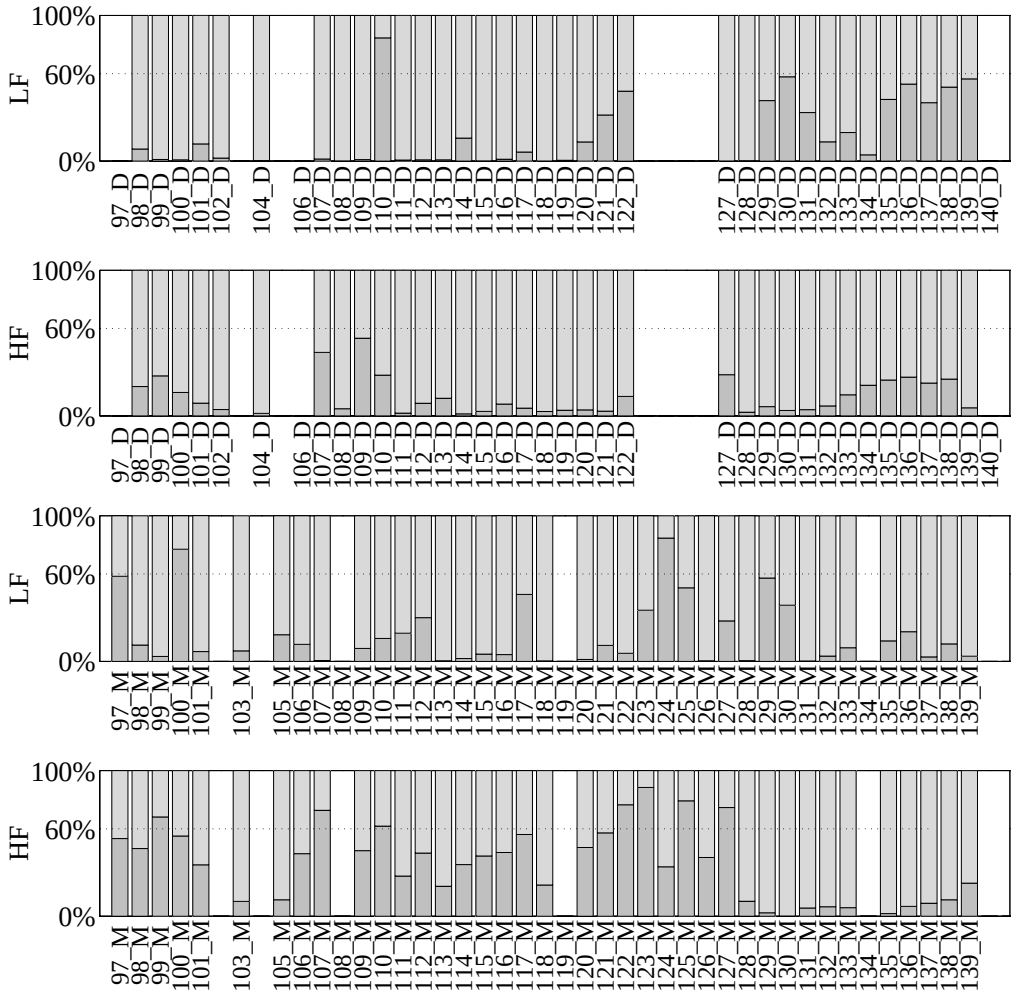

Figure 5.16: QTV fractions estimated in segments from PICU patient 9 (continues in Figure 5.17). HRV driven fraction in darker grey, uncorrelated fraction in lighter.

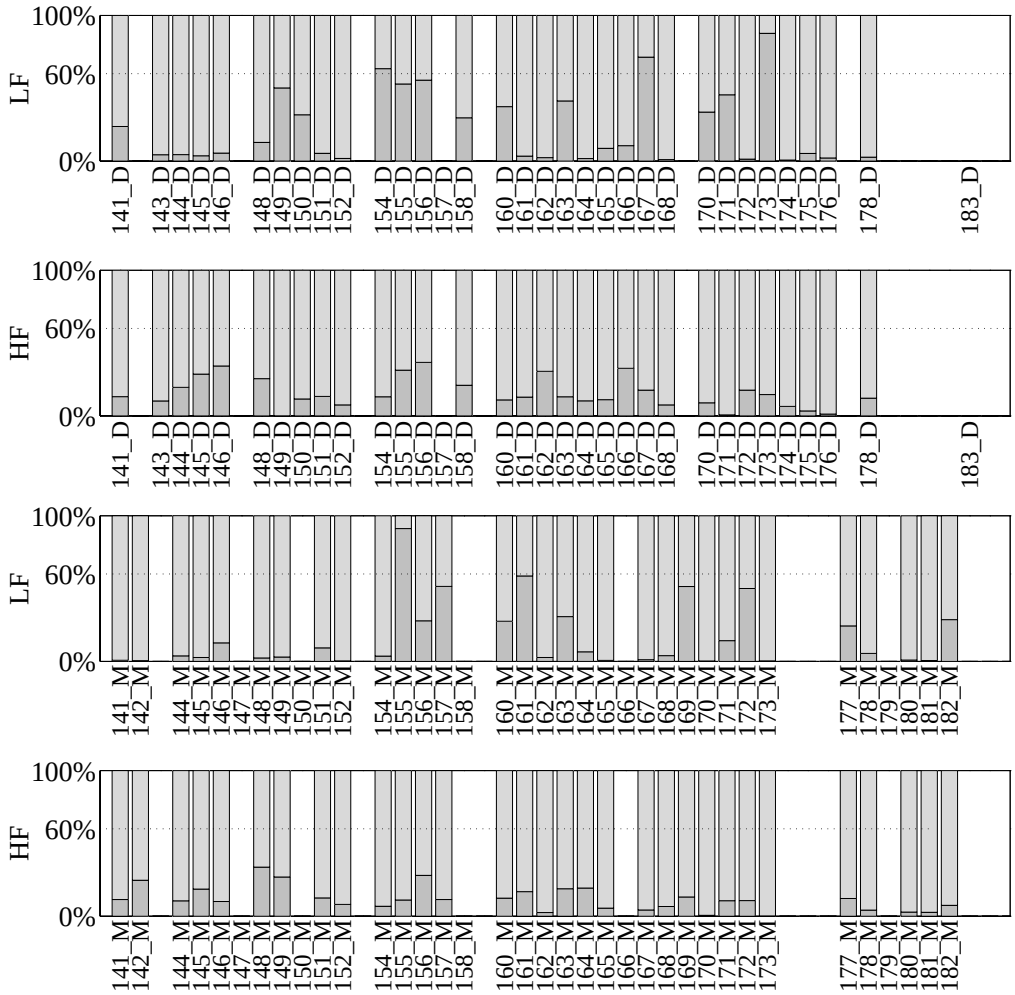

Figure 5.17: QTV fractions estimated in segments from PICU patient 9 (continued from Figure 5.16). HRV driven fraction in darker grey, uncorrelated fraction in lighter.

With respect to the indicative limits of applicability established for the simulated data (Chapter 4), approximately 60% of all real segments fulfilled the limits for *LF* band, but only 18% for the *HF* band. Multilead delineation appears to produce more segments acomplishing those limits than single-lead delineation; again lead set *D* seems preferible to lead set *M*.

It should be recalled that in the results over simulated data (Chapter 4), the level of QT variability (s_{QT}) estimated from the segments obtained after delineation was lower than the reference values used in simulation. Thus, it could be the case that s_{QT} was also underestimated in real data and the method could be in fact applied with lower observed QTV values.

The fraction correlated with HRV was found to be lower than 60% for most of the real data set segments within the indicative limits of applicability, for both frequency bands considered. This result suggests that other factors rather than RR could drive an important part of QTV. It is worthwhile to remark that uncorrelation between that part of QTV and HRV does not imply the absence of physiological dependence between them, since non linear effects were not taken into account.

Some files present SNR level lower than 20 dB and many files low s_{QT} ($<$ 10 ms or lower). Thus, it is likely that the errors in the estimated fractions reach a value of 15% or 20%, in particular for segments that do not fulfill the indicative limits of applicability. Even so it is possible to state that the fraction uncorrelated with HRV still presents a relevant importance in QTV.

A relevant QTV fraction not correlated with HRV was found both in healthy subjects (over 40% in more than 80% of the models for segments in the frame of applicabily) and pediatric patients in PICU (in more than 70% of the models).

This fact may indicate that an important part of QTV is not linearly driven by HRV and may contain complementary information.

Chapter 6

Concluding Notes

The design of automatic methods for ECG processing is a difficult and challenging problem.

The tools need to be adapted to the specificities of the ECG and be robust to the signal variations and noise contamination, particularly regarding their applicability to clinical data. The delineation of the ECG characteristic waves is of extreme importance and is the basis of the study of the signal features.

Automatic methodologies allow to avoid intra/inter-observer variability and the wavelet transform provides a representation of the ECG well suited for the waves delineation.

The delineation of flat boundaries, as it is usually the case of the T wave end, is a particularly challenging task due to the low signal-to-noise ratio (SNR). Also, the incorporation of the information provided by multiple simultaneous ECG leads is crucial to determine the electrical phenomena true duration. Furthermore the spacial information can be used to increase the robustness of delineation.

The robustness and accuracy of automatic methods for ECG delineation are essential to fully access the signal information and take advantage of its diagnostic potential. In particular to explore short term QTV/HRV interactions, the uncertainty in the T end delineation is one of the main problems in measuring the QT interval with precision. In clinical practice noise contamination increases delineation difficulty and can result in spurious QTV.

6.1 ECG automatic delineation

Developing and validating automatic delineation methods was one of the main goals of this thesis.

Single-lead (SL) and multilead (ML) based systems, in particular regarding boundaries location were proposed and validated.

Several approaches were studied in this work:

single-lead delineation over each recorded lead;

single-lead delineation plus post-processing rules

- over the *recorded Frank leads*;
- over the *leads (V5, aVF, V2)* from the 12 standard;
- over the *12 standard leads*;
- over the *15 leads* (12 standard leads plus the Frank leads);

multilead delineation over *recorded Frank leads*, over the *leads (V5, aVF, V2)* from the 12 standard, over the *constructed Frank leads using Dower* matrix.

The results pointed out that both single-lead and multilead methodologies are adequate for ECG waves delineation. In particular, using single-lead with post-processing rules over 12 or 15 leads and with every multilead approaches:

- a *sensitivity* of 100% was found for the QRS complex detection;
- both high sensitivity and high minimum positive predictivity were found for the T wave.

Also, the multilead system

- provided more robust and more accurate boundaries locations than any electrocardiographic lead by itself;
- outperformed multilead strategies based in rule selection after single-lead delineation;

Both automatic delineation systems have taken part of the *"PhysioNet/Computers in Cardiology Challenge 2006: QT Interval Measurement"* competition [1] (Moody *et al.*, 2006).

This competition was organized to address the question: "Can the QT interval be measured by fully automated methods with an accuracy acceptable for clinical evaluations?". It also allowed to create a set of annotated QT intervals, both manually and using several automatic strategies. Among the 28 fully automatic strategies submitted, only 9 achieved global errors in the QT measured intervals lower than 30 ms. Both the single-lead and multilead methodologies presented in this thesis are included in these 9, furthermore, the single-lead approach with was one of the 3 methodologies presenting errors under 20 ms.

[1] See http://www.physionet.org/challenge/2006/ for more details.

Accurate delineation is essential in other approaches for QT and QTV study that use beat-to-beat information (Section 2.1). As a matter of fact, it should be noticed that the use of the robust automatic delineation developed and the advantages of the improvements achieved by the proposed methods are not restrict to the particular variability study presented. In particular, the single-lead delineator here described has already been used with an approach based in independent component analysis (Tomé *et al.*, 2005) and with a time-variant system (Pueyo *et al.*, 2005).

Much *more generally*, the delineation improvements achieved *extend* to the study of other ECG features, being of extreme value for ECG automatic characterization.

One of the main contributions of this thesis is the proposed multilead based delineation system, namely:

- for the first time, instead of locating the fiducial points in one available lead, the delineation system explicitly constructs a new better ECG lead for that purpose; the simultaneous use of 3 orthogonal leads is also a novelty;
- among VCG systems, the lead set F (directly recorded Frank leads) was the one than achieved the best global performance; moreover, the direct comparison between the delineation results using each VCG system showed a clear accordance between the three approaches, indicating that the stability of the measure does not depend on the VCG system used;
- the multilead delineation strategies developed are general and can be applied to any orthogonal lead set; the VCG systems here considered were chosen because they are defined by well known leads, which are likely to be familiar to clinicians; however, any other combination of 3 orthogonal leads could be used instead or other global or individual transformations from 12 lead to 2 leads could be used (for example, using principal components).

6.2 QTV/HRV interactions

The good performance of the delineation methods allows to use the measured intervals to characterize the cardiovascular performance and was illustrated by the beat-to-beat variability study presented. It should be remarked that the model used in the thesis was initially proposed for RTV/HTV interactions, as with the delineation systems available it was not possible to obtain reliable QT measures to study its beat-to-beat variability. The availability of this new methodology allows to proceed with QTV/HRV relations study and quantification.

The parametric model for exploring the QTV/HRV relations was able to correctly estimate both QTV fractions over simulated error free series, with bias and error dispersion depending on the QTV level.

Percentage errors obtained were lower than 5% for most of the series with QTV level corresponding to $\sigma_{QT} \geq 5$ ms.

Considering the more realist situation in which the series are first obtained using the delineation, the QTV estimation quality decreases due to ECG noise, however ensuring usable values for moderate contamination levels.

Using a realistic 3-lead extracted noise (data set C_v^F) was possible to obtain ranges of applicability for the proposed methods. The studied methods were found to be applicable and the QTV fractions can be estimated with an admissible error (less than 25%),

- in LF, band if SNR > 15 dB and $\sigma_{QT} > 5$ ms using single-lead delineation;
- in LF, band if SNR > 15 dB and $\sigma_{QT} > 3$ ms using multilead delineation;
- in HF, band if SNR > 20 dB and $\sigma_{QT} > 10$ ms using any of the delineation strategies.

These values established indicative limits for which the QTV fraction quantification can be considered reliable, as a function of SNR and QTV, attending to the delineation method and frequency band. An alternative and more intuitive way of looking to these limits of applicability is to summarize them graphically as presented in Figure 6.1 and described in Appendix F.

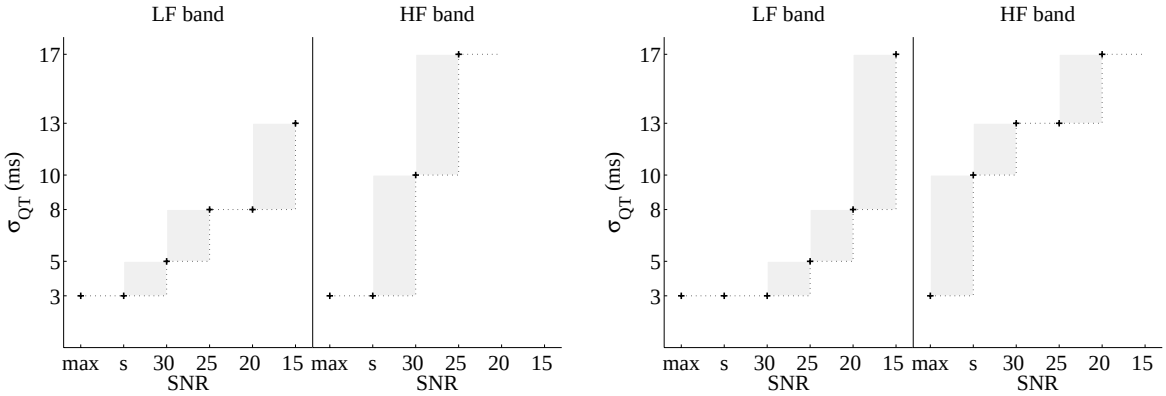

(a) Single-lead based delineation (b) Multilead delineation

Figure 6.1: Minimum σ_{QT} for from data sets for which the percentage errors $\varepsilon^{\mathcal{B}}$ quartile box are within a tolerance degree of 25% (indicative limits of applicability).

The graphic limits were obtained from the percentage errors $\varepsilon^{\mathcal{B}}$ over the simulated data realistic 3-lead extracted noise (Chapter 4). Briefly, for each SNR level it was addressed the minimum QT standard deviation level (QT reference model) for which an error tolerance degree of 25% was accomplished. For the sake of comparison the values found in the datasets corresponding to clean simulated series (max) and signal derived series (s) were also included. As described in Appendix F, data is only available for the values considered in the simulation study, only the σ_{QT} values included in the simulation are indicated in the vertical axis; the grey rectangles correspond to indecision areas (transition between models).

It is clear from the figure that for single-lead delineation the methods present poor robustness in the HF band. The improvement allowed by the multilead delineation is evident, with increased range of applicability and less error for lower QTV levels.

Given a real ECG signal, the estimated QT standard deviation and SNR values can be compared with those limits, what can also be done graphically, as illustrated in Figure 6.2 for the segments from the database PMDB (Chapter 5). It should be noticed that the first two values on the SNR scale of theses figures (40 and 35 dB) are being compared with the indicative limits obtained, respectively, for the clean simulated series and simulated ECG with no noise contamination.

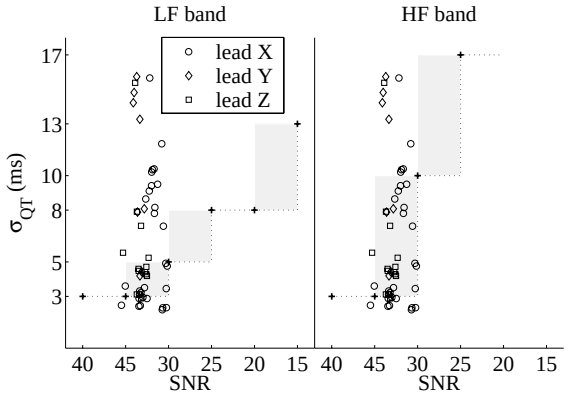

(a) QT standard deviation and SNR estimated in leads X, Y and Z, compared to indicative limits of applicability using single-lead based delineation

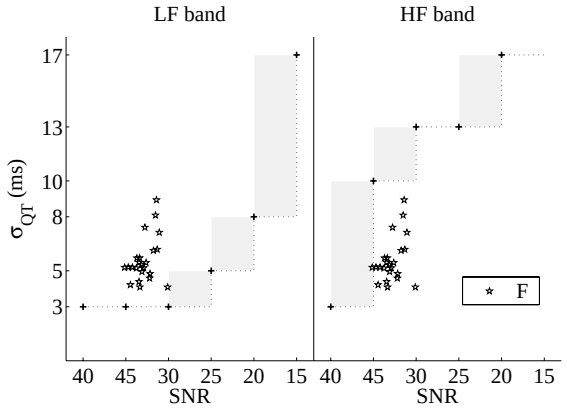

(b) QT standard deviation and SNR estimated over lead set F (Frank leads) compared to indicative limits of applicability using multilead based delineation over

Figure 6.2: Comparison between estimated QT standard deviation and SNR over PMDB data segments and the indicative limits of applicability.

The applicability limits of the methodologies proposed would surely be less restrictive if instead of the QT series the RTapex series were used (Porta *et al.*, 1998), since T peak estimation is less noise sensitive. However the eventual variability (and potential clinical value) of the T peak to T end interval would be lost.

Also, those limits should be considered indicative. As a matter of fact they were obtained using simulated data, that could not reflect all the characteristics of real ECG files. In particular, as no 3-lead noise files were available, the 3-lead noise was extracted from a real file and consequently, this noise contains some ECG like features remaining from the original ECG signal from which it was extracted. Also, as commented in Section 5.3, the SNR calculation used in the noisy data simulation (Sections 4.2.3 and 4.2.4) is quite different to the SNR estimation methods used over real ECG files. Therefore, the use of a real recorded 3-lead noise and considering an eventually different SNR calculation strategy, more easily comparable to a SNR estimation method for real ECG files (Clifford, 2006), would allow to make this limits even more realistic and should be addressed in the future. Also a thinner coverage of the QT standard deviation and SNR values, adjustment of QTV range, regarding the characteristic patterns of pathological conditions, or even the use of an alternative artificial ECG construction strategy can be considered.

Nevertheless, the simulation study allowed to obtain a framework of applicability, that in spite of being merely indicative, can be used to help to decide if the QTV fractions quantification with these methods over a particular ECG segment can be feasible and which error should be expected on it. Making this comparison graphically provides a clear and easy tool, which can be used in practice.

The methods were illustrated in real ECG signals from a standard database and holter files, including pediatric patients under intensive care. A relevant (over 40%) QTV fraction not correlated with HRV was found both in healthy subjects and pediatric patients, indicating that an important part of QTV is not linearly driven by HRV and may contain complementary information. Clinical targeted studies should be considered next to evaluate its potential diagnostic value.

6.3 Final remarks

In this thesis were discussed several issues with *clinical importance*, and it was concluded that:

- *the ECG delineation, in particular the QT interval delineation, can be done automatically using the delineation systems proposed* with low error;
- *the multilead system based on 3 orthogonal leads proposed outperformed any single-lead delineation and allowed to find boundary locations as stable as the ones provided by other methods using much more leads*
- *the automatic methods proposed are adequate to access variability information, as they are accurate and robust to noise and morphology changes;*

- *the VRV and its relations to HRV can be studied using the series of QT and RR variability and the dynamic parametric approach, which allows to correctly estimate the QTV fractions, either correlated or uncorrelated with HRV*
- *the automatic methodologies proposed have showed a good performance over realistically simulated ECG; indicative limits of applicability as function of QTV, SNR and delineation system were established*
- *the QTV fraction not correlated with HRV was found in real data, indicating that an important part of QTV is not linearly driven by HRV and may contain complementary information; its clinical importance remains to be determined.*

Appendix A

Lead synthesis

Different lead systems with specific advantages and diagnosis potential can be used, from orthogonal 3-lead systems to the extremely redundant body surface mapping using as many as 80 or 120 leads.

According to the dipole hypothesis, the electrical activity of the heart can be approximated by a time-variant electrical dipole, called the *electrical heart vector* (EHV). The 3-dimensional record obtained by an orthogonal system is a canonical representation of EHV and defines a *vectocardiogram* (VCG). VCG systems are not redundant, have a solid biophysical interpretation and allow to observe the EHV time evolution in an easy way. Additionally, they provide parameters as loop contour and axis rotation that cannot be directly accessed in the 12-lead ECG and have proven to have important clinical value (Edenbrandt and Pahlm, 1988; Kardys *et al.*, 2003; Malmivuo and Plonsey, 1995).

The most popular 3-lead system is the corrected Frank leads system (X, Y, Z) which is based on three orthogonal body axes defined from the observer point of view as right-to-left (lead X), head-to-foot (lead Y) and front-to-back (lead Z). An example of beat on Frank leads and respective VCG loop can be found in Figures A.1(a) and A.1(b).

Nevertheless, the most widely used system is the standard 12-lead and diagnostic standards are defined over the leads of this system for many pathologies. In spite of being a clearly redundant system, it is the best known by the physicians and thus easier to interpret in clinical practice. It includes leads located either in the vertical plane corresponding to the thorax of a standing individual (*frontal plane*) or in the orthogonal horizontal plane that cross the thorax (*transversal plane*), as illustrated in Figure 1.5 (Malmivuo and Plonsey, 1995; Wagner and Marriott, 1994).

The leads as distributed in the following way:

- 3 *limb* leads in the frontal plane (I, III and II)
- 3 *augmented* leads in the frontal plane (aVL, aVR and aVF)
- 6 *precordial* leads in the transverse (horizontal) plane (V1, V2, V3, V4, V5 and V6).

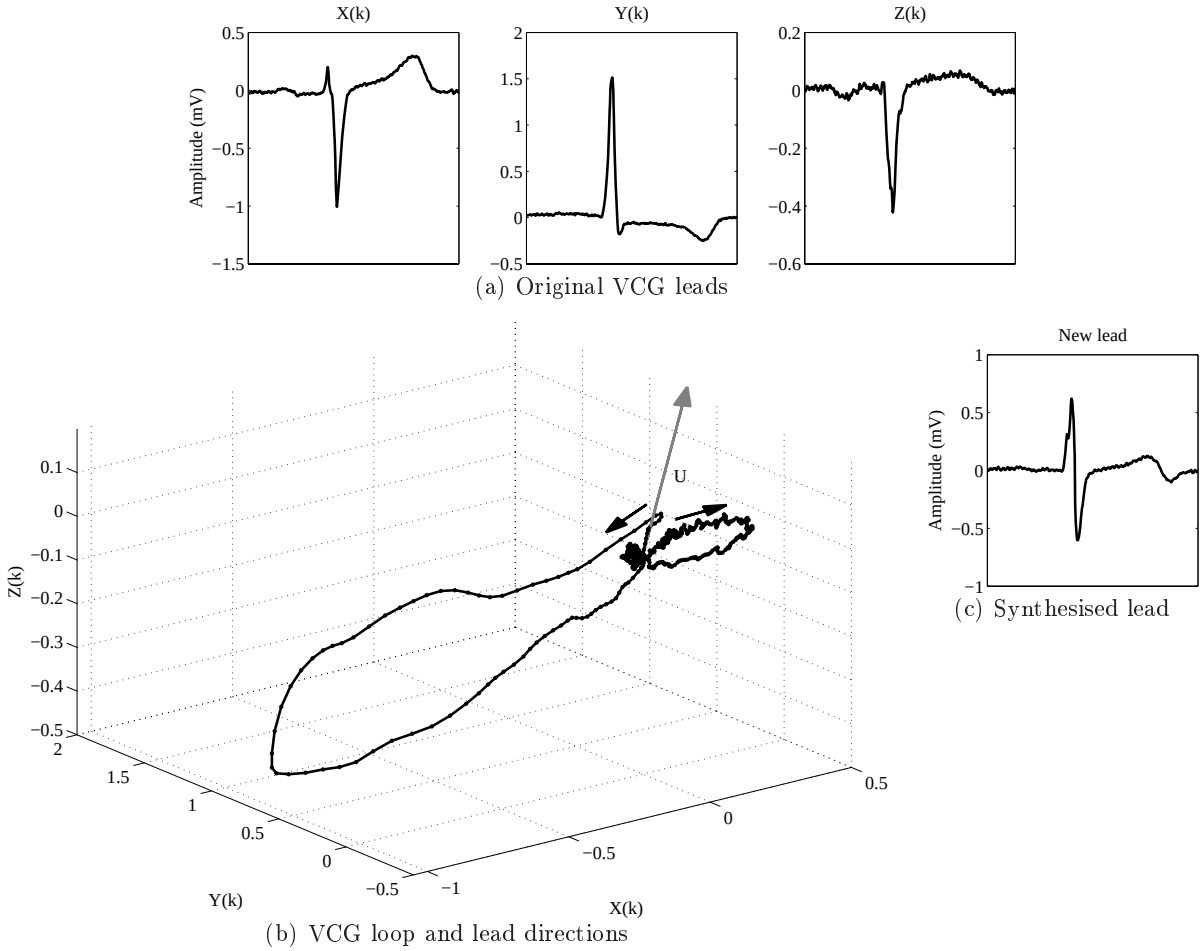

Figure A.1: Example of a beat on original Frank leads, VCG loop and synthesised lead. Black arrows in the loop indicate time direction, with the larger curve corresponding to the QRS complex and smaller to the T wave loop. The new direction **U** (black) for the synthesised lead is marked over the loop (grey arrow). Vectors are multiplied by a constant factor for displaying convenience.

According to Einthoven's law the limb leads are related by:

$$I + III = II.$$

Also the augmented leads can be calculated from I, II and III using the relations:

$$aVR = -1/2(I + II)$$

$$aVL = I - 1/2II$$

$$aVF = II - 1/2I.$$

The precordial leads are considered to detect also *non-dipolar* components with diagnostic significance. Thus the standard lead system includes 8 truly independent (2 limb and the 6 precordial leads).

In terms of the lead axis, the 3 Frank leads (X, Y, Z) correspond respectively to leads I, aVF and -V2, but (X, Y, Z) are constructed taking into consideration the distortions caused by the boundary and internal inhomogeneities of the body, (Malmivuo and Plonsey, 1995).

Much work have been done to find linear transformations between different lead systems (Levkov, 1987). The problem of constructing an orthogonal set of leads from a redundant system can be faced with a least squares approach. The reverse question was investigated by *G. Dower* and his group, by calculating the linear transformations for constructing the 12-lead ECG from the (X, Y, Z) leads, currently known as **Dower matrix** (Dower, 1984). Furthermore, the inverse of this matrix allows to synthesise Frank leads from the 12 standard as

$$X = -0.172V1 - 0.074V2 + 0.122V3 + 0.231V4 + 0.239V5 + 0.194V6 + 0.156I - 0.010II \quad \text{(A.1)}$$

$$Y = 0.057V1 - 0.019V2 - 0.106V3 - 0.022V4 + 0.041V5 + 0.048V6 - 0.227I + 0.887II \quad \text{(A.2)}$$

$$Z = -0.229V1 - 0.310V2 - 0.246V3 - 0.063V4 + 0.055V5 + 0.108V6 + 0.022I + 0.102II, \quad \text{(A.3)}$$

a transformation that has proven to give signals closer to the directly recorded Frank leads than other proposed transformations (Edenbrandt and Pahlm, 1988).

More generally, any arbitrary lead D can be synthesised from a particular lead system using an adequate linear transformation. According to the dipole hypothesis, a cardiac lead corresponds to the projection of the EHV along the axis defined by the electrode sites (Malmivuo and Plonsey, 1995), and it can be identified by an unitary vector $\mathbf{U}$ point from heart to surface. Thus D can be obtained as the projection of the canonical representation of the EHV provided by 3 orthogonal leads over $\mathbf{U}$, that is

$$D(k) = \frac{\mathbf{E}'.\mathbf{U}}{||\mathbf{U}||}. \quad \text{(A.4)}$$

where $\mathbf{E}$ is the matrix with the 3 orthogonal leads, for example the Frank system $\mathbf{E} = [X(k), Y(k), Z(k)]'$. The synthesised lead corresponding to projecting the VCG loop of Figure A.1(b) over the direction U can be found in Figure A.1(c).

ECG recordings are many times done with only 2 simultaneous leads and is that the case of many standard databases, e.g the ones from which the QT database was extracted (Laguna *et al.*, 1997). The two leads are probably non orthogonal but they it should be possible to construct a lead orthogonal to one of the available.

As matter of fact, any hypothetical lead in a plane can be synthesised from a lead system with at least two no parallel leads in that plane. On example of this construction is presented in Figure A.2 in which the lead V2 (inclination of 270^o) is constructed from leads V4 and V5 (inclination of 330^o and 0^o, respectively). This allows to obtain an orthogonal system (V5,V2).

Suppose that U_A and U_B are 2 generic non orthogonal and no collinear vectors, with direction corresponding to leads $A(k)$ and $B(k)$, respectively. Lets's U_C be a vector orthogonal to U_B that defines a lead $C(k)$. Then, lead $A(k)$ is the projection of the points $[C(k), B(k)]'$ over the direction of U_A. Thus, if only $A(k)$ and $B(k)$ leads were available, $C(k)$ can be calculated as a function of U_C, $A(k)$ and $B(k)$, and 2 orthogonal ECG leads are obtained.

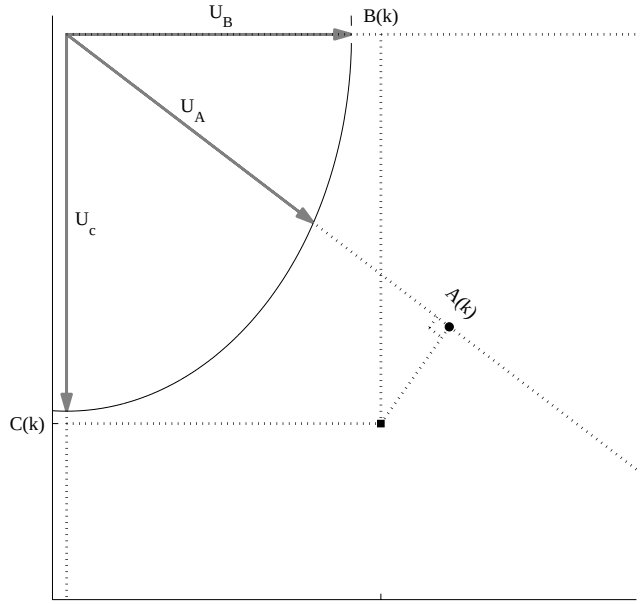

Figure A.2: Example of a lead synthesis from two leads. For some arbitrary sample k, the point $A(k)$ corresponds to $V4$ while the square correspond to the point $[B(k), C(k)]$ in the orthogonal referential $[V5, V2]$ The dot is the orthogonal projection of the square into the vector defining the lead V4. Unitary vectors that define leads V2, V4 and V5 are also plotted.

Appendix B

Physiological and clinical terms

The definitions here presented were simplified, regarding the context of this work, from the correspondent source indicated as reference.

action potential - electrical activity over time of the cardiac cells in each heart region; the summation of the different action potential curves recorded at the body surface correspond to the ECG signal Malmivuo and Plonsey (1995).

arrhythmia - deviation from the normal heartbeat rhythm because of a disturbance in the electrical impulses on the heart (Zaret *et al.*, 1999).

artifact - electrocardiographic wave that arises from sources other than the heart (Wagner and Marriott, 1994).

atrial fibrillation or atrial fluter - arrhythmia in which the atria contract at an excessive and irregular rate (Zaret *et al.*, 1999).

atrioventricular node - a small mass of tissue that slows the impulses travelling from the atria to the ventricles, allowing the pumping synchronization (Wagner and Marriott, 1994).

atrium - heart chamber that receives blood from the veins and passes it to the ventricle (Wagner and Marriott, 1994).

autonomic nervous system (ANS) - one of the two main divisions of the peripheral nervous system, that is structurally and functionally an interface between the internal and external environment conditions, coordinating body functions which ensure homeostasis, as is the case of cardiorespiratory control and adaptive responses to stress (Hamill and Shapiro, 2004).

β-blocker - group of medication used to treat angina, hypertension and cardiac arrhythmia by blocking nerve receptors, thereby reducing the force and rate of the heartbeat (Zaret *et al.*, 1999).

cardiac arrest or **sudden cardiac death** - incident during which the heart stops beating and unconsciousness occurs because of the cutoff of blood flow to the brain. (Zaret *et al.*, 1999).

cardiomyopathy - disease of the heart muscle (Zaret *et al.*, 1999).

chronic heart failure - see heart failure

congestive heart failure (CHF) - complex syndrome resulting from an insult to myocardium in which the sympathetic nervous system is overactive to compensate the effects of decreased cardiac output (Khan and Sinoway, 2004).

defibrillation - electric chock administered to the heart to stabilize an irregular heartbeat or restore a normal heartbeat after cardiac arrest (Zaret *et al.*, 1999).

diabetes mellitus - disorder characterized by problems in glucose (blood sugar) metabolism. In type I diabetes (juvenile-onset or insulin-dependent) the body ceases to produce insulin (the hormone essential for glucose metabolism); in type II (adult-onset or insulin-resistant) the body fails to use insulin (Zaret *et al.*, 1999).

diabetic autonomic neuropathy - (DAN) group of symptoms resulting of nerve impairment caused by Diabetes mellitus that can affect all organ systems innervated by the autonomic system, as it is the case of the cardiovascular system (Ertl *et al.*, 2004).

dilated cardiomyopathy (DMC) - myocardial disorder characterized by an enlargement and inadequate function of the heart walls that leads to heart failure (Zaret *et al.*, 1999).

ectopic beat - beat initiated by other rather than sinoatrial node cells (Zaret *et al.*, 1999).

endocardium - internal membrane of the heart wall (Wagner and Marriott, 1994).

frontal plane - vertical plane of the body which lies perpendicular to the horizontal (transverse) plane (Wagner and Marriott, 1994).

head-up tilt - test that aims to evaluate the response to body position changes, by moving the table where the patient is lying from horizontal to a nearly upright position. This procedure is useful to evaluate patients with recurrent syncope (temporary loss of consciousness) usually related to temporary insufficient blood flow to the brain, and can either have benign causes, as an emotional stress situation, or be sign of a serious disorder (Benditt *et al.*, 1986).

heart block - delay or interruption in the normal electrical path that can be partial or complete (total) (Zaret *et al.*, 1999).

heart failure - inability of the heart to pump sufficient blood to maintain normal circulation (Zaret *et al.*, 1999).

hypertrophy - increase in muscle mass, more common in ventricles when compensating for overload (Wagner and Marriott, 1994).

hypertrophic cardiomyopathy- (HCM) see hypertrophy and cardiomyopathy

infarct - area of necrosis in an organ resulting from an obstruction in its blood supply (Wagner and Marriott, 1994).

ischemia - insufficiency of blood flow to an organ severe enough to cause the disruption of its

functioning (Wagner and Marriott, 1994).

ischemia cardiomyopathy - see ischemia and cardiomyopathy

long QT syndrome (LQTS) - pathophysiological state (congenital or acquired) characterized by the appearance long QT intervals in the electrocardiogram, changes of morphology and rhythm in repolarization waves. They related with a potentially lethal arrhythmia know as *torsade de pointes* (Yan and Antzelevitch, 1998).

myocardium - middle muscular layer of the heart wall (Wagner and Marriott, 1994).

myocardial infarction (MI) - medical term for heart attack, consisting in an area of dead or dying in the heart muscle caused by a marked decrease in the oxygen supply to that area (Zaret *et al.*, 1999).

parasympathetic system - subdivision of the autonomic nervous system that is responsible for the basal autonomic functions as heart rate and respiration in normal conditions (Kim, 2004).

pericardium - external serous membrane of the heart wall (Wagner and Marriott, 1994).

purkinje fibers - modified myocardial cells that are found in the distal aspects of the pacemaking and conduction system that conduct the electrical impulses in a rapid way to several parts of the heart (Wagner and Marriott, 1994).

reentry - electrical impulse that spreads back as result of a conduction abnormality (Wagner and Marriott, 1994).

sinoatrial node - small mass of tissue that is the dominant pacemaker, forming the electrical impulses that are then conducted throughout the heart (Wagner and Marriott, 1994).

sinus arrhythmia - normal variation in sinus rhythm that occurs during the inspiratory and expiratory phases of respiration (Wagner and Marriott, 1994).

sinus rhythm - normal cardiac rhythm originated via impulse formation in the sinoatrial node (Wagner and Marriott, 1994).

stress or **exercise test** - electrocardiogram that is done while the person exercises, usually on a treadmill or a stationary bicycle (Zaret *et al.*, 1999).

sudden cardiac death - see cardiac arrest

sympathetic system - subdivision of the autonomic nervous system that controls the *fight-or-flight* reactions during emergencies by increasing the sympathetic outflow to the heart and other viscera (Kim, 2004).

syncope - transient loss of consciousness and postural tone (fainting) with spontaneous recovery and no neurologic sequelae, caused by a global reversible reduction of blood flow to the neuronal network in the brainstem responsible for supporting consciousness (Kaufmann, 2004).

tachycardia - a rapid heart rate, above 100 bpm in adults (Wagner and Marriott, 1994).

transverse plane - a horizontal plane of the body which lies perpendicular to the vertical (frontal) plane (Wagner and Marriott, 1994).

ventricle - chamber of the heart that receives the blood from the correspondent atrium and then pumps it into the arteries (Wagner and Marriott, 1994).

ventricular fibrillation (VF) - rapid, uncoordinated, and ineffective contraction of the heart initiated by electrical impulses from the ventricles. The pumping action is almost nonexistent and the hear merely quivers. Can be fatal if not reversed (Zaret *et al.*, 1999).

ventricular hypertrophy - see ventricle and hypertrophy

ventricular tachycardia - see ventricle and tachycardia

Appendix C

Simulation parameters

C.1 Auxiliary parameters for reference models construction

$T_R = 1$ sec (mean RR)

RR AR model (Rest) used to simulate $x_{\mathrm{RR}_{\mathrm{Re}}}(n)$ realizations:

$a_{22}^r(z) = 1 - 1.6265z^{-1} + 1.8849z^{-2} - 1.8327z^{-3} + 1.2970z^{-4} - 0.7758z^{-5} + 0.4133z^{-6} - 0.2136z^{-7}$

$\lambda_{\mathrm{RR}}^r = 0.0201$ ms

RR AR model (Tilt) used to simulate $x_{\mathrm{RR}_{\mathrm{Ti}}}(n)$ realizations:

$a_{22}^r(z) = 1 - 1.8149z^{-1} + 2.1365z^{-2} - 2.1703z^{-3} + 1.7194z^{-4} - 0.9221z^{-5} + 0.5311z^{-6} - 0.3262z^{-7}$

$\lambda_{\mathrm{RR}}^r = 0.0117$ ms

auxiliary series: $\tilde{x}_{\mathrm{QT}}(n) = a\left(\sqrt{x_{\mathrm{RR}_{\mathrm{Re}}}(n)} + \sqrt{x_{\mathrm{RR}_{\mathrm{Ti}}}(n)}\right) + b$, where:

$a = \frac{\sigma_{QT}}{s_{\tilde{x}_{RR}}}$

$b = -m_{\tilde{x}_{RR}}$

QT model	1	2	3	4	5	6
σ_{QT}	17 ms	13 ms	10 ms	8 ms	5 ms	3 ms

$m_{\tilde{x}_{RR}}$ and $s_{\tilde{x}_{RR}}$ stand respectively for the mean and standard deviation of $\sqrt{x_{\mathrm{RR}_{\mathrm{Re}}}(n)} + \sqrt{x_{\mathrm{RR}_{\mathrm{Ti}}}(n)}$

C.2 Reference models

$q = 4$ (RR models reference order)

$p = 7$ (QT models reference order)

RR reference model:

$a^r_{22}(z) = 1 - 1.311z^{-1} + 1.113z^{-2} - 0.7662z^{-3} + 0.2054z^{-4} + 0.04246z^{-5} - 0.03863z^{-6} - 0.1218z^{-7}$

$\lambda^r_{\mathrm{RR}} = 0.0235$ ms

QT model 1:

$a^r_{11}(z) = 1 - 1.458z^{-1} + 1.563z^{-2} - 1.191z{-}3 + 0.7042z^{-4}$

$a^r_{12}(z) = 0.3046 - 0.439z^{-1} + 0.4669z^{-2} - 0.3492z^{-3} + 0.2009z^{-4}$

$d^r(z) = 1 + 0.2918z^{-1} - 0.4088z^{-2} - 0.339z^{-3} - 0.08615z^{-4}$

$\lambda^r_{\mathrm{QT}} = 0.0046$ ms

QT model 2:

$a^r_{11}(z) = 1 - 1.456z^{-1} + 1.554z^{-2} - 1.181z{-}3 + 0.6986z^{-4}$

$a^r_{12}(z) = 0.2296 - 0.3287z^{-1} + 0.3466z^{-2} - 0.2587z^{-3} + 0.1508z^{-4}$

$d^r(z) = 1 + 0.3064z^{-1} - 0.4135z^{-2} - 0.3289z^{-3} - 0.08708z^{-4}$

$\lambda^r_{\mathrm{QT}} = 0.0036$ ms

QT model 3:

$a^r_{11}(z) = 1 - 1.45z^{-1} + 1.533z^{-2} - 1.153z{-}3 + 0.6868z^{-4}$

$a^r_{12}(z) = 0.1818 - 0.2613z^{-1} + 0.2747z^{-2} - 0.2026z^{-3} + 0.1177z^{-4}$

$d^r(z) = 1 + 0.4084z^{-1} - 0.3865z^{-2} - 0.4176z^{-3} - 0.11z^{-4}$

$\lambda^r_{\mathrm{QT}} = 0.0029$ ms

QT model 4:

$a_{11}^r(z) = 1 - 1.471z^{-1} + 1.582z^{-2} - 1.196z{-}3 + 0.7122z^{-4}$

$a_{12}^r(z) = 0.1502 - 0.2221z^{-1} + 0.2391z^{-2} - 0.1793z^{-3} + 0.1034z^{-4}$

$d^r(z) = 1 + 0.4055z^{-1} - 0.4504z^{-2} - 0.3869z^{-3} - 0.09823z^{-4}$

$\lambda_{\mathrm{QT}}^r = 0.0023$ ms

QT model 5:

$a_{11}^r(z) = 1 - 1.6423z^{-1} - 0.07797z^{-2} + 0.1242z{-}3 + 0.4097z^{-4}$

$a_{12}^r(z) = 0.09175 - 0.05796z^{-1} - 0.006895z^{-2} + 0.01381z^{-3} + 0.03312z^{-4}$

$d^r(z) = 1 - 0.1703z^{-1} + 0.2563z^{-2} - 0.2004z^{-3} - 0.4844z^{-4}$

$\lambda_{\mathrm{QT}}^r = 0.0017$ ms

QT model 6:

$a_{11}^r(z) = 1 - 0.6825z^{-1} - 0.07077z^{-2} + 0.166z{-}3 + 0.3199z^{-4}$

$a_{12}^r(z) = 0.05466 - 0.03773z^{-1} - 0.004596z^{-2} + 0.01048z^{-3} + 0.01593z^{-4}$

$d^r(z) = 1 - 0.02643z^{-1} + 0.1615z^{-2} - 0.06663z^{-3} - 0.533z^{-4}$

$\lambda_{\mathrm{QT}}^r = 0.0012$ ms

Appendix D

Total least squares criteria for main a lead direction

In this thesis, total least squares (TLS) minimization was used to find the main direction $\mathbf{U}$ of the electrical heart vector (EHV), in a time interval I (Chapter 3).

The temporal evolution of EHV in a scale 2^m and time window I is described by the WT loops $\mathbf{L}_I^m(k) = [W_{2^m}^X(k), W_{2^m}^Y(k), W_{2^m}^Z(k)]', k \in I$, thus $\mathbf{U} = [U^X, U^Y, U^Z]'$ is be the best *line fit* to a WT loop. Furthermore, in order to define a direction, $\mathbf{U}$ must be a *straight line fit*. That is, $\mathbf{U}$ is the vector that minimizes the errors between $\mathbf{L}_I^m(k)$ and $\hat{\mathbf{D}}(k)\,|_{k\in I} = [\hat{d}^X(k), \hat{d}^Y(k), \hat{d}^Z(k)]'\,|_{k\in I}$, where

$$\hat{\mathbf{D}}(k) = [\hat{d}^X(k), \hat{d}^Y(k), \hat{d}^Z(k)]' = (\hat{p}^X, \hat{p}^Y, \hat{p}^Z)' + c_k[U^X, U^Y, U^Z]',\ c_k \in R, \tag{D.1}$$

for an also optimal $(\hat{p}^X, \hat{p}^Y, \hat{p}^Z)' \in R^3$.

The 3 WT signals used to define the data matrix $\mathbf{L}_I^m(k)$ are representations of observed ECG leads and thus all contain errors. However the traditional least squares (LS) criteria assumes that *errors* occur only in one *observed* variable, while the other variables in the data matrix are exactly known. On the other hand, total least squares (TLS) fitting treats the data as *"noisy"*, that is, all variables can contain errors (Van Huffel and Vandewalle, 1991).

From the differences in this underling principle results that the minimization of the distance between the data and fitting line considers:

- for LS, only the residuals on the direction of the *observed* variable,
- for TLS, the deviations orthogonal to the fitted line.

This can be easily visualized by considering a 2-dimensional example with 2 arbitrary variables, as illustrated in figure D.1. The TLS minimization with 3 variables is illustrated in Figure D.2 for the case of a WT loop corresponding to a T wave.

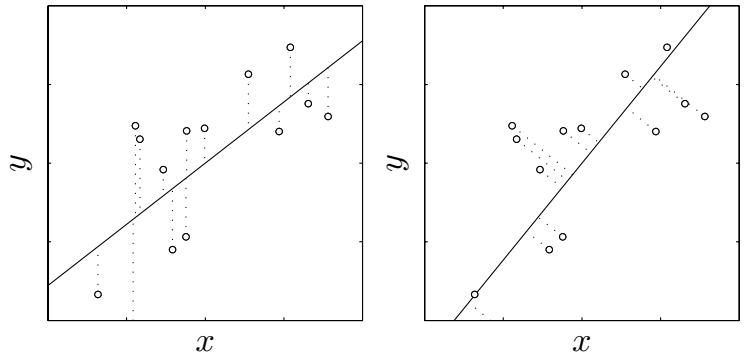

(a) TLS (b) LS

Figure D.1: LS and TLS minimization with 2 arbitrary variables. LS minimize the sum of squared vertical errors and TLS minimize the sum of squared orthogonal errors.

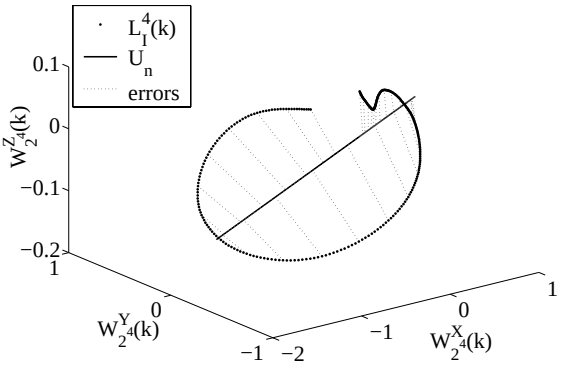

Figure D.2: TLS minimization in a 3-dimensional WT loop. WT loop in scale 2^4, best line fit U_n and residuals (I corresponds to the T wave in the n^{th} beat; for the sake of visualization residuals are only indicated for a sample of the loop in each 10 samples).

TLS can be formulated in different ways, depending on the specific problem. Regarding the goal of finding the main direction of EHV, the linear relationship between the columns of $\mathbf{L}_I^m(k)$ is of interest, with no particular preference in writing one variable as linear combination of the others. Thus the following formulation was used (Van Huffel and Vandewalle, 1991) (N stands for I length):

$$\begin{aligned} &minimize \quad \left\| \mathbf{L}_I^m(k) - \hat{\mathbf{D}}(k) \right\|_F \\ &\quad k \in I \\ &\text{subject to} \quad \hat{d}^Y(k) = \frac{U^Y}{U^X{}_*}(\hat{d}^X(k) - \hat{p}^X) + \hat{p}^Y \\ &\qquad\qquad \hat{d}^Z(k) = \frac{U^Z}{U^X} * (\hat{d}^X(k) - \hat{p}^X) + \hat{p}^Z. \end{aligned} \tag{D.2}$$

The minimization was implemented as a non-linear least squares problem [1]. The initial condition was arbitrary taken as the straight line defined by the points on the limits of the interval I.

[1] The function *lsqnonlin.m* from MATLAB Optimization Toolbox was used, with default options given by *optimset.m*, except for the *maximum number of function evaluations allowed* than was set as 1000.

Appendix E

Additional Tables

Table E.1: Mean and standard deviation of absolute errors $\xi^{\mathcal{B}}$ in data sets with baseline wandering contamination (MIT pre-recorded Noise) ($ms^2, mean \pm sd$); number of valid models (#) are also presented for each data set; reference measures ($P^{\mathcal{B}}_{\mathrm{QT|RR}}$, $P^{\mathcal{B}}_{\mathrm{QT|QT}}$) can be found in Table 2.2.

QT model / data set	#	$\overline{\xi}^{TP} \pm s_{\xi}^{TP}$, ms^2	$\frac{100\lvert\overline{\xi}^{TP}\rvert}{P^{TP}_{\mathrm{QT\lvert RR}}} \pm \frac{100\lvert s_{\xi}^{TP}\rvert}{P^{TP}_{\mathrm{QT\lvert RR}}}$	$\overline{\xi}^{LF} \pm s_{\xi}^{LF}$, ms^2	$\frac{100\lvert\overline{\xi}^{LF}\rvert}{P^{LF}_{\mathrm{QT\lvert RR}}} \pm \frac{100\lvert s_{\xi}^{LF}\rvert}{P^{LF}_{\mathrm{QT\lvert RR}}}$	$\overline{\xi}^{HF} \pm s_{\xi}^{HF}$, ms^2	$\frac{100\lvert\overline{\xi}^{HF}\rvert}{P^{HF}_{\mathrm{QT\lvert RR}}} \pm \frac{100\lvert s_{\xi}^{HF}\rvert}{P^{HF}_{\mathrm{QT\lvert RR}}}$
$1/C^{X}_{bw(30dB)}$	49	-35.8 ± 18.5	-32.9 ± 17.0	-35.8 ± 18.5	-59.2 ± 30.5	-35.8 ± 18.5	-73.9 ± 38.1
$1/C^{X}_{bw(25dB)}$	49	-35.6 ± 17.9	-32.6 ± 16.4	-35.6 ± 17.9	-58.8 ± 29.6	-35.6 ± 17.9	-73.3 ± 36.9
$1/C^{X}_{bw(20dB)}$	49	-35.3 ± 18.4	-32.3 ± 16.9	-35.3 ± 18.4	-58.3 ± 30.4	-35.3 ± 18.4	-72.7 ± 37.9
$1/C^{X}_{bw(15dB)}$	49	-35.3 ± 19.7	-32.4 ± 18.1	-35.3 ± 19.7	-58.3 ± 32.6	-35.3 ± 19.7	-72.7 ± 40.6
$1/C^{X}_{bw(10dB)}$	48	-35.5 ± 19.8	-32.6 ± 18.1	-35.5 ± 19.8	-58.7 ± 32.7	-35.5 ± 19.8	-73.2 ± 40.8
$2/C^{X}_{bw(30dB)}$	48	-20.3 ± 10.8	-32.5 ± 17.3	-20.3 ± 10.8	-59.7 ± 31.8	-20.3 ± 10.8	-71.2 ± 37.9
$2/C^{X}_{bw(25dB)}$	49	-20.2 ± 11.5	-32.4 ± 18.4	-20.2 ± 11.5	-59.5 ± 33.9	-20.2 ± 11.5	-71.0 ± 40.4
$2/C^{X}_{bw(20dB)}$	48	-20.5 ± 11.2	-32.8 ± 17.9	-20.5 ± 11.2	-60.4 ± 32.8	-20.5 ± 11.2	-72.0 ± 39.2
$2/C^{X}_{bw(15dB)}$	49	-19.5 ± 13.6	-31.2 ± 21.8	-19.5 ± 13.6	-57.4 ± 40.1	-19.5 ± 13.6	-68.5 ± 47.9
$2/C^{X}_{bw(10dB)}$	48	-20.1 ± 12.2	-32.1 ± 19.5	-20.1 ± 12.2	-59.1 ± 35.8	-20.1 ± 12.2	-70.5 ± 42.7
$3/C^{X}_{bw(30dB)}$	49	-11.5 ± 7.0	-30.1 ± 18.3	-11.5 ± 7.0	-54.5 ± 33.1	-11.5 ± 7.0	-67.3 ± 40.9
$3/C^{X}_{bw(25dB)}$	49	-12.3 ± 7.2	-32.2 ± 18.8	-12.3 ± 7.2	-58.3 ± 34.0	-12.3 ± 7.2	-71.9 ± 42.0
$3/C^{X}_{bw(20dB)}$	49	-11.8 ± 7.0	-30.9 ± 18.2	-11.8 ± 7.0	-55.9 ± 33.0	-11.8 ± 7.0	-69.0 ± 40.7
$3/C^{X}_{bw(15dB)}$	49	-11.5 ± 7.5	-30.1 ± 19.6	-11.5 ± 7.5	-54.4 ± 35.5	-11.5 ± 7.5	-67.2 ± 43.9
$3/C^{X}_{bw(10dB)}$	48	-12.0 ± 7.7	-31.3 ± 20.0	-12.0 ± 7.7	-56.7 ± 36.3	-12 ± 7.7	-70.0 ± 44.7
$4/C^{X}_{bw(30dB)}$	49	-7.3 ± 5.0	-29.3 ± 19.8	-7.3 ± 5.0	-52.5 ± 35.6	-7.3 ± 5.0	-66.2 ± 44.9
$4/C^{X}_{bw(25dB)}$	49	-7.3 ± 4.9	-29.3 ± 19.5	-7.3 ± 4.9	-52.5 ± 35.0	-7.3 ± 4.9	-66.2 ± 44.1
$4/C^{X}_{bw(20dB)}$	48	-7.2 ± 4.8	-28.5 ± 19.3	-7.2 ± 4.8	-51.1 ± 34.6	-7.2 ± 4.8	-64.4 ± 43.7
$4/C^{X}_{bw(15dB)}$	49	-7.5 ± 5.2	-29.7 ± 20.7	-7.5 ± 5.2	-53.3 ± 37.1	-7.5 ± 5.2	-67.2 ± 46.7
$4/C^{X}_{bw(10dB)}$	48	-7.7 ± 5.1	-30.9 ± 20.2	-7.7 ± 5.1	-55.4 ± 36.2	-7.7 ± 5.1	-69.8 ± 45.7
$5/C^{X}_{bw(30dB)}$	49	-2.8 ± 2.2	-29.3 ± 23.4	-2.8 ± 2.2	-51.1 ± 40.8	-2.8 ± 2.2	-68.5 ± 54.7
$5/C^{X}_{bw(25dB)}$	49	-2.9 ± 2.3	-29.7 ± 24.3	-2.9 ± 2.3	-51.9 ± 42.5	-2.9 ± 2.3	-69.6 ± 57
$5/C^{X}_{bw(20dB)}$	49	-2.5 ± 3.1	-25.8 ± 32.1	-2.5 ± 3.1	-45.1 ± 56.1	-2.5 ± 3.1	-60.5 ± 75.2
$5/C^{X}_{bw(15dB)}$	49	-2.4 ± 2.3	-25.5 ± 24.4	-2.4 ± 2.3	-44.4 ± 42.6	-2.4 ± 2.3	-59.6 ± 57.2
$5/C^{X}_{bw(10dB)}$	48	-2.7 ± 2.7	-28.3 ± 28.1	-2.7 ± 2.7	-49.4 ± 49.1	-2.7 ± 2.7	-66.2 ± 65.9
$6/C^{X}_{bw(30dB)}$	49	-0.8 ± 1.0	-25.3 ± 28.8	-0.8 ± 1.0	-46.3 ± 52.8	-0.8 ± 1.0	-55.6 ± 63.4
$6/C^{X}_{bw(25dB)}$	49	-0.8 ± 0.9	-25.5 ± 26.3	-0.8 ± 0.9	-46.8 ± 48.3	-0.8 ± 0.9	-56.1 ± 57.9
$6/C^{X}_{bw(20dB)}$	49	-0.5 ± 1.2	-14.1 ± 37.0	-0.5 ± 1.2	-25.8 ± 67.8	-0.5 ± 1.2	-31.0 ± 81.4
$6/C^{X}_{bw(15dB)}$	49	-0.5 ± 1.2	-14.2 ± 37.1	-0.5 ± 1.2	-26.1 ± 68.0	-0.5 ± 1.2	-31.3 ± 81.6
$6/C^{X}_{bw(10dB)}$	48	-0.7 ± 1.3	-21.8 ± 39.7	-0.7 ± 1.3	-40.0 ± 72.9	-0.7 ± 1.3	-48.0 ± 87.4

Table E.2: Mean and standard deviation of the absolute errors $\xi^{\mathcal{B}}$ in data sets with electrode movement contamination (MIT pre-recorded Noise) ($ms^2, mean \pm sd$); number of valid models (#) are also presented for each data set; reference measures ($P^{\mathcal{B}}_{\mathrm{QT|RR}}$, $P^{\mathcal{B}}_{\mathrm{QT|QT}}$) can be found in Table 2.2.

QT model / data set	#	$\bar{\xi}^{TP} \pm s_\xi^{TP}$, ms^2	$\frac{100\lvert\bar{\xi}^{TP}\rvert}{\frac{PTP}{\mathrm{QT\|RR}}} \pm \frac{100\lvert s_\xi^{TP}\rvert}{\frac{PTP}{\mathrm{QT\|RR}}}$	$\bar{\xi}^{LF} \pm s_\xi^{LF}$, ms^2	$\frac{100\lvert\bar{\xi}^{LF}\rvert}{\frac{PLF}{\mathrm{QT\|RR}}} \pm \frac{100\lvert s_\xi^{LF}\rvert}{\frac{PLF}{\mathrm{QT\|RR}}}$	$\bar{\xi}^{HF} \pm s_\xi^{HF}$, ms^2	$\frac{100\lvert\bar{\xi}^{HF}\rvert}{\frac{PHF}{\mathrm{QT\|RR}}} \pm \frac{100\lvert s_\xi^{HF}\rvert}{\frac{PHF}{\mathrm{QT\|RR}}}$
$1/C^X_{em(30dB)}$	49	-36.8 ± 17.8	-33.8 ± 16.4	-36.8 ± 17.8	-60.8 ± 29.5	-36.8 ± 17.8	-75.9 ± 36.8
$1/C^X_{em(25dB)}$	49	-36.1 ± 18.4	-33.1 ± 16.9	-36.1 ± 18.4	-59.7 ± 30.4	-36.1 ± 18.4	-74.4 ± 38.0
$1/C^X_{em(20dB)}$	49	-35.3 ± 19.3	-32.4 ± 17.7	-35.3 ± 19.3	-58.4 ± 31.9	-35.3 ± 19.3	-72.9 ± 39.8
$1/C^X_{em(15dB)}$	49	-34.8 ± 21.2	-31.9 ± 19.4	-34.8 ± 21.2	-57.5 ± 35.0	-34.8 ± 21.2	-71.7 ± 43.7
$1/C^X_{em(10dB)}$	49	-16.7 ± 74.4	-15.4 ± 68.3	-16.7 ± 74.4	-27.7 ± 123.0	-16.7 ± 74.4	-34.5 ± 153.5
$2/C^X_{em(30dB)}$	49	-20.6 ± 10.5	-32.9 ± 16.8	-20.6 ± 10.5	-60.5 ± 30.8	-20.6 ± 10.5	-72.2 ± 36.8
$2/C^X_{em(25dB)}$	49	-20.4 ± 10.9	-32.6 ± 17.5	-20.4 ± 10.9	-59.9 ± 32.2	-20.4 ± 10.9	-71.5 ± 38.4
$2/C^X_{em(20dB)}$	49	-19.8 ± 11.7	-31.7 ± 18.7	-19.8 ± 11.7	-58.3 ± 34.4	-19.8 ± 11.7	-69.6 ± 41.0
$2/C^X_{em(15dB)}$	48	-19.0 ± 12.3	-30.5 ± 19.6	-19.0 ± 12.3	-56.0 ± 36.1	-19.0 ± 12.3	-66.8 ± 43.1
$2/C^X_{em(10dB)}$	49	-9.5 ± 23.2	-15.3 ± 37.1	-9.5 ± 23.2	-28.1 ± 68.2	-9.5 ± 23.2	-33.5 ± 81.3
$3/C^X_{em(30dB)}$	49	-11.8 ± 6.2	-31.0 ± 16.2	-11.8 ± 6.2	-56.1 ± 29.4	-11.8 ± 6.2	-69.2 ± 36.2
$3/C^X_{em(25dB)}$	49	-11.0 ± 7.6	-28.9 ± 19.9	-11.0 ± 7.6	-52.3 ± 36.0	-11.0 ± 7.6	-64.5 ± 44.4
$3/C^X_{em(20dB)}$	49	-11.2 ± 7.1	-29.4 ± 18.6	-11.2 ± 7.1	-53.3 ± 33.7	-11.2 ± 7.1	-65.7 ± 41.6
$3/C^X_{em(15dB)}$	49	-10.7 ± 6.2	-27.9 ± 16.2	-10.7 ± 6.2	-50.6 ± 29.2	-10.7 ± 6.2	-62.4 ± 36.1
$3/C^X_{em(10dB)}$	48	2.2 ± 14.9	5.7 ± 39.1	2.2 ± 14.9	10.3 ± 70.8	2.2 ± 14.9	12.8 ± 87.3
$4/C^X_{em(30dB)}$	49	-7.7 ± 4.6	-30.6 ± 18.2	-7.7 ± 4.6	-54.8 ± 32.6	-7.7 ± 4.6	-69.2 ± 41.1
$4/C^X_{em(25dB)}$	49	-7.6 ± 4.8	-30.2 ± 19.0	-7.6 ± 4.8	-54.1 ± 34.1	-7.6 ± 4.8	-68.2 ± 43.0
$4/C^X_{em(20dB)}$	49	-7.1 ± 4.7	-28.5 ± 18.5	-7.1 ± 4.7	-51.1 ± 33.2	-7.1 ± 4.7	-64.4 ± 41.9
$4/C^X_{em(15dB)}$	49	-5.1 ± 6.0	-20.5 ± 24.0	-5.1 ± 6.0	-36.8 ± 43.0	-5.1 ± 6.0	-46.4 ± 54.2
$4/C^X_{em(10dB)}$	48	7.2 ± 13.6	28.7 ± 54.2	7.2 ± 13.6	51.5 ± 97.2	7.2 ± 13.6	64.9 ± 122.7
$5/C^X_{em(30dB)}$	49	-3.2 ± 1.8	-33.5 ± 19.2	-3.2 ± 1.8	-58.5 ± 33.5	-3.2 ± 1.8	-78.5 ± 45.0
$5/C^X_{em(25dB)}$	49	-3.1 ± 1.9	-32.6 ± 19.4	-3.1 ± 1.9	-57.0 ± 33.8	-3.1 ± 1.9	-76.4 ± 45.4
$5/C^X_{em(20dB)}$	49	-2.6 ± 2.2	-27.2 ± 23.1	-2.6 ± 2.2	-47.4 ± 40.3	-2.6 ± 2.2	-63.6 ± 54.0
$5/C^X_{em(15dB)}$	49	-1.7 ± 2.9	-18.0 ± 30.5	-1.7 ± 2.9	-31.4 ± 53.2	-1.7 ± 2.9	-42.2 ± 71.4
$5/C^X_{em(10dB)}$	49	8.9 ± 14.7	92.8 ± 153.0	8.9 ± 14.7	162.0 ± 267.1	8.9 ± 14.7	217.3 ± 358.3
$6/C^X_{em(30dB)}$	49	-1.3 ± 0.6	-40.7 ± 17.2	-1.3 ± 0.6	-74.6 ± 31.5	-1.3 ± 0.6	-89.5 ± 37.9
$6/C^X_{em(25dB)}$	49	-1.1 ± 0.6	-34.1 ± 19.4	-1.1 ± 0.6	-62.5 ± 35.6	-1.1 ± 0.6	-75.0 ± 42.7
$6/C^X_{em(20dB)}$	49	-0.7 ± 0.9	-20.7 ± 26.5	-0.7 ± 0.9	-38.0 ± 48.6	-0.7 ± 0.9	-45.6 ± 58.3
$6/C^X_{em(15dB)}$	49	1.0 ± 4.2	30.3 ± 127.9	1.0 ± 4.2	55.5 ± 234.6	1.0 ± 4.2	66.6 ± 281.5
$6/C^X_{em(10dB)}$	49	9.7 ± 15.8	294.9 ± 479.0	9.7 ± 15.8	540.6 ± 878.2	9.7 ± 15.8	648.8 ± 1053.8

Table E.3: Mean and standard deviation of the absolute errors $\xi^{\mathcal{B}}$ in data sets with muscular artifacts contamination (MIT pre-recorded Noise) ($ms^2, mean \pm sd$); number of valid models (#) are also presented for each data set; reference measures ($P^{\mathcal{B}}_{\mathrm{QT|RR}}$, $P^{\mathcal{B}}_{\mathrm{QT|QT}}$) can be found in Table 2.2.

QT model / data set	#	$\bar{\xi}^{TP} \pm s_\xi^{TP}$, ms^2	$\frac{100\lvert\bar{\xi}^{TP}\rvert}{P^{TP}_{\mathrm{QT\|RR}}} \pm \frac{100\lvert s_\xi^{TP}\rvert}{P^{TP}_{\mathrm{QT\|RR}}}$	$\bar{\xi}^{LF} \pm s_\xi^{LF}$, ms^2	$\frac{100\lvert\bar{\xi}^{LF}\rvert}{P^{LF}_{\mathrm{QT\|RR}}} \pm \frac{100\lvert s_\xi^{LF}\rvert}{P^{LF}_{\mathrm{QT\|RR}}}$	$\bar{\xi}^{HF} \pm s_\xi^{HF}$, ms^2	$\frac{100\lvert\bar{\xi}^{HF}\rvert}{P^{HF}_{\mathrm{QT\|RR}}} \pm \frac{100\lvert s_\xi^{HF}\rvert}{P^{HF}_{\mathrm{QT\|RR}}}$
$1/C^{X}_{ma(30dB)}$	49	-36.6 ± 18.4	-33.6 ± 16.9	-36.6 ± 18.4	-60.5 ± 30.5	-36.6 ± 18.4	-75.4 ± 38.0
$1/C^{X}_{ma(25dB)}$	49	-36.4 ± 19.4	-33.4 ± 17.8	-36.4 ± 19.4	-60.2 ± 32.0	-36.4 ± 19.4	-75.1 ± 39.9
$1/C^{X}_{ma(20dB)}$	48	-34.9 ± 19.7	-32.0 ± 18.1	-34.9 ± 19.7	-57.7 ± 32.6	-34.9 ± 19.7	-72.0 ± 40.6
$1/C^{X}_{ma(15dB)}$	49	-33.0 ± 21.3	-30.3 ± 19.5	-33.0 ± 21.3	-54.5 ± 35.2	-33.0 ± 21.3	-68.0 ± 43.9
$1/C^{X}_{ma(10dB)}$	49	-28.4 ± 23.8	-26.1 ± 21.9	-28.4 ± 23.8	-47.0 ± 39.4	-28.4 ± 23.8	-58.6 ± 49.1
$2/C^{X}_{ma(30dB)}$	49	-20.3 ± 11.1	-32.5 ± 17.8	-20.3 ± 11.1	-59.7 ± 32.6	-20.3 ± 11.1	-71.2 ± 38.9
$2/C^{X}_{ma(25dB)}$	49	-21.4 ± 11.6	-34.3 ± 18.5	-21.4 ± 11.6	-63 ± 34.1	-21.4 ± 11.6	-75.2 ± 40.6
$2/C^{X}_{ma(20dB)}$	48	-19.3 ± 11.2	-30.8 ± 17.9	-19.3 ± 11.2	-56.6 ± 32.9	-19.3 ± 11.2	-67.6 ± 39.2
$2/C^{X}_{ma(15dB)}$	49	-18.0 ± 13.6	-28.8 ± 21.7	-18.0 ± 13.6	-53.0 ± 40.0	-18.0 ± 13.6	-63.2 ± 47.7
$2/C^{X}_{ma(10dB)}$	49	-17.7 ± 13.0	-28.4 ± 20.9	-17.7 ± 13.0	-52.2 ± 38.4	-17.7 ± 13.0	-62.2 ± 45.8
$3/C^{X}_{ma(30dB)}$	49	-12.4 ± 6.9	-32.5 ± 18.0	-12.4 ± 6.9	-58.9 ± 32.6	-12.4 ± 6.9	-72.7 ± 40.3
$3/C^{X}_{ma(25dB)}$	49	-11.4 ± 8.4	-29.9 ± 21.9	-11.4 ± 8.4	-54.2 ± 39.7	-11.4 ± 8.4	-66.9 ± 49.0
$3/C^{X}_{ma(20dB)}$	48	-11.0 ± 7.1	-28.7 ± 18.6	-11.0 ± 7.1	-51.9 ± 33.6	-11.0 ± 7.1	-64.1 ± 41.5
$3/C^{X}_{ma(15dB)}$	49	-9.7 ± 7.9	-25.4 ± 20.8	-9.7 ± 7.9	-46.1 ± 37.6	-9.7 ± 7.9	-56.8 ± 46.4
$3/C^{X}_{ma(10dB)}$	49	-8.8 ± 8.6	-23.0 ± 22.6	-8.8 ± 8.6	-41.7 ± 40.9	-8.8 ± 8.6	-51.5 ± 50.4
$4/C^{X}_{ma(30dB)}$	49	-7.6 ± 4.4	-30.4 ± 17.7	-7.6 ± 4.4	-54.5 ± 31.7	-7.6 ± 4.4	-68.8 ± 40.0
$4/C^{X}_{ma(25dB)}$	49	-7.9 ± 4.5	-31.4 ± 17.9	-7.9 ± 4.5	-56.2 ± 32.1	-7.9 ± 4.5	-70.9 ± 40.4
$4/C^{X}_{ma(20dB)}$	48	-6.9 ± 5.4	-27.4 ± 21.3	-6.9 ± 5.4	-49.2 ± 38.3	-6.9 ± 5.4	-62.0 ± 48.3
$4/C^{X}_{ma(15dB)}$	49	-6.2 ± 6.1	-24.8 ± 24.2	-6.2 ± 6.1	-44.5 ± 43.5	-6.2 ± 6.1	-56.1 ± 54.8
$4/C^{X}_{ma(10dB)}$	49	-4.7 ± 6.5	-18.9 ± 25.8	-4.7 ± 6.5	-33.9 ± 46.2	-4.7 ± 6.5	-42.8 ± 58.3
$5/C^{X}_{ma(30dB)}$	49	-3.2 ± 2.0	-33.7 ± 20.7	-3.2 ± 2.0	-58.8 ± 36.1	-3.2 ± 2.0	-78.9 ± 48.4
$5/C^{X}_{ma(25dB)}$	49	-3.0 ± 2.1	-31.8 ± 21.8	-3.0 ± 2.1	-55.4 ± 38.1	-3.0 ± 2.1	-74.4 ± 51.1
$5/C^{X}_{ma(20dB)}$	48	-2.2 ± 2.8	-22.8 ± 28.7	-2.2 ± 2.8	-39.8 ± 50.2	-2.2 ± 2.8	-53.3 ± 67.3
$5/C^{X}_{ma(15dB)}$	49	-2.2 ± 3.0	-23.4 ± 30.8	-2.2 ± 3.0	-40.9 ± 53.8	-2.2 ± 3.0	-54.8 ± 72.2
$5/C^{X}_{ma(10dB)}$	49	-0.7 ± 4.3	-6.8 ± 44.7	-0.7 ± 4.3	-11.9 ± 78.0	-0.7 ± 4.3	-16.0 ± 104.6
$6/C^{X}_{ma(30dB)}$	49	-1.3 ± 0.7	-38.8 ± 21.8	-1.3 ± 0.7	-71.2 ± 39.9	-1.3 ± 0.7	-85.4 ± 47.9
$6/C^{X}_{ma(25dB)}$	49	-0.9 ± 1.5	-26.4 ± 46.5	-0.9 ± 1.5	-48.4 ± 85.2	-0.9 ± 1.5	-58.1 ± 102.2
$6/C^{X}_{ma(20dB)}$	49	-0.2 ± 2.1	-5.3 ± 64.0	-0.2 ± 2.1	-9.7 ± 117.3	-0.2 ± 2.1	-11.6 ± 140.8
$6/C^{X}_{ma(15dB)}$	49	0.1 ± 1.9	1.7 ± 58.2	0.1 ± 1.9	3.2 ± 106.7	0.1 ± 1.9	3.8 ± 128.0
$6/C^{X}_{ma(10dB)}$	49	1.1 ± 2.5	34.8 ± 76.7	1.1 ± 2.5	63.9 ± 140.6	1.1 ± 2.5	76.6 ± 168.8

Table E.4: Mean and standard deviation of the percentage errors $\varepsilon^{\mathcal{B}}$ in data sets with baseline wandering contamination (MIT pre-recorded Noise) ($\%, mean \pm sd$); the reference value of $R^{\mathcal{B}}_{\mathrm{QT|RR}}$ can be found in Table 2.3.

QT model / data set	$\overline{\varepsilon}^{TP} \pm s_{\varepsilon}^{TP}$	$\overline{\varepsilon}^{LF} \pm s_{\varepsilon}^{LF}$	$\overline{\varepsilon}^{HF} \pm s_{\varepsilon}^{HF}$
$1/C^{X}_{bw(30dB)}$	-9.1 ± 7.1	-2.5 ± 10.2	-20.5 ± 6.2
$1/C^{X}_{bw(25dB)}$	-9.3 ± 6.4	-3.0 ± 9.9	-20.2 ± 6.3
$1/C^{X}_{bw(20dB)}$	-8.4 ± 7.0	-1.9 ± 10.0	-19.5 ± 6.5
$1/C^{X}_{bw(15dB)}$	-9.0 ± 7.1	-2.7 ± 10.9	-19.6 ± 6.2
$1/C^{X}_{bw(10dB)}$	-11.7 ± 6.7	-3.9 ± 10.3	-24.6 ± 6.5
$2/C^{X}_{bw(30dB)}$	-13.8 ± 6.6	-5.6 ± 11.4	-28.3 ± 7.0
$2/C^{X}_{bw(25dB)}$	-13.8 ± 6.8	-5.3 ± 10.0	-28.2 ± 8.9
$2/C^{X}_{bw(20dB)}$	-13.6 ± 7.0	-5.6 ± 10.3	-26.5 ± 7.4
$2/C^{X}_{bw(15dB)}$	-13.6 ± 8.2	-5.0 ± 13.0	-28.0 ± 7.7
$2/C^{X}_{bw(10dB)}$	-17.9 ± 6.8	-8.1 ± 11.7	-32.4 ± 8.0
$3/C^{X}_{bw(30dB)}$	-18.4 ± 6.6	-7.0 ± 10.2	-35.4 ± 7.1
$3/C^{X}_{bw(25dB)}$	-20.4 ± 6.8	-10.2 ± 10.5	-35.4 ± 9.6
$3/C^{X}_{bw(20dB)}$	-19.1 ± 7.3	-8.8 ± 11.3	-35.8 ± 7.2
$3/C^{X}_{bw(15dB)}$	-20.7 ± 6.5	-9.8 ± 11.4	-36.5 ± 6.8
$3/C^{X}_{bw(10dB)}$	-26.5 ± 5.9	-13.9 ± 12.3	-40.9 ± 11.8
$4/C^{X}_{bw(30dB)}$	-24.6 ± 7.1	-11.8 ± 11.0	-44.1 ± 7.6
$4/C^{X}_{bw(25dB)}$	-24.8 ± 7.8	-10.6 ± 13.3	-43.5 ± 11.3
$4/C^{X}_{bw(20dB)}$	-23.8 ± 6.9	-10.2 ± 11.8	-44.4 ± 7.7
$4/C^{X}_{bw(15dB)}$	-25.7 ± 7.5	-11.3 ± 14.9	-45.2 ± 9.4
$4/C^{X}_{bw(10dB)}$	-31.8 ± 7.2	-14.4 ± 17.4	-51.4 ± 11.9
$5/C^{X}_{bw(30dB)}$	-33.8 ± 5.7	-17.9 ± 14.1	-51.6 ± 9.3
$5/C^{X}_{bw(25dB)}$	-35.0 ± 6.5	-19.5 ± 16.3	-51.5 ± 10.6
$5/C^{X}_{bw(20dB)}$	-33.4 ± 7.2	-18.1 ± 13.0	-51.2 ± 8.5
$5/C^{X}_{bw(15dB)}$	-33.5 ± 7.2	-18.4 ± 13.9	-52.2 ± 8.0
$5/C^{X}_{bw(10dB)}$	-39.3 ± 6.6	-26.6 ± 10.3	-54.6 ± 11.6
$6/C^{X}_{bw(30dB)}$	-43.5 ± 4.6	-24.2 ± 19.8	-60.7 ± 4.5
$6/C^{X}_{bw(25dB)}$	-44.5 ± 4.3	-30.5 ± 12.2	-58.2 ± 12.7
$6/C^{X}_{bw(20dB)}$	-42.8 ± 5.4	-27.8 ± 16.2	-58.3 ± 9.7
$6/C^{X}_{bw(15dB)}$	-43.7 ± 4.9	-28.2 ± 18.2	-57.4 ± 14.6
$6/C^{X}_{bw(10dB)}$	-46.7 ± 4.6	-31.1 ± 19.3	-59.7 ± 12.7

Table E.5: Mean and standard deviation of the percentage errors $\varepsilon^{\mathcal{B}}$ in data sets with electrode movement contamination (MIT pre-recorded Noise) $(\%, mean \pm sd)$; the reference value of $R^{\mathcal{B}}_{\mathrm{QT|RR}}$ can be found in Table 2.3.

QT model / data set	$\overline{\varepsilon}^{TP} \pm s_{\varepsilon}^{TP}$	$\overline{\varepsilon}^{LF} \pm s_{\varepsilon}^{LF}$	$\overline{\varepsilon}^{HF} \pm s_{\varepsilon}^{HF}$
$1/C^{X}_{em(30dB)}$	-2.4 ± 6.4	-0.3 ± 9.4	-4.7 ± 5.0
$1/C^{X}_{em(25dB)}$	-3.8 ± 6.7	-1.1 ± 10.1	-7.4 ± 5.2
$1/C^{X}_{em(20dB)}$	-5.9 ± 6.5	-1.8 ± 10.0	-12.4 ± 5.2
$1/C^{X}_{em(15dB)}$	-19.4 ± 10.7	-10.3 ± 12.4	-34.0 ± 12.4
$1/C^{X}_{em(10dB)}$	-37.1 ± 10.5	-20.9 ± 16.3	-55.9 ± 13.0
$2/C^{X}_{em(30dB)}$	-3.1 ± 6.6	-0.2 ± 9.9	-6.9 ± 5.5
$2/C^{X}_{em(25dB)}$	-4.7 ± 7.1	-0.8 ± 10.5	-10.8 ± 5.6
$2/C^{X}_{em(20dB)}$	-8.7 ± 7.4	-2.7 ± 11.3	-18.2 ± 6.1
$2/C^{X}_{em(15dB)}$	-26.3 ± 11.9	-16.1 ± 14.0	-42.7 ± 14.2
$2/C^{X}_{em(10dB)}$	-44.0 ± 7.3	-28.3 ± 13.8	-63.6 ± 8.1
$3/C^{X}_{em(30dB)}$	-3.3 ± 6.7	0.4 ± 10.3	-9.2 ± 5.5
$3/C^{X}_{em(25dB)}$	-6.7 ± 7.3	-1.3 ± 10.5	-15.6 ± 5.5
$3/C^{X}_{em(20dB)}$	-15.3 ± 9.5	-7.5 ± 12.3	-27.8 ± 10.6
$3/C^{X}_{em(15dB)}$	-39.1 ± 10.8	-27.1 ± 13.9	-55.2 ± 13.3
$3/C^{X}_{em(10dB)}$	-49.9 ± 4.4	-32.4 ± 15.7	-66.9 ± 10.2
$4/C^{X}_{em(30dB)}$	-4.9 ± 7.6	-0.6 ± 11.2	-12.5 ± 5.2
$4/C^{X}_{em(25dB)}$	-9.8 ± 7.6	-3.6 ± 11.7	-20.8 ± 6.1
$4/C^{X}_{em(20dB)}$	-18.7 ± 10.6	-8.9 ± 14.4	-35.5 ± 10.8
$4/C^{X}_{em(15dB)}$	-43.1 ± 10.1	-27.8 ± 16.3	-61.4 ± 13.5
$4/C^{X}_{em(10dB)}$	-52.1 ± 4.2	-36.4 ± 13.0	-71.7 ± 5.2
$5/C^{X}_{em(30dB)}$	-10.0 ± 7.4	-3.3 ± 11.2	-20.8 ± 6.3
$5/C^{X}_{em(25dB)}$	-16.6 ± 6.8	-7.2 ± 10.6	-31.1 ± 9.1
$5/C^{X}_{em(20dB)}$	-24.9 ± 7.1	-11.2 ± 13.9	-42.2 ± 12.2
$5/C^{X}_{em(15dB)}$	-43.4 ± 9.5	-28.4 ± 19.4	-61.3 ± 6.7
$5/C^{X}_{em(10dB)}$	-50.2 ± 4.1	-37.7 ± 13.4	-64.6 ± 7.2
$6/C^{X}_{em(30dB)}$	-21.1 ± 7.3	-10.3 ± 12.1	-36.2 ± 8.1
$6/C^{X}_{em(25dB)}$	-29.6 ± 6.3	-15.7 ± 14.7	-45.0 ± 10.3
$6/C^{X}_{em(20dB)}$	-36.9 ± 6.1	-21.4 ± 17.9	-52.6 ± 11.0
$6/C^{X}_{em(15dB)}$	-48.1 ± 5.1	-32.0 ± 19.9	-63.2 ± 7.5
$6/C^{X}_{em(10dB)}$	-50.9 ± 4.1	-39.6 ± 12.0	-64.0 ± 9.7

Table E.6: Mean and standard deviation of the percentage errors $\varepsilon^{\mathcal{B}}$ in data sets with muscular artifacts contamination (MIT pre-recorded Noise) ($\%, mean \pm sd$); the reference value of $R^{\mathcal{B}}_{\mathrm{QT|RR}}$ can be found in Table 2.3.

QT model / data set	$\overline{\varepsilon}^{TP} \pm s_{\varepsilon}^{TP}$	$\overline{\varepsilon}^{LF} \pm s_{\varepsilon}^{LF}$	$\overline{\varepsilon}^{HF} \pm s_{\varepsilon}^{HF}$
$1/C^{X}_{ma(30dB)}$	-6.3 ± 7.5	-2.0 ± 11.2	-13.5 ± 5.6
$1/C^{X}_{ma(25dB)}$	-9.6 ± 7.6	-3.7 ± 11.1	-19.6 ± 6.1
$1/C^{X}_{ma(20dB)}$	-13.4 ± 6.9	-6.7 ± 10.4	-24.5 ± 5.8
$1/C^{X}_{ma(15dB)}$	-16.2 ± 7.4	-7.6 ± 11.2	-29.6 ± 7.4
$1/C^{X}_{ma(10dB)}$	-23.3 ± 13.3	-10.8 ± 17.1	-40.2 ± 17.2
$2/C^{X}_{ma(30dB)}$	-8.8 ± 7.5	-2.3 ± 10.9	-19.4 ± 6.1
$2/C^{X}_{ma(25dB)}$	-15.5 ± 7.9	-8.8 ± 12.5	-26.9 ± 6.8
$2/C^{X}_{ma(20dB)}$	-19.3 ± 6.2	-10.7 ± 9.8	-32.3 ± 5.9
$2/C^{X}_{ma(15dB)}$	-23.4 ± 7.9	-13.1 ± 12.1	-38.8 ± 8.6
$2/C^{X}_{ma(10dB)}$	-33.4 ± 7.0	-20.1 ± 11.3	-51.3 ± 10.3
$3/C^{X}_{ma(30dB)}$	-14.3 ± 7.6	-7.3 ± 11.7	-26.3 ± 7.6
$3/C^{X}_{ma(25dB)}$	-19.7 ± 7.3	-10.7 ± 11.5	-34.3 ± 9.3
$3/C^{X}_{ma(20dB)}$	-25.5 ± 6.2	-15.2 ± 10.5	-39.9 ± 7.3
$3/C^{X}_{ma(15dB)}$	-31.0 ± 7.8	-18.9 ± 12.2	-46.9 ± 10.9
$3/C^{X}_{ma(10dB)}$	-42.0 ± 5.7	-27.1 ± 13.7	-60.1 ± 11.3
$4/C^{X}_{ma(30dB)}$	-18.1 ± 7.2	-8.8 ± 10.4	-32.5 ± 9.5
$4/C^{X}_{ma(25dB)}$	-25.9 ± 6.1	-15.4 ± 12.0	-42.9 ± 7.5
$4/C^{X}_{ma(20dB)}$	-30.6 ± 6.8	-18.3 ± 12.0	-49.4 ± 6.4
$4/C^{X}_{ma(15dB)}$	-36.8 ± 7.0	-24.2 ± 11.1	-54.6 ± 11.7
$4/C^{X}_{ma(10dB)}$	-47.0 ± 4.6	-33.0 ± 8.1	-66.9 ± 8.2
$5/C^{X}_{ma(30dB)}$	-27.7 ± 7.1	-15.8 ± 11.2	-44.6 ± 6.8
$5/C^{X}_{ma(25dB)}$	-35.1 ± 5.6	-24.3 ± 9.5	-51.3 ± 9.8
$5/C^{X}_{ma(20dB)}$	-39.5 ± 5.5	-28.3 ± 9.6	-55.4 ± 6.0
$5/C^{X}_{ma(15dB)}$	-42.9 ± 5.0	-33.6 ± 7.7	-57.3 ± 9.3
$5/C^{X}_{ma(10dB)}$	-48.0 ± 4.1	-35.3 ± 14.0	-61.9 ± 11.0
$6/C^{X}_{ma(30dB)}$	-41.4 ± 4.2	-25.1 ± 16.7	-56.9 ± 7.2
$6/C^{X}_{ma(25dB)}$	-44.8 ± 5.1	-32.5 ± 11.1	-57.8 ± 14.5
$6/C^{X}_{ma(20dB)}$	-46.3 ± 4.6	-35.5 ± 8.0	-59.7 ± 12.2
$6/C^{X}_{ma(15dB)}$	-48.3 ± 3.8	-38.3 ± 7.0	-62.7 ± 6.5
$6/C^{X}_{ma(10dB)}$	-50.7 ± 2.5	-39.3 ± 11.7	-65.2 ± 6.3

Table E.7: Mean and standard deviation of the absolute errors $\xi^{\mathcal{B}}$ in data sets corresponding to single lead based delineation of ECG contaminated with real 3-lead extracted Noise ($ms^2, mean \pm sd$); number of valid models (#) are also presented for each data set; reference measures ($P^{\mathcal{B}}_{\mathrm{QT|RR}}$, $P^{\mathcal{B}}_{\mathrm{QT|QT}}$) can be found in Table 2.2.

QT model / data set	#	$\bar{\xi}^{TP} \pm s_\xi^{TP}$, ms^2	$\frac{100\lvert\bar{\xi}^{TP}\rvert}{P^{TP}_{\mathrm{QT\lvert RR}}} \pm \frac{100\lvert s_\xi^{TP}\rvert}{P^{TP}_{\mathrm{QT\lvert RR}}}$	$\bar{\xi}^{LF} \pm s_\xi^{LF}$, ms^2	$\frac{100\lvert\bar{\xi}^{LF}\rvert}{P^{LF}_{\mathrm{QT\lvert RR}}} \pm \frac{100\lvert s_\xi^{LF}\rvert}{P^{LF}_{\mathrm{QT\lvert RR}}}$	$\bar{\xi}^{HF} \pm s_\xi^{HF}$, ms^2	$\frac{100\lvert\bar{\xi}^{HF}\rvert}{P^{HF}_{\mathrm{QT\lvert RR}}} \pm \frac{100\lvert s_\xi^{HF}\rvert}{P^{HF}_{\mathrm{QT\lvert RR}}}$
$1/C^X_{v(30dB)}$	49	-36.0 ± 17.8	-33.0 ± 16.3	-36.0 ± 17.8	-59.5 ± 29.4	-36.0 ± 17.8	-74.2 ± 36.7
$1/C^X_{v(25dB)}$	49	-34.9 ± 20.0	-32.1 ± 18.3	-34.9 ± 20.0	-57.8 ± 33.0	-34.9 ± 20.0	-72.1 ± 41.2
$1/C^X_{v(20dB)}$	49	-35.8 ± 19.0	-32.8 ± 17.4	-35.8 ± 19.0	-59.1 ± 31.4	-35.8 ± 19.0	-73.7 ± 39.2
$1/C^X_{v(15dB)}$	49	-33.9 ± 21.4	-31.1 ± 19.6	-33.9 ± 21.4	-56.0 ± 35.4	-33.9 ± 21.4	-69.8 ± 44.1
$1/C^X_{v(10dB)}$	43	-30.3 ± 22.3	-27.8 ± 20.4	-30.3 ± 22.3	-50.1 ± 36.8	-30.3 ± 22.3	-62.5 ± 45.9
$2/C^X_{v(30dB)}$	49	-20.3 ± 11.0	-32.5 ± 17.6	-20.3 ± 11.0	-59.8 ± 32.3	-20.3 ± 11.0	-71.3 ± 38.6
$2/C^X_{v(25dB)}$	49	-20.0 ± 12.0	-32.0 ± 19.2	-20.0 ± 12.0	-58.9 ± 35.3	-20.0 ± 12.0	-70.3 ± 42.1
$2/C^X_{v(20dB)}$	49	-20.5 ± 11.4	-32.8 ± 18.3	-20.5 ± 11.4	-60.3 ± 33.6	-20.5 ± 11.4	-72.0 ± 40.1
$2/C^X_{v(15dB)}$	49	-20.4 ± 14.0	-32.6 ± 22.4	-20.4 ± 14.0	-60.0 ± 41.2	-20.4 ± 14.0	-71.6 ± 49.2
$2/C^X_{v(10dB)}$	44	-20.2 ± 13.0	-32.3 ± 20.8	-20.2 ± 13.0	-59.4 ± 38.3	-20.2 ± 13.0	-70.9 ± 45.7
$3/C^X_{v(30dB)}$	49	-11.5 ± 6.5	-30.1 ± 17.1	-11.5 ± 6.5	-54.6 ± 31.0	-11.5 ± 6.5	-67.3 ± 38.3
$3/C^X_{v(25dB)}$	49	-11.3 ± 6.9	-29.6 ± 18.1	-11.3 ± 6.9	-53.6 ± 32.7	-11.3 ± 6.9	-66.1 ± 40.4
$3/C^X_{v(20dB)}$	49	-11.2 ± 7.9	-29.4 ± 20.7	-11.2 ± 7.9	-53.3 ± 37.5	-11.2 ± 7.9	-65.8 ± 46.3
$3/C^X_{v(15dB)}$	49	-9.9 ± 9.3	-25.9 ± 24.4	-9.9 ± 9.3	-46.9 ± 44.2	-9.9 ± 9.3	-57.8 ± 54.5
$3/C^X_{v(10dB)}$	49	-5.7 ± 14.9	-14.9 ± 39.1	-5.7 ± 14.9	-26.9 ± 70.8	-5.7 ± 14.9	-33.2 ± 87.4
$4/C^X_{v(30dB)}$	49	-7.7 ± 4.4	-30.6 ± 17.5	-7.7 ± 4.4	-54.8 ± 31.5	-7.7 ± 4.4	-69.1 ± 39.7
$4/C^X_{v(25dB)}$	49	-7.2 ± 5.2	-28.8 ± 20.5	-7.2 ± 5.2	-51.6 ± 36.8	-7.2 ± 5.2	-65.0 ± 46.5
$4/C^X_{v(20dB)}$	49	-7.0 ± 5.7	-27.8 ± 22.7	-7.0 ± 5.7	-49.8 ± 40.7	-7.0 ± 5.7	-62.9 ± 51.3
$4/C^X_{v(15dB)}$	49	-6.4 ± 6.7	-25.5 ± 26.6	-6.4 ± 6.7	-45.6 ± 47.7	-6.4 ± 6.7	-57.6 ± 60.2
$4/C^X_{v(10dB)}$	49	-2.1 ± 12.2	-8.4 ± 48.5	-2.1 ± 12.2	-15.1 ± 86.9	-2.1 ± 12.2	-19.0 ± 109.6
$5/C^X_{v(30dB)}$	49	-3.0 ± 2.0	-30.7 ± 20.7	-3.0 ± 2.0	-53.7 ± 36.1	-3.0 ± 2.0	-72.0 ± 48.5
$5/C^X_{v(25dB)}$	49	-2.5 ± 2.3	-26.2 ± 24.4	-2.5 ± 2.3	-45.7 ± 42.7	-2.5 ± 2.3	-61.4 ± 57.2
$5/C^X_{v(20dB)}$	49	-2.7 ± 2.4	-28.2 ± 25.4	-2.7 ± 2.4	-49.2 ± 44.3	-2.7 ± 2.4	-66.0 ± 59.4
$5/C^X_{v(15dB)}$	49	-2.4 ± 3.8	-24.5 ± 39.2	-2.4 ± 3.8	-42.8 ± 68.4	-2.4 ± 3.8	-57.4 ± 91.7
$5/C^X_{v(10dB)}$	45	0.0 ± 5.0	0.4 ± 52.1	0.0 ± 5.0	0.7 ± 90.9	0.0 ± 5.0	1.0 ± 122.0
$6/C^X_{v(30dB)}$	49	-1.1 ± 0.7	-34.3 ± 22.5	-1.1 ± 0.7	-63.0 ± 41.2	-1.1 ± 0.7	-75.6 ± 49.4
$6/C^X_{v(25dB)}$	49	-0.9 ± 0.8	-27.5 ± 25.1	-0.9 ± 0.8	-50.4 ± 46.0	-0.9 ± 0.8	-60.4 ± 55.2
$6/C^X_{v(20dB)}$	49	-0.6 ± 1.2	-18.3 ± 36.9	-0.6 ± 1.2	-33.6 ± 67.6	-0.6 ± 1.2	-40.3 ± 81.1
$6/C^X_{v(15dB)}$	49	-0.1 ± 1.7	-2.7 ± 50.8	-0.1 ± 1.7	-4.9 ± 93.1	-0.1 ± 1.7	-5.9 ± 111.7
$6/C^X_{v(10dB)}$	46	3.2 ± 5.4	96.3 ± 163.8	3.2 ± 5.4	176.5 ± 300.3	3.2 ± 5.4	211.8 ± 360.4

Table E.8: Mean and standard deviation of the absolute errors $\xi^{\mathcal{B}}$ in data sets corresponding to multilead based delineation of ECG contaminated with real 3-lead extracted Noise ($ms^2, mean \pm sd$); number of valid models (#) are also presented for each data set; reference measures ($P^{\mathcal{B}}_{\mathrm{QT|RR}}$, $P^{\mathcal{B}}_{\mathrm{QT|QT}}$) can be found in Table 2.2.

QT model / data set	#	$\bar{\xi}^{TP} \pm s_{\xi}^{TP}$, ms^2	$\frac{\lvert\bar{\xi}^{TP}\rvert}{P^{TP}_{\mathrm{QT\|RR}}} \pm \frac{\lvert s_{\xi}^{TP}\rvert}{P^{TP}_{\mathrm{QT\|RR}}}$	$\bar{\xi}^{LF} \pm s_{\xi}^{LF}$, ms^2	$\frac{\lvert\bar{\xi}^{LF}\rvert}{P^{LF}_{\mathrm{QT\|RR}}} \pm \frac{\lvert s_{\xi}^{LF}\rvert}{P^{LF}_{\mathrm{QT\|RR}}}$	$\bar{\xi}^{HF} \pm s_{\xi}^{HF}$, ms^2	$\frac{\lvert\bar{\xi}^{HF}\rvert}{P^{HF}_{\mathrm{QT\|RR}}} \pm \frac{\lvert s_{\xi}^{HF}\rvert}{P^{HF}_{\mathrm{QT\|RR}}}$
$1/C^{F}_{v(30dB)}$	49	-28.9 ± 20.1	-26.5 ± 18.5	-28.9 ± 20.1	-47.8 ± 33.3	-28.9 ± 20.1	-59.7 ± 41.5
$1/C^{F}_{v(25dB)}$	49	-27.7 ± 24.1	-25.4 ± 22.1	-27.7 ± 24.1	-45.8 ± 39.8	-27.7 ± 24.1	-57.1 ± 49.6
$1/C^{F}_{v(20dB)}$	32	-30.1 ± 18.3	-27.7 ± 16.8	-30.1 ± 18.3	-49.8 ± 30.3	-30.1 ± 18.3	-62.1 ± 37.8
$1/C^{F}_{v(15dB)}$	1	-45.1 ± 0.0	-41.4 ± 0.0	-45.1 ± 0.0	-74.6 ± 0.0	-45.1 ± 0.0	-93.1 ± 0.0
$1/C^{F}_{v(10dB)}$	0	-	-	-	-	-	-
$2/C^{F}_{v(30dB)}$	49	-17.0 ± 11.3	-27.1 ± 18.0	-17.0 ± 11.3	-49.9 ± 33.1	-17.0 ± 11.3	-59.5 ± 39.5
$2/C^{F}_{v(25dB)}$	49	-15.9 ± 12.1	-25.5 ± 19.3	-15.9 ± 12.1	-46.9 ± 35.5	-15.9 ± 12.1	-55.9 ± 42.3
$2/C^{F}_{v(20dB)}$	32	-15.1 ± 12.0	-24.2 ± 19.2	-15.1 ± 12.0	-44.4 ± 35.3	-15.1 ± 12.0	-53.0 ± 42.1
$2/C^{F}_{v(15dB)}$	0	-	-	-	-	-	-
$2/C^{F}_{v(10dB)}$	2	-24.3 ± 26.2	-38.9 ± 42.0	-24.3 ± 26.2	-71.5 ± 77.2	-24.3 ± 26.2	-85.3 ± 92.1
$3/C^{F}_{v(30dB)}$	49	-14.9 ± 5.9	-38.9 ± 15.4	-14.9 ± 5.9	-70.4 ± 27.9	-14.9 ± 5.9	-86.9 ± 34.5
$3/C^{F}_{v(25dB)}$	49	-12.4 ± 6.5	-32.5 ± 17.0	-12.4 ± 6.5	-58.9 ± 30.9	-12.4 ± 6.5	-72.7 ± 38.1
$3/C^{F}_{v(20dB)}$	47	-11.8 ± 6.8	-30.9 ± 17.8	-11.8 ± 6.8	-55.9 ± 32.3	-11.8 ± 6.8	-68.9 ± 39.8
$3/C^{F}_{v(15dB)}$	44	-9.2 ± 7.2	-24.2 ± 19.0	-9.2 ± 7.2	-43.8 ± 34.3	-9.2 ± 7.2	-54.0 ± 42.4
$3/C^{F}_{v(10dB)}$	16	1.0 ± 18.7	2.6 ± 49.0	1.0 ± 18.7	4.8 ± 88.7	1.0 ± 18.7	5.9 ± 109.5
$4/C^{F}_{v(30dB)}$	49	-9.4 ± 4.2	-37.5 ± 16.7	-9.4 ± 4.2	-67.3 ± 29.9	-9.4 ± 4.2	-84.9 ± 37.7
$4/C^{F}_{v(25dB)}$	49	-8.3 ± 4.7	-32.9 ± 18.5	-8.3 ± 4.7	-58.9 ± 33.2	-8.3 ± 4.7	-74.3 ± 41.9
$4/C^{F}_{v(20dB)}$	47	-7.2 ± 4.9	-28.7 ± 19.4	-7.2 ± 4.9	-51.5 ± 34.7	-7.2 ± 4.9	-65.0 ± 43.8
$4/C^{F}_{v(15dB)}$	45	-6.2 ± 5.4	-24.7 ± 21.5	-6.2 ± 5.4	-44.3 ± 38.5	-6.2 ± 5.4	-55.9 ± 48.6
$4/C^{F}_{v(10dB)}$	18	5.3 ± 16.0	21.0 ± 63.8	5.3 ± 16.0	37.6 ± 114.4	5.3 ± 16.0	47.4 ± 144.3
$5/C^{F}_{v(30dB)}$	49	-1.8 ± 1.9	-19.1 ± 19.8	-1.8 ± 1.9	-33.4 ± 34.5	-1.8 ± 1.9	-44.8 ± 46.2
$5/C^{F}_{v(25dB)}$	49	-1.9 ± 2.3	-20.2 ± 23.8	-1.9 ± 2.3	-35.2 ± 41.6	-1.9 ± 2.3	-47.3 ± 55.8
$5/C^{F}_{v(20dB)}$	31	-1.8 ± 2.9	-18.4 ± 30.1	-1.8 ± 2.9	-32.1 ± 52.5	-1.8 ± 2.9	-43.0 ± 70.4
$5/C^{F}_{v(15dB)}$	0	-	-	-	-	-	-
$5/C^{F}_{v(10dB)}$	1	11.0 ± 0.0	114.2 ± 0.0	11.0 ± 0.0	199.3 ± 0.0	11.0 ± 0.0	267.4 ± 0.0
$6/C^{F}_{v(30dB)}$	49	-0.5 ± 0.8	-14.1 ± 23.4	-0.5 ± 0.8	-25.8 ± 43	-0.5 ± 0.8	-30.9 ± 51.6
$6/C^{F}_{v(25dB)}$	49	-0.5 ± 0.9	-15.4 ± 28.1	-0.5 ± 0.9	-28.2 ± 51.4	-0.5 ± 0.9	-33.9 ± 61.7
$6/C^{F}_{v(20dB)}$	31	-0.4 ± 1.1	-12.8 ± 33.1	-0.4 ± 1.1	-23.5 ± 60.8	-0.4 ± 1.1	-28.2 ± 72.9
$6/C^{F}_{v(15dB)}$	0	-	-	-	-	-	-
$6/C^{F}_{v(10dB)}$	0	-	-	-	-	-	-

Table E.9: Mean and standard deviation of $\varepsilon^{\mathcal{B}}$in data sets corresponding to single lead based delineation of ECG contaminated with real 3-lead extracted Noise ($\%, mean \pm sd$); the reference value of $R^{\mathcal{B}}_{\mathrm{QT|RR}}$ can be found in Table 2.3.

QT model / data set	$\overline{\varepsilon}^{TP} \pm s_{\varepsilon}^{TP}$	$\overline{\varepsilon}^{LF} \pm s_{\varepsilon}^{LF}$	$\overline{\varepsilon}^{HF} \pm s_{\varepsilon}^{HF}$
$1/C^X_{v(30dB)}$	-4.0 ± 6.1	-0.7 ± 9.0	-9.7 ± 4.8
$1/C^X_{v(25dB)}$	-6.8 ± 7.1	-2.0 ± 10.2	-14.9 ± 5.9
$1/C^X_{v(20dB)}$	-10.6 ± 6.7	-3.4 ± 9.8	-22.7 ± 6.2
$1/C^X_{v(15dB)}$	-18.1 ± 8.5	-8.2 ± 11.4	-33.4 ± 9.4
$1/C^X_{v(10dB)}$	-37.4 ± 8.4	-26.1 ± 10.8	-51.6 ± 16.5
$2/C^X_{v(30dB)}$	-6.3 ± 6.8	-2.0 ± 10.5	-14.0 ± 5.4
$2/C^X_{v(25dB)}$	-10.6 ± 7.2	-4.1 ± 11.1	-21.8 ± 5.8
$2/C^X_{v(20dB)}$	-16.5 ± 6.8	-7.6 ± 10.5	-30.5 ± 7.9
$2/C^X_{v(15dB)}$	-25.2 ± 9.7	-14.0 ± 13.7	-42.0 ± 10.5
$2/C^X_{v(10dB)}$	-44.1 ± 7.6	-31.3 ± 14.2	-57.9 ± 15.6
$3/C^X_{v(30dB)}$	-8.7 ± 7.2	-2.4 ± 10.7	-18.9 ± 6.1
$3/C^X_{v(25dB)}$	-15.2 ± 7.4	-7.1 ± 11.6	-28.0 ± 7.3
$3/C^X_{v(20dB)}$	-22.7 ± 7.9	-11.0 ± 12.3	-39.4 ± 7.6
$3/C^X_{v(15dB)}$	-33.1 ± 9.6	-20.0 ± 14.5	-49.4 ± 12.1
$3/C^X_{v(10dB)}$	-50.7 ± 5.4	-36.6 ± 16.7	-62.8 ± 15.0
$4/C^X_{v(30dB)}$	-12.6 ± 7.2	-5.0 ± 10.1	-25.7 ± 6.3
$4/C^X_{v(25dB)}$	-20.0 ± 7.4	-10.1 ± 11.6	-35.9 ± 7.8
$4/C^X_{v(20dB)}$	-28.8 ± 7.3	-15.9 ± 11.4	-47.2 ± 10.1
$4/C^X_{v(15dB)}$	-38.2 ± 10.0	-22.9 ± 19.0	-57.9 ± 10.8
$4/C^X_{v(10dB)}$	-53.4 ± 4.7	-40.0 ± 13.0	-68.0 ± 13.5
$5/C^X_{v(30dB)}$	-21.0 ± 7.2	-10.2 ± 10.7	-36.6 ± 8.1
$5/C^X_{v(25dB)}$	-29.3 ± 6.7	-17.2 ± 10.4	-46.9 ± 6.1
$5/C^X_{v(20dB)}$	-37.5 ± 5.8	-23.1 ± 12.3	-55.9 ± 4.9
$5/C^X_{v(15dB)}$	-43.6 ± 7.6	-28.5 ± 19.6	-57.6 ± 16.1
$5/C^X_{v(10dB)}$	-52.4 ± 2.7	-44.2 ± 4.8	-62.5 ± 18.0
$6/C^X_{v(30dB)}$	-34.1 ± 5.9	-20.2 ± 15.5	-48.8 ± 13.1
$6/C^X_{v(25dB)}$	-40.8 ± 5.1	-26.6 ± 15.5	-53.1 ± 15.8
$6/C^X_{v(20dB)}$	-45.5 ± 4.5	-28.8 ± 18.3	-61.1 ± 7.9
$6/C^X_{v(15dB)}$	-48.5 ± 3.9	-31.0 ± 18.5	-64.0 ± 5.1
$6/C^X_{v(10dB)}$	-52.5 ± 2.0	-43.1 ± 4.6	-64.5 ± 11.1

Table E.10: Mean and standard deviation of $\varepsilon^{\mathcal{B}}$in data sets corresponding to multilead based delineation of ECG contaminated with real 3-lead extracted Noise ($\%, mean \pm sd$); the reference value of $R^{\mathcal{B}}_{\mathrm{QT|RR}}$ can be found in Table 2.3.

QT model / data set	$\overline{\varepsilon}^{TP} \pm s_{\varepsilon}^{TP}$	$\overline{\varepsilon}^{LF} \pm s_{\varepsilon}^{LF}$	$\overline{\varepsilon}^{HF} \pm s_{\varepsilon}^{HF}$
$1/C^{F}_{v(30dB)}$	-3.2 ± 6.3	-1.2 ± 9.8	-5.7 ± 5.3
$1/C^{F}_{v(25dB)}$	-4.0 ± 7.5	-0.1 ± 10.1	-10.6 ± 6.6
$1/C^{F}_{v(20dB)}$	-7.8 ± 7.4	-3.6 ± 11.0	-16.9 ± 7.0
$1/C^{F}_{v(15dB)}$	-19.8 ± 0.0	-2.1 ± 0.0	-45.9 ± 0.0
$1/C^{F}_{v(10dB)}$	-	-	-
$2/C^{F}_{v(30dB)}$	-4.3 ± 6.7	-1.3 ± 11.4	-9.2 ± 6.1
$2/C^{F}_{v(25dB)}$	-5.8 ± 6.6	-0.9 ± 10.1	-13.9 ± 5.9
$2/C^{F}_{v(20dB)}$	-11.1 ± 8.0	-4.7 ± 9.9	-22.6 ± 8.2
$2/C^{F}_{v(15dB)}$	-	-	-
$2/C^{F}_{v(10dB)}$	-53.5 ± 2.3	-41.9 ± 1.1	-72.2 ± 4.2
$3/C^{F}_{v(30dB)}$	-10.7 ± 7.0	-2.4 ± 10.3	-24.1 ± 6.3
$3/C^{F}_{v(25dB)}$	-14.8 ± 6.9	-6.0 ± 10.6	-28.1 ± 6.8
$3/C^{F}_{v(20dB)}$	-22.0 ± 7.8	-12.3 ± 12.1	-36.2 ± 10.1
$3/C^{F}_{v(15dB)}$	-35.6 ± 6.4	-22.2 ± 14.5	-53.3 ± 11.0
$3/C^{F}_{v(10dB)}$	-53.5 ± 5.1	-42.4 ± 10.2	-70.0 ± 7.5
$4/C^{F}_{v(30dB)}$	-15.4 ± 7.5	-5.5 ± 11.8	-30.8 ± 6.7
$4/C^{F}_{v(25dB)}$	-19.5 ± 7.0	-8.4 ± 12.7	-37.1 ± 8.5
$4/C^{F}_{v(20dB)}$	-27.6 ± 7.1	-15.9 ± 12.8	-43.6 ± 10.3
$4/C^{F}_{v(15dB)}$	-40.4 ± 6.3	-24.8 ± 16.5	-56.2 ± 19.4
$4/C^{F}_{v(10dB)}$	-55.1 ± 3.9	-37.3 ± 16.9	-72.8 ± 9.6
$5/C^{F}_{v(30dB)}$	-10.0 ± 6.9	-3.0 ± 11.2	-21.6 ± 6.2
$5/C^{F}_{v(25dB)}$	-18.7 ± 7.3	-8.3 ± 11.4	-34.4 ± 6.8
$5/C^{F}_{v(20dB)}$	-29.8 ± 7.0	-15.9 ± 14.5	-46.3 ± 9.3
$5/C^{F}_{v(15dB)}$	-	-	-
$5/C^{F}_{v(10dB)}$	-53.5 ± 0.0	-47.0 ± 0.0	-66.7 ± 0.0
$6/C^{F}_{v(30dB)}$	-18.8 ± 6.9	-8.2 ± 12.2	-33.4 ± 6.9
$6/C^{F}_{v(25dB)}$	-30.5 ± 7.1	-17.1 ± 14.4	-46.6 ± 9.8
$6/C^{F}_{v(20dB)}$	-40.0 ± 6.5	-22.2 ± 22.5	-54.8 ± 15.8
$6/C^{F}_{v(15dB)}$	-	-	-
$6/C^{F}_{v(10dB)}$	-	-	-

Table E.11: Pediatric holter data segments description - patient 1, patient 3 and patient 4.

segment	patient	record		segment, beats		x_{QT}		SNR, dB	Applicability	
id	number	number	hour	begin	end	$mean \pm s_{QT}$, ms	V, %	SNR_{ML}	LF	HF
1_D	1	2	1	1467	1816	313.8 ± 7.0	2.2	20.9	yes	no
2_D	1	2	1	2143	2492	316.5 ± 3.2	1.0	21.8	yes	no
i_D	#	1		2				# (yes)	2	0

segment	patient	record		segment, beats		x_{QT}		SNR, dB	Applicability	
id	number	number	hour	begin	end	$mean \pm s_{QT}$, ms	V, %	SNR_{ML}	LF	HF
3_D	3	7	1	2	351	409.9 ± 4.9	1.2	20.2	yes	no
4_D	3	7	1	352	701	408.8 ± 7.4	1.8	20.2	yes	no
5_D	3	7	1	702	1051	406.4 ± 4.2	1.0	19.8	yes	no
6_D	3	7	1	1052	1401	403.0 ± 4.5	1.1	19.8	yes	no
7_D	3	7	1	2297	2646	361.1 ± 7.3	2.0	21.0	yes	no
9_D	3	8	1	192	541	426.0 ± 3.5	0.8	23.8	yes	no
11_D	3	8	1	542	891	425.2 ± 3.0	0.7	24.2	yes	no
13_D	3	8	1	892	1241	422.4 ± 3.0	0.7	24.1	yes	no
15_D	3	8	1	1242	1591	419.8 ± 5.8	1.4	23.4	yes	no
3_M	3	7	1	2	351	413.6 ± 4.4	1.1	25.1	yes	no
4_M	3	7	1	352	701	410.9 ± 12.3	3.0	24.4	yes	yes
5_M	3	7	1	702	1051	410.4 ± 2.9	0.7	24.9	no	no
6_M	3	7	1	1052	1401	407.1 ± 3.1	0.8	24.8	yes	no
7_M	3	7	1	2297	2646	369.0 ± 5.2	1.4	26.2	yes	no
8_M	3	8	1	2	351	426.5 ± 2.6	0.6	26.4	no	no
10_M	3	8	1	352	701	427.4 ± 1.5	0.4	26.9	no	no
12_M	3	8	1	702	1051	425.4 ± 1.8	0.4	26.9	no	no
14_M	3	8	1	1052	1401	421.6 ± 2.2	0.5	26.8	no	no
16_M	3	8	1	1586	1935	419.5 ± 7.5	1.8	26.2	yes	no
17_M	3	8	1	1936	2285	422.6 ± 2.0	0.5	26.9	no	no
i_D	#	2		9				# (yes)	9	0
i_M	#	2		11				# (yes)	5	1

segment	patient	record		segment, beats		x_{QT}		SNR, dB	Applicability	
id	number	number	hour	begin	end	$mean \pm s_{QT}$, ms	V, %	SNR_{ML}	LF	HF
18_D	4	9	1	2	351	314.0 ± 7.6	2.4	24.3	yes	no
19_D	4	9	1	982	1331	303.1 ± 10.3	3.4	23.9	yes	yes
20_D	4	9	1	1332	1681	313.6 ± 9.2	2.9	24.1	yes	no
21_D	4	9	1	1888	2237	304.8 ± 6.8	2.2	24.3	yes	no
22_D	4	9	1	2238	2587	295.2 ± 7.2	2.4	24.2	yes	no
23_D	4	9	1	2588	2937	308.3 ± 8.2	2.7	24.4	yes	no
i_D	#	1		6				# (yes)	6	1

Table E.12: Pediatric holter data segments description - patient 5 (continued in Table E.13).

segment	patient	record		segment, beats		x_{QT}		SNR, dB	Applicability	
id	number	number	hour	begin	end	$mean \pm s_{QT}$, ms	V, %	SNR_{ML}	LF	HF
25_D	5	18	1	272	621	328.5 ± 10.8	3.3	24.9	yes	yes
26_D	5	18	1	1096	1445	325.5 ± 10.3	3.2	25.0	yes	yes
27_D	5	18	1	1503	1852	331.7 ± 7.3	2.2	25.1	yes	no
28_D	5	18	1	1853	2202	329.6 ± 7.4	2.2	24.8	yes	no
29_D	5	18	1	2203	2552	333.8 ± 6.7	2.0	24.9	yes	no
30_D	5	18	1	2553	2902	335.3 ± 6.1	1.8	24.7	yes	no
31_D	5	19	1	2	351	347.0 ± 3.3	1.0	24.2	yes	no
32_D	5	19	1	352	701	338.5 ± 4.2	1.2	23.9	yes	no
33_D	5	19	1	702	1051	338.7 ± 1.9	0.6	24.0	no	no
34_D	5	19	1	1052	1401	338.3 ± 2.1	0.6	24.0	no	no
35_D	5	19	1	1953	2302	337.3 ± 1.7	0.5	23.8	no	no
36_D	5	19	1	2303	2652	339.2 ± 1.6	0.5	23.9	no	no
37_D	5	19	1	2653	3002	339.9 ± 1.8	0.5	23.8	no	no
38_D	5	20	1	2	351	328.3 ± 20.5	6.2	24.1	yes	yes
39_D	5	20	1	573	922	333.1 ± 10.0	3.0	24.0	yes	no
40_D	5	20	1	923	1272	323.7 ± 21.8	6.7	24.0	yes	yes
41_D	5	20	1	1561	1910	310.1 ± 16.4	5.3	23.3	yes	yes
42_D	5	20	1	1911	2260	326.0 ± 6.5	2.0	24.0	yes	no
43_D	5	20	1	2261	2610	325.9 ± 7.3	2.2	23.8	yes	no
44_D	5	20	1	2611	2960	325.5 ± 5.6	1.7	24.0	yes	no
45_D	5	21	1	2	351	344.1 ± 15.0	4.4	22.9	yes	yes
46_D	5	21	1	352	701	346.7 ± 4.3	1.3	23.0	yes	no
47_D	5	21	1	702	1051	348.1 ± 4.7	1.3	22.9	yes	no
48_D	5	21	1	1052	1401	349.8 ± 3.5	1.0	23.2	yes	no
49_D	5	21	1	1560	1909	347.3 ± 3.3	0.9	23.0	yes	no
50_D	5	21	1	1910	2259	345.6 ± 3.1	0.9	22.6	yes	no
51_D	5	21	1	2260	2609	345.4 ± 2.7	0.8	22.8	no	no
52_D	5	22	1	2	351	342.4 ± 4.1	1.2	20.4	yes	no
53_D	5	22	1	352	701	340.2 ± 3.0	0.9	20.2	yes	no
54_D	5	22	1	702	1051	341.5 ± 2.8	0.8	20.1	no	no
55_D	5	22	1	1286	1635	338.0 ± 14.1	4.2	20.3	yes	yes
56_D	5	22	1	1918	2267	330.7 ± 16.5	5.0	20.2	yes	yes
i_D	#	5		32				# (yes)	25	8

Table E.13: Pediatric holter data segments description -patient 5 (continuation of Table E.12).

segment	patient	record		segment, beats		x_{QT}		SNR, dB	Applicability	
id	number	number	hour	begin	end	$mean \pm s_{QT}$, ms	V, %	SNR_{ML}	LF	HF
24_M	5	18	1	2	351	332.2 ± 7.8	2.3	27.5	yes	no
25_M	5	18	1	352	701	327.3 ± 8.5	2.6	27.5	yes	no
26_M	5	18	1	1076	1425	323.0 ± 11.3	3.5	27.5	yes	yes
27_M	5	18	1	1504	1853	331.4 ± 2.0	0.6	27.5	no	no
28_M	5	18	1	1854	2203	329.4 ± 2.2	0.7	27.3	no	no
29_M	5	18	1	2204	2553	332.6 ± 4.3	1.3	27.1	yes	no
30_M	5	18	1	2554	2903	334.5 ± 1.7	0.5	26.5	no	no
31_M	5	19	1	2	351	343.1 ± 3.5	1.0	27.1	yes	no
32_M	5	19	1	352	701	334.6 ± 3.9	1.2	26.8	yes	no
33_M	5	19	1	702	1051	334.3 ± 1.9	0.6	26.9	no	no
34_M	5	19	1	1052	1401	333.5 ± 2.1	0.6	26.9	no	no
35_M	5	19	1	1953	2302	332.0 ± 1.8	0.5	26.9	no	no
36_M	5	19	1	2303	2652	334.0 ± 1.4	0.4	27.1	no	no
37_M	5	19	1	2653	3002	334.8 ± 1.9	0.6	27.2	no	no
39_M	5	20	1	573	922	328.1 ± 9.1	2.8	27.4	yes	no
40_M	5	20	1	923	1272	320.1 ± 20.0	6.2	27.5	yes	yes
41_M	5	20	1	1561	1910	307.6 ± 14.6	4.7	26.9	yes	yes
42_M	5	20	1	1911	2260	321.5 ± 5.3	1.6	27.5	yes	no
43_M	5	20	1	2261	2610	320.8 ± 6.2	1.9	27.2	yes	no
44_M	5	20	1	2611	2960	320.6 ± 4.2	1.3	27.4	yes	no
45_M	5	21	1	2	351	341.8 ± 16.6	4.9	19.9	yes	no
46_M	5	21	1	352	701	345.1 ± 4.3	1.2	19.7	yes	no
47_M	5	21	1	702	1051	346.7 ± 4.8	1.4	19.8	yes	no
48_M	5	21	1	1052	1401	348.4 ± 3.4	1.0	20.0	yes	no
49_M	5	21	1	1560	1909	346.1 ± 3.1	0.9	20.1	yes	no
50_M	5	21	1	1910	2259	344.2 ± 2.9	0.8	20.1	no	no
51_M	5	21	1	2260	2609	344.1 ± 2.6	0.8	20.2	no	no
52_M	5	22	1	2	351	340.1 ± 3.9	1.1	24.4	yes	no
53_M	5	22	1	352	701	337.7 ± 3.0	0.9	25.8	no	no
54_M	5	22	1	702	1051	339.1 ± 2.8	0.8	26.2	no	no
55_M	5	22	1	1165	1514	332.5 ± 17.4	5.2	26.2	yes	yes
56_M	5	22	1	1897	2246	326.5 ± 19.5	6.0	26.0	yes	yes
i_M	#	5		32				# (yes)	20	5

Table E.14: Pediatric holter data segments description - patient 6.

segment	patient	record		segment, beats		x_{QT}		SNR, dB	Applicability	
id	number	number	hour	begin	end	$mean \pm s_{QT}$, ms	V, %	SNR_{ML}	LF	HF
57_D	6	23	1	412	761	307.3 ± 16.7	5.4	22.1	yes	yes
58_D	6	23	1	762	1111	301.5 ± 17.6	5.8	22.1	yes	yes
59_D	6	23	1	1112	1461	295.7 ± 22.0	7.4	21.9	yes	yes
60_D	6	23	1	1462	1811	300.4 ± 22.4	7.5	21.7	yes	yes
61_D	6	23	1	2396	2745	293.7 ± 24.8	8.4	21.1	yes	yes
62_D	6	23	1	2746	3095	289.6 ± 23.6	8.2	21.0	yes	yes
63_D	6	23	1	3096	3445	285.7 ± 25.9	9.1	20.9	yes	yes
64_D	6	25	1	2115	2464	258.0 ± 8.2	3.2	23.5	yes	no
65_D	6	25	1	2959	3308	279.2 ± 10.6	3.8	23.3	yes	yes
i_D	#	2		9				# (yes)	9	8

Table E.15: Pediatric holter data segments description - patient 7.

segment	patient	record		segment, beats		x_{QT}		SNR, dB	Applicability	
id	number	number	hour	begin	end	$mean \pm s_{QT}$, ms	V, %	SNR_{ML}	LF	HF
66_D	7	27	2	2	351	349.7 ± 3.3	0.9	17.1	yes	no
67_D	7	27	2	352	701	348.8 ± 2.6	0.8	17.3	no	no
68_D	7	27	2	702	1051	347.1 ± 1.9	0.5	17.3	no	no
69_D	7	27	2	1052	1401	347.2 ± 1.6	0.5	17.6	no	no
70_D	7	27	3	2	351	347.8 ± 3.0	0.9	17.7	no	no
71_D	7	27	3	352	701	347.7 ± 2.1	0.6	17.4	no	no
72_D	7	27	3	702	1051	352.2 ± 1.9	0.5	17.4	no	no
73_D	7	27	3	1052	1401	354.2 ± 1.7	0.5	17.5	no	no
74_D	7	27	3	1485	1834	354.1 ± 2.5	0.7	17.1	no	no
75_D	7	27	3	1835	2184	353.0 ± 3.3	0.9	16.7	yes	no
76_D	7	27	3	2185	2534	354.6 ± 3.4	0.9	17.0	yes	no
78_D	7	27	8	698	1047	363.3 ± 1.9	0.5	18.0	no	no
79_D	7	27	8	1048	1397	364.8 ± 1.4	0.4	18.0	no	no
80_D	7	27	8	1398	1747	363.2 ± 2.1	0.6	17.9	no	no
81_D	7	27	8	1748	2097	364.3 ± 2.1	0.6	17.9	no	no
82_D	7	27	10	664	1013	313.8 ± 23.3	7.4	16.3	yes	no
84_D	7	27	11	1058	1407	369.3 ± 19.0	5.1	18.7	yes	no
85_D	7	27	11	2037	2386	369.6 ± 20.7	5.6	18.8	yes	no
86_D	7	27	12	301	650	370.5 ± 17.1	4.6	19.0	yes	no
66_M	7	27	2	2	351	352.6 ± 4.9	1.4	29.9	yes	no
67_M	7	27	2	352	701	350.8 ± 4.1	1.2	30.0	yes	no
68_M	7	27	2	702	1051	348.2 ± 2.4	0.7	30.0	no	no
69_M	7	27	2	1052	1401	347.9 ± 1.8	0.5	30.2	no	no
70_M	7	27	3	2	351	348.1 ± 3.0	0.8	30.1	no	no
71_M	7	27	3	352	701	348.0 ± 2.1	0.6	30.5	no	no
72_M	7	27	3	702	1051	352.4 ± 1.8	0.5	30.7	no	no
73_M	7	27	3	1052	1401	354.6 ± 1.6	0.5	30.2	no	no
74_M	7	27	3	1490	1839	354.4 ± 2.2	0.6	26.7	no	no
75_M	7	27	3	1840	2189	353.6 ± 3.0	0.9	25.4	yes	no
76_M	7	27	3	2190	2539	354.8 ± 1.9	0.5	27.0	no	no
77_M	7	27	6	2457	2806	350.9 ± 5.5	1.6	21.2	yes	no
78_M	7	27	8	721	1070	364.4 ± 1.9	0.5	22.7	no	no
80_M	7	27	8	1393	1742	364.0 ± 2.1	0.6	22.7	no	no
83_M	7	27	10	928	1277	337.3 ± 6.9	2.1	19.2	yes	no
84_M	7	27	11	1061	1410	368.5 ± 16.7	4.5	21.8	yes	yes
85_M	7	27	11	2056	2405	365.7 ± 11.7	3.2	21.9	yes	yes
86_M	7	27	12	301	650	368.1 ± 8.2	2.2	22.1	yes	no
i_D	#	6		19				# (yes)	7	0
i_M	#	7		18				# (yes)	8	2

Table E.16: Pediatric holter data segments description - patient 8.

segment	patient	record		segment, beats		x_{QT}		SNR, dB	Applicability	
id	number	number	hour	begin	end	$mean \pm s_{QT}$, ms	V, %	SNR_{ML}	LF	HF
87_D	8	28	1	1737	2086	263.2 ± 7.3	2.8	22.5	yes	no
88_D	8	28	1	2087	2436	265.0 ± 7.8	2.9	22.5	yes	no
89_D	8	28	1	2437	2786	270.4 ± 9.2	3.4	22.6	yes	no
90_D	8	28	1	2787	3136	265.2 ± 9.9	3.7	23.2	yes	no
91_D	8	29	1	1658	2007	271.4 ± 12.4	4.6	24.4	yes	yes
92_D	8	30	1	462	811	311.1 ± 16.2	5.2	23.3	yes	yes
93_D	8	30	1	812	1161	317.8 ± 10.2	3.2	23.1	yes	yes
94_D	8	30	1	1162	1511	312.5 ± 16.0	5.1	23.2	yes	yes
95_D	8	30	1	1512	1861	310.9 ± 12.8	4.1	23.1	yes	yes
96_D	8	30	1	2726	3075	324.4 ± 8.6	2.6	23.1	yes	no
87_M	8	28	1	1737	2086	263.0 ± 7.1	2.7	26.0	yes	no
88_M	8	28	1	2087	2436	264.5 ± 7.3	2.8	26.0	yes	no
89_M	8	28	1	2437	2786	270.0 ± 9.3	3.4	26.1	yes	no
90_M	8	28	1	2787	3136	264.4 ± 9.4	3.5	26.7	yes	no
91_M	8	29	1	1658	2007	273.2 ± 12.4	4.5	27.4	yes	yes
92_M	8	30	1	462	811	312.4 ± 14.9	4.8	26.1	yes	yes
93_M	8	30	1	812	1161	318.6 ± 9.2	2.9	26.1	yes	no
94_M	8	30	1	1162	1511	313.6 ± 14.7	4.7	26.1	yes	yes
95_M	8	30	1	1512	1861	312.6 ± 11.6	3.7	26.0	yes	yes
96_M	8	30	1	2724	3073	324.5 ± 7.3	2.3	26.1	yes	no
i_D	#	3		10				# (yes)	10	5
i_M	#	3		10				# (yes)	10	4

Table E.17: Pediatric holter data segments description - patient 9 (continued in Table E.18).

segment	patient	record		segment, beats		x_{QT}		SNR, dB	Applicability	
id	number	number	hour	begin	end	$mean \pm s_{QT}$, ms	V, %	SNR_{ML}	LF	HF
97_D	9	32	1	367	716	345.3 ± 7.5	2.2	25.7	yes	no
98_D	9	32	1	717	1066	346.1 ± 6.5	1.9	26.0	yes	no
99_D	9	32	1	1067	1416	345.9 ± 6.5	1.9	25.7	yes	no
100_D	9	32	1	1417	1766	344.5 ± 6.8	2.0	25.8	yes	no
101_D	9	32	2	1211	1560	333.6 ± 8.9	2.7	24.9	yes	no
102_D	9	32	2	1733	2082	337.2 ± 14.8	4.4	24.0	yes	yes
104_D	9	32	2	2083	2432	339.6 ± 12.0	3.5	23.8	yes	yes
106_D	9	32	3	2	351	342.5 ± 9.3	2.7	24.2	yes	no
107_D	9	32	3	352	701	343.2 ± 9.0	2.6	24.1	yes	no
108_D	9	32	3	702	1051	343.2 ± 9.1	2.6	24.4	yes	no
109_D	9	32	3	1052	1401	344.2 ± 8.0	2.3	24.7	yes	no
110_D	9	32	4	285	634	365.3 ± 10.9	3	24.7	yes	yes
111_D	9	32	4	635	984	353.2 ± 7.4	2.1	24.4	yes	no
112_D	9	32	4	985	1334	349.8 ± 7.9	2.3	24.4	yes	no
113_D	9	32	4	1335	1684	350.9 ± 7.4	2.1	24.2	yes	no
114_D	9	32	5	2	351	342.7 ± 9.1	2.7	23.7	yes	no
115_D	9	32	5	352	701	342.6 ± 8.7	2.5	24.1	yes	no
116_D	9	32	5	702	1051	343.6 ± 8.9	2.6	23.9	yes	no
117_D	9	32	5	1052	1401	343.6 ± 8	2.3	24.1	yes	no
118_D	9	32	6	2	351	337.1 ± 8.4	2.5	25.2	yes	no
119_D	9	32	6	352	701	335.4 ± 7.8	2.3	25.3	yes	no
120_D	9	32	6	702	1051	333.4 ± 7.5	2.3	25.6	yes	no
121_D	9	32	6	1052	1401	331.2 ± 9.7	2.9	25.0	yes	no
122_D	9	33	1	2	351	352.5 ± 10.3	2.9	29.9	yes	yes
127_D	9	33	1	1840	2189	359.3 ± 11.1	3.1	29.2	yes	yes
128_D	9	34	1	2	351	363.7 ± 4.5	1.2	27.4	yes	no
129_D	9	34	1	352	701	371.0 ± 2.5	0.7	27.9	no	no
130_D	9	34	1	702	1051	370.9 ± 2.7	0.7	28.0	no	no
131_D	9	34	1	1052	1401	368.6 ± 2.7	0.7	27.9	no	no
132_D	9	34	2	2	351	370.5 ± 2.5	0.7	27.8	no	no
133_D	9	34	2	352	701	370.2 ± 2.5	0.7	27.7	no	no
134_D	9	34	2	702	1051	368.5 ± 2.5	0.7	27.8	no	no
135_D	9	34	2	1052	1401	367.3 ± 2.4	0.7	28.0	no	no
137_D	9	34	3	296	645	359.8 ± 2.0	0.6	27.9	no	no
138_D	9	34	3	646	995	359.6 ± 2.1	0.6	28.0	no	no

Table E.18: Pediatric holter data segments description - patient 9 (continuation of Table E.17, continued in Table E.19).

segment	patient	record		segment, beats		x_{QT}		SNR, dB	Applicability	
id	number	number	hour	begin	end	$mean \pm s_{QT}$, ms	V, %	SNR_{ML}	LF	HF
139_D	9	34	3	996	1345	360.3 ± 2.3	0.6	28.0	no	no
140_D	9	34	3	1346	1695	360.9 ± 2.2	0.6	28.0	no	no
141_D	9	34	4	993	1342	341.1 ± 10.9	3.2	25.7	yes	yes
143_D	9	34	6	2	351	389.2 ± 10.1	2.6	28.6	yes	yes
144_D	9	34	6	352	701	391.4 ± 9.5	2.4	28.5	yes	no
145_D	9	34	6	702	1051	393.4 ± 10.3	2.6	28.5	yes	yes
146_D	9	34	6	1052	1401	397.8 ± 10.6	2.7	28.5	yes	yes
148_D	9	34	7	2	351	401.8 ± 1.7	0.4	28.8	no	no
149_D	9	34	7	352	701	402.3 ± 1.7	0.4	28.8	no	no
150_D	9	34	7	2021	2370	356.7 ± 10.9	3.1	22.6	yes	yes
151_D	9	34	8	45	394	368.7 ± 1.2	0.3	26.0	no	no
152_D	9	34	8	395	744	368.9 ± 1.1	0.3	26.0	no	no
154_D	9	34	8	745	1094	368.6 ± 1.7	0.5	26.1	no	no
155_D	9	34	8	1095	1444	368.6 ± 1.2	0.3	25.9	no	no
156_D	9	34	9	2	351	364.3 ± 1.5	0.4	25.9	no	no
157_D	9	34	9	352	701	364.7 ± 1.5	0.4	26.0	no	no
158_D	9	34	9	702	1051	365.1 ± 1.5	0.4	26.0	no	no
160_D	9	34	9	1052	1401	363.6 ± 1.5	0.4	26.0	no	no
161_D	9	34	10	2	351	363.1 ± 1.8	0.5	25.9	no	no
162_D	9	34	10	352	701	364.1 ± 1.8	0.5	25.9	no	no
163_D	9	34	10	702	1051	364.8 ± 1.5	0.4	26.0	no	no
164_D	9	34	10	1052	1401	365.9 ± 1.5	0.4	26.1	no	no
165_D	9	34	11	2	351	351.8 ± 3.9	1.1	25.2	yes	no
166_D	9	34	11	352	701	358.8 ± 1.7	0.5	25.6	no	no
167_D	9	34	11	702	1051	361.1 ± 1.9	0.5	25.6	no	no
168_D	9	34	11	1052	1401	362.5 ± 1.7	0.5	26.0	no	no
170_D	9	34	12	203	552	338.4 ± 4.5	1.3	22.3	yes	no
171_D	9	34	12	553	902	346.5 ± 3.3	1.0	24.9	yes	no
172_D	9	34	12	903	1252	353.5 ± 1.9	0.5	25.2	no	no
173_D	9	34	12	1327	1676	338.4 ± 5.7	1.7	20.6	yes	no
174_D	9	34	12	1677	2026	338.0 ± 4.9	1.5	22.4	yes	no
175_D	9	34	12	2027	2376	345.0 ± 3.4	1.0	24.3	yes	no
176_D	9	34	12	2377	2726	351.8 ± 2.8	0.8	25.0	no	no
178_D	9	34	13	432	781	349.5 ± 5.7	1.6	23.1	yes	no
183_D	9	34	13	2403	2752	356.7 ± 3.6	1.0	24.8	yes	no
i_D	#	19		70				# (yes)	40	10

Table E.19: Pediatric holter data segments description - patient 9 (continuation of Table E.18, continued in Table E.20).

segment	patient	record		segment, beats		x_{QT}		SNR, dB	Applicability	
id	number	number	hour	begin	end	$mean \pm s_{QT}$, ms	V, %	SNR_{ML}	LF	HF
97_M	9	32	1	367	716	348.5 ± 1.6	0.5	28.7	no	no
98_M	9	32	1	717	1066	348.8 ± 1.4	0.4	28.6	no	no
99_M	9	32	1	1067	1416	348.5 ± 1.3	0.4	28.4	no	no
100_M	9	32	1	1417	1766	347.6 ± 1.3	0.4	28.5	no	no
101_M	9	32	2	1211	1560	338.2 ± 4.2	1.2	28.1	yes	no
103_M	9	32	2	1913	2262	343.9 ± 16.8	4.9	26.9	yes	yes
105_M	9	32	2	2263	2612	345.7 ± 9.1	2.6	27.6	yes	no
106_M	9	32	3	2	351	349.3 ± 1.2	0.4	28.1	no	no
107_M	9	32	3	352	701	349.2 ± 1.2	0.3	28.0	no	no
108_M	9	32	3	702	1051	349.4 ± 1.2	0.3	28.0	no	no
109_M	9	32	3	1052	1401	349.5 ± 1.3	0.4	28.0	no	no
110_M	9	32	4	285	634	369.7 ± 8.0	2.2	27.7	yes	no
111_M	9	32	4	635	984	357.1 ± 2.0	0.6	27.9	no	no
112_M	9	32	4	985	1334	354.3 ± 1.3	0.4	27.9	no	no
113_M	9	32	4	1335	1684	354.6 ± 3.1	0.9	27.8	yes	no
114_M	9	32	5	2	351	349.7 ± 1.5	0.4	27.6	no	no
115_M	9	32	5	352	701	349.7 ± 1.5	0.4	27.6	no	no
116_M	9	32	5	702	1051	350.2 ± 1.4	0.4	27.7	no	no
117_M	9	32	5	1052	1401	349.0 ± 1.4	0.4	27.7	no	no
118_M	9	32	6	2	351	341.5 ± 2.7	0.8	29.3	no	no
119_M	9	32	6	352	701	339.7 ± 2.4	0.7	29.2	no	no
120_M	9	32	6	702	1051	338.1 ± 2.3	0.7	29.4	no	no
121_M	9	32	6	1052	1401	336.7 ± 2.1	0.6	29.5	no	no
122_M	9	33	1	126	475	350.4 ± 6.7	1.9	29.7	yes	no
123_M	9	33	1	476	825	356.7 ± 5.3	1.5	29.6	yes	no
124_M	9	33	1	826	1175	356.0 ± 6.0	1.7	29.5	yes	no
125_M	9	33	1	1176	1525	358.1 ± 5.8	1.6	29.4	yes	no
126_M	9	33	1	1535	1884	356.0 ± 8.5	2.4	29.3	yes	no
127_M	9	33	1	1885	2234	359.8 ± 5.5	1.5	28.8	yes	no
128_M	9	34	1	2	351	359.0 ± 4.9	1.4	30.0	yes	no
129_M	9	34	1	352	701	364.7 ± 4.1	1.1	30.4	yes	no
130_M	9	34	1	702	1051	364.1 ± 4.2	1.2	30.5	yes	no
131_M	9	34	1	1052	1401	362.5 ± 4.3	1.2	30.6	yes	no
132_M	9	34	2	2	351	363.5 ± 4.5	1.2	30.4	yes	no
133_M	9	34	2	352	701	363.7 ± 4.8	1.3	30.4	yes	no
134_M	9	34	2	702	1051	362.1 ± 4.5	1.2	30.5	yes	no
135_M	9	34	2	1052	1401	361.2 ± 4.3	1.2	30.5	yes	no
136_M	9	34	3	2	351	354.1 ± 3.9	1.1	30.5	yes	no
137_M	9	34	3	352	701	354.6 ± 3.7	1.0	30.6	yes	no
138_M	9	34	3	702	1051	355.1 ± 4.2	1.2	30.7	yes	no
139_M	9	34	3	1052	1401	354.3 ± 3.7	1.0	30.6	yes	no
141_M	9	34	4	876	1225	331.8 ± 7.8	2.3	28.0	yes	no
142_M	9	34	4	1226	1575	346.6 ± 4.9	1.4	28.9	yes	no

Table E.20: Pediatric holter data segments description - patient 9 (continuation of Table E.19.

segment	patient	record		segment, beats		x_{QT}		SNR, dB	Applicability	
id	number	number	hour	begin	end	$mean \pm s_{QT}$, ms	V, %	SNR_{ML}	LF	HF
144_M	9	34	6	315	664	393.1 ± 11	2.8	31.1	yes	yes
145_M	9	34	6	665	1014	396.8 ± 12.2	3.1	31.1	yes	yes
146_M	9	34	6	1228	1577	407.5 ± 13.6	3.3	31.0	yes	yes
147_M	9	34	6	1857	2206	400.8 ± 10.9	2.7	31.4	yes	yes
148_M	9	34	7	2	351	402.2 ± 1.8	0.5	31.0	no	no
149_M	9	34	7	352	701	402.8 ± 2.0	0.5	31.1	no	no
150_M	9	34	7	2066	2415	357.3 ± 9.4	2.6	28.1	yes	no
151_M	9	34	8	45	394	368.5 ± 1.3	0.4	31.0	no	no
152_M	9	34	8	395	744	368.8 ± 5.8	1.6	31.1	yes	no
154_M	9	34	8	745	1094	368.4 ± 1.6	0.4	30.9	no	no
155_M	9	34	8	1095	1444	368.1 ± 1.3	0.4	30.9	no	no
156_M	9	34	9	2	351	363.8 ± 1.4	0.4	30.7	no	no
157_M	9	34	9	352	701	364.3 ± 1.5	0.4	30.7	no	no
158_M	9	34	9	702	1051	364.7 ± 1.4	0.4	30.8	no	no
160_M	9	34	9	1052	1401	363.2 ± 1.5	0.4	30.7	no	no
161_M	9	34	10	2	351	362.5 ± 1.8	0.5	30.6	no	no
162_M	9	34	10	352	701	363.4 ± 1.9	0.5	30.7	no	no
163_M	9	34	10	702	1051	364.1 ± 1.6	0.4	30.8	no	no
164_M	9	34	10	1052	1401	365.2 ± 1.5	0.4	30.8	no	no
165_M	9	34	11	2	351	351.1 ± 3.7	1.1	29.9	yes	no
166_M	9	34	11	352	701	357.9 ± 1.6	0.4	30.2	no	no
167_M	9	34	11	702	1051	359.8 ± 1.8	0.5	30.2	no	no
168_M	9	34	11	1052	1401	360.8 ± 2.1	0.6	30.6	no	no
169_M	9	34	11	2082	2431	324.0 ± 6.7	2.1	24.8	yes	no
170_M	9	34	12	203	552	337.0 ± 4.9	1.5	27.7	yes	no
171_M	9	34	12	553	902	346.0 ± 3.2	0.9	29.7	yes	no
172_M	9	34	12	903	1252	352.9 ± 1.7	0.5	30.0	no	no
173_M	9	34	12	1253	1602	340.4 ± 7.6	2.2	26.8	yes	no
177_M	9	34	13	2	351	333.7 ± 12.2	3.7	27.4	yes	yes
178_M	9	34	13	432	781	347.3 ± 5.5	1.6	29.1	yes	no
179_M	9	34	13	782	1131	350.7 ± 3.3	0.9	29.3	yes	no
180_M	9	34	13	1396	1745	346.4 ± 4.8	1.4	29.6	yes	no
181_M	9	34	13	1746	2095	351.0 ± 3.6	1.0	29.9	yes	no
182_M	9	34	13	2096	2445	352.7 ± 3.7	1.0	29.9	yes	no
i_M	#	19		77				# (yes)	42	6

Appendix F

Limits of applicability: Graphic display

In Chapter 4, the proposed methodology for ECG delineation and QTV study was jointly validated over simulated ECG signals, considering several types and levels of noise. In particular, realistic 3-lead extracted noise (data set C_v^F) was used to established the indicative range of applicability of the proposed methods, that is, the QTV and SNR levels for which the QTV fractions can be estimated with an admissible error (less than 25%).

These limits are based on the percentage error distributions found in the simulated data presented in Figures 4.15 and 4.16, and repeated in Figure F.1. To allow a more intuitive use, the applicability as function of QTV, SNR and delineation system can be alternatively summarized graphically, as presented in Figure F.2, considering separately the delineation systems and frequency bands.

For each SNR level it was addressed the minimum QT standard deviation level (QT reference model) for which an error tolerance degree d% was accomplished. For that purpose, it was checked if the $\varepsilon^{\mathcal{B}}$ quartile box was within the chosen tolerance degree. That corresponds, for each SNR level, to:

- look to a zero-centered band of semi-amplitude equal to d% over the plots of the percentage error distributions presented in Figure F.1;
- check if the quartile box for the QT model 1 for the SNR level is within that band;
- if so, the quartile box for the QT model 2 is checked and so on until the tolerance degree is not accomplished for a QT model;
- the reference standard deviation value σ_{QT} corresponding to the last model (the one with lowest QTV) for which the criteria is fulfilled is taken as the applicability limit for that SNR level.

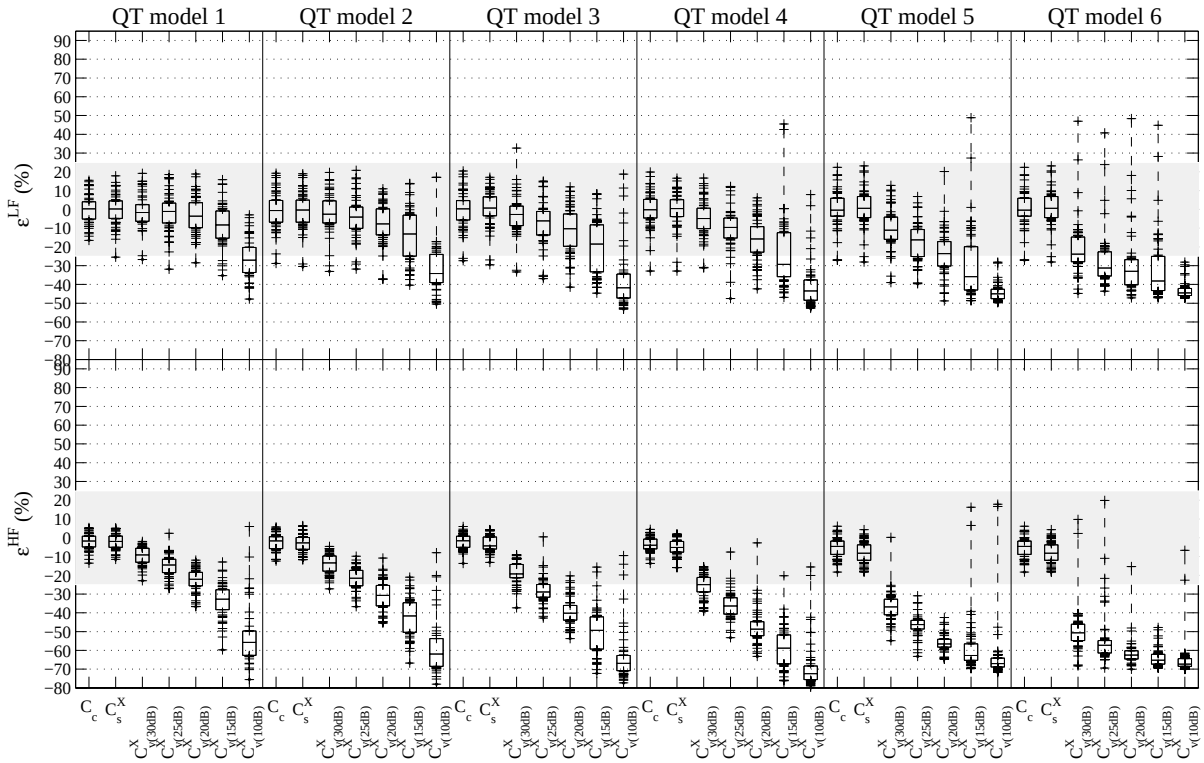

(a) single-lead

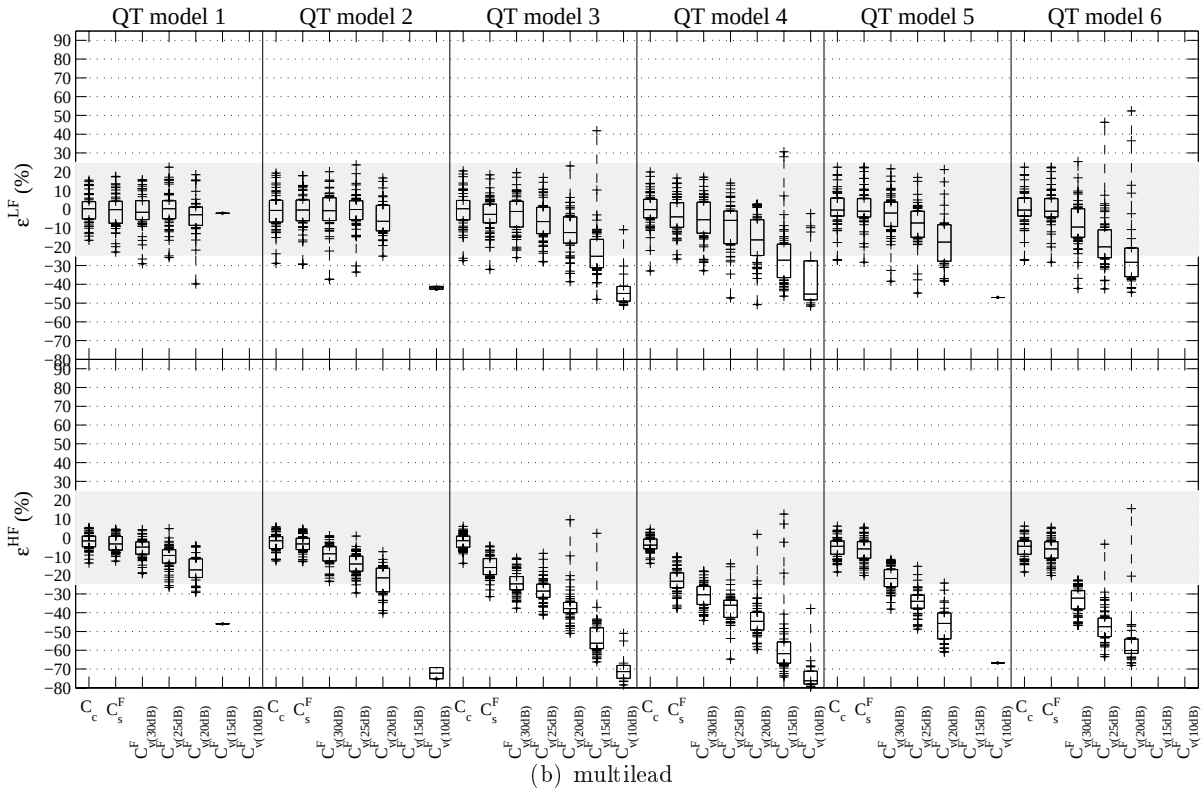

(b) multilead

Figure F.1: Distributions of $\xi^{\mathcal{B}}$ in data sets corresponding to single-lead and multilead based delineation of ECG contaminated with real 3-lead extracted Noise - box-and-whisker plot by data set and frequency band (same plots as in Figures 4.15 4.16) and 25% zero-centered bands.

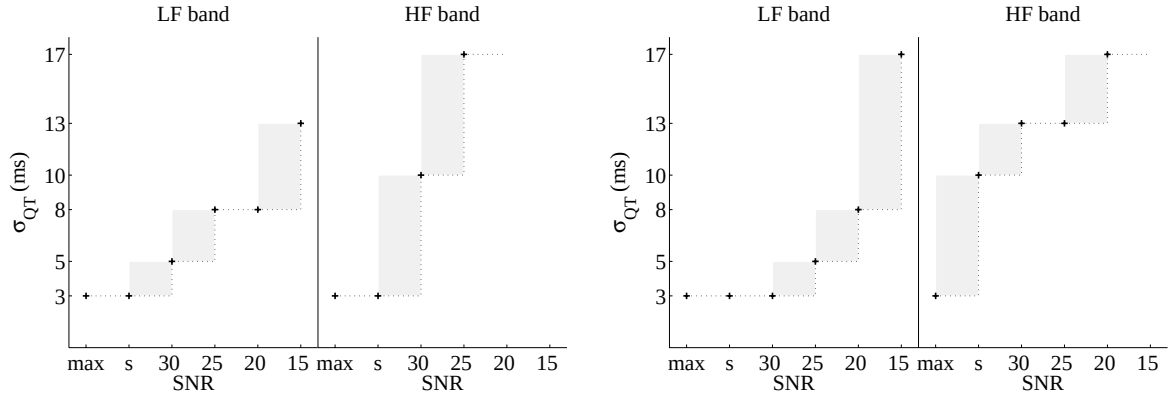

(a) Single-lead based delineation (b) Multilead delineation

Figure F.2: Minimum of σ_{QT} for data sets for which the percentage errors $\varepsilon^{\mathcal{B}}$ quartile box was within a tolerance degree 25% (indicative limits of applicability); "max" stands for values obtained for datasets C_c and "s" for datasets C_s^X or C_s^F.

For the sake of comparison in the Figure F.2 were also included the values found in the dataset C_c with clean simulated series (max), and datasets C_s^X and C_s^F corresponding to the signal derived series(s)datasets. As data is only available for the values considered in the simulation study, only the σ_{QT} values included in the simulation are indicated in the vertical axis; the grey rectangles correspond to indecision areas (transition between models). It should be observed that values for σ_{QT} are presented for a dataset or SNR level only if data from at least one QT reference model fulfilled the criteria.

The same kind of analysis can be done considering different error tolerance degrees as presented in Figure F.3.

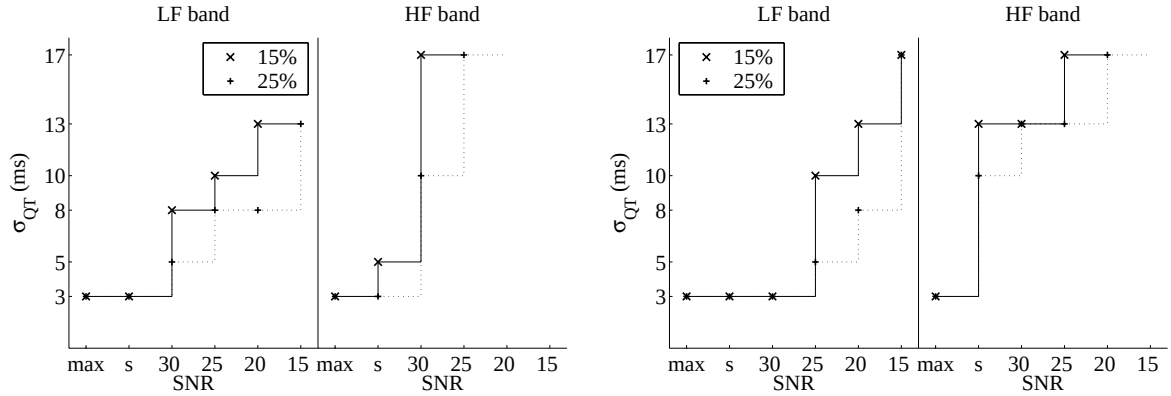

(a) Single-lead based delineation (b) Multilead delineation

Figure F.3: Minimum of σ_{QT} for data sets for which the percentage errors $\varepsilon^{\mathcal{B}}$ quartile box was within a tolerance degree of 15% or 25% (indicative limits of applicability).

List of Tables

List of Figures

References

Addison, P. S. (2005). Wavelet transforms and the ECG: a review. *Physiological Measurement* **26**, R155–R199.

Akay, M. (1996). *Detection and Estimation Methods for Biomedical Signals*. Academic Press. San Diego, CA.

Algra, A., H. Le Brunand and C. Zeelenberg (1987). An algorithm for computer measurement of QT intervals in the 24 hour ECG. In: *Computers in Cardiology 1987*. IEEE Computer Society Press. pp. 117–119.

Almeida, R., A. P. Rocha, E. Pueyo, J. P. Martínez and P. Laguna (2004*a*). Modelling short term variability interactions in ECG: QT versus RR. In: *Computational Statistics 2004*. Physica-Verlag. pp. 597–604.

Almeida, R., E. Pueyo, J. P. Martínez, A. P. Rocha and P. Laguna (2004*b*). Quantification of the QT variability related to HRV: robustness study facing automatic delineation and noise on the ECG. In: *Computers in Cardiology 2004*. Vol. 31. IEEE Computer Society Press. pp. 769–772.

Almeida, R., E. Pueyo, J. P. Martínez, A. P. Rocha, S. Olmos and P. Laguna (2003*a*). A parametric model approach for quantification of short term QT variability uncorrelated with heart rate variability. In: *Computers in Cardiology 2003*. Vol. 30. IEEE Computer Society Press. pp. 165–168.

Almeida, R., E. Pueyo, J. P. Martínez, A. P. Rocha, S. Olmos and P. Laguna (2003*b*). Quantification of short term QT variability versus heart rate variability. In: *Proceedings of 7th Portuguese Conference of Biomedical Engineering, BIOENG03*.

Almeida, R., J. P. Martínez, A. P. Rocha, P. Laguna and S. Olmos (2004*c*). ECG automatic delineation using a wavelet-based multilead approach. In: *Sixth IMA International Conference on Mathematics in Signal Processing*. pp. 15–18.

Almeida, R., J. P. Martínez, A. P. Rocha, P. Laguna and S. Olmos (2006*a*). Automatic multilead VCG based approach for QT interval measurement. In: *Computers in Cardiology 2006*. Vol. 33. pp. 369–372.

Almeida, R., J. P. Martínez, A. P. Rocha, S. Olmos and P. Laguna (2005). Improved QT variability quantification by multilead automatic delineation. In: *Computers in Cardiology 2005*. Vol. 32. IEEE Computer Society Press. pp. 503–506.

Almeida, R., J. P. Martínez, S. Olmos, A. P. Rocha and P. Laguna (2003*c*). Automatic delineation of T and P waves using a wavelet-based multiscale approach. In: *International Congress on Computational Bioengineering - Vol. 1.* pp. 243–247.

Almeida, R., S. Gouveia, A. P. Rocha, E. Pueyo, J. P. Martínez and P. Laguna (2006*b*). QT variability and HRV interactions in ECG: Quantification and reliability. *IEEE Trans. Biomed. Eng.* **53**, 1317–1329.

Aström, M., H. C. Santos, L. Sörnmo and B. Wohlfart (1998). Optimal alignment of vectorcardiographic loop, morphologic beat-to-beat variability and the presence of noise. Technical Report SPR-42. Department of Applied Electronics, Signal Processing Group, Lund University. P. O. BOX 118, S-221 00 Lund, Sweden.

Aström, M., H. C. Santos, L. Sörnmo, P. Laguna and B. Wohlfart (2000). Vectorcardiographic loop alignment and the measurement of morphologic beat-to-beat variability in noisy signals. *IEEE Trans. Biomed. Eng.* **47**(4), 497–506.

Atiga, W. L., L. Fananapazir, D. McAreavey, H. Calkins and R. D. Berger (2000). Temporal repolarization lability in hypertrophic cardiomyopathy caused by β-myosin heavy-chain gene mutations. *Circulation* **101**, 1237–1242.

Badilini, F., P. Maison-Blanche, R. Childers and P. S. Coumel (1998). QT interval analysis on ambulatory electrocardiogram recordings: a selective beat averaging approach. *Med. Biol. Eng. Comput.* **37**, 71–79.

Bahoura, M., M. Hassani and M. Hubin (1997). DSP implementation of wavelet transform for real time ECG wave forms detection and heart rate analysis. *Computer Methods and Programs in Biomedicine* **52**, 35–44.

Bailón, R., L. Sörnmo and P. Laguna (2006*a*). ECG-derived respiratory frequency estimation. In: *Advanced Methods and Tools for ECG data analysis* (G. D. Clifford, F. Azuaje and P. E. McSharry, Eds.). pp. 215–244. Artech House.

Bailón, R., L. Sörnmo and P. Laguna (2006*b*). A robust method for ECG-based estimation of the respiratory frequency during stress testing. *IEEE Trans. Biomed. Eng.* **53**, 1273–1285.

Barbieri, R., A. M. Bianchi, J. K. Triedman, L. T. Mainardi, S. Cerutti and J. P. Saul (1997). Model dependency of multivariate autogressive spectral analysis. *IEEE Eng. in Med. and Biol. Society* pp. 74–85.

Barbieri, R. and J. P. Saul (1999). Autoregressive modeling for assessing closed-loop feedback and fedforward in the arterial baroreflex. In: *Methodology and clinical applications of blood pressure and heart rate analysis* (M. Di Rienzo, G. Mancia, G. Parati, A. Pedotti and A. Zanchetti, Eds.). IOS Press.

Barbosa, P. R. B., J. Barbosa-Filho, I. Cordovil, A. B. Medeiros and J. Nadal (2000). Phase response of the spectral coherence function between heart rate variability and ventricular repolarization

duration in normal subjects. In: *Computers in Cardiology 2000*. IEEE Computer Society Press. pp. 159–162.

Baselli, G., A. Porta and G. Ferrari (1995). Models for the analysis of cardiovascular variability signals. In: *Heart Rate Variability* (M. Malik and A. J. Camm, Eds.). pp. 135–145. Futura Publishing Company Inc. NY.

Baselli, G., A. Porta, O. Rimoldi, M. Pagani and S. Cerutti (1997). Spectral decomposition in multichannel recordings based on multivariate parametric identification. *IEEE Trans. Biomed. Eng.* **44**(11), 1092–1101.

Batchvarov, V., A. Ghuran, P. Smetana, K. Hnatkova, M. Harries, P. Dilaveris, J. Camm and M. Malik (2002). QT-RR relationship in healthy subjects exhibits substantial intersubject variability and high intrasubject stability. *Am J Physiol-Heart C* **282**, H2356–H2363.

Batchvarov, V. and M. Malik (2002). Individual patterns of QT/RR relationship. *Cardiac Electrophysiology Review* **6**, 282–288.

Batsford, W. (1999). Pacemakers and antitachycardia devices. In: *Yale University School of Medicine Heart Book* (B.L. Zaret, M. Moser and L. S. Cohen, Eds.). pp. 331–338. Hearst Books. New York. Available online at http://www.med.yale.edu/library/heartbk/ (accessed in December 2006).

Benditt, D. G., D. W. Fergunson, B. P. Grubb, Kapoor W. N., Kugler J., B. B. Lerman, J. D. Maloney, A. Raviele, B. Ross, R. Sutton, M. J. Wolk and L. Douglas (1986). Tilt table testing for assessing syncope. *JACC* **28**, 263–275.

Benhorin, J., M. Merri, M. Alberti, E. Locati, A. J. Moss, W. J. Hall and L. Cui (1990). Long QT syndrome. New electrocardiographic characteristics. *Circulation* **82**, 521–527.

Berger, R. D. (2003). QT variability. *Journal of Electrocardiology* **36 suppl**(5), 83–87.

Berger, R. D., E. K. Kasper, K. L. Baughman, E. Marban, H. Calkins and G. F. Tomaselli (1997). Beat-to-beat QT interval variability novel evidence for repolarization lability in ischemic and nonischemic dilated cardiomyopathy. *Circulation* **96**(5), 1557–1565.

Christov, I., I. Otsinsky, I. Simova, R. Prokopova, E. Trendafilova and S. Naydenov (2006). Dataset of manually measured QT intervals in the electrocardiogram. *Biomedical Engineering Online* **31**(5), 5–31.

Clifford, G. D. (2006). ECG statistics, noise, artifacts and missing data. In: *Advanced Methods and Tools for ECG data analysis* (G. D. Clifford, F. Azuaje and P. E. McSharry, Eds.). pp. 55–99. Artech House.

Cohen, A. and J. Kovačević (1996). Wavelets: The mathematical background. *Proceedings of the IEEE* **84**(4), 514–522.

Colzani, R. M., M. Emdin, F. Conforti, C. Passino, M. Scalattini and G. Iervasi (2001). Hyperthyroidism is associated with lengthening of ventricular repolarization. *Clinical Endocrinology* **55**(1), 27–32.

Coumel, P., P. Maison-Blanche, D. Catuli, N Neyroud, J. Fayn and P. Rubel (1995). Different circadian behavior of the apex and end of the T wave. *Journal of Electrocardiology* **28 (Supplement)**, 138–142.

Cuomo, S., F. Marciano, M. L. Migaux, F Finizio, E. Pezzella, M. A. Losi and S. Betocchi (2004). Abnormal QT interval variability in patients with hypertrophic cardiomyopathy. Can syncope be predicted?. *Journal of Electrocardiology* **37**(2), 113–119.

Daskalov, I. K. and I. I. Christov (1999*a*). Automatic detection of the electrocardiogram T-wave end. *Med. Biol. Eng. Comput.* **37**, 348–353.

Daskalov, I. K. and I. I. Christov (1999*b*). Electrocardiogram signal preprocessing for automatic detection of QRS boundaries. *Medical Engineering and Physics* **21**, 37–44.

Daskalov, I. K., I. A. Dotsinsky and I. I. Christov (1998). Developments in ECG acquisition, preprocessing, parameter measurement and recording. *IEEE Engineering in Medicine and Biology Magazine* **17**, 50–58.

Davey, P. (1999*a*). A new physiological method for heart rate correction of the *QT* interval. *Heart* **82**, 183–186.

Davey, P. (1999*b*). *QT* interval measurement: *Q* to T_{apex} or Q to T_{end}. *J Intern Med* **246**, 145–149.

de Chazal, P. and B. G. Celler (1994). A critical review of the synthesis of the orthogonal Frank lead ECGs from the 12 lead recordings. In: *Engineering Advances: New Opportunities for Biomedical Engineers. Proceedings of the 16th Annual International Conference of the IEEE.* IEEE Computer Society Press. pp. 958–959.

de Chazal, P. and B.G. Celler (1996). Automatic measurement of the QRS onset and offset in individual ECG leads. In: *Proc 18th Ann. Int. Conf. IEEE Eng. Med. Biol. Soc.*. IEEE. Amsterdam.

Dower, G. E. (1984). The ECGD: a derivation of the ECG from VCG leads. *Journal of Electrocardiology* **17**(2), 189–91.

Edenbrandt, L. and O. Pahlm (1988). Vectorcardiogram synthesized from a 12-lead ECG - superiority of the inverse dower matrix. *Journal of Electrocardiology* **21**(4), 361–367.

Ertl, A. C., M. Pfeifer and S. N. Davis (2004). Diabetic autonomic dysfunction. In: *Primer on the Autonomic Nervous System* (D. Robertson, I. Biaggioni, G Burnstock and P. A. Low, Eds.). second ed.. pp. 328–331. Elsevier Academic Press. Englewood Cliffs, NJ.

Extramiana, F, N. Neyroud, H. V. Huikuri, M. J. Koistinen, P. Coumel and P. Maison-Blanche (1999*a*). QT interval and arrhythmic risk assessment after myocardial infaction. *Am J Cardiol* **83**, 266–269.

Extramiana, F., P. Maison-Blanche, F. Badilini, J. Pinoteau, T. Deseo and P. Coumel (1999*b*). Circadian modulation of the QT rate dependence in healthy volunteers. *Journal of Electrocardiology* **32**(1), 33–43.

Fisch, C. (2000). Centennial of the sting galvanometer and the electrocardiogram. *J Coll Cardiol* **36**(6), 1737–1745.

Franchini, K. G. and A. E. Jr Cowley (2004). Autonomic control of cardiac function. In: *Primer on the Autonomic Nervous System* (D. Robertson, I. Biaggioni, G. Burnstock and P. A. Low, Eds.). second ed.. pp. 134–138. Elsevier Academic Press. Englewood Cliffs, NJ.

Friesen, G. M., T. C. Jannett et al. (1990). A comparison of the noise sensitivity of nine QRS detection algorithms. *IEEE Trans. Biomed. Eng.* **37**(1), 85–98.

Gaita, F., C. Giustetto, F. Bianchi, C. Wolpert, R. Schimpf, R. Riccardi, S. Grossi, E. Richiardi and M. Borggrefe (2003). Short QT syndrome a familial cause of sudden death. *Circulation* **108**, 965–970.

Garcia, J. M., G. Wagner, L. Sörnmo, S. G. Olmos, P. Lander and P. L. Laguna (2000). Temporal evolution of traditional versus transformed ECG-based indexes in patients with induced myocardial ischemia. *Journal of Electrocardiology* **33**(1), 37–47.

Garibyan, L. and L. S. Lilly (2006). The electrocardiogram. In: *Pathophysiology of Heart Disease: A Collaborative Project of Medical Students and Faculty* (L. S. Lilly, Ed.). fourth ed.. pp. 80–117. Lippincott Williams & Wilkins. Sample Chapter available on line at http://connection.lww.com/products/lilly4e/SampleChapters.asp (accessed in December 2006).

Gastaldelli, A., M. Emdin, F. Conforti, S. Camastra and E. Ferrannini (2000). Insulin prolongs the QTc interval in humans. *Am J Physiol Regul Integr Comp Physiol* **279**, R2022–R2025.

Goldstein, B., D. Deking, D. J. Delong, M. H. Kempski, C. Cox, M. M. Kelly, D. D. Nichols and P. D. Woolf (1993). Autonomic cardiovascular state after severe brain injury and brain-death in children. *Critical Care Medicine* **21**, 228–233.

Gritzali, F. (1988). Towards a generalized scheme for QRS detection in ECG waveforms. *Signal Processing* **15**, 183–192.

Guillem, M. S., A. V. Sahakian and S. Swiryn (2006). Derivation of orthogonal leads from the 12-lead ECG. Accuracy of a single transform for the derivation of atrial and ventricular wave. In: *Computers in Cardiology 2006*. Vol. 33. pp. 249–252.

Gulrajani, R. M. (1998). The forward and inverse problems of electrocardiography. Gaining a better qualitative and quantitative understanding of the heart's electrical activity. *IEEE MBE Magazine* **17**(5), 84–101.

Hamill, R. W. and R. E. Shapiro (2004). Peripheral autonomic nervous system. In: *Primer on the Autonomic Nervous System* (D. Robertson, I. Biaggioni, G. Burnstock and P. A. Low, Eds.). second ed.. pp. 20–28. Elsevier Academic Press. Englewood Cliffs, NJ.

Ichimaru, Y. and G.B. Moody (1999). Development of the polysomnographic database on CD-ROM. *Psychiatry and Clinical Neurosciences* **53**, 175–177.

Iyer, V., E. R. Edelman and L. S. Lilly (2006). Basic cardiac structure and function. In: *Pathophysiology of Heart Disease: A Collaborative Project of Medical Students and Faculty* (L. S. Lilly, Ed.). fourth ed.. pp. 1–28. Lippincott Williams & Wilkins. Sample Chapter available on line at http://connection.lww.com/products/lilly4e/SampleChapters.asp (accessed in December 2006).

Jensen, B. T., C. E. Larroude, L. P. Rasmussen, N. H. Holstein-Rathlou, M. V. Hojgaard, E. Agner and J. K. Kanters (2004). Beat-to-beat QT dynamics in healthy subjects. *Ann Noninvas Electro* **9**(1), 3–11.

Jensen, B. T., S. Z. Abildstrom, C. E. Larroude, E. Agner, C. Torp-Pedersen, O. Nyvad, M. Ottesen, K. Wachtell and J. K. Kanters (2005). QT dynamics in risk stratification after myocardial infarction. *Heart Rhythm* **2**, 357–364.

Johnsen, S. and N. Andersen (1978). On power estimation in maximum entropy spectral analysis. *Geophysics* **43**(4), 681–690.

Kardys, I., J. A. Kors, I. M. van der Meer, A. Hofman, D. A. M. van der Kuip and J. C. M. Witteman (2003). Spatial QRS-T angle predicts cardiac death in a general population. *Eur. Heart J.* **24**, 1357–1364.

Kaufmann, H. (2004). Evaluation of the patient with syncope. In: *Primer on the Autonomic Nervous System* (D. Robertson, I. Biaggioni, G. Burnstock and P. A. Low, Eds.). second ed.. pp. 217–220. Elsevier Academic Press. Englewood Cliffs, NJ.

Khan, M. H. and L. I. Sinoway (2004). Congestive heart failure. In: *Primer on the Autonomic Nervous System* (D. Robertson, I. Biaggioni, G. Burnstock and P. A. Low, Eds.). second ed.. pp. 247–248. Elsevier Academic Press. Englewood Cliffs, NJ.

Kim, K. (2004). Mechanism of differentiation of autonomic neurons. In: *Primer on the Autonomic Nervous System* (D. Robertson, I. Biaggioni, G. Burnstock and P. A. Low, Eds.). second ed.. pp. 6–11. Elsevier Academic Press. Englewood Cliffs, NJ.

Kohler, B., C. Hennig and Orglmeister R. (2002). The principles of software QRS detection. *IEEE Engineering in Medicine and Biology Magazine* **21**(1), 42–57.

Laguna, P., R. G. Mark, A. Goldberger and G. B. Moody (1997). A database for evaluation of algorithms for measurement of QT and other waveform intervals in the ECG. In: *Computers in Cardiology 1997*. IEEE Computer Society Press. pp. 673–676.

Laguna, P., R. Jané and P. Caminal (1994). Automatic detection of wave boundaries in multilead ECG signals: Validation with the CSE database. *Comput. Biomed. Res.* **27**(1), 45–60.

Lang, C. C. E., J. M. M. Neilson and A. D. Flapan (2004). Abnormalities of the repolarization characteristics of patients with heart failure progress with symptom severity. *Ann Noninvas Electro* **9**(3), 257–264.

Lass, J., J. Kaik, D. Karai and M. Vainu (2001). Ventricular repolarization evaluation from surface ECG for identification of the patients with increased myocardial electrical instability. In: *23rd*

Annual International Conference of the IEEE. IEEE Engineering in Medicine and Biology Society. pp. 390–393.

Levkov, C. L. (1987). Orthogonal electrocardiogram derived from limb and chest electrodes of the conventional 12-lead system. *Med. Biol. Eng. Comput.* **25**, 155–164.

Li, C., C. Zheng and C. Tai (1995). Detection of ECG characteristic points using wavelet transforms. *IEEE Trans. Biomed. Eng.* **42**(1), 21–28.

Lilly, L. S. (editor) (2006). *Pathophysiology of Heart Disease: A Collaborative Project of Medical Students and Faculty*. fourth ed.. Lippincott Williams & Wilkins. Sample Chapters available on line at http://connection.lww.com/products/lilly4e/SampleChapters.asp (accessed in December 2006).

Ljung, L. (1999). *System identification theory for the user*. second ed.. Prentice Hall PTR. Upper Saddle River, New Jersey.

Lombardi, F., A. Colombo, A. Porta, G. Baselli, S. Cerutti and C. Fiorentini (1998). Assessment of the coupling between RT_{apex} and RR interval as an index of temporal dispersion of ventricular repolarization. *PACE* **21**, 2396–2400.

Magnano, A. R., S. Holleran, R. Ramakrishnan, J. A. Reiffel and D. M. Bloomfield (2002). Autonomic nervous system influences on QT interval in normal subjects. *J Am Coll Cardiol* **39**(11), 1820–1826.

Malik, M. and A. J. Camm (2004). *Dynamic Electrocardiography*. Blackwell Futura.

Malik, M., P. Farbom, V. Batchvarov, K. Hnatkova and J. Camm (2002). Relation between QT and RR intervals is highly individual among healthy subjects: implications for heart rate correction of the QT interval. *Heart* **87**, 220–228.

Mallat, S. (1999). *A Wavelet tour of signal processing*. second ed.. Academic Press.

Mallat, S. and S. Zhong (1992). Characterization of signals from multiscale edge. *IEEE Transactions Pattern Analysis and Machine Intelligence* **14**(7), 710–732.

Mallat, Stephane (1989). Multifrequency channel decompositions of images and wavelet models. *IEEE Trans. Acoust. Speech Signal Processing* **37**, 2091–2110.

Malmivuo, J. and R. Plonsey (1995). *Bioelectromagnetism - Principles and Applications of Bioelectric and Biomagnetic Fields*. Oxford University Press. Available online at http://butler.cc.tut.fi/ malmivuo/bem/bembook/index.htm (accessed in December 2006).

Marciano, F., S. Cuomo, M. L. Migaux and A. Vetrano (1998). Dynamic correlation between QT and RR intervals: how long is QT adaptation to heart rate?. In: *Computers in Cardiology 1998*. IEEE Computer Society Press. pp. 413–416.

Marple, S. L. (1987). *Digital spectral analysis with applications*. Prentice Hall.

Martínez, J. P., R. Almeida, A. P. Rocha, P. Laguna and S. Olmos (2006). Stability of QT measurements in the PTB database depending on the selected lead. In: *Computers in Cardiology 2006*. Vol. 33. pp. 341–344.

Martínez, J. P., R. Almeida, S. Olmos, A. P. Rocha and P. Laguna (2004). Wavelet-based ECG delineator: evaluation on standard databases. *IEEE Trans. Biomed. Eng.* **51**, 570–581.

Martínez, Juan Pablo, Salvador Olmos and Pablo Laguna (2000). Evaluation of a wavelet-based ECG waveform detector on the QT database. In: *Computers in Cardiology 2000*. IEEE Computer Society Press. pp. 81–84.

Mateo, J. and P. Laguna (2000). Improved heart rate variability signal analysis from the beat occurrence times according to the IPFM model heart timing signal. *IEEE Trans. Biomed. Eng.* **47**, 985–996.

Mateo, J. and P. Laguna (2003). Analysis of heart rate variability in the presence of ectopic beats using the heart timing signal. *IEEE Trans. Biomed. Eng.* **50**, 334–342.

McPherson, C. A. and L. E. Rosenfeld (1999). Heart rhythm disorders. In: *Yale University School of Medicine Heart Book* (B.L. Zaret, M. Moser and Cohen L. S., Eds.). pp. 195–204. Hearst Books. New York. Available online at http://www.med.yale.edu/library/heartbk/ (accessed in December 2006).

Meij, S.H., P. Klootwijk, J. Arends and J.R.T.C. Roelandt (1994). An algorithm for automatic beat-to-beat measurement of the QT-interval. In: *Computers in Cardiology 1994*. IEEE Computer Society Press. pp. 597–600.

Merri, M., A. J. Moss, J. Benhorin, E. Locati, M. Alberti and F. Badilini (1992). Relation between ventricular repolarization duration and cardiac cycle length during 24-hour holter recordings. findings in normal patients and patients with long QT syndrome. *Circulation* **85**, 1816–1821.

Merri, M., J. Benhorin, M. Alberti, E. Locati and A. J. Moss (1989). Electrocardiographic quantitation of ventricular repolarization. *Circulation* **80**, 1301–1308.

Merri, M., M. Alberti and A. J. Moss (1993). Dynamic analysis of ventricular repolarization duration from 24-hour holter recordings. *IEEE Trans. Biomed. Eng.* **40**(12), 1219–1225.

Milliez, P., A. Leenhardt, P. Maison-Blanche, E. Vicaut, F. Badilini, C. Siliste, C. Benchetrit and P. Coumel (2005). Usefulness of ventricular repolarization dynamicity in predicting arrhythmic deaths in patients with isquemic cardiomyopathy (from the european myocardial infarct amiodarone trial). *Am J Cardiol* **95**, 821–826.

Molnar, J., J. Weiss, F. Zhang and J. E. Rosenthal (1996). Evaluation of five QT correction formulas using a software-assisted method of continuous QT measurement from 24-hour holter recordings. *Am J Cardiol* **78**, 920–926.

Moody, G. B. and R. G. Mark (1990). The MIT-BIH arrhytmia database on CD-ROM and software for use with it. In: *Computers in Cardiology 1990*. IEEE Computer Society Press. pp. 185–188.

Moody, G. B., H. Koch and U. Steinhoff (2006). The Physionet Computers in Cardiology Challenge 2006: QT interval measurement. In: *Computers in Cardiology 2006*. Vol. 33. pp. 313–316.

Moody, G. B., R. G. Mark, A. Zoccola and S. Mantero (1986). Derivation of respiratory signals from multi-lead ECGs. In: *Computers in Cardiology 1985*. IEEE Computer Society Press. pp. 113–116.

Murabayashi, T., B. Fetics, D. Kass, E. Nevo, B. Gramatikov and R. D. Berger (2002). Beat-to-beat QT interval variability associated with acute myocardial isquemia. *Journal of Electrocardiology* **35**(1), 19–25.

Pahlm, O. and L. Sörnmo (1984). Software QRS detection in ambulatory monitoring - a review. *Med. Biol. Eng. Comp.* **22**, 289–297.

Pathak, A., D. Curnier, J. Fourcade, J. Roncalli, P. K. Stein, P. Hermant, M. Bousquet, P. Massabuau, J. Sénard, J. Montastruc and M. Galinier (2005). QT dynamicity: a prognostic factor for sudden cardiac death in heart failure. *European Journal of Heart Failure* **7**, 269–275.

Pellerin, D., P. Maison-Blanche, F. Extramiana, J. S. Hermida, J. F. Leclercq, A. Leenhardt and P. Coumel (2001). Autonomic influences on ventricular repolarization in congestive heart failure. *Journal of Electrocardiology* **34**(1), 35–40.

Pinciroli, F., G. Pozzi, P. Rossi, M. Piovosi, A. Capo, R. Olivieri and M. Della Torre (1998). A respiration-related EKG database. In: *Computers in Cardiology 1998*. IEEE Computer Society Press. pp. 477–480.

Porta, A., G. Baselli, E. Caiani, A. Malliani, F. Lombardi and S. Cerutti (1998). Quantifying electrocardiogram RT-RR variability interactions. *Med. Biol. Eng. Comput.* **36**, 27–34.

Pueyo, E., M. Malik and P. Laguna (2005). Beat-to-beat adaptation of QT interval to heart rate. In: *27th Annual International Conference of the IEEE Engineering in Medicine and Biology Society, 2005. IEEE-EMBS 2005.*. pp. 2475 – 2478.

Pueyo, E., P. Smetana, M. Malik and P. Laguna (2003). Evaluation of QT interval response to marked RR interval changes selected automatically in ambulatory recordings. In: *Computers in Cardiology 2003*. IEEE Computer Society Press. pp. 157–160.

Risk, M. R., J. S. Bruno, M. Llamedo Soria, P. D. Arini and R. A. M. Taborda (2005). Measurement of QT interval and duration of the QRS complex at different ECG sampling rates. In: *Computers in Cardiology 2005*. IEEE Computer Society Press. pp. 495 – 498.

Rolls, H. K., W. G. Stevenson, G. R. Strichartz and L. S. Lilly (2006). Mechanisms of cardiac arrhythmias. In: *Pathophysiology of Heart Disease: A Collaborative Project of Medical Students and Faculty* (L. S. Lilly, Ed.). fourth ed.. pp. 269–289. Lippincott Williams & Wilkins. Sample Chapter available on line at http://connection.lww.com/products/lilly4e/SampleChapters.asp (accessed in December 2006).

Rubart, M. (2004). Congenital long QT syndrome: looking beyond the heart. *Heart Rhythm* **1**(1), 65–66.

Sagie, A., M. G. Larson, R. J. Goldberg, J. R. Bengston and D. Levy (1992). An improved method for adjusting the QT interval for heart rate (the Framingham Heart Study). *Am. J. Cardiology* **70**, 791–801.

Sahambi, J. S., S. N. Tandon and R. K. P. Bhatt (1997). Using wavelet transform for ECG characterization. *IEEE Eng. in Med. and Biol.* **16**(1), 77–83.

Sahambi, J. S., S. N. Tandon and R. K. P. Bhatt (1998). Wavelet based ST-segment analysis. *Med. Biol. Eng. Comput.* **36**(9), 568–572.

Sarma, J. S. M., R. J. Sarma, M. Bilitch, D. Katz and S. L. Song (1984). An exponential formula for heart rate dependence of QT interval during exercise and cardiac pacing in humans: Reevaluation of Bazett's formula. *Am J. Cardiology* **54**, 103–108.

Shusterman, V., A. Beigel, S. I. Shah, B. Aysin, R. Weiss, V. K. Gottipaty, D. Schartzman and K. P. Anderson (1999). Changes in autonomic activity and ventricular repolarization. *Journal of Electrocardiology* **32 (Supplement)**, 185–192.

Shusterman, V., B. Aysin, S. I. Shah, S. Flanigan and K. P. Anderson (1998). Autonomic nervous system effects on ventricular repolarization and RR interval variability during head-up tilt. In: *Computers in Cardiology 1998*. IEEE Computer Society Press. pp. 717–720.

Soderstrom, T. (1974). Convergence properties of the generalised least squares identification method. *Automatica* **10**, 617–626.

Sörnmo, L. and P. Laguna (2005). *Bioelectrical Signal Processing in Cardiac and Neurological Applications*. Elsevier Academic Press.

Sosnowski, M., Z. Czyz, J. Leski, T. Petelenz and M. Tendera (1996). The coherence spectrum for quantifying beat-to-beat adaptation of RT intervals to heart rate in normal subjects and in postinfartion patients. In: *Computers in Cardiology 1996*. IEEE Computer Society Press. pp. 669–672.

Speranza, G., G. Nollo, F. Ravelli and R. Antolini (1993). Beat-to-beat measurement and analysis of the R-T interval in 24 h ECG Holter recordings. *Med. Biol. Eng. Comput.* **31**(5), 487–494.

Stramba-Badiale, M., E. H. Locati, A. Martinelli, J. Courvillet and P. J. Schwartz (1997). Gender and the relationship between ventricular repolarization and cardiac cycle length during 24-h holter recordings. *Eur. Heart J.* **18**, 1000–1006.

Strumillo, P. (2002). Nested median filtering for detecting T-wave offset in ECGs. *Electronic Letters* **38**(14), 682–683.

Tarvainen, M. P., J. Niskanen, P. A. Karjalainen, Laitinen T. and T. Lyyra-Laitinen (2006). Noise sensitivity of a principal component regression bases RT interval variability estimation method. In: *28th Annual International Conference of the IEEE Engineering in Medicine and Biology Society, 2006. IEEE-EMBS 2006.*. pp. 1145–1147.

Tarvainen, M. P., T. Laitinen, Ti. Lyyra-Laitinen, J. Niskanen and P. A. Karjalainen (2007). A principal component regression approach for estimating ventricular repolarization duration variability. *EURASIP Journal on Advances in Signal Processing* **2007**, Article ID 58358, 10 pages. doi:10.1155/2007/58358 (in press).

Task Force, of The ESC/ASPE (1996). Heart rate variability: Standards of measurement, physiological interpretation, and clinical use. *Eur. Heart J.* **17**, 354–381.

Thakor, N. V., J. G. Webster and W. J. Tompkins (1984). Estimation of QRS complex power spectrum for design of a QRS filter. *IEEE Trans. Biomed. Eng.* **31**(11), 702–706.

The CSE Working Party (1985). Recomendations for measurement standards in quantitative electrocardiography. *Eur. Heart J.* **6**, 815–825.

Tomé, A. M., A. R. Teixeira, E. W. Lang, K. Stadlthanner, A. P. Rocha and R. Almeida (2005). dAMUSE–a new tool for denoising and blind source separation. *Digital Signal Processing* **15**, 400–421.

Valensi, P. E., F. Extramiana, N. B. Johnson, G. Motte, P. Maison-Blanche and P. Coumel (2002). Influence of cardiac autonomic neuropathy on heart rate dependence of ventricular repolarization in diabetic patients. *Diabetes Care* **25**(5), 918–923.

Van Huffel, S. and J. Vandewalle (1991). *The Total Least Squares Problem: Computational Aspects and Analysis*. Vol. 9 of *Frontiers in Applied Mathematics*. Society for Industrial and Applied Mathematics. Philadelphia.

Van Mieghem, C., M. Sabbe and D. Knockaert (2004). The clinical value of the ECG in noncardiac conditions). *Chest* **124**, 1561–1576.

Vila, J. A., Y. Gang, J. M. Presedo, M. Fernandez-Delgado and M. Malik (2000). A New Approach for TU Complex Characterization. *IEEE Trans. Biomed. Eng.* **47**(6), 764–772.

Vullings, H. J. L. M., M. H. G. Verhaegen and H. B. Verbruggen (1998). Automated ECG segmentation with dynamic time warping. In: *Proc. 20th Ann. Int. Conf. of the IEEE Eng. Med. Biol. Soc. "*. IEEE. Hong Kong. pp. 163–166.

Waele, S. and P. M. T. Broersen (2003). Order selection for vector autoregressive models. *IEEE Trans. Acoust., Speech, Signal Processing* **51**(2), 427–433.

Wagner, G. S. and H. J. Marriott (1994). *Marriott's Practical Electrocardiography*. 9 ed.. Williams and Wilkins.

Willems, J. L., P. Arnaud, J. H. van Bemmel, P. J. Bourdillon, R. Degani, B. Denis, I. Graham, Harms F. M., P. W. Macfarlane, G. Mazzocca et al. (1987). A reference data base for multilead electrocardiographic computer measurement programs. *J. Am. Coll. Cardiol.* **10**(6), 1313–1321.

Yan, G. X. and C. Antzelevitch (1998). Cellular basis for the normal T wave and the electrocardiographic manifestations of the long-QT syndrome. *Circulation* **98**, 1928–1936.

Yap, Y. G. and A. J. Camm (2003). Drug induced QT prolongation and torsades de pointes. *Heart* **89**, 1363–1372.

Yasuma, F. and J. Hayano (2004). Respiratory sinus arrhythmia. Why does the heartbeat synchronize with respiratory rhythm?. *Chest* **125**, 683–690.

Yeragani, V. K., S. Adiga, N. Desai and R. D. Berger (2004). Beat-to-beat QT interval variability in atrial fibrillation with and without congestive cardiac failure. *Annals of Noninvasive Electrocardiology* **9**, 304–305.

Zaret, B.L., M. Moser and L. S. Cohen (medical editors) (1999). *Yale University School of Medicine Heart Book*. Hearst Books. New York. Available online at http://www.med.yale.edu/library/heartbk/ (accessed in December 2006).